HAL
open science

Exactly modeling the unitary dynamics of quantum interfaces with collision models

Bruno Ortega Goes

To cite this version:

Bruno Ortega Goes. Exactly modeling the unitary dynamics of quantum interfaces with collision models. Physics [physics]. Université Grenoble Alpes [2020-..], 2023. English. NNT : 2023GRALY070 . tel-04536539

HAL Id: tel-04536539

https://theses.hal.science/tel-04536539v1

Submitted on 8 Apr 2024

HAL is a multi-disciplinary open access archive for the deposit and dissemination of scientific research documents, whether they are published or not. The documents may come from teaching and research institutions in France or abroad, or from public or private research centers.

L'archive ouverte pluridisciplinaire **HAL**, est destinée au dépôt et à la diffusion de documents scientifiques de niveau recherche, publiés ou non, émanant des établissements d'enseignement et de recherche français ou étrangers, des laboratoires publics ou privés.

THÈSE

Pour obtenir le grade de

DOCTEUR DE L'UNIVERSITÉ GRENOBLE ALPES

École doctorale : PHYS - Physique
Spécialité : Nanophysique
Unité de recherche : Institut Néel

Modélisation exacte de la dynamique unitaire des interfaces quantiques avec des modèles de collision

Exactly modeling the unitary dynamics of quantum interfaces with collision models

Présentée par :

Bruno ORTEGA GOES

Direction de thèse :

Alexia AUFFEVES DIRECTRICE DE RECHERCHE, CNRS DELEGATION ALPES	Directrice de thèse

Rapporteurs :

PEROLA MILMAN
DIRECTRICE DE RECHERCHE, CNRS ILE-DE-FRANCE VILLEJUIF
DOMINIQUE SUGNY
PROFESSEUR DES UNIVERSITES, UNIVERSITE DE BOURGOGNE

Thèse soutenue publiquement le **13 novembre 2023**, devant le jury composé de :

PEROLA MILMAN DIRECTRICE DE RECHERCHE, CNRS ILE-DE-FRANCE VILLEJUIF	Rapporteure
DOMINIQUE SUGNY PROFESSEUR DES UNIVERSITES, UNIVERSITE DE BOURGOGNE	Rapporteur
SERGEY SKIPETROV DIRECTEUR DE RECHERCHE, CNRS DELEGATION ALPES	Examinateur
OLIVIER KREBS DIRECTEUR DE RECHERCHE, CNRS DELEGATION ILE-DE-FRANCE SUD	Examinateur
DAVID FERRAND PROFESSEUR DES UNIVERSITES, UNIVERSITE GRENOBLE ALPES	Président

This thesis is dedicated to the memory of my grandma Diomar.

Acknowledgments

I would like to express my sincere gratitude to my advisor, Prof. Alexia Auffèves, for granting me the invaluable opportunity to join her research group. Working in her group has allowed me to work with a timely and fascinating subject and collaborate with brilliant people. Additionally, I extend my thanks to Dr. Maria Maffei, with whom I have had enriching discussions over these years.

I extend my gratitude to the dynamic "quantum gang" in Grenoble, with whom I had the privilege of sharing wonderful moments. Patrice and Gabi, your support has been instrumental, in guiding me through the process of settling into Grenoble and providing support during challenging personal times. I offer a special thanks to Patrice for his cordialness in dedicating time to review and provide substantial insights on the manuscript draft, even though it lay outside his direct responsibilities. To Samyak, I express my gratitude for his exceptional friendship, which has been complemented by his role as an exceptional training partner. Nicolò Piccione, your friendship and readiness to engage in discussions spanning physics and music have enriched my experiences. I am indebted to Dr. Konstantina Koteva and Dr. Robert Whitney for engaging discussions and insightful presentation tips that have contributed to my growth. Collectively, your support and friendship have enriched my journey in immeasurable ways.

I express my gratitude to the exceptional individuals I had the privilege to collaborate with: Dr. Stephen Wein, whose discussions not only enriched my understanding of physics but also introduced me to neat computational techniques using Mathematica; Dr. Loïc Lanco, whose enthusiasm for discussing physics and the experiments were both inspiring and enlightening.

A special note of appreciation goes to Manuel Gundin for our stimulating discussions and his warm hospitality at C2N. His friendship extended beyond the professional realm, culminating in a memorable trip to Egypt.

I extend my thanks to the entire community at C2N (Paris), DTU, and the Niels Bohr Institute (Denmark) for hosting me during my brief secondments. Notably, I am indebted to Prof. Pascale Senellart, Prof. Neils Gregersen, Prof. Luca Vannucci, Prof. Anders Sørensen, Prof. Klaus Mølmer, Ming-Lai Chan, and José Ferreira Neto for their generosity in sharing their expertise. These experiences provided an invaluable opportunity to immerse myself in diverse scientific environments, explore various theoretical approaches, and engage with different experimental settings. This exposure significantly expanded my perspective within the vast landscape of research in this field.

Changing countries during a pandemic was tough. Going somewhere where you do not know the language and people rarely speak English (even though they can)

makes it difficult to develop a social network. Thankfully, I got lucky to meet an incredible crew of people at Néel who were willing to talk somewhere other than the lab and about something other than work. The ones I got closest to are Itália Vallerini, who in the beginning didn't drink alcohol, and by the end of her stay was stealing my whiskey and encouraging people to go to *Bario Latino*. She provided me with a series of fun memories, the '*Italia's moments*', that makes me laugh every time I think of them. For instance, when we were at the Coliseum and she forgot she had sparkling water in her bottle, when she opened it she provided a free shower to everyone around, guide included... well, at 40 degrees, it was welcome; Bruno Silva, the friend I met when struggling with the French embassy in São Paulo, and whom I finally met in Grenoble when I first arrived. He has been kind of a mentor to me. He is not only a great physicist but also a great person. Talking to him always gives me insights about life and science in general; Andrea Montero, my "Colombian" friend whom I could always count on to go on hikes and to pubs to taste some new beer, and of course, dance Cumbia and Bachata; Julio Nuñez, the best trip and social events organizer I've ever met; Ricardo Alvarado for introducing me to the bachata ways; Kylia, for always being up for some happy hour.

Lastly, I thank the gym monster, the organization freak, and my dear friend and roommate Javier(lson) Mayén. This guy took me to the hell known as *Bario Latino* for the first time. We had a lot of fun with the soirées latinas, lifting weights, playing, and discussing for hours about nothing and everything. I can't imagine how the writing process would have been if this guy was not around (in the same situation) to discuss and chill out. I hope someday he realizes that all of Thor's movies are horrible. I also thank André Schützer and Tayane for being there during these years. I had the chance to have André around since university; we had some great times making a true Brazilian barbecue and bouldering in Grenoble.

Desejo expressar minha gratidão aos membros da minha família que, mesmo sem compreender o quê e porquê, sempre apoiaram minha decisão estranha de continuar com a jornada na área da física. Em especial, quero agradecer ao meu pai, Roberto Goes, à minha tia Nelza e aos meus primos Luciane e Diego. Seu apoio inabalável tem sido um pilar fundamental ao longo dessa trajetória.

I extend my heartfelt gratitude to the friends I encountered during my master's journey in Brazil, affectionately known as the "Gangue do Landi" or the former members of QT2. Despite embarking on diverse paths that led us to different corners of the world, our bond remained unbreakable. We sustained a continuous exchange of ideas encompassing life's experiences and scientific pursuits. Our reunions at conferences and schools throughout Europe, as well as our shared travel plans, further fortified our friendship. Of course, I extend my gratitude to the boss of the group, who introduced me to this amazing field of research, Prof. Gabriel Landi.

A special appreciation is reserved for Franklin Luis, whose friendship and good vibes were pivotal over these years.

Furthermore, I am indebted to Mme. Florence Pois, Aurélie Laurant, and Leah Strauss for their assistance in navigating the French and European bureaucratic complexities.

If I have reached this point in my academic journey, it's undoubtedly thanks to the friends I forged during my bachelor's years, the "galera da salinha". Our paths

have diverged since then—some have crossed borders, others have shifted careers (the smart ones), and a few have now embraced family life. However, the shared foundation that took root at the Institute of Physics at USP remains a constant. Our mutual support and assistance have continued to this day, even though our conversations have become occasional. One individual I must mention is the great historian of science, André Fantin. He willingly reviewed my thesis introduction to ensure historical accuracy (much like Alexia, he was genuinely concerned when I initially forgot to cite Bohr... my oversight). It is always illuminating to discuss the history and philosophy of science with him. Additionally, I extend my gratitude to Andrei Sontag for his unwavering patience and friendship throughout the years.

My heartfelt appreciation goes out to my girlfriend and my esteemed philosopher/historian, Coraline. She entered my life unexpectedly, reshaping it in ways I could never have envisioned and brought Mary, the best doggy one can have, as a bonus. I thank her for her patience in recent months and for infusing my life with happiness, motivating me to remain focused on my writing and goals.

Naturally, the aforementioned names are just a few that spring to mind while composing this acknowledgment. I am genuinely grateful to all the individuals who may not have been explicitly mentioned but with whom I had the privilege of crossing paths, even if only briefly. Their contributions made this academic adventure exceedingly enjoyable and rewarding.

I gratefully acknowledge financial support from the European Union Horizon 2020 Research and Innovation Programme under the Marie Skłodowska-Curie Grant Agreement No. 861097.

Finally, I want to express my gratitude to the most important person in my life, the individual to whom this thesis is dedicated, and the one who made it possible for me to achieve this academic milestone: my granny, Diomar. She always encouraged and supported me to pursue the best education possible. She funded my English courses, stood by me as I prepared for university, cheered me on during entrance exams, and celebrated when I was admitted to USP. Despite not understanding what a physicist does, she never questioned my choices and always supported me unconditionally.

Her backing remained as I applied for positions abroad. She oscillated between happiness and sadness when I got the opportunity in France. Right up until I departed from Brazil, she continued to ask if I was certain about my choices. Despite the vast ocean separating us, we managed to maintain contact consistently (how fortunate we are to live in an era where video calls are possible.). I never imagined that the day I left Brazil would mark the final time I would ever see and hug her. Words fall short in conveying the profound *saudade* I feel, as well as my deep gratitude for her contribution to my personal growth and her support and love throughout her life.

Work it harder, make it better
Do it faster, makes us stronger
More than ever, hour after hour
Work is never over.

- Daft punk

Abstract

Quantum interfaces are ubiquitous in quantum technologies as they allow the implementation of several functionalities including quantum memories, quantum repeaters, photonic gates, and highly entangled photonic state generation. Based on the coherent coupling between quantum emitters and propagating pulses of light, they can be realized on a large variety of experimental platforms where quantum non-demolition measurements, entanglement generation, and efficient production of non-classical resources have been reported.

This thesis explores the potential of so-called collision models to model exactly the light-matter dynamics in various kinds of quantum interfaces, providing direct access to their joint entangled states. It allows us to derive analytic expressions of the device performance, whether operated as a measuring apparatus or a source of cluster states. Since our model captures light and matter as a closed system, it verifies global energy conservation, providing access to the energy budget associated with the execution of the quantum task. Initially, we review the theoretical foundation for quantum measurements and introduce figures of merit used throughout the thesis. Subsequently, we review the collision model method, which is based on waveguide quantum electrodynamics (WGQED), setting the stage for subsequent analyses. Then, we address fundamental inquiries. First, we investigate the emergence of non-classical behavior of the field scattered by a quantum emitter that interacts with an intense resonant coherent field. It reveals signatures of quantum contextuality—negativity in the Wigner function and anomalous weak values. Second, we investigate the possibility of non-destructive spin state measurement by limiting the energy budget to at most one photon. We compare the performance of two different fields: coherent field and number state superposition. We demonstrate better performance of the latter in entanglement generation, thus providing a quantum advantage. Lastly, our analysis extends to technological applications. We propose a photon-photon gate, conduct a thorough error analysis, and we perform the modeling of cutting-edge experiments envisioning the deterministic generation of highly entangled states of light.

This theoretical capacity opens the way to directly optimizing the device performance and efficiency as a function of the parameters accessible to experimentalists. It also allows us to fit experimental data with high accuracy.

Résumé

Les interfaces quantiques sont omniprésentes dans les technologies quantiques car elles permettent la mise en œuvre de plusieurs fonctionnalités, notamment les mémoires quantiques, les répéteurs quantiques, les portes photoniques et la génération d'états photoniques hautement intriqués. Basés sur le couplage cohérent entre les émetteurs quantiques et les impulsions lumineuses se propageant, ils peuvent être réalisés sur une grande variété de plates-formes expérimentales où des mesures quantiques de non-démolition, la génération d'intrication et la production efficace de ressources non classiques ont été rapportées.

Cette thèse explore le potentiel des modèles dits de collision pour modéliser exactement la dynamique lumière-matière dans divers types d'interfaces quantiques, fournissant un accès direct à leurs états intriqués communs. Cela nous permet de dériver des expressions analytiques des performances du dispositif, qu'il soit utilisé comme appareil de mesure ou comme source d'états de cluster. Puisque notre modèle capture la lumière et la matière comme un système fermé, il vérifie la conservation globale de l'énergie, donnant ainsi accès au budget énergétique associé à l'exécution de la tâche quantique. Dans un premier temps, nous passons en revue les fondements théoriques des mesures quantiques et introduisons les chiffres de mérite utilisés tout au long de la thèse. Par la suite, nous passons en revue la méthode du modèle de collision, basée sur l'électrodynamique quantique des guides d'ondes (WGQED), ouvrant la voie à des analyses ultérieures. Ensuite, nous abordons les questions fondamentales. Tout d'abord, nous étudions l'émergence d'un comportement non classique du champ diffusé par un émetteur quantique qui interagit avec un champ cohérent résonant intense. Il révèle des signatures de contextualité quantique : négativité dans la fonction de Wigner et valeurs faibles anormales. Deuxièmement, nous étudions la possibilité d'une mesure non destructive de l'état de spin en limitant le budget énergétique à un photon au plus. Nous comparons les performances de deux champs différents : le champ cohérent et la superposition d'états numériques. Nous démontrons de meilleures performances de cette dernière en matière de génération d'intrication, offrant ainsi un avantage quantique. Enfin, notre analyse s'étend aux applications technologiques. Nous proposons une porte photon-photon, effectuons une analyse approfondie des erreurs et effectuons la modélisation d'expériences de pointe envisageant la génération déterministe d'états de lumière hautement intriqués.

Cette capacité théorique ouvre la voie à l'optimisation directe des performances et de l'efficacité du dispositif en fonction des paramètres accessibles aux expérimentateurs. Cela nous permet également d'ajuster les données expérimentales avec une grande précision.

Contents

Introduction **1**

The era of quantum technologies 2

One-dimensional atoms 3

Thesis outline 6

List of publications 7

1 Quantum measurements **9**

1.1 The von Neumann measurement model 9

1.1.1 Classical and quantum Bhattacharyya coefficients 14

1.2 Conclusion 16

2 Closed-system solution of the 1D atom from collision model **17**

2.1 System and model 17

2.2 Time discretization 19

2.3 Collisional model interpretation 20

2.4 Interaction picture input-output operators and input-output relation . 21

2.5 Solution for the spontaneous emission 22

2.6 Intermission: Solution in rotated reference frames 25

2.7 Solution for the coherent field 26

2.7.1 Weak resonant drive 31

2.8 Solution for a single photon pulse 32

2.9 Conclusions 34

3 Quantum weak values and Wigner negativity in a single qubit gate **35**

3.1 Introduction 35

3.2 Witnesses of non-classical quantum states of light 37
3.2.1 Wigner function negativity 37
3.2.2 Weak values theory in a nutshell 38
3.3 System and model 41
3.4 Husimi $Q-$function and field's weak values 44
3.5 Conditional Wigner function and Wigner negativities 48
3.6 Conclusions 50

4 The spin-photon interface: Energy-efficient quantum non-demolition measurement and photon-photon gate proposal 53
4.1 Introduction 53
4.2 The spin-photon interface 55
4.3 Pre-measurement analysis 57
4.3.1 Dynamics solution 57
4.3.2 Coherent state qBhat: from low to high energy 61
4.3.3 Low energy regime 62
4.4 Spin state readout 65
4.5 Application: Protocol for a controlled phase gate 69
4.5.1 The ideal protocol 69
4.5.2 The light-matter interaction map and the non-monochromaticity parameter 73
4.5.3 Non-ideal gate 74
4.5.4 Error analysis 77
4.6 Conclusions and perspectives 81

5 The SPI subjected to an in-plane magnetic field 85
5.1 Introduction 85
5.2 System, protocol and modeling 86
5.2.1 System 86
5.2.2 The ideal Lindner-Rudolph protocol 88
5.2.3 Collisional model 91
5.2.4 Realistic LRP 93

5.3 Spontaneous emission solution 94
5.4 Protocol benchmark: fidelity and cBhat 97
5.4.1 Fidelity 98
5.4.2 cBhat 101
5.5 Discussion and perspectives 102

Conclusions and perspectives **105**

A General solution of time dependent Hamiltonians **107**
A.1 Coarse-graining of time 107

B Confining charges in quantum dots **111**
B.1 Experimental details 112

C Detailed calculation of the final real photonic states **113**

D 4LS subjected to a magnetic field: spontaneous emission solution **115**
D.1 Finding the $f^{(0),\uparrow}_{\uparrow(\downarrow),e}(t_N)$ 117
D.2 Finding the $f^{(1,R),\uparrow}_{\uparrow(\downarrow),e}(t_N, t_j)$ 119
D.3 Continuous time wave-function 121

List of Figures

1.1 **Illustration of the von Neumann measurement model.** 10

1.2 **Example: measurement of a spin 1/2.** 13

1.3 **Bhattacharyya coefficients for spin 1/2 example.** 15

2.1 **Illustration of the collision model of the 1D atom.** 18

3.1 **Number state Wigner functions and Wigner function negativity.** 38

3.2 **Quantum dynamics leading to weak values.** 39

3.3 **Detection of the field's weak values in the single-qubit gate.** 42

3.4 **Comparison of truncations and frequency contribution.** . . . 49

3.5 **Anatomy of the single-qubit gate.** 51

4.1 **The spin-photon interface.** 55

4.2 **Quantum Bhattacharrya coefficient for coherent field.** 61

4.3 **Quantum Bhattacharrya analysis in the low energy regime.** . 63

4.4 **Spin state readout.** 66

4.5 **Pulse temporal shapes.** 74

4.6 **Angle errors, Eq. (4.71).** 76

4.7 **State-averaged fidelity.** 78

4.8 **Error matrices plot.** 80

4.9 **Probabilities plots.** 81

5.1 **Schematic of the spin-photon interface subjected to an in-plane magnetic field.** 86

5.2 **Possible processes.** 94
5.3 **Model validation.** 96
5.4 **Fidelity at the time of re-excitation with perfect magnetic field alignment.** 100
5.5 **Fidelity at the time of re-excitation influenced by parasitic fields.** 101
5.6 **cBhat for the Lindner-Rudolph protocol.** 101

B.1 **Magnetic field configurations.** 111

Introduction

It's a dangerous business, Frodo, going out your door. You step onto the road, and if you don't keep your feet, there's no knowing where you might be swept off to. – Bilbo by J.R.R. Tolkien

In the early years of the 20th century, the nature of radiation emitted by a black body posed significant challenges to theoretical physics. Max Planck proposed a solution by hypothesizing that energy existed in discrete amounts called "quanta"[1, 2]. Building upon Planck's work, Albert Einstein extended this concept to light itself, suggesting that light was also quantized into particles, that became known as "photons" [3], and successfully describing the photo-electric effect [4]. This hypothesis contradicted the prevailing theory of light as electromagnetic waves proposed by James Clerk Maxwell. However, the wave-particle duality of matter and radiation was established with the works of Louis de Broglie, reconciling the two contradictory concepts [5]. Quantum mechanics was formalized in the 1920s thanks to works by Niels Bohr [6], Erwin Schrödinger [7] and Werner Heisenberg [8, 9]. It emerged as a paradigm shift in physical theory that fundamentally changed our understanding of the world setting a new set of rules that physical theories must obey [10].

At the heart of quantum mechanics lie the concepts of superposition and entanglement [11]. Superposition refers to the state of a physical system being in a combination of multiple states simultaneously. Entanglement describes the non-classical correlations between two or more particles, such that measuring one particle instantaneously affects the state of another, even if they are spatially separated. The phenomenon of entanglement puzzled great physicists like Albert Einstein, who, along with Boris Podolsky and Nathan Rosen, described a physical situation known as the EPR paradox. In their seminal paper [12], they presented the EPR paradox as a thought experiment to argue against the completeness of quantum mechanics as a physical theory. By examining an entangled state, they demonstrated that the measurement of one particle instantaneously influenced another particle, regardless of the spatial separation between them. Einstein famously referred to this non-local behavior as "spooky action at a distance". Their findings led them to the conclusion that the wave-function-based quantum mechanical description of physical reality was incomplete [13]. To address this issue, Einstein proposed the existence of hidden variables, which referred to yet unknown local properties of the system that could explain the avoidance of the spooky action at a distance. However, Niels Bohr, in his critique [14], disagreed with the EPR interpretation of the notion of locality, proposing the principle of complementarity. According to Bohr, certain predictions were possible while others were not, as they were related to mutually incompatible

sets. It was not until the 1960s that John Bell's work [15] on Bell's inequalities provided a mathematical criterion to probe the locality of quantum mechanics. The violation of these inequalities indicated the failure of a classical description, pointing towards the non-local nature of quantum mechanics.

In the early 1980s, experimentalists were trying to test Bell's inequalities in the laboratory [16, 17]. Notably, the experiments performed by the 2022 Nobel Prize in physics Alain Aspect[1] revealed the violation of Bell's inequalities, providing experimental evidence supporting the non-local nature of quantum mechanics [18, 19]. Advances in cavity quantum electrodynamics [20, 11] and quantum optical platforms allowed for the validation of several predicted quantum phenomena, including Rabi oscillations [21], which demonstrated the quantization of the electromagnetic field and the generation of entangled particles [22].

The era of quantum technologies

> *Do you guys just put the word "quantum" in front of everything?* – Paul Rudd (as Scott Lang), Ant-Man and the Wasp.

The emergence of quantum information represents a new perspective in the research program of quantum mechanics. While the field of quantum foundations continued investigating the puzzling aspects of quantum mechanics and its connection with physical reality, quantum information focused on the potential use of these strange properties as resources for technological applications [23]. Moreover, Aspect's experiments represented a landmark [24] by corroborating that entanglement and non-locality are characteristics of the physical world, it brought a burst of interest in exploring the possibilities of using them as resources for information technologies, paving the way for the second quantum revolution [25]. Quantum information theory is a paradigm for the technological application of quantum mechanics that have been developed for the last 25 years [23]. It draws inspiration from Shannon's classical information theory [26]. Quantum bits, or qubits, were introduced as the quantum counterpart to classical bits. While classical bits can only exist in the states '0' or '1', qubits represented by $|0\rangle$ and $|1\rangle$ can exist in superpositions states: $c_0|0\rangle + c_1|1\rangle$, where c_0, c_1 are complex amplitudes that encode quantum information. The field of quantum information aims to develop protocols for efficiently processing and transmitting information taking advantage of the power of quantum properties.

This paradigm shift led to the development of quantum technologies, which harness the unique properties of quantum systems to perform useful tasks [27]. Quantum technologies encompass various areas, including quantum computing, which has the potential to solve complex problems more efficiently than the most powerful classical supercomputer by using superposition and entanglement, and quantum communication that seeks to establish secure channels for transmitting encoded information using quantum properties. Quantum key distribution (QKD) protocols [28] provide secure encryption keys, ensuring information confidentiality

[1] The motivation for the prize shared with John Clauser and Anton Zeilinger was: "for experiments with entangled photons, establishing the violation of Bell inequalities and pioneering quantum information science".

and protection against eavesdropping. Additionally, techniques such as quantum teleportation [29] and superdense coding [30] utilize entanglement to make it possible to efficiently transmit data.

A key objective of quantum technologies is the establishment of a quantum network [31], connecting multiple nodes that can interact coherently. This concept relies on two main components: a flying qubit for transmitting information between stationary qubits that store and map information onto the flying qubits. Photons have emerged as the best candidates to be the flying qubit due to the possibility to maintain quantum coherence over long distances, while quantum states of matter are preferred to be the stationary qubit where local storage and processing of information happens [23]. A fundamental challenge lies in quantifying the quality of entanglement generated between light and matter, specifically the mapping of information between stationary and flying qubits.

Waveguide Quantum electrodynamics (WGQED) [32] investigates the interactions of localized quantum systems, the emitters, with propagating electromagnetic fields, hence this framework is suited for the exploration of the physics of light-matter interactions. It has a wide range of applications for quantum technologies and it allows the modeling in a multitude of hardware implementations such as quantum photonics [33], superconducting circuits [34], and atomic physics [35].

Modeling WGQED systems presents inherent challenges from the fact that propagating fields contain an infinite number of frequency modes. To overcome this issue, effective approaches like cavity quantum electrodynamics (cQED) [20, 11, 22] and open quantum systems [36, 37] have been widely employed. In cQED, only a single mode of the field is considered, while open quantum systems treat the propagating field as a bath and focus solely on the quantum emitter's dynamics by tracing out the field's state. However, such effective models suffer from inherent drawbacks as they sacrifice information about the precise state of the propagating fields and the resulting light-matter entanglement. Consequently, these limitations often restrict their ability to accurately characterize technological protocols.

This is where this thesis makes its contribution. Building upon the method developed recently in Refs. [38, 39] that is based on the WGQED allowing for a collisional model interpretation [40], where the propagating fields are viewed as composed of smaller interacting units called ancilla. Within this framework, it is possible to solve the full dynamics of a qubit interacting with a field inside a waveguide. Thus, providing direct access to light-matter entangled states. Importantly, this model can describe feasible experimental platforms based on one-dimensional atoms (1D atoms), two of which will be discussed in this thesis: superconducting circuits [41] and quantum dots embedded in microstructures such as micro pillars [42] or photonic crystals [43].

One-dimensional atoms

When an atom is excited, it can emit a single photon, but the emission occurs in random directions throughout space (isotropic). To enhance the interaction between a single atom and a specific mode of the electromagnetic field, enabling efficient collection or routing of photons in a preferred direction, the atom can be coupled with

a one-dimensional (1D) environment, such as a waveguide [38, 32]. This configuration gives rise to what is called a one-dimensional atom (1D atom). The first experimental realization of such a system was reported in Ref. [44], where a Cesium atom was coupled with a leaky directional cavity. Since then, significant progress has been made in the development of artificial atoms, also known as quantum emitters, which are engineered systems created in controlled environments to mimic the behavior of natural atoms [45]. These artificial atoms have discrete energy levels that can be tuned by external fields. By driving an artificial atom with light, coherent oscillations (Rabi oscillations) can occur between specific levels, encoding the qubit states. The advantage of artificial atoms over natural atoms is that they can be fabricated in a scalable and controlled way [45].

Two implementations of 1D atoms based on artificial atoms have shown promise as platforms for quantum information protocols: superconducting circuits [46, 41] and semiconductor quantum dots [42, 43].

Superconducting circuits

Superconducting circuits are RLC circuits that incorporate a non-linear element called the Josephson junction. These circuits are typically on the scale of micrometers and operate at extremely low temperatures. The superconducting nature of these circuits, which means they have no resistance, eliminates one of the most significant detrimental effects. The Josephson junctions play a crucial role in creating non-uniform energy levels, allowing the utilization of the lowest two levels to encode the qubit. Quantum information can be encoded in various ways in superconducting circuits, such as the number of superconducting electrons on a small island (charge qubit), the direction of current around a loop (flux qubit), and the oscillatory states of the circuit (phase qubit). These qubits can be controlled using microwaves, voltages, magnetic fields, and currents. An essential aspect of this platform, particularly relevant to the present thesis, is the high accuracy in preparing and measuring the qubit state using integrated on-chip instruments [47, 41]. In fact, a recent experiment even indicated that qubit measurement can be more efficient than preparation [48].

Superconducting circuits possess several appealing features, including scalability, straightforward implementation, long coherence times, and compatibility with existing fabrication techniques. These characteristics make them a promising candidate for large-scale, fault-tolerant quantum computing systems [46, 41]. Additionally, superconducting circuits provide an ideal platform for investigating fundamental aspects of quantum mechanics, such as the performance of quantum non-demolition measurements (QND measurements) [49], violation of Bell's inequalities [50, 51], and access to quantum weak values [48, 52, 53].

The investigation presented in Ref. [53] (see Chap. 3) is motivated by recent observations of anomalous weak values reported in Refs. [48, 52, 53], as well as fundamental results reported in Refs. [54] and [55]. In [54], it was mathematically demonstrated that the emergence of anomalous weak values is a signature of the contextual nature of the system, indicating quantum contextuality. Quantum contextuality refers to the property of quantum systems where the measurement outcomes depend not only on the state of the system but also on the choice of measurements and the context in which they are made [13]. Ref. [55] formally showed that contex-

tual systems should exhibit a negative Wigner function, indicating a non-classical state of light.

In Chap. 3, we consider a qubit interacting with an intense resonant coherent field, which is a well-known example of a Gaussian state [56]. The scattered (output) field is continuously measured using a heterodyne measurement scheme. Since this experiment is implemented in a superconducting circuit platform, we can measure the qubit after a certain interaction time, allowing for post-selection of the state. This post-selection leads to the emergence of anomalous weak values of the scattered field, which will be defined and discussed in Chap. 3. In this specific physical platform, we demonstrate that the scattered field exhibits Wigner negativity, indicating its non-Gaussian nature [57]. This finding is significant as non-Gaussian states of light are essential for achieving advantages in quantum computation, as Gaussian states can be efficiently simulated using classical computers [57].

Quantum dots

Quantum dots are tiny structures formed within semiconductor matrices by combining materials with different lattice parameters, typically InAs or GaAs [58]. Discrete bound states providing sharp optical transitions appear due to the confinement of the motion of the charges in all three directions at the nanometer scale. These materials possess a direct band gap and exhibit radiative decay, this property makes them perfect candidates to be single photon sources (artificial atoms) [42]. The confinement of the quantum dot results in the quantization of energy levels, allowing for the definition of a ground state and an excited state that can be accessed optically. This characteristic enables us to model a quantum dot as a two-level system (2LS or qubit) [59].

To improve the performance of quantum dots photonic microstructures can be built to enhance its emission rate, a phenomenon known as the Purcell effect [60]. The development of experimental knowledge and techniques, such as molecular beam epitaxy, electron beam *in-situ* lithography, and etching [43], has greatly possibilited the generation of high-quality single photons from quantum dots [42, 43]. Two widely used nanostructures for this purpose are photonic crystals and micropillar cavities.

Photonic crystals are materials with periodic variations in refractive index, which allow control over light propagation through optical Bragg scattering. Essentially, a hole pattern is constructed in the semiconducting material to create the desired periodic variation [43].

On the other hand, a QD-pillar cavity system is created by embedding the quantum dots into a solid-state cavity, typically made of GaAs, with distributed Bragg mirrors. The mirrors confine light vertically, while lateral confinement is achieved by etching a cylindrical micropillar [61, 62, 33, 63].

These advancements have opened up possibilities for utilizing quantum dots as efficient sources of single photons [64]. Hence, quantum dots embedded in one-dimensional microstructures are valuable 1D atoms [45].

To fulfill the criteria for quantum information processing, as outlined by DiVincenzo in Ref. [65], stationary qubits need to exhibit long coherence times compared to the duration of unitary manipulation (gate operation) of the qubit. Quantum dots (QDs) provide an appealing solid-state platform for implementing stationary

qubits. Unlike trapped ions or atomic platforms (natural atoms), QDs offer easy integration between components, making them well-suited for practical applications. Additionally, QDs can be electrically doped, allowing the insertion or removal of an electron and enabling the spin degree of freedom in quantum dots due to the presence of an electron or hole [66, 43]. The spin coherence time of an electron or hole in a QD can range from nanoseconds to microseconds, while spin manipulation typically takes only a few hundred picoseconds [66]. This coherence-to-manipulation time ratio, surpassing one thousand, holds significant potential for quantum computation [67]. Consequently, the spin-photon interface (SPI) plays a fundamental role in quantum devices, finding applications in various photonic quantum technologies. For instance, one relevant application is the creation of highly entangled photonic states known as cluster states, as proposed by Lindner-Rudolph [68, 63], which holds particular significance for measurement-based quantum computing [69].

In the pursuit of efficient SPIs significant progress has been made in recent years with spin-photon interfaces being developed to ensure that most photons sent into the device interact with a single spin [70]. Experimental demonstrations have shown that a single spin in a micropillar cavity can rotate the polarization of a photon by approximately six degrees to the left or right [71], depending on the spin state. Recent advancements reported in Ref. [72] have achieved even larger rotation amplitudes, such as $\pm\pi/2$ and π. These achievements demonstrate the potential of SPIs in enabling coherent spin-photon interactions for technological applications.

Thesis outline

The aim of this thesis is to explore aspects of generation, characterization, and robustness of non-classical resources. All of this is studied within the fundamental framework of quantum measurements and their applications in the context of quantum information processing.

Chapter 1 serves as the foundation for the subsequent chapters by reviewing measurement theory. We start by discussing the textbook von Neumann measurement model using a simple toy model. This chapter introduces the necessary concepts that will be utilized throughout the thesis and set the stage for understanding the original contributions presented in Chapters 3 and 4.

Chapter 2 focuses on the method for solving the closed dynamics of a two-level system (qubit) coupled with a bosonic field at every time. We review the technique developed in Ref. [73] and highlight its relevance to the subsequent chapters. The solutions obtained through this method are essential for the original contributions presented in Chapters 3 and 4. Additionally, in Chapter 5, we extend the solution by considering the presence of a magnetic field that affects the quantum emitter.

The first two chapters provide the necessary theoretical background and tools for the subsequent chapters, which contain our original contributions.

Chapter 3 presents a detailed analysis of a single qubit gate. We consider a qubit coupled with an intense resonant coherent field. This scenario corresponds to a specific regime of the general solution obtained in Chapter 2. We explore the non-classical features of the scattered field, including the negativity of the Wigner function and the emergence of anomalous weak values. By analytically computing

the weak values and conditional Wigner function using the Hamiltonian solution, we identify the origins of the anomalies and negativities. The findings presented in this chapter are based on results reported in Ref. [53].

In Chapter 4, we investigate the measurement of the spin state in a degenerate four-level system (4LS). Our goal is to achieve a non-demolishing measurement of the spin state with limited energy resources. The system interacts with fields of different natures: a resonant coherent field with Poissonian statistics a superposition of vacuum and a single photon with sub-Poissonian statistics. The restricted energy budget, where both fields have at most one photon on average, poses a challenge. We explore the potential quantum advantage in the pre-measurement process, where entanglement is generated between the field and the 4LS, and in the collapse step, where the light state is measured to infer the spin state. These steps are crucial for key quantum information protocols, such as the generation of cluster states [63]. These findings of fundamental relevance are are reported in Ref. [74]. Additionally, we provide a technological application proposing a single-rail photon-photon gate, which is a two-qubit photonic gate based on the absence (vacuum) or presence (single photon) of a photon as the logical basis. We consider the scenario where the main imperfection arises from the change in the temporal shape of the scattered field. By utilizing the solutions obtained in Chapter 2, we derive an analytical expression to account for this imperfection. We characterize the error by computing the state-averaged fidelity and the error process matrix for the photon-photon gate.

In Chapter 5, we address the realistic scenario where the Lindner-Rudolph protocol is implemented experimentally. We review the protocol and build appropriate theoretical modeling based on a recent experiment reported in [75]. We extend the solutions obtained in Chapter 2 to include the presence of an in-plane magnetic field and assess its influence on key figures of merit of the protocol.

Finally, we conclude the thesis by summarizing the main findings and providing perspectives on future research directions.

List of publications

This thesis is based on results directly developed for projects or inspired by projects to which I contributed. Some of the content has already been published, while others are going to be part of future publication(s). The published material from works where I was a co-author are presented from my perspective and properly cited. Below is a list of the original results presented in this thesis, which have been published in the following papers, along with a brief description of my contribution to each of them:

- Ref. [53], "Anomalous energy exchanges and Wigner-function negativities in a single-qubit gate". Maria Maffei, Cyril Elouard, **Bruno O. Goes**, Benjamin Huard, Andrew N. Jordan, and Alexia Auffèves. Physical Review A 107, 2 (2023). In this work, I contributed during the final stage of the project. Maria Maffei and Cyril Elouard conducted the system modeling. My contribution involved discussing the interpretation and computation of the quasiprobability distributions, particularly the Wigner function using the obtained wave function.

Based on these results, I created the images and wrote the code that generates the plots presented in the paper and in this thesis, which are available in the dedicated GitHub repository [76].

- Ref. [74], "Energy-efficient quantum non-demolition measurement with a spin-photon interface". M. Maffei, **B. O. Goes**, S. C. Wein, A. N. Jordan, L. Lanco, and A. Auffèves. Quantum 7 (2023). In this work, Maria Maffei and I extended the solutions presented in Ref. [38] to the spin-photon interface case. We addressed the entanglement generation and non-demolition measurement of the spin state in the von Neumann measurement model, as well as selected the figures of merit. The experiment proposed for the collapse of the meter state was a significant contribution from Stephen Wein, who also developed efficient codes to compute the main figures of merit proposed.

- Ref. [63], "High-rate entanglement between a semiconductor spin and indistinguishable photons". N. Coste, D. A. Fioretto, N. Belabas, S. C. Wein, P. Hilaire, R. Frantzeskakis, M. Gundin, **B. Goes**, N. Somaschi, M. Morassi, A. Lemaître, I. Sagnes, A. Harouri, S. E. Economou, A. Auffèves, O. Krebs, L. Lanco, and P. Senellart. Nature Photonics (2023). In this work, Stephen Wein and I worked on the theoretical modeling of the system and discussed the computation of the correlation functions and process matrix. Although this paper is not part of this thesis, it directly inspired the research conducted in Chapter 5, which is still unpublished but has the potential for future publication.

Throughout this thesis, I have used the Qutip Python library [77, 78] and the Melt! [79] Mathematica package for generating plots and performing necessary analytical and numerical calculations. The codes used for these tasks are available in a dedicated GitHub repository [76].

Chapter 1

Quantum measurements

The sciences do not try to explain, they hardly even try to interpret, they mainly make models. By model, is meant a mathematical construct which, with the addition of a certain verbal interpretation describes observed phenomena. The justification for such a mathematical construct is solely and precisely that it is expected to work – John von Neumann

1.1 The von Neumann measurement model

John von Neumann was the first to model the measurement process as a whole [80]. In this section we review the von Neumann measurement model and we will see that it provides a physical explanation of how the measurement occurs and how information about the microscopic quantum system can be extracted from a quantum state with a macroscopic object such as a photon detector or a photographic plate.

The model considers that there are two quantum systems: the measured system (or target system), about which we want to obtain information, and the meter that extracts the information required by correlating with the former. The measurement is split into two steps:

1. The pre-measurement, in which the meter system interacts with the measured system and extracts information about it by getting entangled with it, and

2. The collapse, where the state of the meter is measured, and relying on the entanglement generated during the pre-measurement one can infer the state of the measured system.

In the following, we will analyze a simple yet illuminating toy model to explicitly analyze the von Neumann measurement model. The target system S is coupled to a single-mode bosonic meter M. The goal is to encode the information about the system observable B_S probabilities on the meter system. The observable B_S has the following spectral decomposition,

$$B_S = \sum_k b_k |b_k\rangle\langle b_k|_S, \tag{1.1}$$

where b_k are the eigenvalues and $|b_k\rangle_S$ the eigenvectors of B_S.

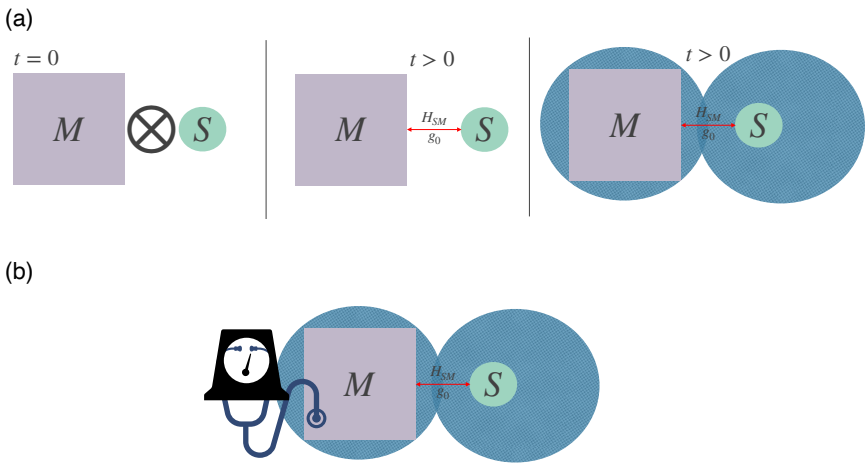

Figure 1.1: **Illustration of the von Neumann measurement model.** (a) Pre-measurement: the meter M and system S start in a product state. At time $t \geq 0$ they interact with strength g_0 becoming entangled. (b) Collapse: a classical apparatus measures the state of the meter. Relying on the entanglement generated during the pre-measurement it is possible to infer the state of the system.

To simplify the analysis we neglected the free evolution during the interaction. The system is coupled to a single bosonic mode of the meter a_M, with an interaction strength g_0. The interaction is assumed to be of the form,

$$H_I = ig_0 B_S \otimes (a_M^\dagger - a_M) = 2g_0 B_S \otimes p_M, \tag{1.2}$$

which is proportional to the momentum operator $p_M = i(a_M^\dagger - a_M)/2$. Thus, this interaction represents a displacement of the mode a_M proportional to the operator B_S (this fact will be demonstrated in what follows).

The target system is initially prepared in an arbitrary state $|\psi(0)\rangle_S$ and the meter is initially in the vacuum state $|\emptyset\rangle_M$. The initial state of the joint system is assumed to be a product state (see Fig. 1.1(a))

$$|\Psi(0)\rangle_{SM} = |\psi(0)\rangle_S \otimes |\emptyset\rangle_M. \tag{1.3}$$

We turn on the interaction at time $t = 0$, Fig. 1.1(b). The joint state at time t (see Fig. 1.1(c)), is given by ($\hbar = 1$)

$$|\Psi(t)\rangle_{SM} = \exp\{-iH_I t\}\, |\Psi(0)\rangle_{SM}. \tag{1.4}$$

We can expand the system state on the basis of the operator B_S, using the closure relation of the eigenbasis $\{|b_k\rangle_S\}$, $\sum_k |b_k\rangle\langle b_k|_S = 1_S$

$$|\psi\rangle_S = \sum_k \langle b_k|\psi(0)\rangle_S |b_k\rangle_S = \sum_k c_k |b_k\rangle_S, \tag{1.5}$$

where the coefficient is $c_k = \langle b_k|\psi(0)\rangle_S$. Substituting Eq. (1.5) in Eq. (1.4) we obtain

$$\begin{aligned}
|\Psi(t)\rangle_{SM} &= \exp\left\{g_0 B_S \otimes (a_M^\dagger - a_M)t\right\} \sum_k c_k |b_k\rangle_S \otimes |\emptyset\rangle_M \\
&= \sum_k c_k \exp\left\{g_0 B_S \otimes (a_M^\dagger - a_M)t\right\} |b_k\rangle_S \otimes |\emptyset\rangle_M \\
&= \sum_k c_k \exp\left\{g_0 t b_k (a_M^\dagger - a_M)\right\} |b_k\rangle_S \otimes |\emptyset\rangle_M \\
&= \sum_k c_k D(g_0 t b_k)|b_k\rangle \otimes |\emptyset\rangle_M
\end{aligned} \tag{1.6}$$

where $D(g_0 b_k t) = \exp\left\{g_0 b_k t(a_M^\dagger - a_M)\right\}$ is the displacement operator $D(\alpha) = \exp\left\{\alpha a_M^\dagger - \bar{\alpha} a_M\right\}$, $D(\alpha)|\emptyset\rangle = |\alpha\rangle$, here $\bar{\alpha}$ represents the complex conjugate of the amplitude α. In our case $\alpha = g_0 b_k t \in \mathbb{R}$. Finally,

$$|\Psi(t)\rangle_{SM} = \sum_k c_k |b_k\rangle_S \otimes |g_0 b_k t\rangle_M. \tag{1.7}$$

Hence, the interaction creates an entangled state at time t from the initial product state. This state is a superposition of the measured system being in the eigenstate $|b_k\rangle_S$, and the meter being in the displaced state $|g_0 t b_k\rangle_M$, with probability $|c_k|^2$. Physically, it means that the initial vacuum state is displaced by a factor that depends on the time and strength of the interaction $g_0 t$ as well as the value of the eigenvalue associated with the eigenstate b_k. We can write the density matrix of the joint state:

$$\rho_{SM}(t) = \sum_{k,q} c_k \bar{c}_q |b_k\rangle_S \langle b_q| \otimes |g_0 b_k t\rangle_M \langle g_0 b_q t| \tag{1.8}$$

The reduced density matrix of the target system is,

$$\begin{aligned}
\rho_S(t) = \mathrm{tr}_M\{\rho_{SM}(t)\} &= \sum_{k,q} c_k \bar{c}_q |b_k\rangle_S \langle b_q| \otimes \mathrm{tr}_M\left\{|g_0 b_k t\rangle_M \langle g b_{0q} t|\right\} \\
&= \sum_{k,q} c_k \bar{c}_q \langle g b_q t | g b_k t\rangle |b_k\rangle_S \langle b_q|
\end{aligned} \tag{1.9}$$

Using the inner product identity between coherent states [81],

$$\langle\beta|\alpha\rangle = \exp\left\{\bar{\beta}\alpha - \frac{1}{2}(|\alpha|^2 + |\beta|^2)\right\}, \tag{1.10}$$

we obtain,

$$\langle g_0 b_q t | g_0 b_k t\rangle = \exp\left\{-\frac{(g_0 t)^2}{2}(b_k - b_q)^2\right\} = \exp\left\{-\frac{(g_0 t)^2}{2}\Delta b_{kq}^2\right\} \tag{1.11}$$

where $\Delta b_{kq} = b_k - b_q$ is the level gap between eigenvalues of the observable. Finally,

$$\boxed{\rho_S(t) = \sum_{k,q} c_k \bar{c}_q \exp\left\{-\frac{(g_0 t)^2}{2}\Delta b_{kq}^2\right\} |b_k\rangle_S \langle b_q|} \tag{1.12}$$

The off-diagonals (coherence terms) $k \neq q$ are damped by an exponential factor, this gives rise to decoherence, which is proportional to the time t the interaction is turned on, the interaction strength itself g_0, and also to how separate b_k is from b_q. The greater the level spacing the higher the damping, hence the faster the system goes to a mixture (diagonal) state. Moreover, when $g_0 t \gg 1$, we have

$$\lim_{g_0 t \to \infty} \exp\left\{-\frac{(g_0 t)^2}{2}(b_k - b_q)^2\right\} = 0, \text{ for } k \neq q \tag{1.13}$$

leading to an incoherent mixture of states. The diagonal entries, $k = q$, are, however, not affected by the exponential damping, leaving the populations $p_k = |c_k|^2$ constant. We note the emergence of a preferred basis in the sense that as soon as we turn on the interaction between the system and the meter, the basis of the operator B_S becomes the preferred one [82]. That is not true before the interaction, and it only happens because we chose to couple B_S with our meter. The preferred basis arises from the fact that the populations and the coherences behave in a different way, the former is kept constant during the dynamics while the latter is washed away. Ultimately, we notice that in this system it is possible to tune between weak and strong measurements [83]. If the product $g_0 t$ is small we do not perturb the system so much, but also we do not get much information about it. This can happen if the coupling g_0 is small, meaning that a small amount of entanglement is generated, or if the time t of interaction is really short, in a way that the meter did not have time to extract enough information about the system. On the other hand, we can extract a lot of information if we have a large $g_0 t$, i.e., we disturb the system strongly or for a long time.

So far we have a description of the pre-measurement process, with this example, we understood how the interaction of the meter with the measured system creates a global entangled state, and how the information about the system state gets encoded onto the meter. It depends on the eigenvalue b_k of the observable, the interaction strength g_0, and the time of the interaction, t. The interaction with the meter itself leads to the decoherence process in the target system.

Now we turn our attention to the meter, which will ultimately collapse. The reduced density matrix of the meter is

$$\begin{aligned}\rho_M = \mathrm{tr}_S\{\rho_{SM}\} &= \sum_u \sum_{k,q} c_k \bar{c}_q \langle b_u|b_k\rangle_S \langle b_q|b_u\rangle \otimes |g_0 b_k t\rangle_M \langle g_0 b_q t| \\ &= \sum_k |c_k|^2 |g_0 b_k t\rangle_M \langle g_0 b_k t|,\end{aligned} \tag{1.14}$$

which is just a statistical mixture of the coherent states $|g_0 b_k t\rangle_M$. These states encode the measured system's state, they are referred to as *pointer states* [82]. The

experiment that will be performed depends on one's goals, a good choice in this particular case is to perform a heterodyne measurement on the meter [84]. The probability of obtaining the coherent state $|\mu\rangle_M$ as the outcome for this type of measurement is given by the Husimi $Q-$function [81, 56](see App. A of Ref. [85]).

$$\begin{aligned} p_{b_k}(\mu) = Q(\mu, \bar{\mu}; b_k) &= \frac{1}{\pi}\langle\mu|\rho_M|\mu\rangle = \frac{1}{\pi}|\langle g_0 b_k t|\mu\rangle|^2 \\ &= \frac{1}{\pi}\sum_k |c_k|^2 \exp\left\{-|\mu - g_0 b_k t|^2\right\} \end{aligned} \tag{1.15}$$

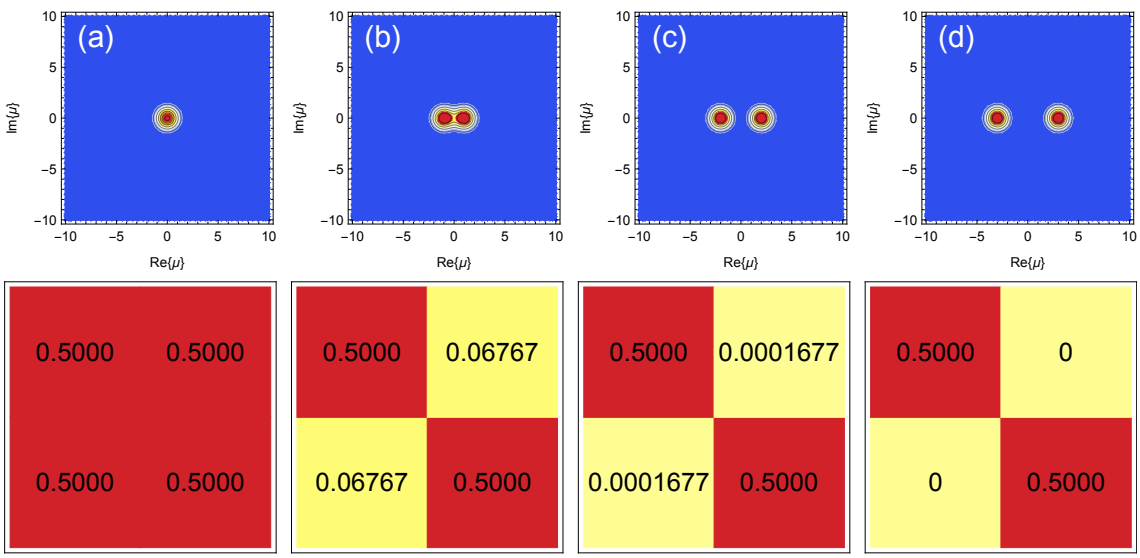

Figure 1.2: **Example: measurement of a spin** $1/2$**.** Here, $B = \sigma_z = \text{diag}\{1/2, -1/2\}$. The upper panel shows the Husimi Q-functions, Eq. (1.15) and the lower panel the Hinton diagrams of the measured system density matrix, Eq. (1.12). (a) $g_0 t = 0$, (b) $g_0 t = 1$, (c) $g_0 t = 2$, and (d) $g_0 t = 5$. The measured system starts in a balanced superposition of its spin states $c_\downarrow = c_\uparrow = 2^{-\frac{1}{2}}$, and the field starts in the vacuum state.

In Fig. 1.2, we apply this formalism for a spin 1/2 measuring $B_S = \sigma_z$. We plot the Hinton diagram (a representation of the density matrix) of the measured system density matrix, and the associated $Q-$function, Eq. (1.15), in the quantum phase space for different values of $g_0 t$. We observe that as the joint system evolves the coherences are washed away while the probability distribution of the classical measurement $p_{\mu=g_0 t b_k}$ becomes distinguishable. For negative eigenvalues, the initial state of the meter (vacuum state $|\emptyset\rangle_M$) is displaced to the left, while the positive displaces it to the right of the real line. The vanishing coherences indicate that entanglement is generated and the right choice of the measurement provides disjoint probabilities distributions. In the next section, we introduce the figures of merit that allow the quantification of the entanglement and readout quality of a physical process as proposed in Refs. [86, 87].

1.1.1 Classical and quantum Bhattacharyya coefficients

At this point, we introduce two important figures of merit that are going to be used in Chap. 4: the Bhattacharyya coefficients. Let the joint state of the target system and meter be

$$|\Psi(t)\rangle = |k\rangle_S \otimes |\phi_k\rangle_M + |l\rangle_S \otimes |\phi_l\rangle_M, \tag{1.16}$$

where $\{|k\rangle_S, |l\rangle_S\}$ are the two possible final states of a two-level system, and $\{|\phi_k\rangle_M, |\phi_l\rangle_M\}$ the two pointer states.

The quantum Bhattacharyya coefficient (qBhat) quantifies the quality of the pre-measurement. It is defined as the modulus of the overlap between the pointer states (proposition 4 of Ref. [87]),

$$\mathscr{B}_q(t) = |\langle\phi_l(t)|\phi_m(t)\rangle|. \tag{1.17}$$

a good pre-measurement is hallmarked by a vanishing qBhat: $\mathscr{B}_q(t) = 0$, complete orthogonal pointer states. It can be easily verified that the off-diagonal matrix elements of the measured system are directly proportional to this quantity, $\rho_{lm} = \langle l|\Psi(t)\rangle\langle\Psi(t)|m\rangle \propto \mathscr{B}_q$, meaning that when the system attains a completely mixed state, the meter has extracted all the information and the joint system-meter are perfectly entangled.

As we have just discussed, after the pre-measurement takes place one can extract the information about the quantum system by measuring the meter state with a classical measuring apparatus [82]. As a result of the measurement, one obtains statistical distributions of its outcomes. For a general experiment, the probability distribution induced by the measured system's states is denoted by p_j. A perfect measurement of the target system state yields two disjoint statistical samples, i.e., there is no overlap between the outcomes associated with spin $|l\rangle$ or $|m\rangle$, $l \neq m$.

The quantity that measures the amount of overlap between two samples, or in other words, how distinguishable they are, is the classical Bhattacharyya coefficient (cBhat) defined as (see definition 7 in Ref. [87]),

$$B_{cl}(p_l, p_m) = \sum_{x\in\mathscr{X}} \sqrt{p_l(x)p_m(x)}, \tag{1.18}$$

where x labels the outcomes of the experiment, $\mathscr{X}$ denotes the set of possible outcomes and $p_j(x)$ is the probability of obtaining the outcome x given that the measured state is j. If the distributions are identical, no information is acquired by the measurement because they are indistinguishable and one has $B_{cl}(p_l, p_m) = 1$. On the other hand, if the distributions are disjoint, i.e., completely distinguishable one obtains $B_{cl}(p_l, p_m) = 0$. The closer to zero the cBhat is the better one can distinguish between the different outcomes. We emphasize that the cBhat is not a distance in the mathematical sense but it can be associated with such a concept by taking its arccos. Importantly, the cBhat is lower bounded by the qBhat

$$\mathscr{B}_q(t) \leq B_{cl}(p_i, p_j), \tag{1.19}$$

the equality holding only when both vanish.

For our toy model, considering the situation of Fig. 1.2, where the observable is $B_S = \sigma_z$, the state of the joint system at time t can be expressed in general as

$$|\Psi(t)\rangle = c_\uparrow|\uparrow\rangle \otimes |\phi_\uparrow(t)\rangle + c_\downarrow|\downarrow\rangle \otimes |\phi_\downarrow(t)\rangle, \tag{1.20}$$

where we have the pointer states $|\phi_{\uparrow(\downarrow)}\rangle$. These states are normalized but not necessarily orthogonal. We can compute the total density matrix $\rho(t) = |\Psi(t)\rangle\langle\Psi(t)|$ and trace over the meter to obtain the measured system (S) density matrix

$$\rho_S(t) = \begin{bmatrix} |c_\uparrow|^2 & c_\uparrow\bar{c}_\downarrow\langle\phi_\downarrow(t)|\phi_\uparrow(t)\rangle \\ \bar{c}_\uparrow c_\downarrow\overline{\langle\phi_\downarrow(t)|\phi_\uparrow(t)\rangle} & |c_\downarrow|^2 \end{bmatrix}. \tag{1.21}$$

Computing the qBhat by definition we have

$$\begin{aligned} \mathscr{B}_q(t) &= |\langle\phi_\downarrow(t)|\phi_\uparrow(t)\rangle| && (1.22) \\ &= \sqrt{\Re\left\{\langle\phi_\downarrow(t)|\phi_\uparrow(t)\rangle\right\}^2 + \Im\left\{\langle\phi_\downarrow(t)|\phi_\uparrow(t)\rangle\right\}^2}, \\ &= \sqrt{\frac{|\langle\sigma_x\rangle|^2+|\langle\sigma_y\rangle|^2}{4|c_\uparrow\bar{c}_\downarrow|^2}}. && (1.23) \end{aligned}$$

For the example presented in Fig. 1.2, we have a balanced superposition $c_\downarrow = c_\uparrow = 2^{-\frac{1}{2}}$, and for $\langle\phi_\downarrow(t)|\phi_\uparrow(t)\rangle$ real. The qBhat reduces to

$$\mathscr{B}_q = |\langle\sigma_x\rangle| = e^{-2(g_0t)^2}. \tag{1.24}$$

The cBhat must be computed between the probability distributions $p_{\pm\frac{1}{2}}(\mu)$, Eq. (1.15), where μ is a continuous complex variable. In this case, the sum becomes an integral over the phase space yielding

$$B_{cl}(p_{-\frac{1}{2}}(\mu), p_{\frac{1}{2}}(\mu)) = \int d^2\mu\, \sqrt{p_{-\frac{1}{2}}(\mu)p_{\frac{1}{2}}(\mu)} = e^{-\frac{(g_0t)^2}{4}}, \tag{1.25}$$

In Fig. 1.3 we plot Eqs. (1.24) and (1.25) and a function of g_0t. We observe the

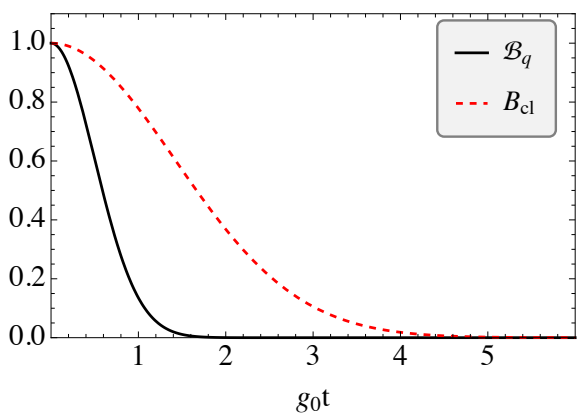

Figure 1.3: **Bhattacharyya coefficients for spin** 1/2 **example.**

inequality Eq. (1.19) holds and both vanish when $g_0 t \geq 5$.

1.2 Conclusion

In this chapter, we reviewed the von Neumann measurement model [80, 82] with a simple toy model, see Figs. 1.1 and 1.2. It provides the theoretical ground for the original contribution to be presented in Chaps. 4 and 3.

When the measurement is concerned, having access to the joint state of the target system and meter, found for our simple toy model in Eq. (1.7), is of ultimate importance. This is a notably difficult problem when the meter system is light, as obtaining the field wave function at any time is not a simple problem. A solution for the scattered wave function at the long-time limit is provided in Ref. [88], while Ref. [89] provides a solution if a particular mode is concerned. In Ref. [73] this problem was solved using the collisional model approach. The method is reviewed in the next chapter, which completes the set of theoretical grounds and tools necessary for the comprehension of the original works presented in Chaps. 3, 4 and 5.

Chapter 2

Closed-system solution of the 1D atom from collision model

Be wise, discretize! – Mark Kac

In this chapter we review and detail the results of Ref. [73] which provide the backbone for the studies carried out in Refs. [53] and [74], and the following chapters of this thesis. The closed dynamics of a 2-level system (referred to as 2LS or qubit interchangeably) interacting with a field is solved. Analytical expressions for the joint wave-function of the qubit and the field, in different initial states are obtained.

2.1 System and model

Following Ref. [73], the system considered is a qubit coupled with a multimode electromagnetic field in a one-dimensional waveguide (WG). The qubit is positioned at $x = 0$. The states of the qubit are the ground and excited states $\{|g\rangle, |e\rangle\}$, with lowering operator $\sigma = |g\rangle\langle e|$. The field is assumed to propagate from left to right, with group velocity v on a segment L. It is described by the annihilation operator a_k which destroys a photon with frequency $\omega_k = (2\pi v/L)k$, and obeys the bosonic relation $[a_k, a_l^\dagger] = \delta_{kl}$. The total system is described by the Hamiltonian

$$H = H_q + H_f + V_{qf}, \tag{2.1}$$

with bare Hamiltonians

$$\begin{aligned} H_q &= \omega_0 \sigma^\dagger \sigma, \\ H_f &= \sum_{k=0}^{\infty} \omega_k a_k^\dagger a_k, \end{aligned} \tag{2.2}$$

where ω_0 is the natural frequency of the qubit and ω_k is the $k-$th mode frequency.

The interaction is assumed to be weak enough so that only frequency modes close to ω_0 play a role (quasi-monochromatic approximation) [90]. In this regime, the rotating wave approximation is allowed [91, 81], leading to the uniform coupling

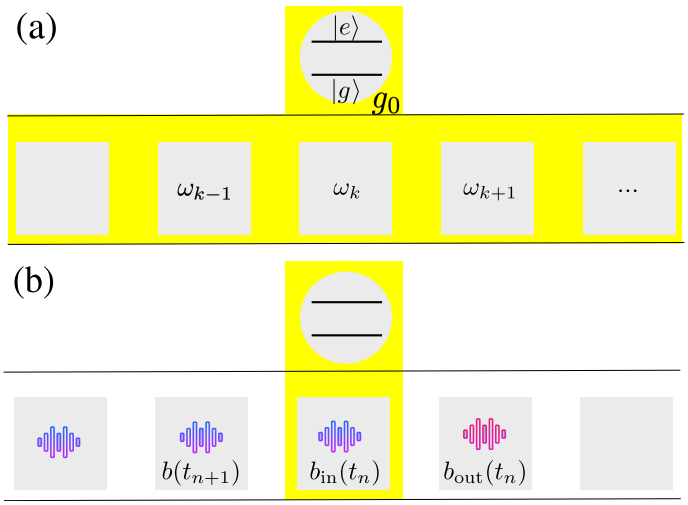

Figure 2.1: **Illustration of the collision model of the 1D atom.** The qubit is located at $x = 0$, and the field is assumed to be propagating from the left to right with a constant group velocity v. It is decomposed into discrete temporal modes created by the bosonic operators $b(t_n) = b_n$, Eq. (2.10). Time and space are discretized: $t \to t_n = n\Delta t$ and $x \to x_n = nv\Delta t$. (a) In the $k-$space the emitter is coupled with all the frequencies $\{\omega_k\}$ at the same time with the same strength g_0. (b) Snapshot of the system at time t_n, beginning of the $n-$th collision. The input operator Eq. (2.18) is defined as the temporal mode created by the operator $b_n^\dagger$ that is arriving at the qubit where it is going to interact. The output operator Eq. (2.17) is defined as the temporal mode created by the operator $b_{n-1}^\dagger$ that has just interacted with the qubit.

with all frequencies [92] and an exchange interaction of Jaynes-Cummings type

$$V_{qf} = ig_0 \sum_{k=0}^{\infty} \left(\sigma^\dagger a_k - a_k^\dagger \sigma \right), \tag{2.3}$$

where g_0 is the interaction strength.

We move to interaction picture with respect to $H_0 = H_q + H_f$ [93]

$$V_{qf} \xrightarrow{H_0} V_{qf}(t) = ig_0 \sum_{k=0}^{\infty} \left(\sigma^\dagger(t) e^{-i\omega_k t} a_k - e^{i\omega_k t} a_k^\dagger \sigma(t) \right). \tag{2.4}$$

where we defined the qubit's dipole in the interaction picture as $\sigma(t) = e^{-i\omega_0 t}\sigma$. To solve the closed dynamics of the system, we discretize time and apply the method discussed in App. A.

2.2 Time discretization

Let N be an a-dimensional number, and t be the total time of the dynamics, then a time step is defined as

$$\Delta t = \frac{t}{N} \to \begin{cases} t_n & = n\Delta t \\ t_N & = N\Delta t = t \end{cases} \tag{2.5}$$

This discretization of time induces a discretization of the space in the waveguide, $\Delta x = v\Delta t$.

Dividing and multiplying Eq. (2.4) by the square root of the mode density $\varrho = L/v$ and the time step Δt, and substituting $t \to t_n$, we obtain

$$\begin{aligned} V_{qf}(t_n) &= ig_0 \sqrt{\frac{L}{v}} \sqrt{\frac{v}{L}} \sqrt{\frac{\Delta t}{\Delta t}} \sum_{k=0}^{\infty} \left(\sigma^\dagger(t_n) e^{-i\omega_k t_n} a_k - e^{i\omega_k t_n} a_k^\dagger \sigma(t_n) \right) \\ &= i\sqrt{g_0^2 \frac{L}{v} \frac{1}{\Delta t}} \sqrt{\frac{v\Delta t}{L}} \sum_{k=0}^{\infty} \left(\sigma^\dagger(t_n) e^{-i\omega_k t_n} a_k - e^{i\omega_k t_n} a_k^\dagger \sigma(t_n) \right) \\ &= i\sqrt{\frac{\gamma}{\Delta t}} \sqrt{\frac{\Delta t}{\varrho}} \sum_{k=0}^{\infty} \left(\sigma^\dagger(t_n) e^{-i\omega_k t_n} a_k - e^{i\omega_k t_n} a_k^\dagger \sigma(t_n) \right) \\ &= i\sqrt{\frac{\gamma}{\Delta t}} \left[\sigma^\dagger(t_n) \left(\sqrt{\frac{\Delta t}{\varrho}} \sum_{k=0}^{\infty} e^{-i\omega_k t_n} a_k \right) - \left(\sqrt{\frac{\Delta t}{\varrho}} \sum_{k=0}^{\infty} e^{i\omega_k t_n} a_k^\dagger \right) \sigma(t_n) \right] \end{aligned} \tag{2.6}$$

where we defined the vacuum decay rate to the WG

$$\gamma = g_0^2 \frac{L}{v}. \tag{2.7}$$

At this point, we define the annihilation operator at a position x of the waveguide as,

$$b(x,t) = \frac{1}{\sqrt{\varrho}} \sum_{k=0}^{\infty} e^{-i\omega_k\left(t-\frac{x}{v}\right)} a_k = b\left(0, \tau = t - \frac{x}{v}\right) \tag{2.8}$$

This mode is the (discrete) Fourier transform of the annihilation modes in the momentum space. Thus, they can be interpreted as *spatial modes* that annihilate a field excitation at position x. We note, however, that it depends on a single temporal parameter $\tau = t - \frac{x}{v}$, and these modes obey the bosonic commutation relation

$$[b(x,t), b^\dagger(x',t')] = [b(0,\tau), b^\dagger(0,\tau')] = \delta(\tau - \tau'). \tag{2.9}$$

Finally, since the qubit is assumed to be at $x = 0$, we observe that it naturally appeared as the spatial mode depending only on the temporal parameter t_n in Eq. (2.6)

$$\boxed{b(0,t_n) = b(t_n) \equiv \frac{b_n}{\sqrt{\Delta t}} = \sqrt{\frac{\Delta t}{\varrho}} \sum_{k=0}^{\infty} e^{-i\omega_k t_n} a_k}. \tag{2.10}$$

Although rigorously it is a spatial mode that at time t_n annihilates an excitation at position $x = 0$ we will dub the modes that only have a time as a parameter as a *temporal mode*, following the nomenclature of Refs. [88, 94, 40, 73]. It obeys the bosonic algebra for different times, from Eq. (2.9)

$$[b_n, b_m^\dagger] = \delta_{nm}. \tag{2.11}$$

The $b(t_n)$ operators can be interpreted as annihilation operators of a bosonic excitation at time t_n. Finally, the interaction Hamiltonian assumes the form,

$$\boxed{V_{qf}(t_n) = i\sqrt{\frac{\gamma}{\Delta t}} \left[\sigma^\dagger(t_n) b(t_n) - b^\dagger(t_n)\sigma(t_n)\right]} \tag{2.12}$$

2.3 Collisional model interpretation

In the interaction picture, the interaction Hamiltonian in Eq. (2.12) evolves the state of the system [93]. The propagator is given by,

$$U(t_n) = \exp\left\{-iV_{qf}(t_n)t_n\right\}. \tag{2.13}$$

The state at time t_n is given by,

$$\rho(t_n) = U(t_{n-1})\rho_{n-1}U^\dagger(t_{n-1}). \tag{2.14}$$

Let us recall a basic formula that is necessary at this point: Let A, B be arbitrary operators, the Baker–Campbell–Hausdorff (BCH) formula is,

$$e^{kA}Be^{-kA} = B + k[A,B] + \frac{k^2}{2!}[A,[A,B]] + \frac{k^3}{3!}[A,[A,[A,B]]] + \ldots, \tag{2.15}$$

applying Eq. (2.15) to Eq. (2.14) one can verify that (here $\rho_n = \rho(t_n)$),

$$\frac{\rho_n - \rho_{n-1}}{\Delta t} = -i[V_{qf}(t_n), \rho_{n-1}] + \gamma[\tilde{V}_{qf}(t_n), [\tilde{V}_{qf}(t_n), \rho_{n-1}]] + \mathscr{O}(\Delta t) \tag{2.16}$$

where $\tilde{V}_{qf}(t_n) = V_{qf}(t_n)/\big(i\sqrt{\frac{\gamma}{\Delta t}}\big)$.

The interpretation is clear, by decomposing the evolution of the state as a series of infinitesimal evolutions, we obtain a series of "collisions". The collisions happen between the qubit and *one* time bin of the field. The unitary couples the qubit only with one temporal mode at a time, see Fig. 2.1(b), that never interacts with the system again due to the unidimensionality of the system. Importantly, all the unitaries are the same due to the flatness of the spectrum, i.e., the assumptions that the qubit couples with all the $k-$modes with the same strength g_0. For an in-depth discussion about the collisional model, we refer to the authoritative Refs. [94, 40].

We note that Eq. (2.16) resembles a discrete-time version of the Lindblad master equation [95]. Indeed, if the field is initially uncorrelated in the time domain, when the continuous-time limit is taken it gives rise to a Markovian dynamics and Eq. (2.16) reduces to a Lindbladian when the field is traced out, i.e. when only the dynamics of the qubit is concerned [94, 40]. Otherwise, the reduced dynamics of the qubit will be non-markovian, which is physically intuitive because once the first time-bin has interacted with the qubit it will generate a correlation between it and the next time bin that has not yet interacted, due to the presence of initial correlations.

2.4 Interaction picture input-output operators and input-output relation

From Eq. (2.8) we can define the field input and output operators [92]. The output operator is intuitively defined as the last temporal mode that has interacted with the qubit, that is, it is leaving the position $x = 0$ from the right:

$$\boxed{b_{\text{out}}(t_n) \equiv \lim_{\epsilon\to 0^+} b(\epsilon, t_n) = \frac{b_{n-1}}{\sqrt{\Delta t}}}. \tag{2.17}$$

The input operator is the temporal mode that will interact with the system, i.e., it is approaching $x = 0$ from the left:

$$\boxed{b_{\text{in}}(t_n) \equiv \lim_{\epsilon\to 0^-} b(\epsilon, t_n) = \frac{b_n}{\sqrt{\Delta t}}}. \tag{2.18}$$

In the regions $x < 0$ and $x > 0$, a wave packet evolves without deformation from the left to the right. Noticing that,

$$\lim_{\epsilon\to 0^\pm} b(\epsilon, t_n) = \lim_{\epsilon\to 0^\pm} \frac{1}{\sqrt{\varrho}} \sum_{k=0}^{\infty} e^{-i\omega_k\left(t-\frac{\epsilon}{v}\right)} a_k = \frac{1}{\sqrt{\varrho}} \sum_{k=0}^{\infty} e^{-i\omega_k t} a_k = b(0, t_n), \tag{2.19}$$

implies the following relation between the input and output fields,

$$b(0,t) \equiv b(t) = \frac{b_{\text{in}}(t) + b_{\text{out}}(t)}{2}. \tag{2.20}$$

Moreover, assuming the time of interaction to be much shorter than the lifetime of radiative decay, i.e. $\Delta t \ll \gamma^{-1}$, one can compute.

$$\begin{aligned} \langle b_{\text{out}}(t_n)\rangle &= \text{tr}\left\{\frac{b(t_{n-1})}{\sqrt{\Delta t}} U(t_{n-1})\rho_{n-1}U^\dagger(t_{n-1})\right\} \\ &= \text{tr}\left\{\frac{U^\dagger(t_{n-1})b(t_{n-1})U(t_{n-1})}{\sqrt{\Delta t}}\rho_{n-1}\right\} \end{aligned} \tag{2.21}$$

we expand the operators' product using the BCH formula Eq. (2.15) to first order in Δt,

$$\begin{aligned} \frac{U^\dagger(t_{n-1})b(t_{n-1})U(t_{n-1})}{\sqrt{\Delta t}} &= \frac{b(t_{n-1})}{\sqrt{\Delta t}} \\ &+ \sqrt{\gamma}\left[b(t_{n-1}), \left(\sigma^\dagger(t_n)b_n - b_n^\dagger\sigma(t_n)\right)\right] \\ &- \sqrt{\Delta t}\gamma\left[\sigma^\dagger(t_n)b_n - b_n^\dagger\sigma(t_n)\right] b(t_{n-1})\left[\sigma^\dagger(t_n)b_n - b_n^\dagger\sigma(t_n)\right] \\ &+ \frac{\gamma}{2}\sqrt{\Delta t}\left\{b(t_{n-1}), \left[\sigma^\dagger(t_n)b_n - b_n^\dagger\sigma(t_n)\right]^2\right\} \\ &+ \frac{\gamma}{2}\sqrt{\gamma}\Delta t\left[\left(\sigma^\dagger(t_n)b_n - b_n^\dagger\sigma(t_n)\right)^2, b(t_{n-1})\left(\sigma^\dagger(t_n)b_n - b_n^\dagger\sigma(t_n)\right)\right] \end{aligned} \tag{2.22}$$

by taking the trace of the last equation, using the cyclic property, and performing the algebra we have that the terms proportional to $\sqrt{\Delta t}, \Delta t$ vanish. Finally,

$$\langle b_{\text{out}}(t_n)\rangle = \langle b_{\text{in}}(t_{n-1})\rangle - \sqrt{\gamma}\langle\sigma(t_{n-1})\rangle. \tag{2.23}$$

This is similar to the celebrated input-output equation found in Ref. [92] but in the interaction picture for the expectation values of the operators.

2.5 Solution for the spontaneous emission

Employing the developed collisional model one can start to solve the dynamics for the simplest case possible: the spontaneous emission (SE). This instance provides the main building block used to find the solution to more complicated and interesting cases such as the field initially in a coherent state or being composed of a single photon.

Let the qubit be initially excited $|e\rangle$, and the field in the vacuum state, that is there is no photon in any time-bin $|\emptyset\rangle = \bigotimes_{k=0}^{N-1}|\emptyset_k\rangle$. The initial state of the joint system is,

$$|\Psi_{\text{SE}}(0)\rangle = |e\rangle|\emptyset\rangle. \tag{2.24}$$

where the subscript "SE" stands for spontaneous emission. Since the Jaynes-Cummings interaction preserves the number of excitations we can restrict our analysis

to the subspace spanned by the vacuum and a single photon for each temporal bin [90]

$$\{|\emptyset_n\rangle, b_n^\dagger|\emptyset_n\rangle\}. \tag{2.25}$$

The only mechanism responsible for photon creation is spontaneous emission. Based on this physical reasoning, and following Refs. [88, 96], we may write an *Ansatz* for the wave-function at time t as

$$|\Psi_{\mathrm{SE}}(t_N)\rangle = f_e(t_N)|e\rangle|\emptyset\rangle + \sum_{k=0}^{N-1} f_g(t_N;t_k)b^\dagger(t_k)|g\rangle|\emptyset_k\rangle. \tag{2.26}$$

It captures the two physical possibilities: the qubit can remain in the excited state, with probability $p_e(t_N) = |f_e(t_N)|^2$ or it can decay to the ground state $|g\rangle$, by emitting one photon at some time t_k, $b^\dagger(t_k)|\emptyset_k\rangle$, with probability $p_g(t_N) = \sum_{k=0}^{N-1}|f_g(t_N;t_k)|^2$. It satisfies $p_g(t_k) + p_e(t_k) = 1$ for all t_k. Hence, the solution boils down to finding the time-dependent coefficients $f_e(t_N)$ and $f_g(t_N;t_k)$. Using Eq. (A.6), we have

$$\begin{aligned}|\Psi_{\mathrm{SE}}(t_N)\rangle &= f_e(t_N)|e\rangle|\emptyset\rangle + \sum_{k=0}^{N-1} f_g(t_N;t_k)b^\dagger(t_k)|g\rangle|\emptyset_k\rangle \\ &= \left(\prod_{k=0}^{N-1} U_k\right)|e\rangle|\emptyset\rangle\end{aligned} \tag{2.27}$$

To find the coefficient $f_e(t_N)$ we project the wave-function onto the $|e\rangle|\emptyset\rangle$ subspace, resulting

$$f_e(t_N) = \langle e|\left(\prod_{k=0}^{N-1}\langle\emptyset|U_k|\emptyset\rangle\right)|e\rangle. \tag{2.28}$$

We have,

$$\begin{aligned}\prod_{n=0}^{N-1}\langle\emptyset|U_n|\emptyset\rangle &= \langle\emptyset|\left(\mathbb{1} + \sqrt{\Delta t}\sqrt{\gamma}\left[\sigma^\dagger(t_n)\cancel{b_n} - \cancel{b_n^\dagger}\sigma(t_n)\right] + \frac{\gamma}{2}\Delta t\left[\sigma^\dagger(t_n)b_n - b_n^\dagger\sigma(t_n)\right]^2\right)|\emptyset\rangle \\ &= \mathbb{1} - \frac{\gamma}{2}\Delta t\langle\emptyset|\left[\sigma^\dagger(t_n)\sigma(t_n)b_nb_n^\dagger + \sigma(t_n)\sigma^\dagger(t_n)\cancel{b_n^\dagger b_n}\right]|\emptyset\rangle \\ &= \mathbb{1} - \frac{\gamma}{2}\Delta t\langle\emptyset|\left[\sigma^\dagger(t_n)\sigma(t_n)b_nb_n^\dagger\right]|\emptyset\rangle \\ &= \mathbb{1} - \frac{\gamma}{2}\Delta t\langle\emptyset|\left[\sigma^\dagger(t_n)\sigma(t_n)\left(b_n^\dagger b_n + \mathbb{1}\right)\right]|\emptyset\rangle \\ &= \mathbb{1} - \frac{\gamma}{2}\Delta t\sigma^\dagger(t_n)\sigma(t_n)\end{aligned} \tag{2.29}$$

It yields,

$$\langle e|\left(\mathbb{1} - \frac{\gamma}{2}\Delta t\sigma^\dagger(t_n)\sigma(t_n)\right)|e\rangle = 1 - \frac{\gamma}{2}\Delta t \approx e^{-\frac{\gamma}{2}\Delta t} \tag{2.30}$$

$$\langle g|\left(\mathbb{1} - \frac{\gamma}{2}\Delta t\sigma^\dagger(t_n)\sigma(t_n)\right)|g\rangle = 1 \tag{2.31}$$

leading to,

$$f_e(t_N) = \langle e| \left(\prod_{k=0}^{N-1} \langle \emptyset | U_k | \emptyset \rangle \right) |e\rangle = e^{-\frac{\gamma}{2} t_N} \tag{2.32}$$

Finally, we obtain,

$$\boxed{f_e(t_N) = e^{-\frac{\gamma}{2} t_N}.} \tag{2.33}$$

To find the coefficient $f_g(t_N)$ we project the wave-function onto the $\{b_j^\dagger |g\rangle |\emptyset_j\rangle\}$ subspace. Firstly, we use the semigroup property of the propagator [36] to split it into three parts,

$$\prod_{k=0}^{N-1} \langle \emptyset | U_k | \emptyset \rangle = \left(\prod_{l=j+1}^{N-1} U_l \right) U_j \left(\prod_{m=0}^{j-1} U_m \right), \tag{2.34}$$

since $|\emptyset\rangle = \bigotimes_{k=0}^{N-1} |\emptyset_k\rangle$, we can write,

$$f_g(t_N; t_j) = \langle g| \langle \emptyset | b_j \left[\left(\prod_{l=j+1}^{N-1} U_l \right) U_j \left(\prod_{m=0}^{j-1} U_m \right) \right] |e\rangle |\emptyset\rangle, \tag{2.35}$$

$$= \langle g| \left[\left(\prod_{l=j+1}^{N-1} \bigotimes_{l=j+1}^{N-1} \langle \emptyset_l | U_l | \emptyset_l \rangle \right) \langle \emptyset_j | b_j U_j | \emptyset_j \rangle \left(\prod_{m=0}^{j-1} \bigotimes_{m=0}^{j-1} \langle \emptyset_m | U_m | \emptyset_m \rangle \right) \right] |e\rangle. \tag{2.36}$$

We need to find the expression for the term highlighted in red. The other two terms are known. Intuitively, we can expect this term to promote the jump from the excited state to the ground state at the collision tagged by the time-bin j, i.e. at time $t_j = j\Delta t$ a photon is created at the expense of the relaxation of the atom: a quantum jump occurs [84]. This is the mechanism that creates the photon in the field. Performing the algebra,

$$\begin{aligned} \langle \emptyset_j | b_j U_j | \emptyset_j \rangle &= \langle \emptyset_j | \left(-\sqrt{\Delta t} \sqrt{\gamma} \sigma(t_j) b_j b_j^\dagger - \frac{\gamma}{2} \Delta t \sigma^\dagger(t_j) \sigma(t_j) b_j b_j b_j^\dagger \right) |\emptyset_j\rangle \\ &= \langle \emptyset_j | \left[-\sqrt{\Delta t} \sqrt{\gamma} \sigma(t_j) \left(\cancel{b_j^\dagger b_j} + \mathbb{1} \right) - \frac{\gamma}{2} \Delta t \sigma^\dagger(t_j) \sigma(t_j) \left(2\cancel{b_j} + b_j^\dagger \cancel{b_j^2} \right) \right] |\emptyset_j\rangle \\ &= -\sqrt{\Delta t \gamma} \sigma(t_j) = -\sqrt{\Delta t \gamma} e^{-i\omega_0 t_j} |g\rangle \langle e| \end{aligned} \tag{2.37}$$

Finally,

$$\boxed{\langle \emptyset_j | b_j U_j | \emptyset_j \rangle = -\sqrt{\Delta t \gamma} e^{-i\omega_0 t_j} |g\rangle \langle e|} \tag{2.38}$$

Substituting into Eq. (2.36), we obtain

$$f_g(t_N; t_j) = -\sqrt{\Delta t \gamma} e^{-i\omega_0 t_j} \langle g| \left(\prod_{l=j+1}^{N-1} \bigotimes_{l=j+1}^{N-1} \langle \emptyset_l | U_l | \emptyset_l \rangle \right) |g\rangle \langle e| \left(\prod_{m=0}^{j-1} \bigotimes_{m=0}^{j-1} \langle \emptyset_m | U_m | \emptyset_m \rangle \right) |e\rangle \tag{2.39}$$

$$= -\sqrt{\Delta t \gamma} e^{-i\omega_0 t_j} e^{-\frac{\gamma}{2} t_j},$$

where we used the identities Eqs. (2.32) and (2.38). The coefficient for the ground state is,

$$\boxed{f_g(t_N;t_j) = -\sqrt{\Delta t\gamma}e^{-i\omega_0 t_j}e^{-\frac{\gamma}{2}t_j}} \tag{2.40}$$

Finally, the spontaneous emission wave function, in discrete time, is

$$\boxed{|\Psi_{\text{SE}}(t_N)\rangle = e^{-\frac{\gamma}{2}t_N}|e\rangle|\emptyset\rangle - \sqrt{\Delta t\gamma}\sum_{k=0}^{N-1} e^{-i\omega_0 t_k}e^{-\frac{\gamma}{2}t_k}b^\dagger(t_k)|g\rangle|\emptyset_k\rangle.} \tag{2.41}$$

The wave function in continuous time is found by replacing,

$$\begin{aligned} t_N &\to t, \\ t_k &\to u, \text{ (dummy integration variable)} \\ \frac{b_k}{\sqrt{\Delta t}} &\to b(u), \\ \sum_{j=0}^{N-1}\Delta t &\to \int_0^t du. \end{aligned} \tag{2.42}$$

Thus, coming back to the continuous time we obtain,

$$|\Psi_{\text{SE}}(t)\rangle = e^{-\frac{\gamma}{2}t}|e\rangle|\emptyset\rangle - \sqrt{\gamma}\int_0^t du\, e^{-\left(\frac{\gamma}{2}+i\omega_0\right)t}b^\dagger(t)|g\rangle|\emptyset\rangle. \tag{2.43}$$

This result is precisely what was expected. This solution was first obtained by Wigner and Weisskopf in Ref. [97] (see also Sec. 14.3.4 of Ref. [98]).

2.6 Intermission: Solution in rotated reference frames

In the last section, we presented the detailed calculations for the simplest scenario, in this section we want to show how the same technique can be used for experimentally relevant fields such as a coherent field $|\alpha\rangle = D(\alpha)|\emptyset\rangle$, where $D(\alpha)$ is the displacement operator. We will develop a procedure to find the solution for an initial state of the field that can be written as a unitary $U(\lambda)$, where λ is some (set of) complex parameter(s) acting on the vacuum state. We start considering the initial state of the system to be

$$|\Psi(0)\rangle = |\psi\rangle \otimes |\lambda\rangle \tag{2.44}$$

where $|\lambda\rangle$ is the initial state of the field, and $|\psi\rangle$ is the arbitrary initial state of the system. We assume that the field state is obtained by a unitary operation applied to the vacuum state

$$|\lambda\rangle = U(\lambda)|\emptyset\rangle, \tag{2.45}$$

then the state at time t is given by,

$$\begin{aligned} |\Psi(t)\rangle &= \exp\{-iHt\}\,|\Psi(0)\rangle \\ &= \exp\{-iHt\}\,U(\lambda)|\psi\rangle \otimes |\emptyset\rangle. \end{aligned} \tag{2.46}$$

We multiply both sides on the left by $U^\dagger(\lambda)$, and use the fact that the unitary operators can infiltrate into the exponential [23],

$$\begin{aligned} U^\dagger(\lambda)|\Psi(t)\rangle &= U^\dagger(\lambda)\exp\{-iHt\}\,U(\lambda)|\psi\rangle\otimes|\emptyset\rangle \\ &= \exp\left\{-i\left[U^\dagger(\lambda)HU(\lambda)\right]t\right\}|\psi\rangle\otimes|\emptyset\rangle \\ |\Psi_\lambda(t)\rangle &= \exp\{-iH_\lambda t\}\,|\psi\rangle\otimes|\emptyset\rangle \end{aligned} \tag{2.47}$$

where we defined the state $|\Psi_\lambda(t)\rangle = U^\dagger(\lambda)|\Psi(t)\rangle$ and the Hamiltonian

$$H_\lambda = U^\dagger(\lambda)HU(\lambda) \tag{2.48}$$

in a basis rotated by the parameter λ. This is dubbed the *rotated frame*. In this frame, the only mechanism responsible for photon creation is the spontaneous emission. Hence, the procedure to find the solution in a rotated frame is analogous to the spontaneous emission case.

Solution in rotated reference frames

When the initial state is of the form

$$|\Psi(0)\rangle = U(\lambda)|\psi\rangle|\emptyset\rangle,\ U(\lambda)\text{ unitary.} \tag{2.49}$$

We have to:

1. Rotate the Hamiltonian:

$$H_\lambda = U^\dagger(\lambda)HU(\lambda). \tag{2.50}$$

2. Write an *Ansatz* for the wave-function in the displaced frame $|\Psi_\lambda(t)\rangle$, and follow steps analogous to those presented in Sec. 2.5.

3. Finally, if necessary, come back to the laboratory frame:

$$|\Psi(t)\rangle = U(\lambda)|\Psi_\lambda(t)\rangle. \tag{2.51}$$

2.7 Solution for the coherent field

Consider a qubit initially in one of its energy eigenstates, denoted as $|\zeta\rangle$ with $\zeta = g, e$. The qubit interacts with a coherent field $|\alpha_d\rangle = D(\alpha_d)|\emptyset\rangle$, which is tuned to the drive frequency $\omega_d = \omega_0 - \delta$, where $\delta = \omega_0 - \omega_d$ represents the detuning between the qubit's natural frequency and the drive frequency. We assume that the detuning is small, i.e., $|\delta| \ll \omega_0$. The initial state of the joint system, in the laboratory frame, is,

$$|\Psi_0\rangle = D(\alpha_d)|\zeta\rangle\otimes|\emptyset\rangle. \tag{2.52}$$

From the definition of the temporal mode, Eq. (2.10), we have,

$$b_j = \sqrt{\frac{\Delta t}{\varrho}} \sum_k e^{-i\omega_k t_j} a_k \rightarrow a_k = \sqrt{\frac{\Delta t}{\varrho}} \sum_j e^{i\omega_k t_j} b_j, \text{ (inverse Fourier transform)}$$

so,

$$\boxed{a_d = \sqrt{\frac{\Delta t}{\varrho}} \sum_j e^{i\omega_d t_j} b_j} \tag{2.53}$$

We substitute Eq. (2.53) in the displacement operator,

$$\begin{aligned} D(\alpha_d) &= \exp\left\{\sum_j \left[\sqrt{\frac{\Delta t}{\varrho}} \left(\alpha_d e^{-i\omega_d t_j} b_j^\dagger - \bar{\alpha}_d e^{i\omega_d t_j} b_j\right)\right]\right\} \\ &= \bigotimes_{j=0}^{N} \exp\left\{\beta_j b_j^\dagger - \bar{\beta}_j b_j\right\} \equiv \bigotimes_{j=0}^{N} D(\beta_j) \end{aligned} \tag{2.54}$$

with,

$$\beta_j = \sqrt{\frac{\Delta t}{\varrho}} \alpha_d e^{-i\omega_d t_j} \tag{2.55}$$

being the $j-$th temporal mode displacement amplitude. The relation between the mean number of photons in the frequency mode ω_d and the temporal frequency mode t_j is given by: $|\alpha_d|^2 = \varrho|\beta_j|^2/\Delta t$. Let's recall a basic property of displacement operators that is necessary at this point: Let c be a generic annihilation operator and χ the related displacement amplitude, then it is known that [81]: $D^\dagger(\chi) c D(\chi) = c + \chi$. To obtain the displaced interaction Hamiltonian, we use

$$\bigotimes_{l,m=0}^{N} D^\dagger(\beta_l) b_j D(\beta_m) = b_j + \beta_j. \tag{2.56}$$

The Hamiltonian in the displaced frame, following the prescription in Sec. 2.6, give

$$\begin{aligned} \bigotimes_{l,m=0}^{N} D^\dagger(\beta_l) V_{qf}(t_n) D(\beta_m) &= i\sqrt{\frac{\gamma}{\Delta t}} \left[\sigma^\dagger(t_n)(b(t_n) + \beta_n) - \left(b^\dagger(t_n) + \bar{\beta}_n\right)\sigma(t_n)\right] \\ &= V_{qf}(t_n) + i\sqrt{\frac{\gamma}{\Delta t}} \left[\sigma^\dagger(t_n)\beta_n - \bar{\beta}_n \sigma(t_n)\right] \\ &= V_{qf}(t_n) - \frac{1}{2}\left(2\sqrt{\frac{\gamma}{\Delta t}}\beta_n\right) \underbrace{i\left(\sigma(t_n) - \sigma^\dagger(t_n)\right)}_{\sigma_y}, \quad (\beta_n \in \mathbb{R}) \\ &= V_{qf}(t_n) - \frac{\Omega_y}{2}\sigma_y(t_n) \\ &\equiv V_{qf}(t_n) + H_D(t_n) \end{aligned} \tag{2.57}$$

where, without loss of generality, in the third line we considered the amplitude of the coherent field to be real, $\beta_n \in \mathbb{R}$.

We defined the Rabi frequency,

$$\begin{aligned}\Omega_y &= 2\sqrt{\frac{\gamma}{\Delta t}}\beta_n \\ &= 2\sqrt{\gamma\frac{v}{L}}\alpha_d e^{-i\omega_d t_j} \\ &= 2g_0\alpha_d e^{-i\omega_d t_j}\end{aligned} \tag{2.58}$$

where we used Eq. (2.7). Hence,

$$|\Omega_y| = 2g_0\alpha_d. \tag{2.59}$$

The presence of the coherent field naturally creates a Hamiltonian that drives the qubit promoting coherent dynamics between the excited and ground states as a rotation around the $y-$axis:

$$H_D = -\frac{\Omega_y}{2}\sigma_y(t_n) \tag{2.60}$$

The propagator in the reference frame displaced by β is given by

$$U_{\beta,n} = \exp\left\{-iV_{qf}(t_n)\Delta t + i\frac{\Omega_y}{2}\Delta t\sigma_y(t_n)\right\}. \tag{2.61}$$

If we consider the classical limit of the coherent field $|\alpha_d| \gg 1$, the leading term in the propagator is that of the drive Hamiltonian H_D [99], then

$$U_{\beta,n} \approx U_{\text{cl}} = \exp\left\{i\frac{\Omega_y}{2}\Delta t\sigma_y(t_n)\right\} = \exp\left\{i\frac{\Delta\theta}{2}\sigma_y(t_n)\right\} = R_y(\theta). \tag{2.62}$$

where the we have an infinitesimal rotation by an angle $\Delta\theta = \Omega_y\Delta t$. In the continuous limit, considering the full dynamics in the interval $t' \in [0, t]$, it becomes a finite rotation by an angle

$$\theta = \Omega_y t. \tag{2.63}$$

Thus, in the classical limit of the resonant coherent field ($\delta = 0$) we have a single qubit gate.

This observation and Eqs. (2.63) and (2.59) are the starting point for the study to be presented in Chap. 3, where we use the solution developed in this section to compute the conditional Wigner and Husimi $Q-$function [81].

Proceeding with the solution, we introduce the short-hand notation $\tilde{U}_k = U_{\beta,k}$ for the propagator in the displaced frame. The wave function *Ansatz* for the solution is

$$\begin{aligned}|\Psi^{\zeta}_{\beta}(t_N)\rangle &= \left(\prod_{k=0}^{N-1}\tilde{U}_k\right)|\Psi^{\zeta}_{\beta}(0)\rangle \\ &= \sum_{\varepsilon=g,e}\left[\tilde{f}^{(0)}_{\varepsilon,\zeta}(t_N) + \sum_{n_1=0}^{N-1}\tilde{f}^{(1)}_{\varepsilon,\zeta}(t_N,t_{n_1})b^{\dagger}_{n_1} + \sum_{n_2=n_1+1}^{N-1}\sum_{n_1=0}^{N-1}\tilde{f}^{(2)}_{\varepsilon,\zeta}(t_N;t_{n_2},t_{n_1})b^{\dagger}_{n_2}b^{\dagger}_{n_1} + \dots\right]|\varepsilon\rangle|\emptyset\rangle\end{aligned} \tag{2.64}$$

where the ellipses represent the components with more photon emissions events. The $|\Psi_\beta^\zeta(t_N)\rangle$ is the wave-function in the $\beta-$displaced frame at time t_N conditioned on the initial energy state $|\zeta\rangle$. We introduced the notation for the coefficients in the displaced frame:

$$\tilde{f}^{\text{number of photons emitted}}_{\text{final qubit state, initial qubit state}}. \tag{2.65}$$

For future reference, this equation can be cast in the form,

$$|\Psi_\beta^\zeta(t_N)\rangle = \sqrt{P_g(t)}|g\rangle|\phi_g(t)\rangle + \sqrt{P_e(t)}|e\rangle|\phi_e(t)\rangle \tag{2.66}$$

where the pointer states are,

$$|\phi_\varepsilon\rangle = \frac{1}{\sqrt{P_\varepsilon(t)}}\left[\sqrt{p_{0,\varepsilon}}\tilde{f}^{(0)}_{\varepsilon,\zeta}(t) + \sum_{m=1}^{\infty}\sqrt{p_{m,\varepsilon}(t)}\int_0^t d\mathbf{s}_m \tilde{f}^{(m)}_{\varepsilon,\zeta}(t,\mathbf{s})\prod_{i=1}^{m} b_m^\dagger\right]|\emptyset\rangle \tag{2.67}$$

with $\mathbf{s}_m = \{t_1, t_2, \ldots, t_n\}$ being an ordered time vector $t_1 < t_2 < t_3 < \cdots < t$. We have $|\tilde{f}^{(0)}_{\varepsilon,\zeta}(t)|^2 = 1$ and $\int_0^t d\mathbf{s}_m |\tilde{f}^{(m)}_{\varepsilon,\zeta}(t,\mathbf{s})|^2 = 1$ for all m. Also, $P_\varepsilon(t) = \sum_{m=0}^{\infty} p_{m,\varepsilon}(t)$ as the total probability of the qubit being in the state ε at time t. Continuing, we find the expressions for the tilted coefficients $\tilde{f}^{(m)}_{\varepsilon,\zeta}(t)$. The coefficient $\tilde{f}^{(0)}_{\varepsilon,\xi}(t_N)$ is found by projecting the state (2.64) onto the subspace $\{|\varepsilon\rangle \otimes |\emptyset\rangle\}$, this gives

$$\tilde{f}^{(0)}_{\varepsilon,\xi}(t_N) = \langle\varepsilon|\left(\prod_{k=0}^{N-1}\langle\emptyset|\tilde{U}_k|\emptyset\rangle\right)|\xi\rangle \tag{2.68}$$

Now, we set $k = 1$,

$$\begin{aligned}\langle\emptyset|\tilde{U}_1|\emptyset\rangle &= \langle\emptyset|\left[\exp\left\{-iV_{qf}(t_1)\Delta t + i\frac{\Omega_y}{2}\Delta t\sigma_y(t_1)\right\}\right]|\emptyset\rangle \\ &= 1 + \langle\emptyset|\left[-iV_{qf}(t_1)\Delta t + i\frac{\Omega_y}{2}\Delta t\sigma_y(t_1)\right]|\emptyset\rangle \\ &+ \frac{1}{2}\langle\emptyset|\left[-iV_{qf}(t_1)\Delta t + i\frac{\Omega_y}{2}\Delta t\sigma_y(t_1)\right]^2|\emptyset\rangle\end{aligned} \tag{2.69}$$

Performing the algebra one finds,

$$\begin{aligned}\langle\emptyset|\tilde{U}_1|\emptyset\rangle &= \mathbb{1} + \Delta t\left(i\frac{\Omega_y}{2}\sigma_y - \frac{\gamma}{2}\sigma^\dagger\sigma\right) \\ &\approx \exp\left\{-i\frac{\Delta t}{2}\left[(-i\gamma + 2\delta)\,\sigma^\dagger\sigma - \Omega_y\sigma_y\right]\right\}\end{aligned} \tag{2.70}$$

Finally,

$$\boxed{\tilde{f}^{(0)}_{\varepsilon,\zeta}(t) = \langle\varepsilon|\left[\exp\left\{-i\frac{t}{2}\left[(-i\gamma + 2\delta)\,\sigma^\dagger\sigma - \Omega_y\sigma_y\right]\right\}\right]|\zeta\rangle.} \tag{2.71}$$

The coefficients for the qubit initially in the ground state are of particular interest in

Chaps. 3 and 4, hence we write them here for future reference:

$$\tilde{f}^{(0)}_{e,g}(t) = \frac{\Omega_y}{\Omega_B} e^{-\frac{(\gamma+2i\delta)}{4}} \sin\left(\frac{\Omega_B}{2}t\right) \tag{2.72}$$

$$\tilde{f}^{(0)}_{g,g}(t) = e^{-\frac{(\gamma+2i\delta)}{4}} \left[\cos\left(\frac{\Omega_B}{2}t\right) + \frac{(\gamma+2i\delta)}{2\Omega_B} \sin\left(\frac{\Omega_B}{2}t\right)\right] \tag{2.73}$$

where we defined the modified Rabi frequency:

$$\Omega_B = \sqrt{\left(\delta - i\frac{\gamma}{2}\right)^2 + \Omega_y^2}, \tag{2.74}$$

these expressions were found in a Mathematica notebook that can be found in the dedicated GitHub repository [76]. To find the single photon emission component we do,

$$\begin{aligned}\tilde{f}^{(1)}_{\varepsilon,\zeta}(t_N; t_{n_1}) &= \langle\zeta|\langle\emptyset|b_j \left[\left(\prod_{l=n_1+1}^{N-1} \tilde{U}_l\right) \tilde{U}_{n_1} \left(\prod_{m=0}^{n_1-1} \tilde{U}_m\right)\right] |\varepsilon\rangle|\emptyset\rangle \qquad (2.75)\\ &= \langle\zeta| \left[\left(\prod_{l=n_1+1}^{N-1} \bigotimes_{l=n_1+1}^{N-1} \langle\emptyset_l|\tilde{U}_l|\emptyset_l\rangle\right) \langle\emptyset_{n_1}|b_{n_1}\tilde{U}_{n_1}|\emptyset_{n_1}\rangle \left(\prod_{m=0}^{n_1-1} \bigotimes_{m=0}^{n_1-1} \langle\emptyset_m|\tilde{U}_m|\emptyset_m\rangle\right)\right] |\varepsilon\rangle\end{aligned}$$

Computing the term in red analogously to the spontaneous emission case leads to,

$$\langle\emptyset_{n_1}|b_{n_1}\tilde{U}_{n_1}|\emptyset_{n_1}\rangle = -\sqrt{\Delta t\gamma}\sigma(t_{n_1}) = -\sqrt{\Delta t\gamma} e^{-i\omega_0 t_{n_1}} |g\rangle\langle e|, \tag{2.76}$$

then,

$$\begin{aligned}\tilde{f}^{(1)}_{\varepsilon,\zeta}(t_N; t_j) &= -\sqrt{\Delta t\gamma} e^{-i\omega_0 t_{n_1}} \langle\zeta| \left(\prod_{l=n_1+1}^{N-1} \bigotimes_{l=n_1+1}^{N-1} \langle\emptyset_l|\tilde{U}_l|\emptyset_l\rangle\right) |g\rangle\langle e| \left(\prod_{m=0}^{n_1-1} \bigotimes_{m=0}^{n_1-1} \langle\emptyset_m|\tilde{U}_m|\emptyset_m\rangle\right) |\varepsilon\rangle\\ &= -\sqrt{\Delta t\gamma} \tilde{f}^{(0)}_{\zeta,g}(t_N - t_{n_1}) e^{-i\omega_0 t_{n_1}} \tilde{f}^{(0)}_{e,\varepsilon}(t_{n_1}). \qquad (2.77)\end{aligned}$$

The physical interpretation of Eq.(2.77) is neat: the system evolves coherently from $|\varepsilon\rangle$ to $|e\rangle$, then at time t_{n_1} a jump takes place leaving the system in the $|g\rangle$ state and creating a photon. Finally, the system can continue its coherent evolution to the final state $|\zeta\rangle$.

To compute the two-photon component the same strategy is used,

$$\begin{aligned}
\tilde{f}^{(2)}_{\varepsilon,\zeta}(t_N;t_{n_2},t_{n_1}) &= \langle\zeta|\langle\emptyset|b_j b_k\left[\left(\prod_{l=n_2+1}^{N-1}\tilde{U}_l\right)\tilde{U}_{n_2}\left(\prod_{l=n_1+1}^{n_2-1}\tilde{U}_l\right)\tilde{U}_{n_1}\left(\prod_{m=0}^{n_1-1}\tilde{U}_m\right)\right]|\varepsilon\rangle|\emptyset\rangle \\
&= \langle\zeta|\left[\left(\prod_{l=n_2+1}^{N-1}\bigotimes_{l=n_2+1}^{N-1}\langle\emptyset_l|\tilde{U}_l|\emptyset_l\rangle\right)\langle\emptyset_{n_2}|b_{n_2}\tilde{U}_{n_2}|\emptyset_{n_2}\rangle\right. \\
&\times\left.\left(\prod_{l=n_1+1}^{N-1}\bigotimes_{l=n_1+1}^{N-1}\langle\emptyset_l|\tilde{U}_l|\emptyset_l\rangle\right)\langle\emptyset_{n_1}|b_{n_1}\tilde{U}_{n_1}|\emptyset_{n_1}\rangle\left(\prod_{m=0}^{n_1-1}\bigotimes_{m=0}^{n_1-1}\langle\emptyset_m|\tilde{U}_m|\emptyset_m\rangle\right)\right]|\varepsilon\rangle \\
&= f^{(0)}_{\zeta,g}(t_N-t_{n_2})\left(-\sqrt{\Delta t\gamma}e^{-i\omega_0 t_{n_2}}\right)f^{(0)}_{e,g}(t_{n_2}-t_{n_1})\left(-\sqrt{\Delta t\gamma}e^{-i\omega_0 t_{n_1}}\right)f^{(0)}_{e,\varepsilon}(t_{n_1}) \\
&= \left(-\sqrt{\Delta t\gamma}\right)^2 f^{(0)}_{\zeta,g}(t_N-t_{n_2})e^{-i\omega_0(t_{n_2}+t_{n_1})}f^{(0)}_{e,g}(t_k-t_{n_1})f^{(0)}_{e,\varepsilon}(t_{n_1})
\end{aligned} \tag{2.78}$$

In words: the qubit evolves coherently from the state $|\varepsilon\rangle$ to the excited state $|e\rangle$, at some time t_{n_1} it emits a photon going instantaneously to the ground state $|g\rangle$. To emit a second photon, it must go back to the excited state at some time between the first emission and the second emission, i.e. during $t_{n_2}-t_{n_1}$, hence $e^{-i\omega_0(t_k+t_j)}f^{(0)}_{e,g}(t_{n_2}-t_{n_1})$. At t_{n_2} it jumps to the ground state emitting if no other emission event occurs it evolves from $|g\rangle$ to $|\zeta\rangle$ without emitting any photon for a time $t_N-t_{n_2}$.

At this point, a clear pattern emerges to obtain the m photons emission coefficient. Based on the two-photon emission component, and the physical interpretation just discussed, we can write the $m>2$ photons emission component as,

$$\boxed{\tilde{f}^{(m)}_{\varepsilon,\zeta}(t_N;\mathbf{t}) = \left(-\sqrt{\Delta t\gamma}\right)^m f^{(0)}_{\zeta,g}(t_N-t_{n_m})\left[\prod_{i=2}^{m}e^{-i\omega_0 t_{n_{i-1}}}f^{(0)}_{e,g}(t_{n_i}-t_{n_{i-1}})\right]f^{(0)}_{e,\varepsilon}(t_{n_1}).} \tag{2.79}$$

with $\mathbf{t}=\{t_{n_m},\dots,t_{n_1}\}$, the time-ordered vector: $t_{n_m}>\cdots>t_{n_1}$.

2.7.1 Weak resonant drive

In this section, we discuss a relevant regime for Chap. 4: the weak resonant drive. The resonant drive, $\delta=0$, assumption leads to the modified Rabi frequency:

$$\Omega_B=\sqrt{\Omega_y^2-\frac{\gamma^2}{4}}. \tag{2.80}$$

We also assume the drive is weak: $\Omega_y\ll\gamma$. This is referred as the *linear regime*. In this case, it can be shown that the Rabi frequency reduces to,

$$\Omega_B=\sqrt{\Omega_y^2-\frac{\gamma^2}{4}}\approx i\frac{\gamma}{2}. \tag{2.81}$$

Assuming the qubit is initially in the ground state $|g\rangle$. Substituting Eq. (2.81) in Eqs. (2.72) and (2.73), we obtain

$$\tilde{f}^{(0)}_{e,g}(t) \approx \frac{\Omega_y}{\gamma}(1 - e^{-\frac{\gamma}{2}t}) \tag{2.82}$$

$$\tilde{f}^{(0)}_{g,g}(t) \approx 1 \tag{2.83}$$

meaning that if the system starts in the ground state, it will most probably remain there during the dynamics. The probability that it goes to the excited state is proportional to $\frac{\Omega_y}{\gamma}$ which is assumed to be small. Hence, it is a very rare event, meaning that in this regime the probability of emission events is small.

The average value of the lowering operator can be readily computed,

$$\langle\sigma\rangle = e^{-i\omega_0 t}\tilde{f}^{(0)}_{e,g}(t)\left(\tilde{f}^{(0)}_{g,g}(t)\right)^* + e^{-i\omega_0 t}\sum_{m=1}^{\infty}\int_0^t d\mathbf{s}_m \tilde{f}^{(m)}_{e,g}(t,\mathbf{s})\left(\tilde{f}^{(m)}_{g,g}(t,\mathbf{s})\right)^*. \tag{2.84}$$

where for the ease of notation we used z^* to represent the complex conjugate of the value z[1].

The input field is

$$\langle b_{\text{in}}(t)\rangle = \beta_j = \frac{\alpha_0}{\sqrt{\varrho}}e^{-i\omega_0 t_j}, \tag{2.85}$$

and the mean of the lowering operator, $\sigma = |g\rangle\langle e|$, is

$$\langle\sigma\rangle \approx e^{-i\omega_0 t}\frac{\Omega_y}{\gamma}(1 - e^{-\frac{\gamma}{2}t}) = \frac{2}{\sqrt{\gamma}}\frac{\alpha_0}{\sqrt{\varrho}}e^{-i\omega_0 t}. \tag{2.86}$$

Substituting Eqs. (2.85), (2.86) and (2.23), we obtain

$$\langle b_{\text{out}}(t)\rangle = \langle b_{\text{in}}(t)\rangle - \sqrt{\gamma}\langle\sigma\rangle = -\langle b_{\text{in}}(t)\rangle \tag{2.87}$$

This means that in the linear regime, we simply have a $\pi-$phase shift of the input field. This is an important remark for what is going to be discussed in Chap. 4.

2.8 Solution for a single photon pulse

We consider a single photon wave-packet with central frequency $\omega_p = \omega_0 - \delta$, where the detuning $\delta \ll \omega_0$. In the temporal basis it is written,

$$|1\rangle = \sum_{n=0}^{\infty}\sqrt{\Delta t}\xi(t_n)b_n^\dagger|\emptyset\rangle, \text{ where} \tag{2.88}$$

$$\sum_{n=0}^{\infty}\Delta t|\xi(t_n)| = 1.$$

[1] In general complex conjugates are denoted by an overbar $\overline{z}$ except in cases such as this expression where we use the * instead to not overload the text.

We notice that the single photon wave packet is already correlated on the temporal basis before the interaction with the qubit. From the collisional model point of view, it is a correlated initial bath, hence leading to non-Markovian dynamics of the reduced system [94, 40]. The strategy to solve this case is different from the previous one. Instead of providing an *Ansatz* for the wave-function, we replace the propagator U_n with an effective map $\mathscr{M}_n$ as follows,

$$\begin{aligned}|\Psi(t_N)\rangle &= U_{N-1}U_{N-2}\dots U_0|\Psi(0)\rangle \\ &\approx \mathscr{M}_{N-1}\mathscr{M}_{N-2}\dots\mathscr{M}_0|\Psi(0)\rangle \\ &= \mathscr{M}_{N-1}|\Psi(t_{N-1})\rangle \\ &\equiv |\phi_g(t_N)\rangle|g\rangle + |\phi_e(t_N)\rangle|e\rangle. \end{aligned} \tag{2.89}$$

For any n the map acts in the following way,

$$\begin{aligned}\mathscr{M}_n|g\rangle|\phi_g(t_n)\rangle &= e^{-\frac{\gamma}{2}}|g\rangle|\phi_g(t_n)\rangle + \sqrt{1-e^{-\gamma\Delta t}}e^{i\omega_0 t_n}b_n|e\rangle|\phi_g(t_n)\rangle \\ \mathscr{M}_n|e\rangle|\phi_e(t_n)\rangle &= e^{-\frac{\gamma}{2}}|e\rangle|\phi_e(t_n)\rangle - \sqrt{1-e^{-\gamma\Delta t}}e^{-i\omega_0 t_n}b_n^\dagger|g\rangle|\phi_e(t_n).\rangle \end{aligned} \tag{2.90}$$

It draws inspiration from the iterative application of the collisional model to the spontaneous emission instance. The goal is to find a recursive relation for the un-normalized field wave-functions $|\phi_\epsilon(t_n)\rangle$, where $\epsilon = g, e$. From Eq. (2.89), we have

$$|\phi_\epsilon(t_N)\rangle = \langle\epsilon|\Psi(t_N)\rangle = \langle\epsilon|\mathscr{M}_{N-1}|\Psi(t_{N-1})\rangle, \tag{2.91}$$

now,

$$\begin{aligned}\mathscr{M}_{N-1}|\Psi(t_{N-1})\rangle &= \mathscr{M}_{N-1}|\phi_g(t_{N-1})\rangle|g\rangle + \mathscr{M}_{N-1}|\phi_e(t_{N-1})\rangle|e\rangle \\ &= e^{-\frac{\gamma}{2}}|g\rangle|\phi_g(t_{N-1})\rangle + \sqrt{1-e^{-\gamma\Delta t}}e^{i\omega_0 t_n}b_n|e\rangle|\phi_g(t_{N-1})\rangle \\ &\quad + e^{-\frac{\gamma}{2}}|e\rangle|\phi_e(t_{N-1})\rangle - \sqrt{1-e^{-\gamma\Delta t}}e^{-i\omega_0 t_n}b_n^\dagger|g\rangle|\phi_e(t_{N-1})\rangle \end{aligned} \tag{2.92}$$

Performing the projection we obtain the recursive relations,

$$|\phi_g(t_N)\rangle = e^{-\frac{\gamma}{2}}|\phi_g(t_{N-1})\rangle - \sqrt{1-e^{-\gamma\Delta t}}e^{-i\omega_0 t_{N-1}}b_{N-1}^\dagger|\phi_e(t_{n-1})\rangle, \tag{2.93}$$

$$|\phi_e(t_N)\rangle = e^{-\frac{\gamma}{2}}|\phi_e(t_{N-1})\rangle + \sqrt{1-e^{-\gamma\Delta t}}e^{i\omega_0 t_{N-1}}b_{N-1}|\phi_g(t_{N-1})\rangle. \tag{2.94}$$

These relations result in the following wave functions for the qubit initially in the ground state interacting with a single photon, i.e. $|\Psi(0)\rangle = |g\rangle|1\rangle$,

$$\begin{aligned}|\phi_g(t_N)\rangle = &\sum_{n=0}^{N-1}\left[\sqrt{\Delta t}\xi(t_n) - \gamma\Delta t e^{-\left(\frac{\gamma}{2}+i\omega_0\right)t_n}\sum_{m=0}^{n}\left(e^{\left(\frac{\gamma}{2}+i\omega_0\right)t_m}\sqrt{\Delta t}\xi(t_m)\right)\right]b_n^\dagger|\emptyset\rangle \\ &+ \sum_{n=N}^{\infty}\sqrt{\Delta t}\xi(t_n)b_n^\dagger|\emptyset\rangle \end{aligned} \tag{2.95}$$

$$|\phi_e(t_N)\rangle = \sqrt{\gamma}e^{-\frac{\gamma}{2}t_N}\sum_{n=0}^{N-1}\Delta t e^{\left(\frac{\gamma}{2}+i\omega_0\right)t_n}\xi(t_n)|\emptyset\rangle \tag{2.96}$$

Substituting in Eq. (2.89), we obtain

$$
\begin{aligned}
|\Psi_{\mathrm{SP}}(t_N)\rangle = &\left(\sqrt{\gamma}\sqrt{\Delta t}e^{-\frac{\gamma}{2}t_N}\sum_{n=0}^{N-1}\sqrt{\Delta t}e^{\left(\frac{\gamma}{2}+i\omega_0\right)t_n}\xi(t_n)|\emptyset\rangle\right)|e\rangle \\
&+\left(\sum_{n=0}^{N-1}\left[\sqrt{\Delta t}\xi(t_n)-\gamma\Delta t e^{-\left(\frac{\gamma}{2}+i\omega_0\right)t_n}\sum_{m=0}^{n}\left(e^{\left(\frac{\gamma}{2}+i\omega_0\right)t_m}\sqrt{\Delta t}\xi(t_m)\right)\right]b_n^\dagger|\emptyset\rangle\right)|g\rangle \\
&+\left(\sum_{n=N}^{\infty}\sqrt{\Delta t}\xi(t_n)b_n^\dagger|\emptyset\rangle\right)|g\rangle.
\end{aligned}
\tag{2.97}
$$

Finally, taking the continuous-time limit, using Eq. (2.42), leads to the wave function,

$$
|\Psi_{\mathrm{SP}}(t)\rangle = \sqrt{\gamma}\tilde{\xi}(t)|\emptyset\rangle|e\rangle + \left[\int_0^t du\Upsilon(u) + \int_t^\infty du\xi(u)\right]b^\dagger(t)|\emptyset\rangle|g\rangle, \tag{2.98}
$$

where we defined

$$
\Upsilon(u) = \xi(u) - \gamma\tilde{\xi}(u)e^{-i\omega_0 u}, \tag{2.99}
$$

and

$$
\tilde{\xi}(t) = e^{-\frac{\gamma}{2}t}\int_0^t du\; e^{\left(\frac{\gamma}{2}+i\omega_0\right)u}\xi(u) \tag{2.100}
$$

Tracing out the field in Eq. (2.98) results in the qubit's state obtained in Refs. [100, 101], and in the long-time limit, one obtains the scattered field's state derived in [102], demonstrating the accuracy of the method.

2.9 Conclusions

In this chapter, we have reviewed the formalism presented in Refs. [39, 73] for solving the dynamics of systems governed by time-dependent Hamiltonians. Specifically, we focused on the interaction between a qubit and a multimode electromagnetic field in a unidimensional wave-guide, described by a Jaynes-Cummings Hamiltonian within the interaction picture.

An original contribution was presented in Section 2.6, where we developed a general method for handling fields obtained through a unitary transformation of the vacuum state. This method offers a versatile approach to analyzing various field configurations.

The main result of this chapter is the derivation of an analytical formula that describes the joint state of the qubit and field at any given time, t. This formalism serves as a powerful tool for investigating the fields of interest that will be explored in the subsequent chapters of this dissertation. The codes used to obtain some of the results of this chapter are available on a dedicated GitHub repository [76].

Chapter 3

Quantum weak values and Wigner negativity in a single qubit gate

Physics is like sex. Sure, it may give some practical results, but that's not why we do it. – Richard P. Feynmann

3.1 Introduction

Quantum contextuality is a fundamental property of quantum systems, stating that the probability of the measurement outcomes is dependent not only on the state of the system but also on the choice of measurements performed and the context in which they are made [103]. In other words, the result of a measurement is context-dependent and cannot be explained solely by the properties of the measured system. Contextuality is not only significant at a fundamental level but has also been recognized as a crucial ingredient for achieving quantum advantage in information-processing tasks [104, 105, 106].

Entanglement is another widely recognized resource to provide a quantum advantage. The seminal work by John Bell introduced Bell's inequalities, which demonstrates that entangled bipartite quantum systems violate certain inequalities, indicating the non-local nature of these systems, a strong non-classical effect [107]. Regarding quantum contextuality, it is essential to identify quantities that, as the Bell's inequalities, serve as signatures of a system's contextual behavior. Two hallmarks of contextuality have been identified: the negativity of quasiprobability distributions [108] and the emergence of anomalous weak values [55].

Eugene Wigner developed the concept of quantum phase space to describe the state of bosonic fields, which are infinite-dimensional entities. In Ref. [109] he proposed a function to serve as a visualization tool for the quantum phase space, considering the uncertainty principle for the field's quadratures. The Wigner function, as it became known, is a quasi-probability distribution that can exhibit negative values for purely quantum states, such as Fock states. The negativity of the Wigner function has been recognized as a witness of the non-classical nature of bosonic field states [110]. The emergence of negativities in quasi-probability distributions and the presence of contextuality were shown to be mutually equivalent notions of non-classicality in Ref. [108]. In other words, the observation of negativities

indicates the contextual behavior of the system. Additionally, Ref. [55] established a specific equivalence between contextuality and Wigner negativity for homodyning (or heterodyning) measurements, that target the generalized position and momentum quadrature measurements [84].

Another witness of contextuality is the emergence of anomalous weak values. Introduced in Ref. [111], quantum weak values are a quantum variable arising from averaging over pre- and post-selected weak measurements. Recently, Ref. [54] showed that anomalous weak values are proofs of quantum contextuality, providing a fundamental result that indicates the contextual nature of a system whenever anomalous weak values appear.

Based on the fundamental mathematical physical results discussed above, this chapter aims to verify the emergence of both quantum contextuality witnesses within a specific paradigmatic physical system. Anomalous weak values can appear when we have a qubit interacting with a resonant intense coherent field as demonstrated in Refs. [48] and [52]. Thus, we focus our attention to this system. The set-up is the following: the qubit is initially in its ground state and it interacts with a resonant strong coherent field. The output field is continuously measured using heterodyne monitoring, granting access to the quadratures. After a specific interaction time τ, the qubit state is projected onto its energy eigenbasis. Subsequently, we can post-select the quadratures, that is, the field state is post-selected based on the qubit measurement outcome. The post-selection of the heterodyne measurement is not considered in the results proven in Ref. [55], thus representing an additional feature for the measurement scheme. This system is fundamental to the implementation of a single qubit gate, whereby the qubit undergoes a rotation by an angle $\theta = \Omega_y \tau$ (refer to Eq. (2.58) in Chap. 2).

Although the measurement setting described above involves post-selection on a qubit's final state, differs from the one proposed in Ref. [55], the emergence of anomalous weak values implies the contextual nature of the field's state based on the fundamental result presented in Ref. [54]. Therefore, our goal is to investigate whether the field's Wigner function, corresponding to the post-selection choices that yield anomalous weak values, exhibits negativity. In other words, we seek to establish a connection between anomalous weak values and Wigner negativity in these measurement settings involving post-selection. As will be discussed, the answer is affirmative, suggesting that the equivalence found in Ref. [55] between contextuality and negative Wigner distributions can be extended to more complex measurement settings involving post-selection.

Furthermore, the analytical approach discussed in Chap. 2 provides valuable insights into the underlying physics of the system by utilizing the collisional model solution from Eq. (2.66). It allows us to identify the specific terms that give rise to the distinctive features observed.

This chapter is organized as follows:

- In Sec. 3.2, we provide a comprehensive review and discussion of the physical interpretation of the two key witnesses of the quantum nature of a bosonic field: Wigner function negativity and anomalous weak values.

- In Sec. 3.3, we define the specific physical scenario under investigation and

elaborate on its experimental implementation.

- In Sec. 3.4, we analytically compute the weak values of the field, as presented in Eq. (3.35). This constitutes our first main result, and we illustrate it graphically in Fig. 3.3(b) as a function of time. Additionally, we present Fig. 3.5(a) to further demonstrate the emergence of anomalous values as a function of the gate angle for a fixed time of interaction τ.

- In Sec. 3.5, we calculate the conditional Wigner function, conditioned on the post-selection state. This serves as our second main result, and we showcase it in Fig. 3.5(b)-(c) to reveal the interplay between anomalous values and Wigner function negativity.

3.2 Witnesses of non-classical quantum states of light

3.2.1 Wigner function negativity

The Wigner function, as defined in [81] (see Chap. 4), is given by

$$\mathscr{W}(\alpha,\overline{\alpha}) = \frac{1}{\pi^2}\int d^2\lambda\ \exp\left\{-\lambda\overline{\alpha}+\overline{\lambda}\alpha\right\}\chi_S(\lambda,\overline{\lambda}), \tag{3.1}$$

where $\chi_S(\lambda,\overline{\lambda})$ is the symmetric quantum characteristic function,

$$\chi_S(\lambda,\overline{\lambda}) = \mathrm{tr}\{\exp\left\{-\overline{\lambda}a\right\}\exp\left\{\lambda a^\dagger\right\}\rho\}. \tag{3.2}$$

The Wigner function is a quasi-probability distribution, that may assume negative values in certain regions of the quantum phase space for non-classical states of light, such as number states or superposition of coherent states, also known as Schrödinger cat states [57, 81]. These negativities can be regarded as a signature of the non-classical behavior exhibited by quantum states, resulting from quantum interference effects that classical physics fails to explain [110].

One way to quantify the presence of negativity in the Wigner function is by using the Wigner negativity as a figure of merit. It is defined as [110]:

$$N(\mathscr{W}) \equiv \int d^2\alpha\ |\mathscr{W}(\alpha,\overline{\alpha})| - 1. \tag{3.3}$$

where $d^2\alpha$ represents the integral over the entire quantum phase space. The quantity $N(\mathscr{W})$ vanishes for coherent and squeezed vacuum states, for which the Wigner function is non-negative. The negativity of the Wigner function serves as an indicator of the non-classicality of a quantum state. Recently, its connection to the contextuality of quantum mechanics has been demonstrated in Ref. [55]. Figure 3.1 presents contour plots of the Wigner functions associated with the first four number states $\{|0\rangle,|1\rangle,|2\rangle,|3\rangle\}$, along with their corresponding Wigner negativities. The vacuum state, $|0\rangle$, has a Gaussian-shaped Wigner function centered at the origin of the

quantum phase space and does not exhibit any negativity, see Fig. 3.1(a). However, when we examine the Wigner functions of purely quantum states, Fig. 3.1(b), (c), and (d), negative regions emerge, which are captured by the Wigner negativity that grows monotonically with the value of n [110].

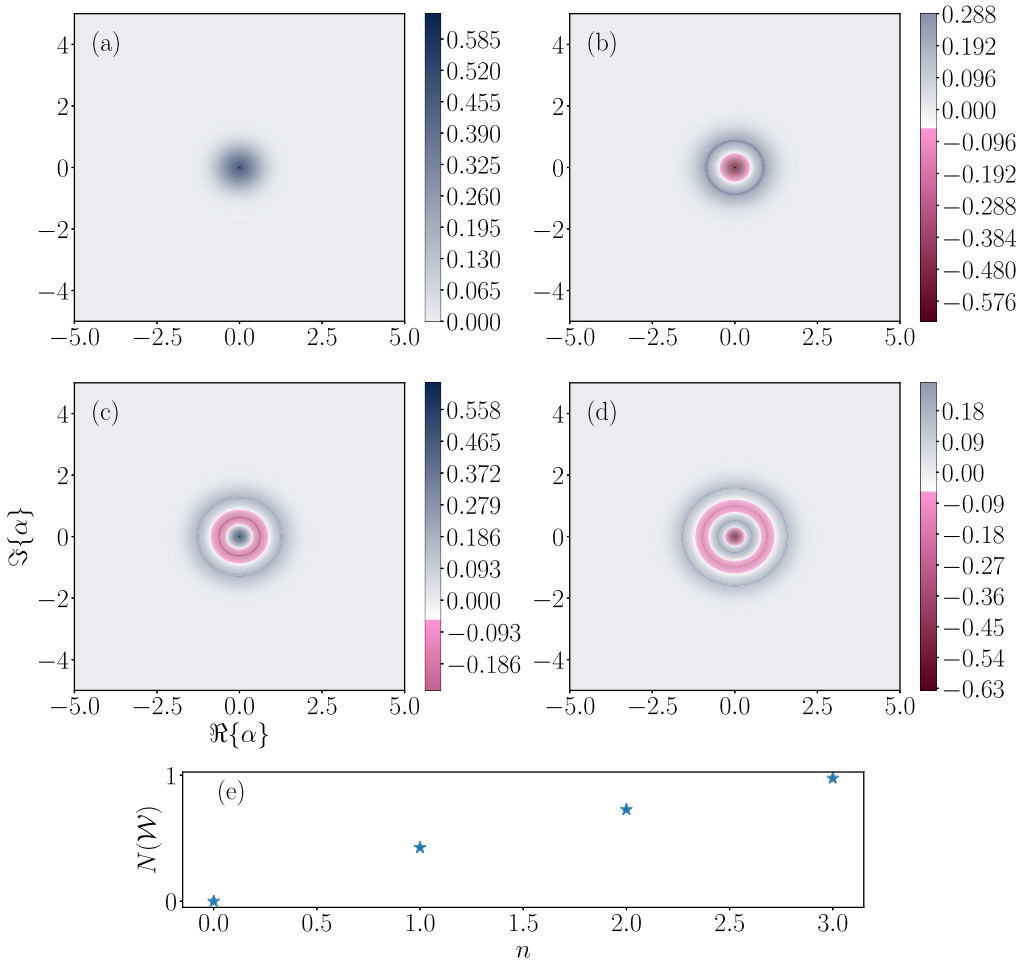

Figure 3.1: **Number state Wigner functions and Wigner function negativity.** Contour plots of the Wigner function (Eq. (3.1)) in the quantum phase space for Fock states $|n\rangle$ are presented. (a) Vacuum state: $|0\rangle$ exhibits no negativity, consistent with it being a Gaussian state [57]. (b) Single excitation: $|1\rangle$ shows the presence of a negative region. (c) Two excitations:$|2\rangle$. (d) Three excitations:$|3\rangle$. (e) The Wigner negativity (Eq. (3.3)) is plotted as a function of the number of excitations and grows monotonically.

3.2.2 Weak values theory in a nutshell

The emergence of weak values occurs in a scenario similar to the one discussed in Chap. 1. We consider a measured system initially prepared in the state $|i\rangle_S$, which interacts weakly with a meter also in some initial state $|\phi_i\rangle$. This weak interaction results in weak entanglement between the system and the meter. Unlike in the von Neumann scheme, where the classical measurement apparatus projects the meter's

state, weak values involve using the apparatus to collapse the state of the measured system, which is assumed to be $|f\rangle_S$, associated with the field state $|\phi_f\rangle$. The preparation, $|i\rangle_S$, and final collapse, $|f\rangle_S$, of the measured system define the pre- and post-selection states, respectively.

When continuously observing an observable of the meter, weak values corresponding to *the states of the meter* emerge. Importantly, these weak values can exceed the range of allowed eigenvalues of the measured observable, as we will discuss. These exceptional values are commonly referred to as *anomalous weak values*.

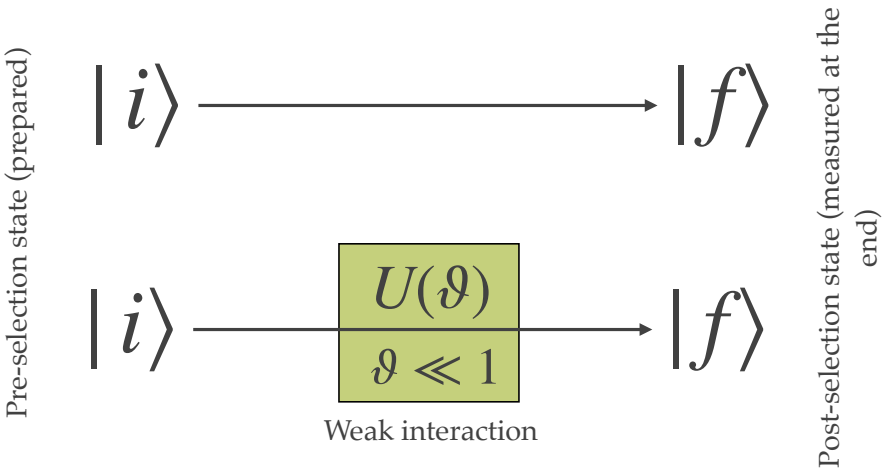

Figure 3.2: **Quantum dynamics leading to weak values.** (a) Free evolution from the initial state $|i\rangle_S$ to the final state $|f\rangle_S$, with the corresponding probability given by Eq. (3.13). (b) Evolution with a small perturbation $U(\vartheta) = \exp\{-i\vartheta\,(B_S \otimes p_M)\}$, where ϑ is a small parameter, with the probability described by Eq. (3.8).

To derive the formula for weak values and develop a clear physical understanding of its interpretation, we follow the methodology outlined in Ref. [112] and Chap. 1. The initial state of the composite system is given by:

$$|i\rangle_S \otimes |\phi_i\rangle_M, \tag{3.4}$$

The system is left to evolve unitarily and finally, when the state of the system is collapsed, we have the final state of the composite system is given by:

$$|f\rangle_S \otimes |\phi_f\rangle_M. \tag{3.5}$$

This evolution captures the transformation of the combined system as it goes from the pre-selection, $|i\rangle_S$, state to the post-selection state, $|f\rangle_S$.

Let B_S denote an arbitrary operator of the system that undergoes a projective measurement at the end of the evolution, and p_M represent the momentum operator of the meter (as discussed in Chap. 1). The interaction between the system and the

meter is described by the unitary operator:

$$\begin{aligned} U(\vartheta) &= \exp\left\{-i\vartheta\left(B_S \otimes p_M\right)\right\} \\ &\approx 1 - i\vartheta\left(B_S \otimes p_M\right) + \mathscr{O}(\vartheta^2) \end{aligned} \tag{3.6}$$

where ϑ is a real parameter assumed to be sufficiently small (in Chap. 1 it was $\vartheta = g_0 t$), allowing us to perform a Taylor expansion as shown in the second line. The state of the joint system after the interaction is given by:

$$|\Psi(\vartheta)\rangle = U(\vartheta)\left(|i\rangle_S \otimes |\phi_i\rangle_M\right). \tag{3.7}$$

We can investigate the role of the interaction in two aspects:

1. The probability of obtaining $|f\rangle_S \otimes |\phi_f\rangle_M$ starting from the state $|i\rangle_S \otimes |\phi_i\rangle_M$, as a function of the parameter ϑ, denoted as $P_{i\to f}(\vartheta)$, is given by:

$$P_{i\to f}(\vartheta) = |\langle\phi_f|\langle f|\Psi(\vartheta)\rangle|^2 \tag{3.8}$$
$$= |\langle\phi_f|\langle f|U(\vartheta)|i\rangle|\phi_i\rangle|^2. \tag{3.9}$$

   we drop the subscripts labeling the system and meter in the states in what follows for ease of notation.

2. The unnormalized final state of the meter, $|\tilde{\phi}_f\rangle$, obtained by projecting the final state of the joint system $|\Psi(\vartheta)\rangle$ onto $|f\rangle$,

$$\begin{aligned} |\tilde{\phi}_f\rangle &= \langle f|\Psi(\vartheta)\rangle \\ &= \langle f|(U(\vartheta)|i\rangle \otimes |\phi_i\rangle) \end{aligned} \tag{3.10}$$

These two objects allow us to analyze the probabilistic evolution of the system and the resulting state of the meter in the context of the system-meter weak interaction.

Let's begin by investigating the final state of the meter. If the initial state of the meter is modified during its evolution by the unitary operator $U(\vartheta)$, we have:

$$\begin{aligned} \langle f|\Psi(\vartheta)\rangle &= \langle f|[U(\vartheta)|i\rangle \otimes |\phi_i\rangle] \\ &\approx \left(\langle f|i\rangle - i\vartheta\langle f|B_S|i\rangle p_M\right)|\phi_i\rangle \\ &= \langle f|i\rangle\left(1 - i\vartheta\frac{\langle f|B_S|i\rangle}{\langle f|i\rangle}p_M\right)|\phi_i\rangle \end{aligned} \tag{3.11}$$

This naturally introduces the concept of the first-order weak value:

$$(B_S)^1_w = \frac{\langle f|B_S|i\rangle}{\langle f|i\rangle}. \tag{3.12}$$

This sheds light on the effect of the weak interaction on the state of the meter: as soon as we project the system onto the state $|f\rangle_S$ the meter is displaced proportionally to the weak value $(B_S)^1_w$. As the pre- and post-selected states become orthogonal ($\langle f|i\rangle \to 0$) the value of $(B_S)^1_w$ diverges, meaning it lies outside the range of eigenvalues of B_S [111, 113]. The emergence of these values leads to a significant displacement

of the initial state of the meter [114, 115].

Now, let's examine the effect of the interaction on the transition probability given by Eq. (3.8). Firstly, in the absence of interaction ($\vartheta = 0$), the probability of finding the system in its final state is given by:

$$P_{i\to f}(0) = |\langle f|i\rangle\langle\phi_f|\phi_i\rangle|^2. \tag{3.13}$$

This equation describes the probability of the system transitioning from the initial state $|i\rangle_S$ to the final state $|f\rangle_S$ in the absence of any interaction. It depends on the overlap between the pre-selection and post-selection states ($\langle f|i\rangle$).

Now, let's consider the case where there is a weak interaction ($\vartheta \neq 0$). In this case, we have:

$$\begin{aligned} P_{i\to f}(\vartheta) &= |\langle f|\langle\phi_f|U(\vartheta)|i\rangle|\phi_i\rangle|^2 \\ &\approx |\langle f|\langle\phi_f|(1 - i\vartheta B_S \otimes p_M)\,|i\rangle|\phi_i\rangle|^2 \\ &= |\langle f|i\rangle\langle\phi_f|\phi_i\rangle|^2 \left|\left(1 + 2\vartheta\Im\{\frac{\langle f|B_S|i\rangle}{\langle f|i\rangle}\frac{\langle\phi_f|p_M|\phi_i\rangle}{\langle\phi_f|\phi_i\rangle}\right)\right|^2 \end{aligned} \tag{3.14}$$

Hence, we find that:

$$\begin{aligned} \frac{P_{i\to f}(\vartheta)}{P_{i\to f}(0)} - 1 = 2\vartheta \Bigg[&\Im\left\{\frac{\langle f|B_S|i\rangle}{\langle f|i\rangle}\right\}\Re\left\{\frac{\langle\phi_f|p_M|\phi_i\rangle}{\langle\phi_f|\phi_i\rangle}\right\} \\ &+\Re\left\{\frac{\langle f|B_S|i\rangle}{\langle f|i\rangle}\right\}\Im\left\{\frac{\langle\phi_f|p_M|\phi_i\rangle}{\langle\phi_f|\phi_i\rangle}\right\}.\Bigg] \end{aligned} \tag{3.15}$$

This expression reveals the operational interpretation of the weak value. It characterizes the relative correction to the detection probability $P_{i\to f}(0)$ due to a small perturbation $U(\vartheta)$ that results in a modified detection probability $P_{i\to f}(\vartheta)$. We note as well the appearance of the weak value associated with the meter:

$$(p_M)^1_w = \frac{\langle\phi_f|p_M|\phi_i\rangle}{\langle\phi_f|\phi_i\rangle} \tag{3.16}$$

3.3 System and model

In Chap. 2, we investigated the dynamics of a qubit interacting with a field in a closed system. In this chapter, we focus on a specific scenario depicted in Fig. 3.3(a). Here, a qubit with a natural frequency ω_0 is initially in the ground state $|g\rangle$ and interacts with a resonant strong coherent input field (*in*). The output field (*out*) is continuously measured using a heterodyne detection scheme over a time interval $t \in [0, \tau]$. This measurement provides access to the quadratures $\Im\langle b_{\text{out}}(t)\rangle$ and $\Re\langle b_{\text{out}}(t)\rangle$, which enables the computation of $\langle b^\dagger_{\text{out}}(t)b_{\text{out}}(t)\rangle$. At $t = \tau$, a projective measurement is performed on the qubit's state, allowing post-selection of the field's state and inducing a weak measurement on it [48]. This setup implements a single-qubit gate, as discussed in Sec. 2.7, using Eqs. (2.60) and (2.62), where the fidelity of the gate is limited by the generation of qubit-field correlations [116].

Superconducting circuits are the ideal platform for implementing the detection

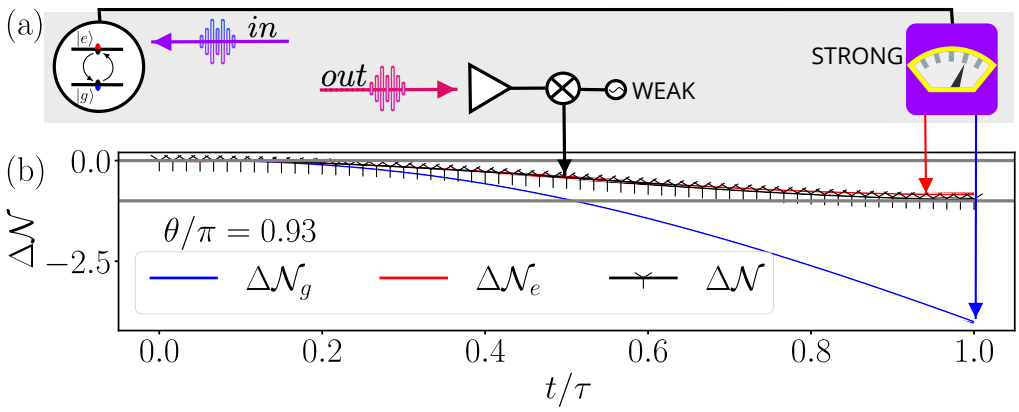

Figure 3.3: **Detection of the field's weak values in the single-qubit gate.** (a) Schematic of the detection process: The gate is implemented by coherently driving a 1D atom using an input pulse (*in*) with an area $\theta = \Omega_y \tau$. The output field (*out*) is continuously monitored during the time interval $[0, \tau]$ through a heterodyne measurement scheme (weak measurement). At the time τ, a projective (strong) measurement is performed on the qubit, and the acquired heterodyne data are post-selected based on the outcome $\epsilon = g, e$. (b) Change in the number of field excitations over time: The plot illustrates the weak values $\Delta\mathcal{N}_e$ (solid red line) and $\Delta\mathcal{N}_g$ (dotted blue line) corresponding to post-selection on the qubit's excited and ground states, respectively. The unconditional value, $\Delta\mathcal{N}$ (black chicken foot), is also included and falls within the allowed range of values. The anomalous weak values are represented by $\Delta\mathcal{N}_g$ values below the solid gray line (-1). This plot was generated using a driving pulse with an area $\theta = 0.93\pi$ and duration $\tau = 3/40\gamma^{-1}$, where γ represents the emitter's vacuum decay rate. These parameter values were chosen to clearly visualize the emergence of anomalous weak values and are otherwise arbitrary.

scheme shown in Fig. 3.3, allowing independent access to the qubit and the field states. Notably, experiments investigating anomalous weak values have been conducted in this context. In Ref. [48], the authors detected resonance fluorescence emitted by a qubit outside a cavity, demonstrating its correspondence to weak continuous monitoring of the qubit's lowering operator, $\sigma = |g\rangle\langle e|$. They observed interference effects between Rabi oscillations associated with past and future states [117, 118].

In a more recent experiment, reported in Ref. [52], the authors studied the field's quadratures. They experimentally probed the energy of the driving pulse conditioned on the measured state of the qubit and observed a change in the pulse energy due to pre-measurement entanglement. Notably, the pulse energy could change by more than one quantum depending on the qubit energy outcome, revealing the subtle back-action of qubit measurements on the drive pulse. The collisional model provides a precise description of the field's state between the pre-selection and post-selection of the qubit, enabling the study of anomalous energy exchanges between the qubit and the field.

The system is described by the Hamiltonian in Eq. (2.60) and it is driven by a strong resonant coherent pulse with amplitude

$$\langle b_{\text{in}}(t)\rangle = \beta_{\text{in}}(t) = \frac{\alpha_0 e^{-i\omega_0 t}}{\sqrt{\varrho}}, \tag{3.17}$$

where $\alpha_0 \in \mathbb{R}$. The field's state at the initial time $t = 0^-$ is given by

$$|\alpha_0\rangle = D(\alpha_0)|\emptyset\rangle \tag{3.18}$$

where the displacement operator is

$$D(\alpha_0) = \exp\left\{\alpha_0 a_0^\dagger - \bar{\alpha}_0 a_0\right\} = \exp\left\{\int dt \beta_t b^\dagger(t) - \bar{\beta}_t b(t)\right\} \tag{3.19}$$

(see Sec. 2.7).

In the classical limit of the field, the reduced dynamics of the qubit is solely determined by the driving term in Eq. (2.60), acting as a rotation around the $y-$axis (2.62) by a finite angle (Eq. (2.62))

$$\theta = \Omega_y \tau, \tag{3.20}$$

where τ is the interaction time. Therefore, we have

$$|\Psi_0\rangle = |g\rangle \otimes |\alpha_0\rangle \xrightarrow{\tau} |\Psi(\theta)\rangle = \left[\cos\left(\frac{\theta}{2}\right)|g\rangle + \sin\left(\frac{\theta}{2}\right)|e\rangle\right] \otimes |\alpha_0\rangle \tag{3.21}$$

The joint solution of the qubit-field state is given by Eq. (2.66), and the discrete-time Lindblad equation, Eq. (2.16), governing the qubit's state takes the following form,

$$\frac{\rho_n - \rho_{n-1}}{\Delta t} = \frac{\Omega_y}{2}[\sigma - \sigma^\dagger, \rho_{n-1}] + \gamma\left(\sigma\rho_{n-1}\sigma^\dagger - \frac{1}{2}\{\sigma^\dagger\sigma, \rho_{n-1}\}\right). \tag{3.22}$$

3.4 Husimi $Q-$function and field's weak values

In the scenario presented in Fig. 3.3(a), our focus is on studying the *change in the number of excitations* of the field. This change is given by the expression:

$$\Delta\mathscr{N}_\epsilon = \int_0^\tau dt \langle b_{\text{out}}^\dagger(t) b_{\text{out}}(t)\rangle_\epsilon - |\beta_{\text{in}}(t)|^2. \tag{3.23}$$

Here, the subscript $\epsilon = g, e$ represents the post-selection outcome. When there is no subscript, we consider the case where the outcomes are *not* post-selected, i.e., unconditional.

Once the qubit can absorb or emit one excitation of the field, one would expect the modulus of the difference, $|\Delta\mathscr{N}_\epsilon|$, to fall within the range of $[0, 1]$. Specifically, $\Delta\mathscr{N} = -1$ is expected when the qubit absorbs one excitation from the field, transitioning to the excited state $|e\rangle$.

To compute Eq. (3.23), we first calculate the conditioned Husimi $Q-$function based on the outcome ϵ. For a system in the state $\rho(t_n) = \rho_q(t_n) \otimes |\beta_n\rangle\langle\beta_n|$, where $\rho_q(t_n)$ represents the emitter's state at time t_n, the $Q-$function is defined as [81]:

$$Q_\epsilon(s_n) = \frac{1}{\pi}\langle s_n|\rho(t_n)|s_n\rangle, \tag{3.24}$$

with

$$\begin{aligned} |s_n\rangle &= D^{(n)}(s_n)|\emptyset_n\rangle, \text{ and} \\ D^{(n)}(s) &= \exp\left\{s_n b_n - \overline{s}_n b_n^\dagger\right\}. \end{aligned} \tag{3.25}$$

Here, $|s_n\rangle = D^{(n)}(s_n)|\emptyset_n\rangle$, is the coherent state with amplitude s_n, and $D^{(n)}(s_n) = \exp\left\{s_n b_n - \overline{s}_n b_n{}^\dagger\right\}$ is the displacement operator of the n-th temporal mode with amplitude s_n. The computation of the $Q-$function is motivated by three reasons. Firstly, it can be interpreted as a valid probability distribution since, by definition, it is always positive [81]. Secondly, it represents the probability distribution of the outcomes of a heterodyne measurement (see App. A of Ref. [85]), which is precisely the measurement being considered here. Finally, it allows us to express the intensity of the output field in terms of the $Q-$function as [81]:

$$\langle b_{\text{out}}^\dagger(t_n) b_{\text{out}}(t_n)\rangle_\epsilon = \lim_{\Delta t\to 0}\frac{1}{\Delta t}\int d^2 s_n\, (|s_n|^2 - 1) Q_\epsilon(s_n). \tag{3.26}$$

This expression is necessary to obtain the weak values in Eq. (3.23).

Two approaches can be employed to compute the $Q-$function. The first approach involves directly utilizing the wavefunction result obtained in Chap. 2, Eq. (2.66), which leads to an analytical formula dependent on the coefficients. The second approach utilizes the past quantum state formalism proposed in Refs. [117, 118] and is well-suited for numerical simulations. Both approaches yield consistent results. We will begin by presenting the latter approach, and then present the steps using the former.

We begin by defining the projector as $\Pi_{s_n} = |s_n\rangle\langle s_n|$. Using the cyclic property

of the trace, we rewrite Eq. (3.24) as

$$Q_\epsilon(s_n) = \frac{1}{\pi} \operatorname{tr}\left\{\Pi_{s_n}\rho(t_n)\right\}, \tag{3.27}$$

To investigate how the outcome ϵ for the qubit energy at time τ affects the weak values of the field, we utilize the past quantum state formalism [117, 118] that applies to closed and open dynamics. This formalism introduces an effect matrix $E_\epsilon(\tau, t) = U^\dagger(\tau - t)|\epsilon\rangle\langle\epsilon|U(\tau - t)$, where $U(t)$ is the propagator. The effect matrix backpropagates the effect of the measurement outcome $|\epsilon\rangle$ at time τ. Equation (3.27) can be expressed in terms of the effect matrix as follows:

$$Q_\epsilon(s_n) = \frac{1}{\pi P_\epsilon(\tau)} \operatorname{tr}\left\{E_\epsilon(\tau, t_{n+1})\Pi_{s_n}\rho(t_{n+1})\right\}. \tag{3.28}$$

Here, $P_\epsilon(\tau)$ represents the probability of measuring ϵ at time τ (see Eq. (2.66)). Using $\rho(t_{n+1}) = U(t_n)\rho_n U^\dagger(t_n) = U(t_n)\left(\rho_q(t_n) \otimes |\beta_n\rangle\langle\beta_n|\right)U^\dagger(t_n)$, we obtain:

$$\begin{aligned} Q_\epsilon(s_n) &= \frac{1}{\pi P_\epsilon(\tau)} \operatorname{tr}\left\{E_\epsilon(\tau - t_n)\Pi_{s_n}U(t_n)\rho_n U^\dagger(t_n)\right\} \\ &= \frac{1}{\pi P_\epsilon(\tau)} \operatorname{tr}\left\{\langle s_n|E_\epsilon(\tau - t_{n+1})|s_n\rangle\langle s_n|U(t_n)\rho_q(t_n) \otimes |\beta_n\rangle\langle\beta_n|U^\dagger(t_n)\right\} \\ &= \frac{1}{\pi P_\epsilon(\tau)} \operatorname{tr}\left\{E_\epsilon(\tau - t_{n+1})\langle s_n|U(t_n)\underbrace{|\beta_n\rangle\rho_q(t_n)\langle\beta_n|}_{=\rho(t_n)}U^\dagger(t_n)|s_n\rangle\right\} \end{aligned} \tag{3.29}$$

Applying the BCH formula, Eq. (2.15), in the red term up to second order in Δt, and defining

$$\mathbb{E} = \frac{\exp\{-|s_n - \beta_n|^2\}}{\pi} \tag{3.30}$$

we obtain

$$\begin{aligned} \frac{Q_\epsilon(s_n)}{\mathbb{E}} &= \frac{1}{P_\epsilon(\tau)} \operatorname{tr}\left\{E_\epsilon(\tau, t_{n+1})\rho(t_{n+1})\right\} \\ &+ \frac{1}{P_\epsilon(\tau)}\gamma\Delta t(|\beta_n - s_n|^2 - 1) \operatorname{tr}\left\{E_\epsilon(\tau, t_{n+1})\sigma\rho(t_n)\sigma^\dagger\right\} \\ &+ \frac{1}{P_\epsilon(\tau)}\sqrt{\gamma\Delta t}(\overline{\beta}_n - \overline{s}_n) \operatorname{tr}\left\{E_\epsilon(\tau, t_{n+1})\sigma(t_n)\rho(t_n)\right\} + \text{h.c.} \end{aligned} \tag{3.31}$$

where "h.c." stands for hermitian conjugate. Noticing the identities,

$$P_\epsilon(\tau) = \operatorname{tr}\left\{E_\epsilon(\tau, t_{n+1})\rho(t_{n+1})\right\}, \tag{3.32}$$

$$\langle\sigma(t_n)\rangle_\epsilon = \frac{\operatorname{tr}\left\{E_\epsilon(\tau, t_{n+1})\sigma(t_n)\rho(t_n)\right\}}{P_\epsilon(\tau)}, \tag{3.33}$$

allows the simplification to,

$$Q_\epsilon(s_n) = \mathbb{E}\left[1 + \Delta t(|\alpha_n - s_n|^2 - 1)\gamma\mathscr{J}_\epsilon(t_n) + 2\sqrt{\gamma\Delta t}\Re\left\{(\overline{s}_n - \overline{\alpha}_n)\langle\sigma(t_n)\rangle_\epsilon\right\}\right], \tag{3.34}$$

where it was defined,

$$\gamma\mathscr{J}_\epsilon(t_n) = \frac{1}{P_\epsilon(\tau)}\,\mathrm{tr}\left\{|\epsilon\rangle\langle\epsilon|U(\tau - t_n)\sigma\rho_q(t_n)\sigma^\dagger U^\dagger(\tau - t_n)\right\}.$$

Equation (3.34) gives the final form of the conditional Husimi $Q-$function of the field's temporal modes. It predicts the outcomes of a continuous heterodyne detection subjected to post-selection on the outcome ϵ.

Finally, by substituting this equation into Eq. (3.23) and evaluating the integral, we obtain the conditional variation of the number of excitations:

$$\boxed{\Delta\mathscr{N}_\epsilon = \int_0^\tau dt\left(\gamma\mathscr{J}_\epsilon(t_n) - \Omega_y\Re\left\{\langle\sigma(t_n)\rangle_\epsilon\right\}\right).} \tag{3.35}$$

Physically, the first term

$$\int_0^\tau dt\gamma\mathscr{J}_\epsilon(t_n) = \sum_{j\geq 1}\frac{p_\epsilon^j(\tau)}{P_\epsilon(\tau)}, \tag{3.36}$$

represents the total probability of spontaneous emission events occurring during the evolution of the qubit from the ground state $|g\rangle$ to the final state $|\epsilon\rangle$. The second term,

$$\begin{aligned} -\int_0^\tau dt\Omega\Re\left\{\langle\sigma(t_n)\rangle_\epsilon\right\} &= 2\int_0^\tau dt\Re\left\{\langle b_{\mathrm{in}}(t)\rangle^*\left(\langle b_{\mathrm{out}}(t)\rangle_\epsilon - \langle b_{\mathrm{in}}(t)\rangle\right)\right\} \\ &= 2\left[\int_0^\tau dt\Re\left\{\langle b_{\mathrm{in}}(t)\rangle^*\langle b_{\mathrm{out}}(t)\rangle_\epsilon\right\} - \int_0^\tau dt\Re\left\{|\langle b_{\mathrm{in}}(t)\rangle|^2\right\}\right] \end{aligned} \tag{3.37}$$

comprises the total input intensity, $|\langle b_{\mathrm{in}}(t)\rangle|^2$, and the interference between the input and the emitter's fluorescence output post-selected on state $|\epsilon\rangle$ (highlighted in red): $\langle b_{\mathrm{in}}(t)\rangle^*\langle b_{\mathrm{out}}(t)\rangle_\epsilon$. The latter is the term in $\Delta\mathscr{N}_\epsilon$ can exceed 1, giving rise to the observed anomalous values.

In Fig. 3.3(b), we plot the conditional weak values $\Delta\mathscr{N}_{g(e)}$, and the unconditioned variation of the number of excitations $\Delta\mathscr{N}$ for a gate angle smaller than π, i.e., $\theta = \Omega_y\tau < \pi$. If the angle was a π rotation, we would certainly observe a population inversion of the qubit. In this case, we observe that $\Delta\mathscr{N}_e$ and $\Delta\mathscr{N}$ fall within the allowed range of values, while $\Delta\mathscr{N}_g$ starts to exceed one after a sufficiently long interaction time. The physical interpretation is clear: even if the angle is smaller than π, driving the system long enough makes it *unlikely* to find the qubit in the ground state. Therefore, the qubit is most probably in the excited state. For the sake of completeness, we will now outline the main steps to compute the Q-function using the analytical solution provided in Eq. (2.66). In the laboratory frame and

considering the truncation to the two-photon component, the state can be written as

$$|\tilde{\phi}_\epsilon\rangle = \left\{ \bigotimes_n \frac{D^{(n)}(\beta_n)}{\sqrt{P_\epsilon(\tau)}} \left[f_\epsilon^{(0)}(\tau) + \sum_{n=1}^{N-1} \sqrt{\Delta t} f_\epsilon^{(1)}(\tau, t_n) b_n^\dagger + \sum_{n=1}^{N-1} \sum_{n'>n} \Delta t f_\epsilon^{(2)}(\tau, t_{n'}, t_n) b_{n'}^\dagger b_n^\dagger \right] |\emptyset\rangle \right\}. \tag{3.38}$$

The $Q-$function is then given by,

$$Q_\epsilon(s_n) = \frac{1}{\pi} \operatorname{tr} \left\{ \Pi_{s_n - \beta_n} \eta_\epsilon^{(n)} \right\}, \tag{3.39}$$

where $\eta_\epsilon^{(n)}$ represents the reduced density matrix of the mode b_n in the displaced frame, and $\Pi_{s_n-\beta_n} = |s_n - \beta_n\rangle\langle s_n - \beta_n|$. The field state in the displaced frame, in discrete time, can be expressed as

$$|\phi_\epsilon\rangle = \frac{1}{\sqrt{P_\epsilon(\tau)}} \left[f_\epsilon^{(0)}(\tau) + \sum_{n=1}^{N-1} \sqrt{\Delta t} f_\epsilon^{(1)}(\tau, t_n) b_n^\dagger + \sum_{n=1}^{N-1} \sum_{n'>n} \Delta t f_\epsilon^{(2)}(\tau, t_{n'}, t_n) b_{n'}^\dagger b_n^\dagger + \dots \right] |\emptyset\rangle. \tag{3.40}$$

To obtain the state $\eta_\epsilon^{(n)}$, we need to trace over all modes $m \neq n$, leading to

$$\begin{aligned} \eta_\epsilon^{(n)} &= \operatorname{tr}_{m\neq n} \left\{ |\phi_\epsilon\rangle\langle\phi_\epsilon| \right\} \qquad (3.41) \\ &= \frac{1}{P_\epsilon(\tau)} \left[|\phi_\epsilon^{01}\rangle\langle\phi_\epsilon^{01}| + \sum_{n'\neq n} |\phi_\epsilon^{12}(n')\rangle\langle\phi_\epsilon^{12}(n')| + \sum_{n'\neq n} \sum_{m\neq n} |f_\epsilon^{(2)}(\tau, t_m, t_{n'})|^2 |\emptyset_n\rangle\langle\emptyset_n| \right]. \end{aligned}$$

Here, we define the following states:

$$\begin{aligned} |\phi_\epsilon^{01}\rangle &= f_\epsilon^{(0)}(\tau)|\emptyset_n\rangle - \sqrt{\Delta t} f_\epsilon^{(1)}(\tau, t_n) e^{-i\omega_0 t_n} |1_n\rangle \qquad (3.42) \\ |\phi_\epsilon^{12}(m)\rangle &= -\sqrt{\Delta t} f_\epsilon^{(1)}(\tau, t_m) e^{-i\omega_0 t_n} |1_n\rangle + \Delta t \left(f_\epsilon^{(2)}(\tau, t_m, t_n) + f_\epsilon^{(2)}(\tau, t_n, t_m) \right) e^{-i\omega_0(t_n+t_m)} |1_n\rangle \end{aligned}$$

Finally, substituting Eq. (3.41) into Eq. (3.39) yields:

$$\begin{aligned} \frac{\mathscr{Q}_\epsilon^{(n)}(s)}{\mathbb{E}} &= P_\epsilon(\tau) \qquad (3.43) \\ &+ \Delta t \left(|f_\epsilon^{(1)}(\tau, t_n)|^2 + \sum_{m>n} \Delta t |f_\epsilon^{(2)}(\tau, t_n, t_m)|^2 + \sum_{m<n} \Delta t |f_\epsilon^{(2)}(\tau, t_m, t_n)|^2 \right) (|\beta_n - s_n|^2 - 1) \\ &- 2\sqrt{\Delta t} \operatorname{Re} \left\{ e^{i\omega_0 t_n} (s_n - \beta_n) \left(f_\epsilon^{(1)}(\tau, t_n) f_\epsilon^{(0)}(\tau) + \sum_{m>n} \Delta t f_\epsilon^{(2)}(\tau, t_n, t_m) f_\epsilon^{(1)}(\tau, t_m) \right) \right\} \\ &- 2\sqrt{\Delta t} \operatorname{Re} \left\{ e^{i\omega_0 t_n} (s_n - \beta_n) \sum_{m<n} \Delta t f_\epsilon^{(2)}(\tau, t_m, t_n) f_\epsilon^{(1)}(\tau, t_m) \right\} \end{aligned}$$

This expression leads to,

$$
\begin{aligned}
P_\epsilon(\tau)\Delta\mathscr{N}_\epsilon = p_\epsilon^{(1)}(\tau) + p_\epsilon^{(2)}(\tau) \\
&- 2\Re\left\{ f_\epsilon^{(0)}(\tau)\int_0^\tau dt \bar{\beta}_t e^{-i\omega_0 t} f_\epsilon^{(1)}(\tau,t)\right\} \\
&- 2\Re\left\{ \int_0^\tau dt \int_t^\tau dt' f_\epsilon^{(1)}(\tau,t') f_\epsilon^{(2)}(\tau,t,t')\bar{\beta}_t e^{-i\omega_0 t}\right\} \\
&- 2\Re\left\{ \int_0^\tau dt \int_0^t dt' f_\epsilon^{(1)}(\tau,t') f_\epsilon^{(2)}(\tau,t',t)\bar{\beta}_t e^{-i\omega_0 t}\right\}
\end{aligned}
\tag{3.44}
$$

which is equivalent to the expression presented in Eq. (3.35).

Alternatively, we can numerically solve the system dynamics and utilize the final state to calculate the Q-function using built-in functions of QuTip [77, 78]. Figure 3.4 illustrates the emergence of anomalous weak values by comparing the values of $\Delta\mathscr{N}_\epsilon$ obtained from the numerical simulation and the analytical formulas with different photon truncations. In Fig. 3.4(a) we plot $\Delta\mathscr{N}_\epsilon$ from the numerical simulation, and the analytical solution for both the single-photon and two-photon truncations. We observe a perfect match for the two-photon truncation, while a similar quantitative behavior persists even when considering only a single photon emission. This observation significantly speeds up the evaluation of integrals, as computing the single integral for the one-photon emission coefficient is much faster than the double integral. In Fig. 3.4(b), we present a comparison between the numerical and analytical solutions considering $\Delta\mathscr{N}_\epsilon \approx \Delta\mathscr{N}_\epsilon(\omega_0)$, and they exhibit an excellent agreement. This is expected since the resonant regime employed for single-qubit gates results in the central frequency being the most populated.

3.5 Conditional Wigner function and Wigner negativities

In this section, we compute the Wigner function (Eq. 3.1) for the mode with frequency ω_0, which corresponds to the qubit's frequency and the center of the field's spectrum. This is motivated by the fact that the resonant regime that is used to implement single-qubit gates makes the central frequency ω_0 be the most populated, as verified in the last section. Consequently, we have that

$$
\mathscr{N}(\omega_0) = \langle a_0^\dagger a_0\rangle \approx \int_0^\tau dt\ \langle b^\dagger(t) b(t)\rangle, \tag{3.45}
$$

allowing us to approximate the conditional change in the field's excitation number, Eq. (3.23), as

$$
\Delta\mathscr{N}_\epsilon \approx \Delta\mathscr{N}_\epsilon(\omega_0) = \langle a_0^\dagger a_0\rangle_\epsilon - |\alpha|^2 \tag{3.46}
$$

Furthermore, we compute the Wigner negativity, Eq. (3.3), and demonstrate that when anomalous weak values occur for a certain gate angle, the conditioned Wigner function for the outcome g exhibits non-classical behavior (see Fig. 3.5(a)-(b)).

The Wigner function can be readily computed using its definition and the proper-

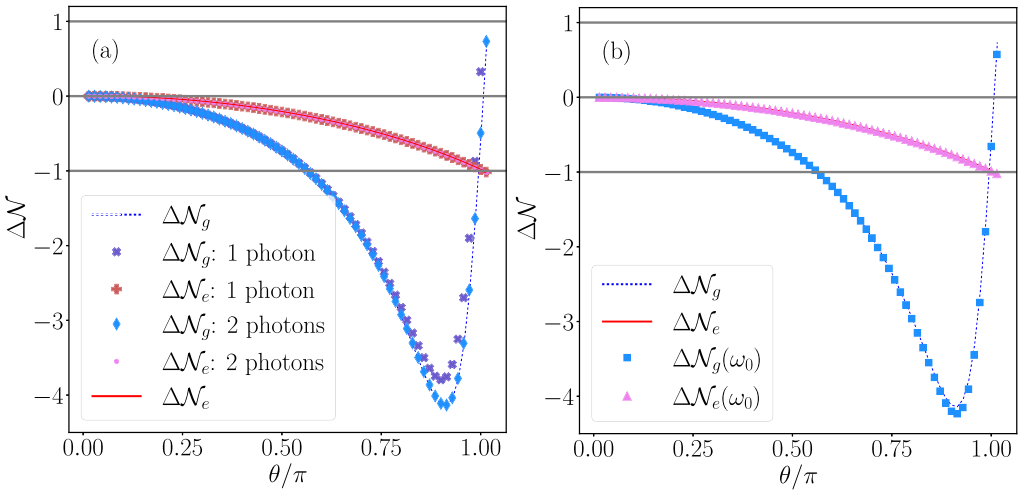

Figure 3.4: **Comparison of truncations and frequency contribution.** (a) The graph compares the values of $\Delta\mathscr{N}_\epsilon$ as a function of θ obtained using different truncations of the field's wave function. The exact values of $\Delta\mathscr{N}_e$ (represented by the solid red line) and $\Delta\mathscr{N}_g$ (represented by the dotted blue line) are computed by numerically integrating the qubit's forward and backward Lindblad master equation, as described in Refs. [117, 118]. We observe that the weak values obtained by truncating the field's wave function at the component with two emitted photons, as given by Eq. (3.44), align perfectly with the exact solutions: $\Delta\mathscr{N}_e$ (depicted by the pink circle) and $\Delta\mathscr{N}_g$ (depicted by the light blue diamond). However, the weak values computed with the truncation at one emitted photon, $\Delta\mathscr{N}_e$ (shown as the brown plus) and $\Delta\mathscr{N}_g$ (shown as the purple cross), deviate from the exact results for θ values larger than approximately 0.8π. (b) This plot compares the exact change in the total number of excitations of the field, $\Delta\mathscr{N}_\epsilon$, with the change in the field's number of excitations centered at frequency ω_0, namely $\Delta\mathscr{N}_e(\omega_0)$ (illustrated by the pink triangle) and $\Delta\mathscr{N}_g(\omega_0)$ (depicted by the light blue square), in the considered regime. The discrepancy between the two data sets is negligible. This indicates that the output field is effectively monochromatic. The gate angle is fixed to $\gamma\tau = 3/40$.

ties of displaced number states (see Ref. [119]). In particular, the following identity is needed:

$$\langle m|D(\alpha)|n\rangle = \sqrt{\frac{n!}{m!}}\alpha^{(m-n)}e^{-\frac{1}{2}|\alpha|^2}L_n^{(m-n)}(|\alpha|^2) \tag{3.47}$$

which provides the matrix element of the displacement operator with amplitude α in the Fock state basis. Here $L_n^{(m-n)}$ is the Laguerre polynomial (for a derivation see App. B of Ref. [120]).

The conditional Wigner function of the mode ω_0 is obtained by following steps similar to those outlined for the Q-function. It can be expressed as:

$$\mathscr{W}_\epsilon(\mu) = \frac{1}{\pi^2}\int d^2\lambda \exp\left\{-\lambda\bar{\mu}+\bar{\lambda}\mu\right\} \mathrm{tr}\left\{\exp\left\{-\bar{\lambda}a_0+\lambda a_0^\dagger\right\}|\psi_\epsilon(\tau)\rangle\langle\psi_\epsilon(\tau)|\right\}, \tag{3.48}$$

Evaluating the expression, we have:

$$\begin{aligned}\left(\frac{2\exp\left\{-2|\mu-\alpha|^2\right\}}{\pi P_\epsilon(\tau)}\right)^{-1}\mathscr{W}_\epsilon(\mu) = \Big[&\Big(P_\epsilon(\tau) - |\tilde{f}_\epsilon^{(1)}(\tau,0)|^2 - 2|\tilde{f}_\epsilon^{(2)}(\tau,0,0)|^2\Big)\\ &- |\tilde{f}_\epsilon^{(1)}(\tau,0)|^2 L_1(4|\mu-\alpha|^2) + 2|\tilde{f}_\epsilon^{(2)}(\tau,0,0)|^2 L_2(4|\mu-\alpha|^2)\\ &- 8\Re\left\{\left(\tilde{f}_\epsilon^{(2)}(\tau,0,0)\right)^* \tilde{f}_\epsilon^{(1)}(\tau,0)(\overline{\mu}-\overline{\alpha})\right\}\left(2|\mu-\alpha|^2-1\right)\\ &+ 8\Re\left\{\left(\tilde{f}_\epsilon^{(2)}(\tau,0,0)\right)^* \tilde{f}_\epsilon^{(0)}(\tau)(\mu-\alpha)\right\}\\ &-4\Re\left\{\left(\tilde{f}_\epsilon^{(1)}(\tau,0)\right)^* \tilde{f}_\epsilon^{(0)}(\tau)(\mu-\alpha)\right\} + \dots\Big].\end{aligned}$$

Here, $L_n(x) = L_n^1(x)$ are the Laguerre polynomials. In Fig. 3.5(a), we demonstrate that for a fixed interaction time τ, the change in the excitation number of the field, conditioned on the ground state $\Delta\mathscr{N}_g$, exhibits anomalous values within a specific range of gate angles θ. Figs. 3.5(b) and 3.5(c) display the conditioned Wigner functions for the ground and excited states, respectively, highlighting a clear negative region in $\mathscr{W}_g$ for a fixed angle $\theta < \pi$ (see caption). In Fig. 3.5(d), we plot the Wigner negativity (Eq. (3.3)) as a function of the angle, while Fig. 3.5(e) focuses on the range of angles where anomalous weak values are observed. We make a crucial observation: the Wigner function is conditioned on the ground state $\mathscr{W}_g$ exhibits negative values when $\Delta\mathscr{N}_g$ assumes anomalous values below -1 for certain gate angles. Thus, we demonstrate that this paradigmatic setup showcases the coexistence of anomalous weak values and Wigner negativities, which are distinctive non-classical features.

3.6 Conclusions

In conclusion, we investigated the emergence of two indicators of non-classicality exhibited by the scattered field use to implement a single qubit gate: Wigner function negativity and anomalous weak values. These phenomena are intimately connected to foundational aspects of quantum mechanics, specifically quantum contextuality. The continuous monitoring of the output field through a heterodyne measurement, coupled with post-selection based on the qubit's measurement outcomes, forms the basis of

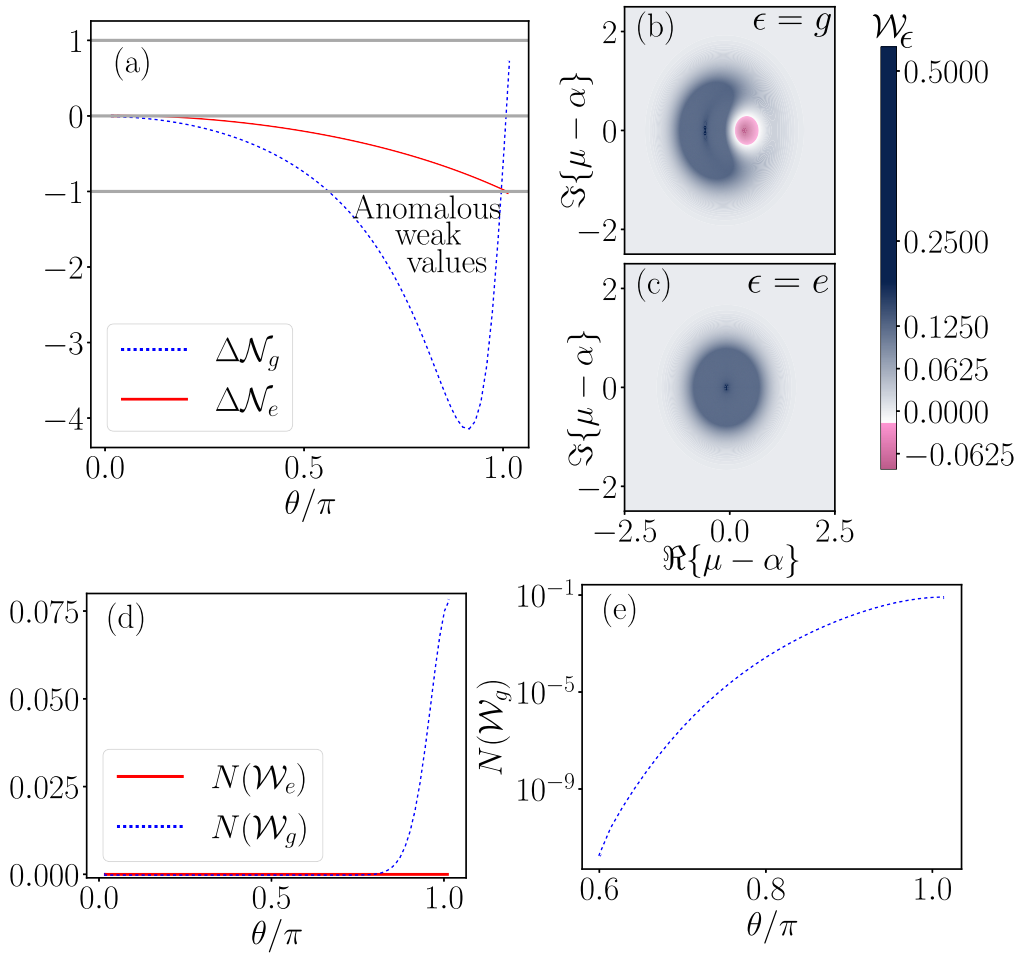

Figure 3.5: **Anatomy of the single-qubit gate.** (a) Weak values of the change in the number of field excitations as a function of the gate's angle: $\Delta\mathscr{N}_e$ (solid red line) and $\Delta\mathscr{N}_g$ (dotted blue line). (b)-(c) Contour plots of the conditional Wigner functions $\mathscr{W}_g$ and $\mathscr{W}_e$ for $\theta/\pi = 0.93$, respectively. The Wigner function conditioned on the ground state $\mathscr{W}_g$ exhibits a highlighted pink region of negative values. (d) Wigner function's negativity [57], $N(\mathscr{W}_\epsilon) = \int d^2\mu |\mathscr{W}_\epsilon(\mu)| - 1$, as a function of θ: $\mathscr{W}_e$ (solid red line) is always positive, hence it has zero negativity. On the other hand, $\mathscr{W}_g$ (dotted blue line) can take negative values in the region of anomalous weak values of $\Delta\mathscr{N}_g$. (e) Plot of $\mathscr{W}_g$ (in log scale) in the region of anomalous values of $\Delta\mathscr{N}_g$, i.e., $\theta \in [0.6\pi, \pi]$. All the plots were obtained for $\tau = 3/40\gamma^{-1}$. The choice of parameters is arbitrary; the selected ones clearly illustrate the emergence of anomalous weak values and the negativity of the Wigner function.

our experimental setup. By employing the results of the CM developed in Chap. 2, we derived analytical expressions for two quasi-probability distributions conditioned on the post-selected state outcomes: the Husimi Q-function, enabling access to the field's anomalous weak values [54], and the Wigner function, exhibiting expected negative regions in accordance with foundational results [55]. The significance of this work lies in the presentation of a realistic experimental setup that presents simultaneously both indicators of non-classical behavior, namely Wigner negativity and anomalous weak values, establishing a connection between them.

We established a connection between anomalous weak values and Wigner negativity. This paves the way for the investigation of the equivalence found in Ref. [55] between contextuality and negative Wigner distributions can be extended to more complex measurement settings involving post-selection, such as the one described in this chapter.

The code I wrote to generate the plots presented in this chapter and the paper Ref. [53] is available on this GitHub link [76].

Chapter 4

The spin-photon interface: Energy-efficient quantum non-demolition measurement and photon-photon gate proposal

When things get tough, there are two things that make life worth living: Mozart, and quantum mechanics. – Victor Frederick Weisskopf

4.1 Introduction

Photonic quantum technologies require high-rate and high-fidelity quantum emitters. Quantum emitters that host a spin offer the capability to generate entanglement between the spin and photon, resulting in a spin-photon interface (SPI) [121, 43]. The SPI is engineered to facilitate the transfer of information between a stationary qubit (represented by the spin) and a flying qubit (represented by light) in a deterministic and coherent manner. This feature makes SPIs particularly valuable in measurement-based quantum computing [122, 123, 124] and quantum network applications [125, 31, 126, 127, 128, 129, 130]. They play a crucial role in various photonic quantum technologies, including quantum memories [131], photon-photon gates [132, 133, 134], and the generation of highly entangled photonic states, also known as cluster states [68, 135, 63].

Before considering specific applications, it is important to pause and ponder a fundamental question: How is information about the spin state (the system being measured, as discussed in Chapter 1) effectively transferred to the light state (the meter system) in a coherent manner? By exploring this question, we can gain insights into the importance of selecting the right meter and experimental measurement scheme to extract the most information possible. This is the motivation for the investigation presented in this chapter.

This chapter builds upon the findings reported in Ref. [74], where we conducted an analysis of the performance of the SPI in achieving a quantum non-demolition measurement (QND) of the spin state [136]. Our investigation encompasses both the pre-measurement level and the complete measurement protocol. We employ the

qBhat coefficient (Eq. (1.17)) to evaluate the quality of the information encoding and the cBhat coefficient (Eq. (1.18)) to quantify the effectiveness of the meter read-out, as discussed in Chapter 1. Our objective is to optimize the readout performance by selecting the appropriate type of light (meter) that probes the system. Specifically, we set a constraint on the energy budget, considering at most one photon to interact with the spin. This enables the comparison between classical and quantum resources [137]. The classical resource is represented by a coherent state (Poissonian statistics), while the quantum resource is represented by a superposition of vacuum and a single photon (sub-Poissonian statistics) [59]. The central research question we aim to address is as follows:

- Within the von Neumann measurement model and under the energy budget limitation of at most one photon, does the use of quantum resource offer any advantage over the classical resource?

The analysis is based on the closed dynamics solution obtained from the collisional model in Chap. 2. We have access to the joint state of the spin and light at any given time t, which considers the pulse deformations induced by the interaction of light with the spin and all the temporal modes of light. This is a significant advantage of the model compared to effective approaches like cavity quantum electrodynamics (cQED) [20, 11, 22] and open quantum systems [36, 37]. We recall that in the former, only a single mode of the field is taken into account in the modeling, while the latter treats the propagating field as a bath and focuses solely on the quantum emitter's dynamics by tracing out the field's state.

This chapter is organized as follows:

- In Sec. 4.2, we introduce the Spin-Photon Interface (SPI).
- In Sec. 4.3, we present the solution of the dynamics, building upon the solutions obtained in Chap. 2, and we analyze the pre-measurement stage of the von Neumann measurement, where we present the first major result and identify two important regimes, namely the monochromatic regime and the pulsed regime.
- Sec. 4.4 is dedicated to the analysis of the collapse stage, proposing a measurement protocol tailored for the monochromatic regime.
- In Sec. 4.5, we consider a technological application. We outline the ideal protocol for implementing the photon-photon controlled σ_z phase gate which can be implemented in the monochromatic regime (refer to Figure 4.3(b)). We introduce a parameter that quantifies the deviation of the scattered field from the monochromatic regime, which is the primary source of error. Expressions for both the ideal gate and the real gate as a function of this parameter are provided. We also carry out the error analysis of the protocol by evaluating the state-average fidelity [138] and the error matrix [139, 140].
- Finally, in Sec. 4.6, we discuss the results of this investigation and outline directions for further studies.

The codes with the analytical results and plots presented in this chapter are available in the dedicated GitHub repository [76].

4.2 The spin-photon interface

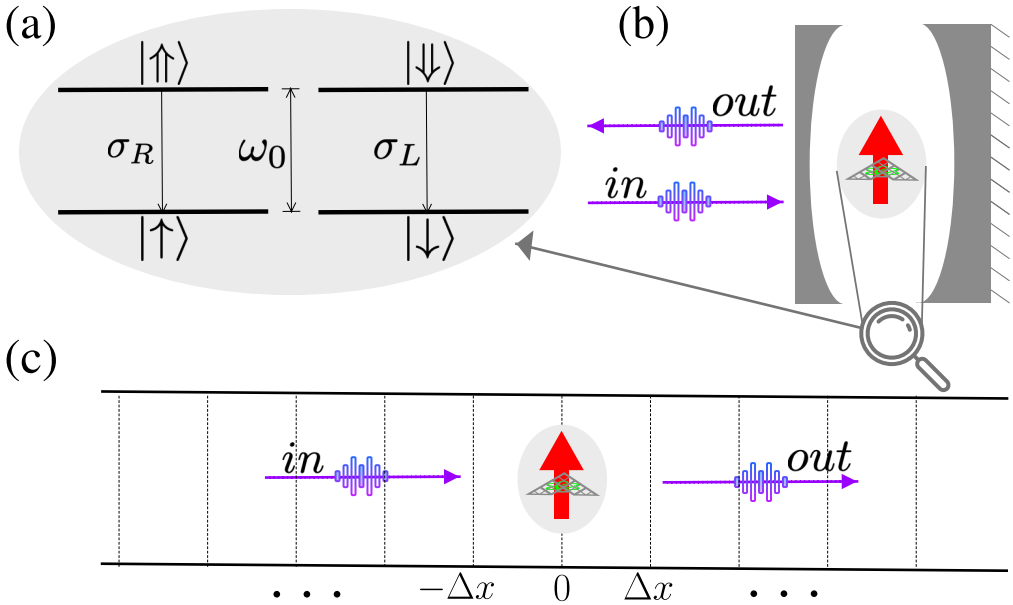

Figure 4.1: **The spin-photon interface.** (a) Energetic structure of the quantum emitter. The system is a 4-level system (4LS) with two degenerate transitions. Each branch is coupled to left and right circularly polarized light. (b) The interface comprises a quantum emitter with a spin degree of freedom, represented by the red arrow within the shaded gray area. The emitter is coupled to a 1D waveguide. (c) Unfolded waveguide. The SPI is at the origin, $x = 0$, and interacts sequentially with the input ancillas.

We investigate a spin-photon interface (SPI) consisting of a degenerate 4-level system (4LS) [141], as shown in Fig. 4.1(a). The interface is composed of two ground (spin) states denoted by $\{|\uparrow\rangle, |\downarrow\rangle\}$, with zero energy, and two excited (trion) states $\{|\Uparrow\rangle|\Downarrow\rangle\}$, with energy ω_0. The spin projections for these states are $\pm 1/2$ and $\pm 3/2$, respectively (here $\hbar = 1$). Importantly, the transitions

$$\begin{aligned} |\downarrow\rangle &\rightarrow |\Downarrow\rangle \\ |\uparrow\rangle &\rightarrow |\Uparrow\rangle \end{aligned} \tag{4.1}$$

are selectively driven by left (L) and right (R) circularly polarized light, corresponding to helicity -1 and $+1$, respectively. This level configuration is usually observed in quantum dots where an electron is confined [43, 68] (see also App. B). The emitter is coupled to a waveguide (WG) that has two baths of circularly polarized modes with frequencies ω_k.

The total system of the SPI is described by the Hamiltonian:

$$H = H_{\text{4LS}} + H_{f,\text{RL}} + H_{\text{SPI}}. \tag{4.2}$$

The bare Hamiltonian of the 4LS is given by:

$$H_{\text{4LS}} = \sum_{j=R,L} \omega_0 \sigma_j^\dagger \sigma_j, \tag{4.3}$$

where the lowering operators are defined as:

$$\sigma_L = |\downarrow\rangle\langle\Downarrow| \text{ ,and} \tag{4.4}$$
$$\sigma_R = |\uparrow\rangle\langle\Uparrow|. \tag{4.5}$$

Similar to Chap. 2, the emitter is located at $x = 0$ of the WG, and we assume light can only propagate from the left to the right (see Fig. 4.1(c)).

The fields in the WG are described by:

$$H_{f,\text{RL}} = \sum_{j=\text{R,L}} \left(\sum_{k=0}^{\infty} \omega_k a_{j,k}^\dagger a_{j,k} \right), \tag{4.6}$$

where $a_{j,k}$ are annihilation operators that remove an excitation of angular frequency ω_k with polarization j. The dispersion relation of the field is given by $k = \omega_k/v$, where v is the group velocity of the field and $k \geq 0$ is the wave vector. This condition on k ensures the unidirectionality of the field.

The interaction between the spin and the field is described by the spin-photon interface Hamiltonian:

$$H_{\text{SPI}} = i g_0 \sum_{j=\text{R,L}} \left[\sum_{k=0}^{\infty} \left(\sigma_j^\dagger a_{j,k} - a_{j,k}^\dagger \sigma_j \right) \right], \tag{4.7}$$

where g_0 is the light-matter interaction strength, assumed to be the same for both polarizations and constant across the frequencies.

Following the method discussed in Chap. 2, we move to the interaction picture with respect to $H_0 = H_{\text{4LS}} + H_{f,\text{RL}}$ [39, 73]. The time-dependent interaction Hamiltonian becomes:

$$H_{\text{SPI}}(t) = i\sqrt{\gamma} \sum_{j=\text{R,L}} \left[\sigma_j^\dagger(t) b_j(t) - b_j^\dagger(t) \sigma_j(t) \right], \tag{4.8}$$

where we defined the interaction picture $j-$polarized lowering operator

$$\sigma_j(t) = e^{-i\omega_0 t} \sigma_j, \tag{4.9}$$

and the $j-$polarized photon annihilation operator at time t as[1], $b_j(t) = \varrho^{-\frac{1}{2}} \sum_k e^{-i\omega_k t} a_{i,k}$, obeying the bosonic algebra for different polarizations at different times is defined by $\left[b_j(t), b_k^\dagger(s) \right] = \delta_{jk}\delta(t-s)$. The parameter ϱ is the density of modes in the WG and we have the vacuum decay rate of the 4LS to the WG given by $\gamma = g^2 \varrho$ [92, 142].

[1]More precisely, the annihilation operator at position $x = 0$ as discussed in Chap. 2.

4.3 Pre-measurement analysis

4.3.1 Dynamics solution

We consider the 4LS initially prepared in a superposition of its spin states and the field in a horizontally polarized state, denoted by $|\Phi_{\rm H}(0)\rangle$, so that it interacts with both spin states. Thus, the joint system is initially in the product state:

$$|\Psi(0)\rangle = (c_\uparrow|\uparrow\rangle + c_\downarrow|\downarrow\rangle) \otimes |\Phi_{\rm H}(0)\rangle, \tag{4.10}$$

where $|c_\uparrow|^2+|c_\downarrow|^2= 1$. The system evolves unitarily according Eq. (4.8), and at time t it is found to be in the entangled state

$$|\Psi(t)\rangle = c_\uparrow\left(|\uparrow\rangle \otimes |\phi_\uparrow(t)\rangle + |\Uparrow\rangle \otimes |\phi_\Uparrow(t)\rangle\right) + c_\downarrow\left(|\downarrow\rangle \otimes |\phi_\downarrow(t)\rangle + |\Downarrow\rangle \otimes |\phi_\Downarrow(t)\rangle\right), \tag{4.11}$$

where $|\phi_{\uparrow(\downarrow)}(t)\rangle$ represents the field's wave-functions induced by the spin states, and $|\phi_{\Uparrow(\Downarrow)}(t)\rangle$ represents the field's wave functions induced by the trion states.

Next, we consider the long-time (asymptotic) limit, $\gamma t \to \infty$, in which the system has decayed to its ground state [59]:

$$|\Psi_{\rm SS}\rangle \equiv \lim_{\gamma t\to\infty} |\Psi(t)\rangle = c_\uparrow|\uparrow\rangle \otimes |\phi_\uparrow\rangle + c_\downarrow|\downarrow\rangle \otimes |\phi_\downarrow\rangle, \tag{4.12}$$

where "SS" stands for steady state. In this limit, the pointer states are given by $|\phi_{\uparrow(\downarrow)}\rangle$ [82]. As discussed in Chap. 1, the quality of the entanglement generated between the field and the spin is quantified by the quantum Bhattacharyya coefficient (qBhat), given by Eq. (1.17) [143, 87, 86].

The pointer states associated with the coherent field are represented by $|\phi^{\rm cs}_{\uparrow(\downarrow)}\rangle$ where the superscript "cs" stands for the classical state, while the pointer states associated with the superposition of zero and one photon are represented by $|\phi^{\rm qs}_{\uparrow(\downarrow)}\rangle$ with "qs" denoting the quantum state. We will compute the qBhat, Eq. (1.17), for both: $\mathscr{B}^{\rm qs}_q = |\langle\phi^{\rm qs}_\downarrow|\phi^{\rm qs}_\uparrow\rangle|$ and $\mathscr{B}^{\rm cs}_q = |\langle\phi^{\rm cs}_\downarrow|\phi^{\rm cs}_\uparrow\rangle|$.

Coherent state

We consider the initial horizontally polarized coherent state, $|\beta_{\rm H}\rangle = D(\beta_{\rm H})|\emptyset\rangle$, where $\beta_{\rm H}$ is the amplitude:

$$\begin{aligned}
|\Phi^{\rm cs}_{\rm H}(0)\rangle = |\beta_{\rm H}\rangle &= D\left(\beta_{\rm H} b^\dagger_{\rm H} - \overline{\beta}_{\rm H} b_{\rm H}\right)|\emptyset\rangle \\
&= D\left(\beta_{\rm H}\frac{(b^\dagger_{\rm R} + b^\dagger_{\rm L})}{\sqrt{2}} - \overline{\beta}_{\rm H}\frac{(b_{\rm R} + b_{\rm L})}{\sqrt{2}}\right)|\emptyset\rangle \\
&= D\left(\frac{(\beta_{\rm H} b^\dagger_{\rm R} - \overline{\beta}_{\rm H} b_{\rm R})}{\sqrt{2}} + \frac{(\beta_{\rm H} b^\dagger_{\rm L} - \overline{\beta}_{\rm H} b_{L})}{\sqrt{2}}\right)|\emptyset\rangle \\
&= \left|\beta_{\rm L} = \frac{\beta_{\rm H}}{\sqrt{2}}\right\rangle_{\rm L} \otimes \left|\beta_{\rm R} = \frac{\beta_{\rm H}}{\sqrt{2}}\right\rangle_{\rm R}.
\end{aligned} \tag{4.13}$$

Then, we have the initial system given by:

$$|\Psi^{\rm cs}(0)\rangle = (c_\uparrow|\uparrow\rangle + c_\downarrow|\downarrow\rangle) \otimes \left|\frac{\beta_{\rm H}}{\sqrt{2}}\right\rangle_{\rm L} \otimes \left|\frac{\beta_{\rm H}}{\sqrt{2}}\right\rangle_{\rm R} \tag{4.14}$$

Since $|\uparrow\ (\downarrow)\rangle$ only interacts with R(L) polarized light, we can import the solution obtained in Chap. 2, Eq. (2.66), for each polarization. We have the following map for each spin state:

$$\begin{aligned} |\downarrow\rangle \otimes \left|\frac{\beta_{\rm H}}{\sqrt{2}}\right\rangle &\rightarrow |\downarrow\rangle \otimes |\phi^{\rm cs}_\downarrow\rangle \\ |\uparrow\rangle \otimes \left|\frac{\beta_{\rm H}}{\sqrt{2}}\right\rangle &\rightarrow |\uparrow\rangle \otimes |\phi^{\rm cs}_\uparrow\rangle \end{aligned} \tag{4.15}$$

where we have introduced the pointer states,

$$|\phi^{\rm cs}_\downarrow\rangle = \left(\frac{D(\beta_H/\sqrt{2})}{\sqrt{P_\downarrow(t)}}\left[\sqrt{p_{0,\downarrow}}\tilde{f}^{(0)}_\downarrow(t) + \sum_{m=1}^{\infty}\sqrt{p_{m,\downarrow}(t)}\int_0^t d\mathbf{s}_m \tilde{f}^{(m)}_\downarrow(t,\mathbf{s})\prod_{i=1}^{m} b^\dagger_{m,\rm L}\right]|\emptyset\rangle\right) \tag{4.16}$$

$$|\phi^{\rm cs}_\uparrow\rangle = \left(\frac{D(\beta_H/\sqrt{2})}{\sqrt{P_\uparrow(t)}}\left[\sqrt{p_{0,\uparrow}}\tilde{f}^{(0)}_\uparrow(t) + \sum_{m=1}^{\infty}\sqrt{p_{m,\uparrow}(t)}\int_0^t d\mathbf{s}_m \tilde{f}^{(m)}_\uparrow(t,\mathbf{s})\prod_{i=1}^{m} b^\dagger_{m,\rm R}\right]|\emptyset\rangle\right),$$

where the coefficients $\tilde{f}^{(n)}_{\uparrow(\downarrow)}$ are given by Eqs. (2.68), (2.79), and the probabilities are defined below Eq. (2.67). It is important to remark that spin $\uparrow$ only emits the right polarized photons while spin $\downarrow$ only emits left polarized photons. When we evaluate the qBhat using Eq. (1.17) only the vacuum component is non-zero, i.e., from Eq. (1.17), we obtain

$$\mathscr{B}^{\rm cs}_q = p_0 \equiv \sqrt{\frac{p_{0,\downarrow}p_{0,\uparrow}}{P_\downarrow P_\uparrow}}\left(\tilde{f}^{(0)}_\downarrow\right)^* \tilde{f}^{(0)}_\uparrow. \tag{4.17}$$

This result is significant as it establishes a fundamental limit on the quality of the entanglement generated with a coherent field: The probability of the trion state not undergoing re-emission, represented by p_0, is the fundamental constraint to the quality of the entanglement.

Quantum superposition of zero and one photon

Next, we examine the initial superposition of a vacuum and a single horizontally polarized photon (qs):

$$|\Phi^{\rm qs}_{\rm H}(0)\rangle = c_\emptyset|\emptyset\rangle + c_1|1_{\rm H}\rangle, \tag{4.18}$$

where $c_\emptyset$ and c_1 are complex coefficients whose square moduli sum to unity. The single photon component is,

$$\begin{aligned} |1_{\rm H}\rangle &= \frac{|1_{\rm L}\rangle + |1_{\rm R}\rangle}{\sqrt{2}} \\ &= \left(\frac{b_{\rm L}(t) + b_{\rm R}(t)}{\sqrt{2}}\right)|\emptyset\rangle \equiv b_{\rm H}(t)|\emptyset\rangle. \end{aligned} \tag{4.19}$$

We need three ingredients to derive the solution:

1. Let j represent the polarization of the single photon, and $\beta(t)$ be the temporal shape of the pulse. Then,

$$|1_j\rangle = \int_0^\infty dt\ \beta_j(t) b_j^\dagger(t)|\emptyset\rangle, \tag{4.20}$$
$$\int_0^\infty dt\ |\beta_j(t)|^2 = 1.$$

2. The map,

$$\begin{aligned} |\uparrow(\downarrow)\rangle \otimes |1_{\mathrm{R(L)}}\rangle &\to |\uparrow(\downarrow)\rangle \otimes |1_{\tilde{\mathrm{R}}(\tilde{\mathrm{L}})}\rangle \\ |\uparrow(\downarrow)\rangle \otimes |1_{\mathrm{L(R)}}\rangle &\to |\uparrow(\downarrow)\rangle \otimes |1_{\mathrm{R(L)}}\rangle \end{aligned} \tag{4.21}$$

   which says that a single R(L)-photon interacts has its temporal shape deformed, represented by $\tilde{\mathrm{R}}(\tilde{\mathrm{L}})$, after interacting with spin $\uparrow(\downarrow)$.

3. The solution obtained in Chap. 2, the scattered photon is:

$$\begin{aligned} |1_{\tilde{j}}\rangle &= \int_0^\infty dt\ \Upsilon(t) b_j^\dagger(t)|\emptyset\rangle, \\ \Upsilon(t) &= \beta(t) - \gamma\tilde{\beta}(t) \\ \tilde{\beta}(t) &= e^{-\gamma t/2}\int_0^t dt' \left[e^{\frac{\gamma t'}{2}}\beta(t')\right] \end{aligned} \tag{4.22}$$

Using these three ingredients we obtain:

$$|\uparrow(\downarrow)\rangle \otimes |\Phi_{\mathrm{H}}^{\mathrm{qs}}(0)\rangle \to |\uparrow(\downarrow)\rangle \otimes |\phi_{\uparrow(\downarrow)}^{\mathrm{qs}}(t)\rangle \tag{4.23}$$

where the pointer states are:

$$|\phi_{\uparrow(\downarrow)}^{\mathrm{qs}}(t)\rangle = c_\emptyset|\emptyset\rangle + \frac{c_1}{\sqrt{2}}\int_0^\infty dt\left[\beta(t) b_{\mathrm{L(R)}}^\dagger(t) + \Upsilon(t) b_{\mathrm{R(L)}}^\dagger(t)\right]|\emptyset\rangle, \tag{4.24}$$

There is a crucial difference between Eqs. (4.16) and (4.24): the latter has an additional L(R)-photon component in the pointer state associated with spin $|\uparrow\rangle$ ($|\downarrow\rangle$) (highlighted in red). This component emerges from the part of the field that does not interact with the spin, hence the shape is not modified, $\beta(t)$.

Next, we proceed with the computation of the qBhat for the coherent superposition

of a vacuum and a single photon. From Eq. (4.24) we have the overlap:

$$\begin{aligned}\langle\phi_{\downarrow}^{\mathrm{qs}}(t)|\phi_{\uparrow}^{\mathrm{qs}}(t)\rangle &= |c_{\emptyset}|^2+\frac{|c_1|^2}{2}\left[\iint dsdt\ \bar{\beta}(s)\Upsilon(t)\langle 0|b_L(s)b_L^{\dagger}(t)|0\rangle\right. \\ &\qquad\left.+\iint dsdt\ \beta(t)\bar{\Upsilon}(s)\langle 0|b_R(s)b_R^{\dagger}(t)|0\rangle\right] \\ &= |c_{\emptyset}|^2+\frac{|c_1|^2}{2}\left[\iint dsdt\ \bar{\beta}(t)\Upsilon(t)\delta(s-t)+\iint dsdt\ \beta(t)\bar{\Upsilon}(t)\delta(s-t)\right] \\ &= |c_{\emptyset}|^2+\frac{|c_1|^2}{2}\left[\int dt\ \bar{\beta}(t)\Upsilon(t)+\int dt\ \beta(t)\bar{\Upsilon}(t)\right] \\ &= |c_{\emptyset}|^2+|c_1|^2\Re\left\{\int dt\ \bar{\beta}(t)\Upsilon(t)\right\} \\ &= p_{\emptyset}+p_{\mathrm{H}}\int dt\ \Re\left\{\bar{\beta}(t)\Upsilon(t)\right\}\end{aligned} \tag{4.25}$$

where we defined the single photon horizontal component probability as $p_{\mathrm{H}} = |c_1|^2$ and the vacuum probability component as $p_{\emptyset} = |c_{\emptyset}|^2$. We can simplify the equation further by expanding the product $\bar{\beta}(t)\Upsilon(t)$ and using the fact that $\beta(t)$ is normalized and the identity $p_{\emptyset} + p_{\mathrm{H}} = 1$. This yields the following expression:

$$\langle\phi_{\downarrow}^{\mathrm{qs}}(t)|\phi_{\uparrow}^{\mathrm{qs}}(t)\rangle = 1-\gamma p_{\mathrm{H}}\int dt\ \Re\left\{\beta(t)\tilde{\beta}(t)\right\}. \tag{4.26}$$

Finally, the qBhat for the quantum state is:

$$\mathscr{B}_q^{\mathrm{qs}} = \left|1-\gamma p_{\mathrm{H}}\int dt\ \Re\left\{\beta(t)\tilde{\beta}(t)\right\}\right|. \tag{4.27}$$

At this point, we have an important result. It is possible to achieve perfect entanglement for the quantum state, i.e. $\mathscr{B}_q^{qs} = 0$, by tuning p_{H} such that:

$$p_{\mathrm{H}} = \frac{1}{\gamma\int dt\ \Re\left\{\beta(t)\tilde{\beta}(t)\right\}}. \tag{4.28}$$

for *any* given pulse temporal shape $\beta(t)$.

To sum up, in this section we obtained the qBhat for the classical and quantum states. The qBhat of the for the coherent state, Eq. (4.17), is fundamentally limited by the probability of no re-emission of the trion states while the qBhat for the coherent superposition of vacuum and a single horizontally polarized photon, Eq. (4.27), can provide perfect entanglement for any pulse shape, $\beta(t)$, as long as the single photon component probability is adjusted according to Eq. (4.28). Next, we investigate the possibility of a quantum advantage in the low energy (at most one photon) the regime that is the focus of our investigation.

4.3.2 Coherent state qBhat: from low to high energy

We set the initial state of the 4LS as a balanced superposition of its spin states

$$|\psi_{4\mathrm{LS}}(0)\rangle = \frac{|\uparrow\rangle + |\downarrow\rangle}{\sqrt{2}}. \tag{4.29}$$

Figure 4.2 shows the value of Eq. (4.17) for a coherent input pulse, in the steady

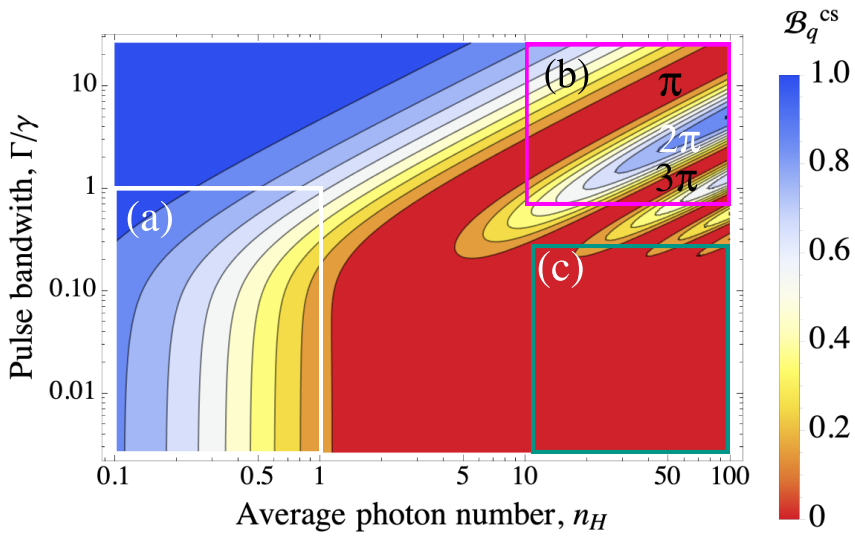

Figure 4.2: **Quantum Bhattacharrya coefficient for coherent field.** The input pulse is H-polarized with a square amplitude $\beta(t) = \sqrt{\Theta\Gamma}$. In the long-time limit, due to the area law, it is equivalent to a decreasing exponential pulse given by Eq. (4.30). The horizontal axis represents the average number of photons per pulse, $\overline{n}_{\mathrm{H}} = \langle a_{\mathrm{H}}^{\dagger} a_{\mathrm{H}} \rangle = \Theta$, while the vertical axis corresponds to the pulse bandwidth, Γ, measured in units of the 4LS vacuum decay rate γ. The colormap indicates the value of the qBhat, ranging from red ($\mathscr{B}_q = 0$) to blue (representing $\mathscr{B}_q = 1$). (a) The low-energy regime, (b) High-energy, short-pulse regime where the system undergoes Rabi oscillations, and (c) High-energy, long-pulse regime.

state, with a square temporal shape given by a square pulse: $\beta(t) = \sqrt{\Theta\Gamma}$, Θ is an a-dimensional parameter representing the area of the pulse and Γ is the pulse bandwidth. The area theorem states that the shape of the pulse is not as important as its timescale, see Refs. [144, 145, 146, 147, 148]. This means that in the steady state the square pulse presents the same behavior as if the simulations were performed with a decreasing pulse:

$$\beta(t) = \sqrt{\Theta\Gamma} e^{-\left(\frac{\Gamma}{2} - i\omega_0\right)t}, \tag{4.30}$$

with the advantage that it is computationally more efficient to simulate.

The plot is divided into three distinct regions, referred to as energy sectors. The region 4.2(a), delimited by $\overline{n}_H \leq 1$, corresponds to the low-energy sector that is the main focus of our investigation. In this sector, $\mathscr{B}_q^{\mathrm{cs}}$ never vanishes, indicating that the pointer states $|\phi_{\uparrow(\downarrow)}^{\mathrm{cs}}\rangle$ are never orthogonal, hence not distinguishable. When the input pulses are longer than the trion state lifetime ($\Gamma \ll \gamma$) we are in the

monochromatic regime, we found ourselves in the linear regime discussed in Sec. 2.7.1. The field is very attenuated, in such circumstances the scattered pulses acquire a π-phase shift, yielding the pointer states:

$$|\phi_{\uparrow}^{\mathrm{cs}}\rangle \to \left|\beta_{\mathrm{L}} = \frac{\beta_{\mathrm{H}}}{\sqrt{2}}\right\rangle \otimes \left|\beta_{\mathrm{R}} = \frac{e^{i\pi}\beta_{\mathrm{H}}}{\sqrt{2}}\right\rangle, \tag{4.31}$$
$$|\phi_{\downarrow}^{\mathrm{cs}}\rangle \to \left|\beta_{\mathrm{L}} = \frac{e^{i\pi}\beta_{\mathrm{H}}}{\sqrt{2}}\right\rangle \otimes \left|\beta_{\mathrm{R}} = \frac{\beta_{\mathrm{H}}}{\sqrt{2}}\right\rangle.$$

In regions 4.2(b) and 4.2(c), we are in the high-energy sector, indicated by an average of more than 10 photons, $\overline{n}_H \geq 10$ in the coherent input field. Region (b) focuses on the behavior of short and strong pulses with $\gamma < \Gamma \leq 10^2\gamma$. Fringes appear in this region, corresponding to Rabi oscillations. Red fringes correspond to odd π-pulses, resulting in a complete inversion of the 4LS populations to the trion states. After such a process, spontaneous emission occurs, leading to $p_0 = 0$, hence with intense short pulses it is possible to generate maximal entanglement between the spin and the coherent field. This is the regime used to generate cluster states as reported in the experiments of Refs. [135, 63]. We also observe blue regions corresponding to even π-pulses, the complete Rabi oscillations that bring the 4LS back to its ground state. In this scenario, photons are scattered only in the driving mode, and there is no spin state information encoded in the scattered photons. Finally, region (c) represents the high-energy and long pulses, $10^{-2}\gamma < \Gamma \leq \gamma$. In this situation, since the light and the 4LS system interact for a sufficient amount of time, the 4LS will certainly emit photons in modes other than the driving one. As a result, information about the spin state will always be available in the scattered field.

4.3.3 Low energy regime

By substituting the decreasing temporal shape Eq. (4.30), with $\Theta = 1$, into Eq. (4.27), we obtain:

$$\mathscr{B}_q^{\mathrm{qs}} = \left|1 - \frac{2p_{\mathrm{H}}\gamma}{\gamma + \Gamma}\right|. \tag{4.32}$$

This expression becomes zero when the equality

$$p_{\mathrm{H}} = \frac{1}{2}\left(1 + \frac{\Gamma}{\gamma}\right) \tag{4.33}$$

is satisfied. Consequently, we can identify two extreme limits of the pulse bandwidth, namely when we have long (square) pulses with the bandwidth $\Gamma \to 0$ and for very short pulses $\Gamma \to \gamma$, it is possible to achieve perfectly distinguishable pointer states. This defines the interval $1/2 \leq p_{\mathrm{H}} \leq 1$, where a perfect mapping between the state of the spin and the pointer states can be achieved. This is the first main result of this chapter: we observe a quantum advantage at the pre-measurement level as the quantum state allows perfect spin-light entanglement. In Fig. 4.3 we present this result graphically. We compare the qBhat in Eqs. (4.17) (focused on the low energy sector) and (4.32).

Based on Figure 4.3(b) and Eq. (4.32), we define two regimes:

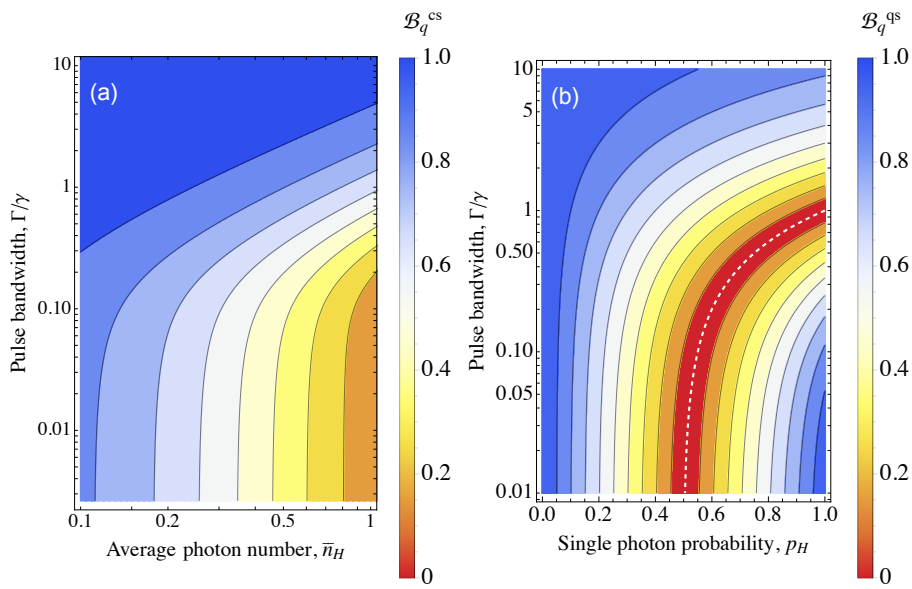

Figure 4.3: **Quantum Bhattacharrya analysis in the low energy regime.** The input pulse is H-polarized, with its amplitude determined by Eq. (4.30). The horizontal axis represents the average number of photons per pulse, $\overline{n}_H = \Theta$, for the coherent pulse (a) and the single photon probability, p_{H}, for the superposition of vacuum and single-photon (b), while the vertical axis corresponds to the pulse bandwidth, Γ, measured in units of the 4LS vacuum decay rate γ. The color map indicates the value of the qBhat, ranging from red ($\mathscr{B}_q = 0$) to blue (representing $\mathscr{B}_q = 1$). (a) Zoomed-in view of 4.2 specifically focused on the low-energy sector. In this region, it is evident that the qBhat never reaches 0, implying that the pointer states are not orthogonal. (b) qBhat analysis for the superposition of a vacuum and a single horizontally polarized photon. The white line highlights the points where $\mathscr{B}_q^{\mathrm{qs}} = 0$, illustrating a quantum advantage over the coherent pulse at the pre-measurement level.

1. **Monochromatic limit**: In this regime, we have a long pulse with $\Gamma \ll \gamma$ and $p_{\mathrm{H}} = 1/2$ (balanced superposition of vacuum and single photon). The interaction of light with the spin states can be described by the following map for circular polarization:

$$\begin{aligned} &|\uparrow\rangle \otimes |1_{\mathrm{R}}\rangle \to |\uparrow\rangle \otimes \left(e^{i\pi}|1_{\mathrm{R}}\rangle\right), \\ &|\uparrow\rangle \otimes |1_{\mathrm{L}}\rangle \to |\uparrow\rangle \otimes |1_{\mathrm{L}}\rangle, \\ &|\downarrow\rangle \otimes |1_{\mathrm{R}}\rangle \to |\downarrow\rangle \otimes |1_{\mathrm{R}}\rangle, \\ &|\downarrow\rangle \otimes |1_{\mathrm{L}}\rangle \to |\downarrow\rangle \otimes \left(e^{i\pi}|1_{\mathrm{L}}\rangle\right). \end{aligned} \tag{4.34}$$

   Alternatively, in terms of linear polarization, we can write:

$$\begin{aligned} &|\uparrow\rangle \otimes |1_{\mathrm{H}}\rangle \to |\uparrow\rangle \otimes \left(i|1_{\mathrm{V}}\rangle\right), \\ &|\downarrow\rangle \otimes |1_{\mathrm{H}}\rangle \to |\downarrow\rangle \otimes \left(-i|1_{\mathrm{V}}\rangle\right). \end{aligned} \tag{4.35}$$

2. **Mode-matched limit**: In this regime, we have a pulse with a duration comparable to the trion's lifetime, $\Gamma \approx \gamma$ and $p_{\mathrm{H}} = 1$ (single photon).

Let's analyze the monochromatic limit. Substituting Eq. (4.18) into Eq. (4.10), we have:

$$\begin{aligned} |\Psi^{\mathrm{qs}}(0)\rangle &= \left(c_{\uparrow}|\uparrow\rangle + c_{\downarrow}|\downarrow\rangle\right) \otimes \left(\frac{|\emptyset\rangle + |1_{\mathrm{H}}\rangle}{\sqrt{2}}\right), \\ &\xrightarrow{(4.35)} c_{\uparrow}|\uparrow\rangle \otimes \left(\frac{|\emptyset\rangle + i|1_{\mathrm{V}}\rangle}{\sqrt{2}}\right) + c_{\downarrow}|\downarrow\rangle \otimes \left(\frac{|\emptyset\rangle - i|1_{\mathrm{V}}\rangle}{\sqrt{2}}\right), \\ &= c_{\uparrow}|\uparrow\rangle \otimes |\phi^{\mathrm{qs}}_{\uparrow}\rangle + c_{\downarrow}|\downarrow\rangle \otimes |\phi^{\mathrm{qs}}_{\downarrow}\rangle. \end{aligned} \tag{4.36}$$

Here, the pointer states are:

$$\begin{aligned} |\phi^{\mathrm{qs}}_{\uparrow}\rangle &= \frac{|\emptyset\rangle + i|1_{\mathrm{V}}\rangle}{\sqrt{2}}, \\ |\phi^{\mathrm{qs}}_{\downarrow}\rangle &= \frac{|\emptyset\rangle - i|1_{\mathrm{V}}\rangle}{\sqrt{2}}. \end{aligned} \tag{4.37}$$

Interestingly the vacuum component, $|\emptyset\rangle$, plays a crucial role in the emergence of the orthogonality of the pointer states.

In the mode-matched regime, the scattering process induces a phase shift in $|1_{\mathrm{L(R)}}\rangle$ results in a clockwise (counterclockwise) rotation of the pulse polarization. Additionally, the temporal shape of the pulse is modified during the scattering process. The final polarization and pulse shape depend on the pulse area Θ, its duration Γ^{-1}, and the input shape $\beta_{\mathrm{in}}(t)$ itself. Here, the information about the spin state is encoded in the polarization of $|\phi^{\mathrm{cs}}_{\uparrow(\downarrow)}\rangle$, the map is:

$$\begin{aligned} &|\uparrow\rangle \otimes |1_{\mathrm{H}}\rangle \xrightarrow[p_{\mathrm{H}}=1]{\Gamma=\gamma} |\uparrow\rangle \otimes |1_{\mathrm{R}}\rangle, \\ &|\downarrow\rangle \otimes |1_{\mathrm{H}}\rangle \xrightarrow[p_{\mathrm{H}}=1]{\Gamma=\gamma} |\downarrow\rangle \otimes |1_{\mathrm{L}}\rangle. \end{aligned} \tag{4.38}$$

In all other cases, within the bandwidth range $1/2 < p_{\mathrm{H}} < 1$, the pulse temporal shape gets modified during the scattering process. This causes the entanglement to spread over different degrees of freedom: polarization and temporal mode shape of the scattered light. This insight reveals that the temporal degrees of freedom contribute to non-idealities in SPI for both quantum information protocols and classical information extraction. The latter is the subject of analysis in the next section, followed by an example of the former: a photon-photon gate. This non-ideality is the most fundamental aspect of this system since photonic quantum information protocols require pulses with a finite duration.

To summarize, within the two investigated regimes, namely (1) Monochromatic limit and (2) Mode-matched limit, using a superposition of vacuum and a single photon offers a clear advantage over a low-energy coherent state for generating spin-light entanglement. In other words, quantum light provides a better pre-measurement of the spin state compared to classical light, demonstrating a quantum advantage [137].

4.4 Spin state readout

As discussed in Chap. 1, pre-measurements are followed by collapses of the meter state. In this section, we present a measurement scheme depicted in Fig. 4.4 that includes both pre-measurement and collapse of the meter state, focusing on the monochromatic regime (1). As discussed in Sec. 2.7.1 of Chap. 2, in this regime, the information about the spin state is encoded in the phase of the field. Therefore, we propose a measurement protocol that targets the phase acquired by the light scattered by the SPI. This choice is further motivated due to the fact that it provides a different perspective on the measurement set as the polarization of light is already widely used in the community [71, 72].

The measurement scheme is illustrated in Fig. 4.4(a). It consists of a Michelson interferometer, with the meter assumed to be right circularly polarized light. On the left arm, we have a source that produces the input field. The pulse is directed toward a 50/50 beam splitter (BS), which splits the pulse into two parts. The portion of the pulse transmitted to the right arm of the BS interacts with the SPI, while the portion transmitted to the upper arm of the BS is reflected by a mirror. A tunable phase shifter, φ, is inserted to optimize the interference of the two reflected beams. Finally, the reflected beams are recombined at the BS and directed towards a photondetector[2]. The light-matter interaction can be described by the following map:

$$\begin{aligned} |\uparrow\rangle \otimes |\Psi_{\mathrm{in}}\rangle &\rightarrow |\uparrow\rangle \otimes |\Psi_{\uparrow}\rangle \\ |\downarrow\rangle \otimes |\Psi_{\mathrm{in}}\rangle &\rightarrow |\downarrow\rangle \otimes |\Psi_{\downarrow}\rangle. \end{aligned} \tag{4.39}$$

The measurement protocol can be described as follows:

[2]The beams in the output port have been transmitted once and reflected once by the BS. We assume that the BS is a half-silvered mirror consisting of a glass plate with a semi-reflective coating on one side and an anti-reflection coating on the other.

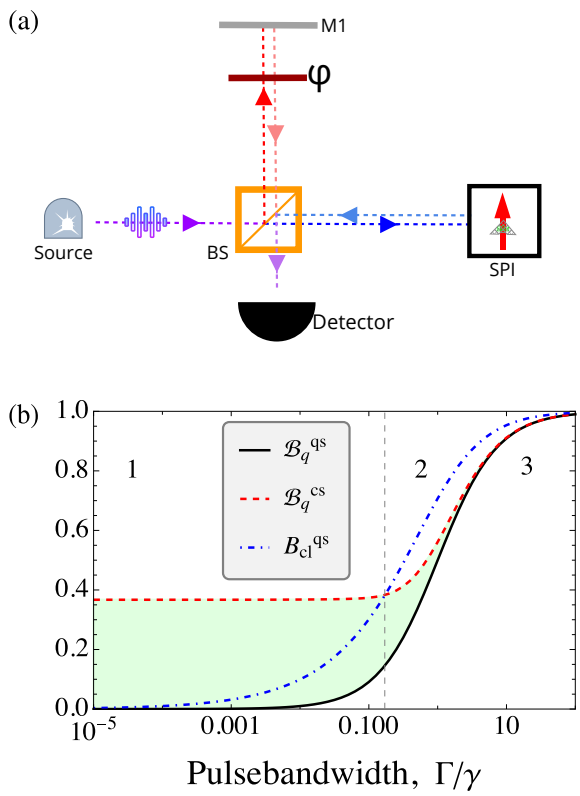

Figure 4.4: **Spin state readout.** (a) The figure illustrates the setup of the Michelson interferometer. The SPI is situated in the right arm, while the upper arm has a tunable phase plate (φ). BS represents a 50/50 beam-splitter. The source emits either a coherent pulse (representing the classical state, cs), with an average of one photon or a single photon (representing the quantum state, qs). Both cases involve right circularly polarized photons. (b) qBhat coefficients are depicted: the black curve represents the quantum state (single photon), the red dotted line represents the coherent state (classical light), and the blue dashed line represents the classical Bhattacharyya coefficient for the quantum state. The qBhat for the quantum state serves as the lower bound for the cBhat. These coefficients are equal when both vanish in the monochromatic limit. All coefficients are calculated in the long-time limit, with the pulse bandwidth Γ as the variable. Region 1 demonstrates the presence of a quantum advantage, with the blue curve below the red curve. Region 2 indicates that the proposed experimental protocol does not effectively target the desired variable. Region 3, below the black curve, represents an inaccessible region where the desired measurement outcomes cannot be achieved.

1. The spin is prepared in one of its eigenstates: $|\uparrow\rangle$ or $|\downarrow\rangle$.

2. A source of monochromatic circularly right-polarized light is used to probe the spin state. This source can provide either a single-photon, $|1_{\mathrm{R}}\rangle \otimes |\emptyset_{\mathrm{L}}\rangle$, or a low-intensity coherent state with an average of one photon, $|\beta_{\mathrm{R}} = 1\rangle \otimes |\emptyset_{\mathrm{L}}\rangle$.

3. The light pulse is directed into a Michelson interferometer.

   (a) The interferometer consists of the SPI in the right arm and a tunable phase plate (φ) in the upper arm, along with a 50/50 beam splitter. Our objective is to measure the phase.

4. The pulse exits the interferometer in one of the pointer states: $|\Psi_{\uparrow}\rangle$ or $|\Psi_{\downarrow}\rangle$, which are correlated with the spin states $|\uparrow\rangle$ or $|\downarrow\rangle$, respectively. This step represents the pre-measurement and is quantified by the qBhat equation (Eq. (1.17)).

5. A photodetector is positioned at the output port of the interferometer to collapse the state of the meter. The possible outcome is the detection of a photon, referred to as a "click" in the detector, or the absence of a photon, termed a "no click".

6. Since the spin is probed with right-polarized light, the phase of the phase plate (φ) is chosen such that $p_{\uparrow}(\text{click}) = 1$ ($p_{\downarrow}(\text{click}) = 0$) if the spin is $|\uparrow\rangle(|\downarrow\rangle)$.

By observing the presence or absence of light in the photon detector, assuming a lossless system, we can infer the spin's state. In this scenario, the cBhat equation (Eq. (1.18)) can be written as:

$$\begin{aligned} B_{\mathrm{cl}} &= \sqrt{p_{\uparrow}(\text{click})p_{\downarrow}(\text{click})} + \sqrt{p_{\uparrow}(\text{no click})p_{\downarrow}(\text{no click})} \\ &= \sqrt{p_{\uparrow}(\text{click})p_{\downarrow}(\text{click})} + \sqrt{(1 - p_{\uparrow}(\text{click}))\,(1 - p_{\downarrow}(\text{click}))}, \end{aligned} \tag{4.40}$$

where $p_j(\text{click})$ represents the probability of a detection event (click in the detector) given that the spin is prepared in the state $|j\rangle$, with $j = \uparrow, \downarrow$.

To derive the expression for the output state $|\Psi_{\uparrow(\downarrow)}\rangle$, we need the 50/50 beam splitter map:

$$\begin{aligned} |1\rangle \otimes |\emptyset\rangle &\to \frac{|\emptyset\rangle \otimes |1\rangle + |1\rangle \otimes |\emptyset\rangle}{\sqrt{2}}, \\ |\emptyset\rangle \otimes |1\rangle &\to \frac{|\emptyset\rangle \otimes |1\rangle - |1\rangle \otimes |\emptyset\rangle}{\sqrt{2}}. \end{aligned} \tag{4.41}$$

Let $|\Psi_{\text{in}}\rangle$ be R-polarized input field state, we obtain:

$$\begin{aligned}
|\Psi_{\text{in}}\rangle \otimes |\emptyset\rangle &\xrightarrow{\text{BS}} \frac{|\emptyset\rangle \otimes |\Psi_{\text{in}}\rangle + |\Psi_{\text{in}}\rangle \otimes |\emptyset\rangle}{\sqrt{2}} \\
&\xrightarrow{\text{SPI}} \frac{|\emptyset\rangle \otimes |\psi_j\rangle \otimes |j\rangle + |\Psi_{\text{in}}\rangle \otimes |\emptyset\rangle \otimes |j\rangle}{\sqrt{2}} \\
&\xrightarrow{\text{BS}} \frac{1}{2}\left[(|\Psi_{\text{in}}\rangle - |\psi_j\rangle) \otimes |\emptyset\rangle + |\emptyset\rangle \otimes (|\Psi_{\text{in}}\rangle + |\psi_j\rangle)\right] \otimes |j\rangle \\
&\rightarrow |\Psi_j\rangle \otimes |j\rangle,
\end{aligned} \tag{4.42}$$

where

$$|\Psi_j\rangle = \frac{1}{2}\left[(|\Psi_{\text{in}}\rangle - |\psi_j\rangle) \otimes |\emptyset\rangle + |\emptyset\rangle \otimes (|\Psi_{\text{in}}\rangle + |\psi_j\rangle)\right] \tag{4.43}$$

is the final photonic state that arrives at the detector. The qBhat coefficient for this system is $\mathscr{B}_q^{\text{qs}} = |\langle\Psi_\downarrow|\Psi_\uparrow\rangle|$ is the same as the one evaluated considering the sole spin-photon interface interacting with an input field having $p_{\text{H}} = 1/2$.

In 4.4(b), we compare the cBhat and qBhat values for the quantum state (B_{cl}^{qs} and $\mathscr{B}_q^{\text{qs}}$, respectively). The inequality $\mathscr{B}_q^{\text{qs}} \leq B_{cl}^{\text{qs}}$, and the equality occurs when both coefficients vanish [87]. We also include the qBhat plot for the classical state $\mathscr{B}^{\text{cs}}$, which does not vanish due to the no re-emission probability. The plot is divided into three regions:

1. Region (1) corresponds to long pulses, where $\Gamma/\gamma \leq 10^{-1}$. In this region, a clear quantum advantage is observed, as the classical measurement performed on the quantum state consistently extracts more information than coherent fields with equivalent energy and temporal profiles. This indicates that the quantum advantage observed at the pre-measurement stage remains robust at the collapse level. It is important to note the significant advantage in this region.

2. Region (2) represents short pulses, where $\Gamma/\gamma > 10^{-1}$. In this region, the qBhat values for both quantum and classical states are similar, suggesting that phase measurement may not be the most suitable approach to extract information. As discussed previously, polarization measurement, which is widely used in the literature [72], could be a better choice for extracting information in this region.

3. Region (3), below the black curve, represents an inaccessible region where the desired measurement outcomes cannot be achieved.

In summary, the analysis presented in Fig. 4.4 provides insights into the behavior of the cBhat and qBhat for different pulse durations and highlights the importance of selecting the appropriate measurement scheme based on the specific characteristics of the pulse. Here, we demonstrate that within this experimental set-up, the quantum advantage is robust at the classical level yielding orthogonal (distinguishable) pointer states. Hence, the quantum advantage is also verified at the collapse step. This constitutes the second main result of this chapter.

4.5 Application: Protocol for a controlled phase gate

In this section, we propose a controlled σ_z phase gate between two photons. The non-linear element responsible for implementing this gate is the spin in the quantum dot [149, 150, 151]. We focus on addressing the error caused by one fundamental source of imperfection: changes in the shape of scattered light. For this analysis, we consider only this intrinsic source of error and exclude the influence of other sources of noise, especially due to the system's decoherence stemming from the solid state matrix. To achieve this, we use two tools to proceed with the error analysis: state-average gate fidelity [138] and error matrix [139, 140].

The error analysis is critical in quantum computation as it inspires quantum error correction techniques [138, 152, 139]. The accurate knowledge of the errors a system is subjected to is extremely important to the development of robust quantum computing systems [149, 151, 152, 153]. Firstly, the gate fidelity is the most used figure of merit quantifying the accuracy of quantum gate operations [23], this is the basis of the state-average gate fidelity [138] used in this chapter. The improvement of this figure of merit is essential for any quantum computation task. Since the state-average gate fidelity is simply a number it does not provide any clue about what is the nature of the error, or how would it possible to correct it. To gain information about the source of errors it is necessary to correctly model it. The error matrix informs if an error is present and its elements provide insights on the errors [139, 140].

4.5.1 The ideal protocol

In this section, we present the protocol used to implement the controlled phase gate with a spin-photon interface (SPI) in the ideal scenario, and then we proceed to study how the modifications in the shape of the output field of the single photon impacts the performance of the gate.

The ideal protocol is implemented within the (quasi-)monochromatic regime. This regime assumes a long pulse with $\Gamma \ll \gamma$, referring to Fig. 4.3(b) it corresponds to the single photon component probability being $p_H = 1/2$, in short, we consider a pulse consisting of a superposition of zero and one photon. In this regime, assuming circularly right polarized light, a single photon interacts exclusively with the spin-up state, introducing a π-phase shift. This interaction can be described by the following map:

$$\begin{aligned} |\uparrow\rangle \otimes |\emptyset\rangle &\to |\uparrow\rangle \otimes |\emptyset\rangle, \\ |\downarrow\rangle \otimes |\emptyset\rangle &\to |\downarrow\rangle \otimes |\emptyset\rangle, \\ |\uparrow\rangle \otimes |\mathrm{R}\rangle &\to -|\uparrow\rangle \otimes |\mathrm{R}\rangle, \\ |\downarrow\rangle \otimes |\mathrm{R}\rangle &\to |\downarrow\rangle \otimes |\mathrm{R}\rangle. \end{aligned} \tag{4.44}$$

Here, $|\emptyset\rangle$ represents the field vacuum state, and $|\mathrm{R}\rangle$ represents the circularly right-polarized single-photon (R-photon) state.

The logical basis corresponds to the absence or the presence of a R-photon in

one optical mode. This is known as the single rail basis [154]. It is defined as:

$$\{|0\rangle, |1\rangle\} \equiv \{|\emptyset\rangle, |\mathrm{R}\rangle\}. \tag{4.45}$$

The protocol is composed of two ingredients: three spin rotations, $U^{[l]}$, with $l = 0, 1, 2$, and 2 identical light pulses, $|\Phi_{\mathrm{in}}^{[i]}\rangle$, with $i = 1, 2$. Specifically, we establish:

$$|\Phi_{\mathrm{in}}^{[i]}\rangle = \frac{|\emptyset\rangle_i + |\mathrm{R}\rangle_i}{\sqrt{2}}, \; i = 1, 2 \tag{4.46}$$

$$U^{[0]} = U^{[1]} = U^{[2]} = R_y\left(\frac{\pi}{2}\right) = \exp\left\{-i\frac{\pi}{4}\sigma_y\right\} \tag{4.47}$$

The rotations are assumed to happen instantaneously. Although we assume their equality here, this assumption is not constraining. The protocol can be outlined in the following manner:

1. **Spin initialization:** We start by assuming that the spin is initially prepared in the $|\uparrow\rangle$ state. To initiate the protocol, a rotation of $\pi/2$ around the y-axis, denoted as $U^{[0]}$, is applied, resulting in

$$|\psi_0\rangle_{\mathrm{spin}} = U^{[0]}|\uparrow\rangle = \frac{|\downarrow\rangle + |\uparrow\rangle}{\sqrt{2}} = |+\rangle \tag{4.48}$$

2. **First pulse:** After the spin is in the $|+\rangle$ state, the first step involves sending the initial light pulse, $|\Phi_{\mathrm{in}}^{[1]}\rangle$. This can be expressed as follows:

$$\begin{aligned}\left(\frac{|\emptyset\rangle_1 + |\mathrm{R}\rangle_1}{\sqrt{2}}\right) \otimes \left(\frac{|\downarrow\rangle + |\uparrow\rangle}{\sqrt{2}}\right) &= \frac{1}{2}\left(|\emptyset\rangle_1 + |\mathrm{R}\rangle_1\right)|\downarrow\rangle + \left(|\emptyset\rangle_1 + |\mathrm{R}\rangle_1\right)|\uparrow\rangle \\ &\xrightarrow{\text{Map. (4.44)}} \frac{1}{2}\left[\left(|\emptyset\rangle_1 + |\mathrm{R}\rangle_1\right)|\downarrow\rangle + \left(|\emptyset\rangle_1 - |\mathrm{R}\rangle_1\right)|\uparrow\rangle\right]\end{aligned} \tag{4.49}$$

3. **Spin rotation:** Following the first pulse, a second rotation, denoted as $U^{[1]}$, is applied to the spin:

$$\begin{aligned}&\frac{1}{2}\left[\left(|\emptyset\rangle_1 + |\mathrm{R}\rangle_1\right)|\downarrow\rangle + \left(|\emptyset\rangle_1 - |\mathrm{R}\rangle_1\right)|\uparrow\rangle\right] \\ \xrightarrow{U^{[1]}} &\frac{1}{2\sqrt{2}}\left(|\emptyset\rangle_1 + |\mathrm{R}\rangle_1\right)\left(|\downarrow\rangle - |\uparrow\rangle\right) + \left(|\emptyset\rangle_1 - |\mathrm{R}\rangle_1\right)\left(|\downarrow\rangle + |\uparrow\rangle\right) \\ &= \frac{1}{\sqrt{2}}\left(|\emptyset\rangle_1|\downarrow\rangle - |\mathrm{R}\rangle_1|\uparrow\rangle\right)\end{aligned} \tag{4.50}$$

4. **Second pulse:** Subsequently, the second pulse, denoted as $|\Phi_{\text{in}}^{[2]}\rangle$, is sent:

$$\begin{aligned}
&\left(\frac{|\emptyset\rangle_2 + |\mathrm{R}\rangle_2}{\sqrt{2}}\right) \otimes \left[\frac{1}{\sqrt{2}}\left(|\emptyset\rangle_1|\downarrow\rangle - |\mathrm{R}\rangle_1|\uparrow\rangle\right)\right] \\
&= \frac{1}{2}\left(|\emptyset\rangle_2 + |\mathrm{R}\rangle_2\right)\left(|\emptyset\rangle_1|\downarrow\rangle - |\mathrm{R}\rangle_1|\uparrow\rangle\right) \\
&= \frac{1}{2}\left(|\emptyset\rangle_2|\emptyset\rangle_1|\downarrow\rangle + |\mathrm{R}\rangle_2|\emptyset\rangle_1|\downarrow\rangle - |\emptyset\rangle_2|\mathrm{R}\rangle_1|\uparrow\rangle - |\mathrm{R}\rangle_2|\mathrm{R}\rangle_1|\uparrow\rangle\right) \\
&\xrightarrow{\text{Map. (4.44)}} \frac{1}{2}\left(|\emptyset\rangle_2|\emptyset\rangle_1|\downarrow\rangle + |\mathrm{R}\rangle_2|\emptyset\rangle_1|\downarrow\rangle - |\emptyset\rangle_2|\mathrm{R}\rangle_1|\uparrow\rangle + |\mathrm{R}\rangle_2|\mathrm{R}\rangle_1|\uparrow\rangle\right)
\end{aligned} \tag{4.51}$$

where we have emphasized the term that undergoes a phase change when the map is applied.

5. **Erase spin state information:** To reset the spin state information, a third rotation, denoted as $U^{[2]}$, is applied to the spin:

$$\begin{aligned}
&\to \frac{1}{2}\left(|\emptyset\rangle_2|\emptyset\rangle_1\left(\frac{|\downarrow\rangle - |\uparrow\rangle}{\sqrt{2}}\right) + |\mathrm{R}\rangle_2|\emptyset\rangle_1\left(\frac{|\downarrow\rangle - |\uparrow\rangle}{\sqrt{2}}\right)\right) \\
&+\frac{1}{2}\left(-|\emptyset\rangle_2|\mathrm{R}\rangle_1\left(\frac{|\downarrow\rangle + |\uparrow\rangle}{\sqrt{2}}\right) + |\mathrm{R}\rangle_2|\mathrm{R}\rangle_1\left(\frac{|\downarrow\rangle + |\uparrow\rangle}{\sqrt{2}}\right)\right) \\
&= \frac{1}{\sqrt{2}}\left[|\downarrow\rangle\left(\frac{|\emptyset\rangle_2|\emptyset\rangle_1 - |\emptyset\rangle_2|\mathrm{R}\rangle_1 + |\mathrm{R}\rangle_2|\emptyset\rangle_1 + |\mathrm{R}\rangle_2|\mathrm{R}\rangle_1}{2}\right)\right] \\
&+\frac{1}{\sqrt{2}}\left[-|\uparrow\rangle\left(\frac{|\emptyset\rangle_2|\emptyset\rangle_1 + |\mathrm{R}\rangle_2|\emptyset\rangle_1 + |\emptyset\rangle_2|\mathrm{R}\rangle_1 - |\mathrm{R}\rangle_2|\mathrm{R}\rangle_1}{2}\right)\right] \\
&= \frac{1}{\sqrt{2}}\left[|\downarrow\rangle|\psi_{\downarrow}^{\text{ideal}}\rangle - |\uparrow\rangle|\psi_{\uparrow}^{\text{ideal}}\rangle\right],
\end{aligned} \tag{4.52}$$

where

$$\begin{aligned}
|\psi_{\downarrow}^{\text{ideal}}\rangle &= \frac{|\emptyset\rangle_2|\emptyset\rangle_1 - |\emptyset\rangle_2|\mathrm{R}\rangle_1 + |\mathrm{R}\rangle_2|\emptyset\rangle_1 + |\mathrm{R}\rangle_2|\mathrm{R}\rangle_1}{2} \\
|\psi_{\uparrow}^{\text{ideal}}\rangle &= \frac{|\emptyset\rangle_2|\emptyset\rangle_1 + |\mathrm{R}\rangle_2|\emptyset\rangle_1 + |\emptyset\rangle_2|\mathrm{R}\rangle_1 - |\mathrm{R}\rangle_2|\mathrm{R}\rangle_1}{2}
\end{aligned} \tag{4.53}$$

6. **Spin measurement:** Ultimately, we perform a spin measurement to ascertain the final photonic state $|\psi_j^{\text{ideal}}\rangle$, where $j = \uparrow, \downarrow$ signifies the spin outcome. This projection establishes the two-photon gate conditioned on the spin result j. If the final spin state is j, the corresponding ideal gate is denoted by G_j^{ideal}. We have:

$$|\psi_j^{\text{ideal}}\rangle = G_j^{\text{ideal}}|\Phi_{\text{in}}^{\text{Tot}}\rangle. \tag{4.54}$$

Here, $|\Phi_{\text{in}}^{\text{Tot}}\rangle \equiv |\Phi_{\text{in}}^{[2]}, \Phi_{\text{in}}^{[1]}\rangle = |\Phi_{\text{in}}^{[2]}\rangle \otimes |\Phi_{\text{in}}^{[1]}\rangle$ is the total input photonic state.

Introducing the short-hand notation $|a\rangle_2 \otimes |b\rangle_1 = |ab\rangle$ for the logical basis. If the

final spin state is $j = \downarrow$, we have

$$
\begin{aligned}
|00\rangle &\xrightarrow{G_{\downarrow}^{\text{ideal}}} |00\rangle, \\
|01\rangle &\xrightarrow{G_{\downarrow}^{\text{ideal}}} -|01\rangle, \\
|10\rangle &\xrightarrow{G_{\downarrow}^{\text{ideal}}} |10\rangle, \\
|11\rangle &\xrightarrow{G_{\downarrow}^{\text{ideal}}} |11\rangle,
\end{aligned}
\tag{4.55}
$$

while if the final spin state is $j = \uparrow$ we obtain:

$$
\begin{aligned}
|00\rangle &\xrightarrow{G_{\uparrow}^{\text{ideal}}} -|00\rangle, \\
|01\rangle &\xrightarrow{G_{\uparrow}^{\text{ideal}}} -|01\rangle, \\
|10\rangle &\xrightarrow{G_{\uparrow}^{\text{ideal}}} -|10\rangle, \\
|11\rangle &\xrightarrow{G_{\uparrow}^{\text{ideal}}} |11\rangle.
\end{aligned}
\tag{4.56}
$$

In the basis $\mathscr{B}_2 = \{|00\rangle, |01\rangle, |10\rangle, |11\rangle\}$, the ideal gate matrices implemented on the logical qubits, conditioned on the measurement outcome $j \in \uparrow, \downarrow$ of the spin state are given by:

$$
\begin{aligned}
G_{\downarrow}^{\text{ideal}} &= \begin{bmatrix} 1 & 0 & 0 & 0 \\ 0 & -1 & 0 & 0 \\ 0 & 0 & 1 & 0 \\ 0 & 0 & 0 & 1 \end{bmatrix}, \text{ and} \\
G_{\uparrow}^{\text{ideal}} &= (-1) \begin{bmatrix} 1 & 0 & 0 & 0 \\ 0 & 1 & 0 & 0 \\ 0 & 0 & 1 & 0 \\ 0 & 0 & 0 & -1 \end{bmatrix}
\end{aligned}
\tag{4.57}
$$

It's worth noting that for the spin $\uparrow$ case, we have factored out the global phase factor of the gate [139]. Consequently, by applying $\pi/2$ rotations on the spin state after each light pulse in the quasi-monochromatic regime, it becomes possible to achieve a controlled σ_z-phase gate on the logical qubit:

$$
\begin{aligned}
|01\rangle &\xrightarrow{G_{\downarrow}^{\text{ideal}}} e^{i\pi}|01\rangle, \text{ and} \\
|11\rangle &\xrightarrow{G_{\uparrow}^{\text{ideal}}} e^{i\pi}|11\rangle.
\end{aligned}
\tag{4.58}
$$

4.5.2 The light-matter interaction map and the non-monochromaticity parameter

We now consider the realistic situation, where the interaction of a single R-photon of finite length with spin up not only introduces a π-phase but also changes its shape resulting in a non-monochromatic output, $|\tilde{\mathrm{R}}\rangle$. The light-matter interaction map in this situation is the following:

$$\begin{aligned} |\uparrow\rangle \otimes |\emptyset\rangle &\rightarrow |\uparrow\rangle \otimes |\emptyset\rangle, \\ |\downarrow\rangle \otimes |\emptyset\rangle &\rightarrow |\downarrow\rangle \otimes |\emptyset\rangle, \\ |\uparrow\rangle \otimes |\mathrm{R}\rangle &\rightarrow -|\uparrow\rangle \otimes |\tilde{\mathrm{R}}\rangle, \\ |\downarrow\rangle \otimes |\mathrm{R}\rangle &\rightarrow |\downarrow\rangle \otimes |\mathrm{R}\rangle. \end{aligned} \tag{4.59}$$

Here, $|\emptyset\rangle$ represents the field vacuum state, and $|\tilde{\mathrm{R}}\rangle$ represents the circularly right-polarized single-photon state. The notation $\tilde{\mathrm{R}}$ indicates that the shape of the photon may be different from the input R-photon after the scattering process.

The non-monochromatic output state $|\tilde{\mathrm{R}}\rangle$ does not lie in the chosen logical basis, as defined in Eq. (4.45). To account for this, we consider a third component $|\mathrm{R}_\perp\rangle$, which is orthogonal to both $|\mathrm{R}\rangle$ and $|\emptyset\rangle$: $\langle \mathrm{R}_\perp|\mathrm{R}\rangle = \langle \mathrm{R}_\perp|\emptyset\rangle = 0$. The expression for the non-monochromatic output can be written as:

$$|\tilde{\mathrm{R}}\rangle = c_\perp|\mathrm{R}_\perp\rangle + c_R|\mathrm{R}\rangle, \tag{4.60}$$

where $c_\perp$ and c_R are coefficients whose squared moduli sum to unity. It is important to note that part of the scattered field leaks out of the computational basis when $c_\perp \neq 0$. Our objective is to study the gate's performance in the presence of this leakage. To quantify the non-monochromaticity of the scattering process and the orthogonality between $|\mathrm{R}\rangle$ and $|\tilde{\mathrm{R}}\rangle$, we introduce the parameter

$$\boxed{\tilde{m} = \langle \mathrm{R}|\tilde{\mathrm{R}}\rangle} \tag{4.61}$$

When $|\tilde{m}|= 1$, the process is perfectly monochromatic, while $|\tilde{m}|= 0$ indicates complete orthogonality between the input field $|\mathrm{R}\rangle$ and the scattered field $|\tilde{\mathrm{R}}\rangle$ (non-monochromatic output). Moreover, we can relate $\tilde{m}$ to the mean photon overlap measured by a Hong-Ou-Mandel (HOM) interference experiment as $M_{\mathrm{R}\tilde{\mathrm{R}}} = |\tilde{m}|^2$ [42]. In terms of this parameter we can write:

$$|\tilde{\mathrm{R}}\rangle = \tilde{m}|\mathrm{R}\rangle + \sqrt{1-|\tilde{m}|^2}|\mathrm{R}_\perp\rangle. \tag{4.62}$$

Using Eq. (4.20) for the input photon and the solution, Eq. (4.22), for the scattered photon, we can express Eq. (4.61) analytically in terms of the input and output shapes of the single photon, $\beta(t)$ and $\Upsilon(t)$, as:

$$\boxed{\tilde{m}(\beta, \Upsilon) = \int_0^\infty ds\ \bar{\beta}(s)\Upsilon(s).} \tag{4.63}$$

where $\bar{\beta}(s)$ denotes the complex conjugate of $\beta(s)$. This equation bridges the microscopic physical parameters (Γ, γ) encoded in the input and output shapes of the field (β, Υ) with the variable that fundamentally controls the quality of the gate: $\tilde{m}$. In the monochromatic regime, where the input pulse shape is normalized, we obtain $\tilde{m} = 1$ as expected.

Using the decreasing exponential pulse shape, we have:

$$\beta(t) = \sqrt{\Gamma} \exp\left\{-\frac{\Gamma}{2}t\right\}, \tag{4.64}$$

$$\Upsilon(t) = \sqrt{\Gamma} e^{-\frac{(\gamma+\Gamma)}{2}t} \frac{\left[2\gamma e^{\frac{\Gamma}{2}t} - (\gamma+\Gamma)e^{\frac{\gamma}{2}t}\right]}{\Gamma - \gamma}.$$

The non-monochromaticity resulting from the decreasing pulse shape can be expressed as:

$$\tilde{m}(\Gamma, \gamma) = \frac{2\gamma}{\gamma + \Gamma} - 1. \tag{4.65}$$

The input and output intensities can be computed as $I_x(t) = |x(t)|^2$, where $x = \beta$, Υ respectively. The shapes of these intensities, as well as the non-monochromaticity parameter, are presented in Fig. 4.5. Figures 4.5(a) and 4.5(b) show the output temporal shape of the intensity as Γ/γ increases. It presents visually the increasing non-monochromaticity which is captured by the parameter in Eq. (4.65), represented in Fig. 4.5(c) showing that as the ratio Γ/γ increases, the non-monochromaticity of the pulse becomes more prominent, deviating from the unity which represents the ideal quasi-monochromatic pulse.

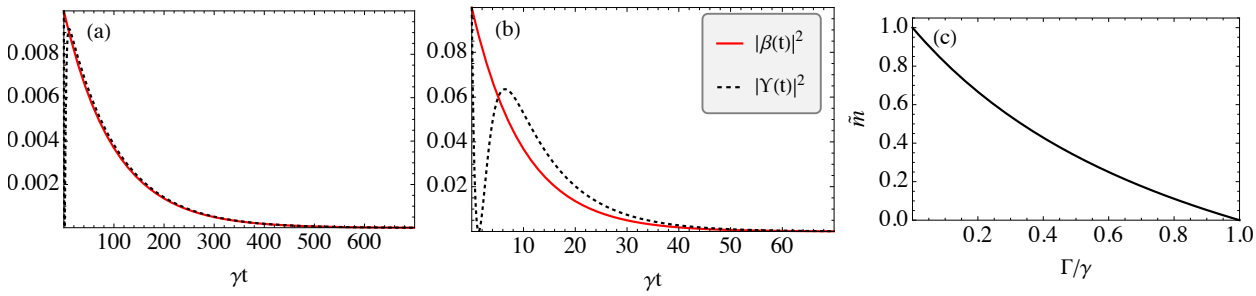

Figure 4.5: **Pulse temporal shapes.** Comparison of input (continuous red line) and output (dashed black line) pulse temporal shapes at different values of Γ/γ as a function of time. (a) $\Gamma/\gamma = 10^{-2}$ corresponding to the quasi-monochromatic regime, where the shapes are nearly identical. (b) $\Gamma/\gamma = 10^{-1}$, showing a decrease in monochromaticity as the output field differs from the input. (c) Non-monochromaticity parameter, Eq. (4.65) as a function of Γ/γ.

4.5.3 Non-ideal gate

We follow the steps (1)-(4) described in Sec. 4.5 using the general non-monochromatic map defined by Eq. (4.59) to obtain the real gates. The final photonic states are:

$$
\begin{aligned}
|\psi_{\downarrow}^{\text{real}}\rangle &= \frac{1}{2}\left(|\emptyset\rangle_2\left(|\emptyset\rangle_1 + (\frac{|\mathrm{R}\rangle_1 - |\tilde{\mathrm{R}}\rangle_1}{2})\right) + |\mathrm{R}\rangle_2\left(|\emptyset\rangle_1 + (\frac{|\mathrm{R}\rangle_1 - |\tilde{\mathrm{R}}\rangle_1}{2})\right)\right) \\
&+ \frac{1}{2}\left(-|\emptyset\rangle_2(\frac{|\mathrm{R}\rangle_1 + |\tilde{\mathrm{R}}\rangle_1}{2}) + |\tilde{\mathrm{R}}\rangle_2(\frac{|\mathrm{R}\rangle_1 + |\tilde{\mathrm{R}}\rangle_1}{2})\right) \\
|\psi_{\uparrow}^{\text{real}}\rangle &= -\frac{1}{2}\left(|\emptyset\rangle_2\left(|\emptyset\rangle_1 + (\frac{|\mathrm{R}\rangle_1 - |\tilde{\mathrm{R}}\rangle_1}{2})\right) + |\mathrm{R}\rangle_2\left(|\emptyset\rangle_1 + (\frac{|\mathrm{R}\rangle_1 - |\tilde{\mathrm{R}}\rangle_1}{2})\right)\right) \\
&- \frac{1}{2}\left(|\emptyset\rangle_2(\frac{|\mathrm{R}\rangle_1 + |\tilde{\mathrm{R}}\rangle_1}{2}) - |\tilde{\mathrm{R}}\rangle_2(\frac{|\mathrm{R}\rangle_1 + |\tilde{\mathrm{R}}\rangle_1}{2})\right)
\end{aligned}
\tag{4.66}
$$

In the monochromatic limit, $|\tilde{\mathrm{R}}\rangle_i = |\mathrm{R}\rangle_i$, the Eqs. (4.66) reduce to Eqs. (4.53) (the detailed calculation can be found in the App. C). We want to find the real gates, G_j^{real}, defined by $|\psi_j^{\text{real}}\rangle = G_j^{\text{real}}|\Phi_{\text{in}}^{\text{Tot}}\rangle$ represented in the logical basis. Using Eq. (4.62), we can write,

$$
\frac{|\mathrm{R}\rangle_i \pm |\tilde{\mathrm{R}}\rangle_i}{2} = \frac{1 \pm \tilde{m}}{2}|\mathrm{R}\rangle_i \pm \frac{\sqrt{1-|\tilde{m}|^2}}{2}|\mathrm{R}_{\perp}\rangle_i. \tag{4.67}
$$

Substituting the expression from Eq. (4.67) into Eqs. (4.66) and projecting the final state onto the logical basis, yields the real gate actions. For the spin $|\downarrow\rangle$ state, we obtain:

$$
\begin{aligned}
|00\rangle &\xrightarrow{G_{\downarrow}^{\text{real}}} |00\rangle \\
|01\rangle &\xrightarrow{G_{\downarrow}^{\text{real}}} -\tilde{m}|01\rangle = -e^{i\varepsilon_{\downarrow}}|01\rangle \\
|10\rangle &\xrightarrow{G_{\downarrow}^{\text{real}}} |10\rangle \\
|11\rangle &\xrightarrow{G_{\downarrow}^{\text{real}}} \frac{1}{2}(\tilde{m}^2+1)|11\rangle = e^{i\delta_{\downarrow}}|11\rangle.
\end{aligned}
\tag{4.68}
$$

For the spin $|\uparrow\rangle$ state, the gate is:

$$
\begin{aligned}
|00\rangle &\xrightarrow{G_{\uparrow}^{\text{real}}} -|00\rangle \\
|01\rangle &\xrightarrow{G_{\uparrow}^{\text{real}}} -|01\rangle \\
|10\rangle &\xrightarrow{G_{\uparrow}^{\text{real}}} -|10\rangle \\
|11\rangle &\xrightarrow{G_{\uparrow}^{\text{real}}} \frac{1}{2}(\tilde{m}^2+2\tilde{m}-1)|11\rangle = e^{i\varepsilon_{\uparrow}}|11\rangle
\end{aligned}
\tag{4.69}
$$

In this context, the non-ideal σ_z phase gates are characterized by the parameter $\varepsilon_{\downarrow(\uparrow)}$, which corresponds to the actual angles acquired during the inte0raction, and the angle $\delta_{\downarrow}$ signifies an additional unitary error. In the ideal scenario, both angles satisfy

the condition $\varepsilon_{\downarrow(\uparrow)} = \delta_{\downarrow} = 2\pi$. We observe that the map is completely positive but not trace-preserving due to the leakage of information into the orthogonal subspace spanned by $|\mathrm{R}_{\perp}\rangle$, which is not part of the logical basis (Eq. (4.45)). The actual gate angles acquired during the protocol, as functions o $\tilde{m}$, are given by,

$$\varepsilon_{\downarrow} = 2\pi - i\log\{-\tilde{m}\}\,, \tag{4.70}$$

$$\varepsilon_{\uparrow} = 2\pi - i\log\left\{-\frac{(\tilde{m}^2 + 2\tilde{m} - 1)}{2}\right\}, \tag{4.71}$$

$$\delta_{\downarrow} = 2\pi - i\log\left\{\frac{\tilde{m}+1}{2}\right\}.$$

The real and imaginary parts of the real angles are shown in Fig. 4.6. The matrix representations in the logical basis Eq. (4.45), as functions of the non-monochromaticity parameter is given by:

$$G_{\downarrow}^{\text{real}} = \begin{bmatrix} 1 & 0 & 0 & 0 \\ 0 & -\tilde{m} & 0 & 0 \\ 0 & 0 & 1 & 0 \\ 0 & 0 & 0 & \frac{(\tilde{m}^2+1)}{2} \end{bmatrix} = \begin{bmatrix} 1 & 0 & 0 & 0 \\ 0 & -e^{i\varepsilon_{\downarrow}} & 0 & 0 \\ 0 & 0 & 1 & 0 \\ 0 & 0 & 0 & e^{i\delta_{\downarrow}} \end{bmatrix}, \text{ and} \tag{4.72}$$

$$G_{\uparrow}^{\text{real}} = -\begin{bmatrix} 1 & 0 & 0 & 0 \\ 0 & 1 & 0 & 0 \\ 0 & 0 & 1 & 0 \\ 0 & 0 & 0 & -\frac{(\tilde{m}^2+2\tilde{m}-1)}{2} \end{bmatrix} = -\begin{bmatrix} 1 & 0 & 0 & 0 \\ 0 & 1 & 0 & 0 \\ 0 & 0 & 1 & 0 \\ 0 & 0 & 0 & -e^{i\varepsilon_{\uparrow}} \end{bmatrix}.$$

In the quasi-monochromatic regime, where $\tilde{m} = 1$, the ideal gate matrices in Eq. (4.57) are recovered. In Fig. 4.6(a), it is evident that the real component of $\varepsilon_{\downarrow}$

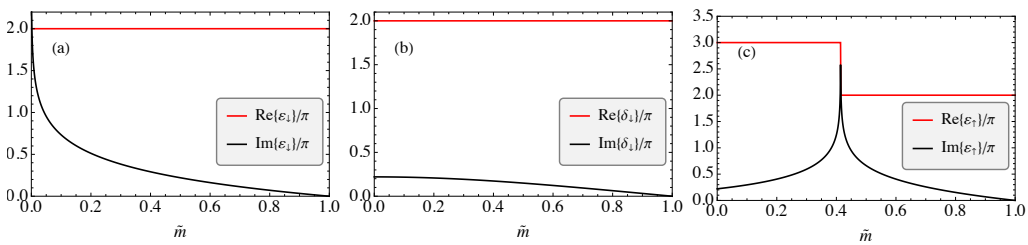

Figure 4.6: **Angle errors, Eq. (4.71).**

remains constant at 2π, while the imaginary component emerges as $\tilde{m}$ approaches 0, resulting in a rotational angle error. In Fig. 4.6(b), the real part of the angle $\delta_{\downarrow}$ also maintains a constant value of 2π for all $\tilde{m}$ values, and the imaginary part is much smaller than 2π as $\tilde{m}$ approaches 0, ultimately becoming a constant error for $\tilde{m} < 0.4$. In Fig. 4.6(c), we observe that achieving the desired σ_z-gate requires the $\tilde{m}$-parameter to exceed 0.4; otherwise, the real part of the angle $\varepsilon_{\uparrow}$ becomes 3π, leading to an identity gate. Focusing on the region where $\tilde{m} > 0.4$, we confirm that the real component of $\varepsilon_{\uparrow}$ remains 2π. For the range $0.4 < \tilde{m} < 1$, the imaginary part introduces a tilt in the gate, resulting in an error. Based on these observations, we will focus our analysis for values $\tilde{m} > 0.4$.

In the next section, we analyze the gate error as a function of the parameter $\tilde{m}$ and study deeper into the error analysis by modeling the error itself. The tools used to perform this analysis are the state-averaged fidelity [138] and the error matrix [139, 140].

4.5.4 Error analysis

State-average gate fidelity

The fidelity measure we employ for evaluating the gate (or process) is constructed from the state fidelity, which is the squared inner product between the ideal and realized final (pure) states [23]. The state-averaged fidelity, proposed in Ref. [138], offers a succinct and clear means to access the average fidelity of general quantum operations within a finite-dimensional space. Specifically, for a four-dimensional context, the state-averaged fidelity takes the form:[3]

$$F_{\text{ave}}(U_{\text{real}}, U_{\text{target}}) \equiv \frac{\text{tr}\left\{U_{\text{real}}^{\dagger} U_{\text{real}}\right\} + |\text{tr}\left\{U_{\text{target}}^{\dagger} U_{\text{real}}\right\}|^2}{20}. \tag{4.73}$$

In our context, $U_{\text{real}} = G_j^{\text{real}}$ represents the realized operation projected into the pertinent logical subspace, while $U_{\text{target}} = G_j^{\text{ideal}}$, where $j = \uparrow, \downarrow$ corresponds to the desired ideal gate operation conditioned on spin j. It is important to note that the projected U_{real} is not necessarily unitary [139]. The first term, $\text{tr}\left\{U_{\text{real}}^{\dagger} U_{\text{real}}\right\}$, captures the potential non-unitarity stemming from any leakage originating in the computational basis. The second term, $|\text{tr}\left\{U_{\text{target}}^{\dagger} U_{\text{real}}\right\}|^2$, quantifies the square of the Hilbert-Schmidt inner product between U_{target} and U_{real}. This term reflects the similarity or overlap between the realized operation and the ideal target operation in the logical subspace.

It is crucial to emphasize that the validity of Eq. (4.73) relies on the assumption that the initial and the final state involved are pure. Consequently, this equation is inapplicable for mixed states.

We compute Eq. (4.73) with Mathematica (notebook available the dedicated GitHub repository [76]) and we obtain,

$$F_{\text{ave}}^{j} = \frac{1}{20}\left(4 + \frac{1}{4}\left(5 + \tilde{m}(2 + \tilde{m})\right)^2\right) \tag{4.74}$$

for both cases $j = \uparrow, \downarrow$. Figure 4.7 displays the plot of the state-average fidelity for values of $\tilde{m}$ greater than 0.4, where the real part of both real angles is 2π (as shown in Fig. 4.6). Notably, we observe that the fidelity consistently surpasses $F_{\text{ave}}^{j} \geq 0.6$, eventually reaching unity in the monochromatic limit.

[3] The factor 1/20 is specific for the 4-dimensional space we are considering, for a $d-$dimensional space the denominator takes the value $d^2 + d$.

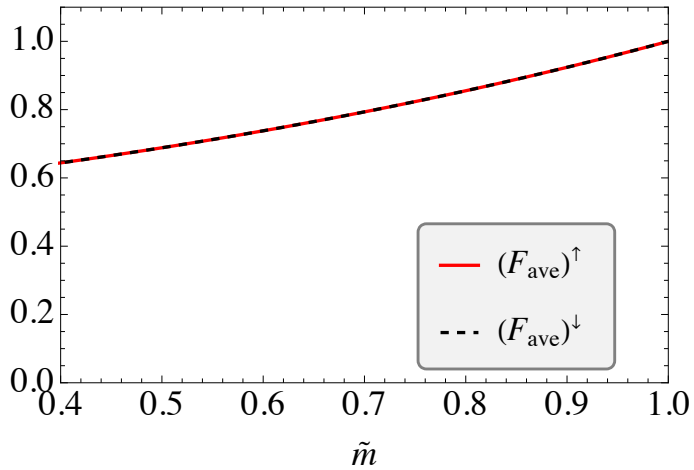

Figure 4.7: **State-averaged fidelity, Eq.** (4.74)**.**

Error matrix

We can analyze the deviation of the real gate G_j^{real} from the ideal gate G_j^{ideal} by representing it as a composition of the ideal gate and an error matrix, as discussed in Ref. [140]. This error matrix, denoted as E_j, is expressed as follows: $G_j^{\text{real}} = E_j G_j^{\text{ideal}}$. Given that G_j^{ideal} is invertible, the error matrix can be calculated using the relationship:

$$E_j = G_j^{\text{real}} \left(G_j^{\text{ideal}}\right)^{-1}, \tag{4.75}$$

where $j = \uparrow, \downarrow$. A convenient way to model errors is through the Pauli error channel [155, 23]. The Pauli error channel operates on a general quantum state by applying the Pauli operators

$$\mathscr{B}_P = \{I \equiv \mathbb{1},\ \sigma_x \equiv X,\ \sigma_y \equiv Y,\ \sigma_z \equiv Z\} \tag{4.76}$$

with certain probabilities. The Pauli operators capture different types of errors that can affect the state:

- I is the identity operator, this operator represents no error.
- X implements a bit flip between the computational basis elements.
- Y combines a phase flip with a bit flip.
- Z introduces a phase flip.

For our proposed photon-photon gate, we characterize the error E_j using a two-qubit Pauli error channel. This channel is defined in terms of the tensor product of two single-qubit Pauli operator sets:

$$\mathscr{B}_2 = (\mathscr{B}_P)^{\otimes 2} = \{I_1, X_1, Y_1, Z_1\} \otimes \{I_2, X_2, Y_2, Z_2\}, \tag{4.77}$$

Thus, the real gate's behavior is represented as the application of the ideal gate followed by the two-qubit Pauli error channel [139, 155]. The resulting photonic

state transformation can be expressed as:

$$\rho_0^{\text{photonic}} \to \sum_{B\in\mathscr{B}_2} p_B B\rho B^\dagger \tag{4.78}$$

where $\rho_0^{\text{photonic}} = |\Phi_{\text{in}}^{[2]}, \Phi_{\text{in}}^{[1]}\rangle\langle\Phi_{\text{in}}^{[1]}, \Phi_{\text{in}}^{[2]}|$, and our goal is to determine the probabilities p_B. This approach is particularly effective for modeling errors in single or multiqubit processes, making it well-suited for addressing both decoherence-induced errors and intrinsic gate errors. Specifically, intrinsic gate errors refer to deviations stemming from sources other than decoherence, such as inaccuracies in unitary qubit rotations. For instance, if the process is trace-preserving, then $\sum_{B\in\mathscr{B}_n} p_B = 1$. However, in the presence of significant errors leading to leaks out of the logical basis, we might observe $\sum_{B\in\mathscr{B}_n} p_B < 1$.
Furthermore, the Pauli error channel model is straightforward to apply and allows us to obtain simple analytical formulas for the Pauli-error probabilities p_B. From a practical standpoint, these probabilities can be directly measured without the need for full-process tomography, as they correspond to the diagonal elements of the process matrix when expressed in the Pauli basis [156, 157, 23]. As a result, this approach provides valuable insights into the error characteristics of the quantum process, avoiding the requirement for more resource-intensive and comprehensive tomographic procedures. We calculate the error matrix by employing Eq. (4.75) and then expand it within the basis provided by Eq. (4.77). The resulting error matrices are as follows:

$$E_\uparrow(\tilde{m}) = \begin{pmatrix} \frac{1}{8}(\tilde{m}(\tilde{m}+2)+5) & 0 & 0 & -\frac{1}{8}(\tilde{m}-1)(\tilde{m}+3) \\ 0 & 0 & 0 & 0 \\ 0 & 0 & 0 & 0 \\ -\frac{1}{8}(\tilde{m}-1)(\tilde{m}+3) & 0 & 0 & \frac{1}{8}(\tilde{m}-1)(\tilde{m}+3) \end{pmatrix},$$

$$E_\downarrow(\tilde{m}) = \begin{pmatrix} \frac{1}{8}(\tilde{m}(\tilde{m}+2)+5) & 0 & 0 & -\frac{1}{8}(\tilde{m}-1)(\tilde{m}+3) \\ 0 & 0 & 0 & 0 \\ 0 & 0 & 0 & 0 \\ -\frac{1}{8}(\tilde{m}-1)^2 & 0 & 0 & \frac{1}{8}(\tilde{m}-1)^2 \end{pmatrix} \tag{4.79}$$

We can visually represent them for some values of $\tilde{m}$. It is observed that only the error amplitudes $e^j_{Z_1Z_2}$, $e^j_{Z_1I_2}$, $e^j_{I_1Z_2}$, and $e^j_{I_1I_2}$ are non-zero. Therefore, based on Eq. (4.78) the transformation of the initial photonic state ρ_0^{photonic} can be expressed as follows:

$$\rho_0^{\text{photonic}} \to p^j_{II}\rho^j + p^j_{Z_1I}Z_1\rho^j Z_1 + p^j_{IZ_2}Z_2\rho^j Z_2 + p^j_{IZ_2}Z_2\rho^j Z_2 + p^j_{Z_1Z_2}Z_2Z_1\rho^j Z_1Z_2 \tag{4.80}$$

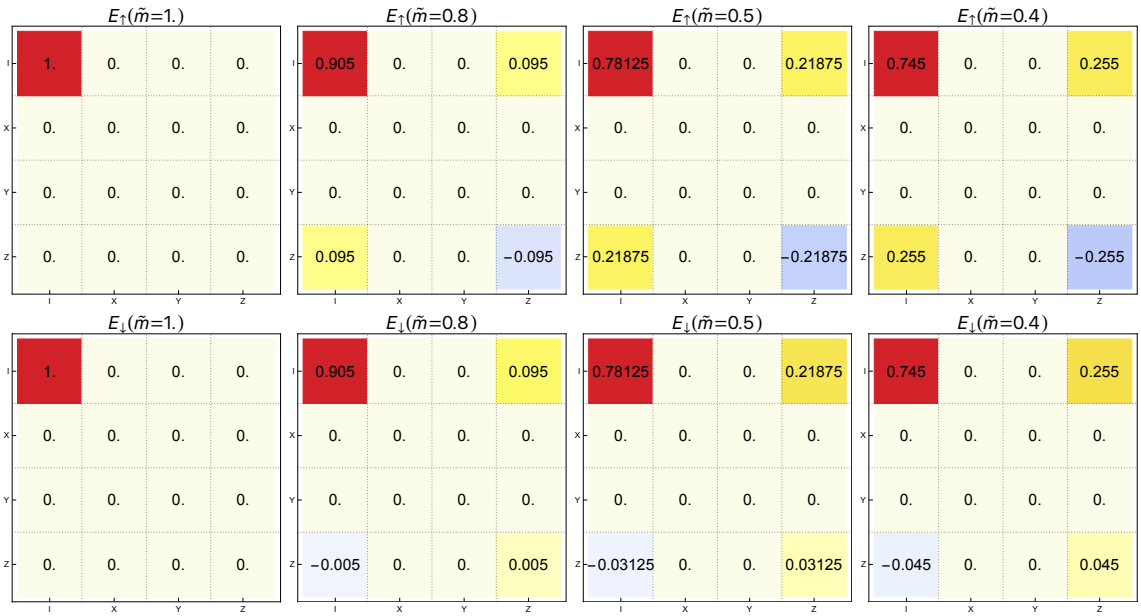

Figure 4.8: **Error matrices plot.** Upper panel showcases the error matrices for $E_\uparrow$ and the lower panel presents the error matrices for $E_\downarrow$for certain values of $\tilde{m}$.

with probabilities,

$$
\begin{aligned}
p^{\downarrow}_{II} = p^{\uparrow}_{II} &= \left|\frac{1}{8}(\tilde{m}(\tilde{m}+2)+5)\right|^2, \\
p^{\uparrow}_{Z_1 I} = p^{\downarrow}_{Z_1 I} = p^{\uparrow}_{I Z_2} &= \left|\frac{1}{8}(\tilde{m}-1)(\tilde{m}+3)\right|^2, \\
p^{\downarrow}_{I Z_2} &= \left|\frac{1}{8}(\tilde{m}-1)^2\right|^2, \\
p^{\uparrow}_{Z_1 Z_2} &= \left|\frac{1}{8}(\tilde{m}-1)(\tilde{m}+3)\right|^2, \\
p^{\downarrow}_{Z_1 Z_2} &= \left|\frac{1}{8}(\tilde{m}-1)^2\right|^2.
\end{aligned}
\tag{4.81}
$$

These probabilities are depicted in Fig. 4.9. The blue line represents the sum of all probabilities and demonstrates the amount of leakage from the logical basis, i.e., it is the quantity $\mathrm{tr}\left\{U^{\dagger}_{\mathrm{real}} U_{\mathrm{real}}\right\}$. We now proceed to interpret the significance of these error amplitudes:

- The probability p_{II} corresponds to a scenario where no error has occurred, indicating that the final photonic state matches the target state established by the ideal gate, as described in Eq. (4.53). The error amplitude e^{j}_{II} consistently holds a nonzero value and is related to the fidelity of the process [140]. It assumes a value of one when the ideal gate is perfectly executed ($\tilde{m} = 1$), while all other elements vanish. However, as the system moves away from the monochromatic regime, the fidelity of the process is impacted: $e^{j}_{II} < 1$, leading

to the emergence of the other amplitudes.

- The error amplitudes e^j_{ZI} and e^j_{IZ} are found along the first row/column of the error matrix and are real. This distinct feature indicates a non-unitary alteration in the state, unrelated to the presence of decoherence processes, as discussed in Ref. [140]. In our specific context, their emergence is connected to the phenomenon of the scattered field leaking into a component that is not considered in the logical basis—specifically, the leakage into $|\mathrm{R}_\perp\rangle$.

- Lastly, e^j_{ZZ} hallmarks the presence of correlated errors. The alteration in the shape of the scattered first pulse is linked to a corresponding alteration in the shape of the scattered second pulse. This error correlation stems from the interaction between photons and spin [139]. This insight highlights an important fact: it becomes necessary to develop appropriate error correction strategies to address this correlated error [152].

This analysis highlights the significance of the error matrix. The process fidelity is encapsulated in the element e_{II}, making it sufficient to focus on this element to extract information about the implemented process. Furthermore, the other elements offer valuable insights into the nature of errors, thereby providing a complete error characterization.

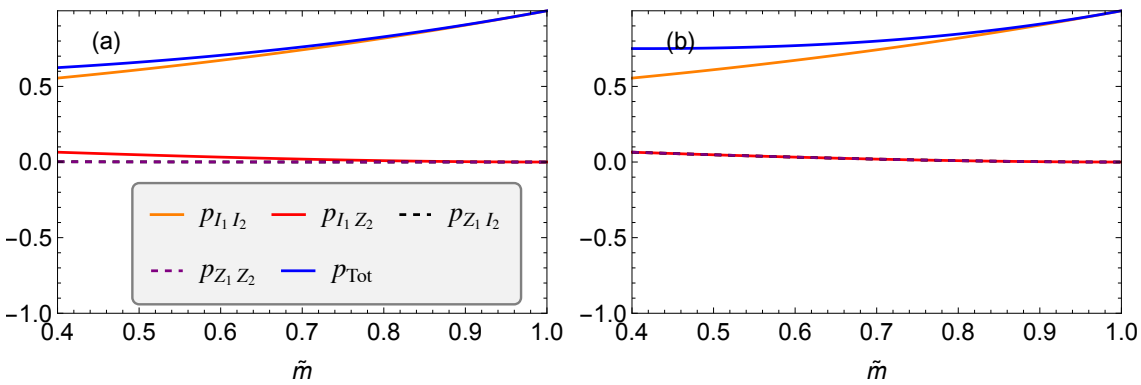

Figure 4.9: **Probabilities plots.** Error probabilities, Eq. (4.81), for (a) $E_\downarrow$, and (b) $E_\uparrow$.

4.6 Conclusions and perspectives

In this chapter, we have examined the interaction between 4LS, and a traveling pulse of light, which forms the SPI. Our focus was on the investigation of the entanglement generation, in other words, the potential for a QND measurement, at a low-energy regime, where we considered at most one photon. We compared the performance of a coherent field with a quantum superposition of zero and single-photon states. Our analysis is based on the von Neumann measurement model, which involves two steps: the pre-measurement and the collapse (as discussed in Chap. 1).

The first major finding is that the superposition of zero and single photons effectively entangle with the spin state, resulting in perfectly orthogonal pointer

states, for any pulse shape as evidenced by Eq. (4.28), while the coherent field does not with a low energy budget. This demonstrates a quantum advantage at the pre-measurement stage.

During the pre-measurement, we observed that information about the spin state may be distributed across different degrees of freedom. This implies that a fine-tuning of the measured observable is necessary to extract information about the spin state from the light, depending on the energy budget and the pulse bandwidth. Taking this into consideration, we focused on the monochromatic regime and proposed an experimental protocol based on the interaction of the spin with light and the phase shift acquired between the pulses. The proposed experiment constitutes a Michelson interferometer, and we observed that the quantum advantage is maintained at the collapse stage after the light has interacted with the SPI.

The Hamiltonian model of the SPI serves as a powerful tool for studying errors in photonic quantum computing, particularly concerning light pulses of finite duration [134] holding importance for fundamental questions and technological applications. Following the latter, we have presented a protocol for implementing a photon-photon gate in the single-rail basis using a 4LS as a non-linear device, inferred from the measurement of the spin state. The gate operation is determined by Eq. (4.57), achieved through the light-matter interaction defined by Eq. (4.59), along with unitary manipulations of the spin state. To characterize the non-monochromaticity of the scattering process, we introduced a parameter defined in Eq. (4.61) and established an analytical expression relating it to microscopic parameters obtained from the collisional model solution [73], as shown in Eq. (4.63). Throughout our analysis, we focused on the quasi-monochromatic regime and the deviation from it. We obtained the ideal gate matrix given by Eq. (4.57). Furthermore, we determined the matrices representing the real process in terms of the non-monochromaticity parameter, and modeled it as a two-qubit Pauli error channel, given by Eq. (4.72). They are not trace-preserving unless the process is monochromatic, this is due to the component that is orthogonal to the chosen logical basis, leading to a loss of information.

A thorough error analysis was performed based on state-average fidelity [138] and the error matrix [140, 139]. By examining the error amplitudes of the error matrix and associated probabilities, we can gather information about the specific types of errors occurring in the system. In the case of the study presented here, we have theoretical control over the nature of the error, namely the change in the shape of the scattered field, which represents a coherent error. We observed the signature of coherent errors, indicated by non-vanishing real elements in the first row and columns of the error matrix [140]. Furthermore, we identified an error due to the correlation between errors arising from the difference in the shapes of the scattered pulses [155]. It is interesting to notice that when considering the average state fidelity, both gates appear to perform similarly. However, upon closer examination of the error matrix, we observe distinct error contributions in the Pauli channel for each gate, providing further insight into their error characteristics.

As a perspective, we can consider the possibility of improving the performance by applying different inter-pulse rotations. These findings represent the first step towards the goal of characterizing the errors in SPIs based on quantum dots, which

can allow the proposition appropriate error correction schemes to facilitate gate-based and measurement-based quantum computation with the SPI.

Chapter 5

The SPI subjected to an in-plane magnetic field

Experiment is the only means of knowledge at our disposal. Everything else is poetry and imagination. – Max Planck

5.1 Introduction

In recent years, there has been a growing interest in the implementation of the Lindner-Rudolph protocol (LRP) [68] due to its potential for generating linear cluster states through spin-photon entanglement [135, 63]. Cluster states are highly entangled photonic states that serve as a fundamental resource for measurement-based quantum computing (MBQC), a paradigm that takes advantage of the redundant information encoded in these states to process quantum information effectively [122, 158, 69]. MBQC offers several advantages including robustness against photon losses, the ability to perform computations in parallel, and reduced operation overhead [69]. However, the successful implementation of the LRP poses several experimental challenges that need to be addressed, especially in terms of preparing the specific superposition states required for the protocol.

The progress made in spin-photon interfaces utilizing quantum dots has established it as an excellent platform for implementing the LRP. A significant achievement in this field was the realization of linear cluster states using quantum dots with dark excitons, reported in Ref. [135]. More recently, a development was made and reported in Ref. [63] demonstrating the efficient generation of three-partite cluster states involving a semiconductor electronic spin and two indistinguishable photons.

In this chapter, we focus on analyzing the spin dynamics in the LRP under realistic experimental conditions of Refs. [75, 63]. We consider a system where the ground state encompasses the two spin states of the trapped electron and the excited state comprises the two spin states of the optically excited spin-hole pair (the trion), see App. B. Both are influenced by the magnetic field with characteristic Larmor frequencies: Ω_g and Ω_e, respectively. The presence of parasitic fields affecting the electron spin introduces an inherent physical difference between these frequencies, which affects the fidelity of spin rotations. Another significant complication is the necessity to optically excite the electron spin state that is processing. This dynamic

nature introduces complexities in accurately timing the pulse delivery.

This chapter aims to address these intrinsic imperfections and gain insights into the performance of the LRP by applying the collisional model to a realistic experimental scenario. Our analytical solution enables us to investigate important performance metrics, such as the fidelity of spin rotations.

By making a comprehensive analysis of spin dynamics, we contribute to enhance the understanding of the LRP's performance optimization, paving the way for future advancements in the field of MBQC. The chapter is organized as follows:

- In Sec. 5.2, we provide a concise overview of the ideal LRP, emphasizing its key components, underlying conditions, and essential parameters for successful implementation. We also formulate the main research questions addressed in this chapter. We introduce our model for the experimental setup and examine the protocol within the framework of this realistic scenario.
- In Sec. 5.3, we present the solution for spontaneous emission and validate the model's accuracy by fitting it to actual experimental data reported in Ref. [75].
- In Sec. 5.4, we attack the central question of the chapter, where we investigate how the imperfections captured by the Hamiltonian solution impacts the protocol.

5.2 System, protocol and modeling

5.2.1 System

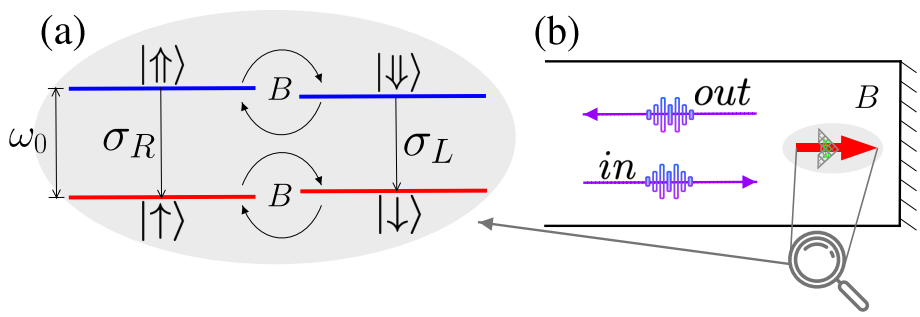

Figure 5.1: **Schematic of the spin-photon interface subjected to an in-plane magnetic field.** a) Energy structure. The system is represented by a quasi-degenerate 4-level system under the influence of a low in-plane magnetic field $\vec{B}$ (Voigt configuration, see App. B). The conservation of angular momentum leads to the selective transitions $|\downarrow\rangle \to |\Downarrow\rangle (|\uparrow\rangle \to |\Uparrow\rangle)$ by left (right) polarized light. The magnetic field $\vec{B}$ induces precession of the spin states. (b) The interface comprises a quantum emitter with a spin degree of freedom (depicted by a red arrow in the gray shaded area) coupled to a 1D waveguide, which is subjected to an external magnetic field $\vec{B}$.

The Lindner-Rudolph protocol (LRP) generates a string of photonic cluster states using two ingredients: light pulses and spin rotations. The protocol considers a

4LS degenerate system, as the one investigated in Chap. 4. The ground states are represented by $\{|\uparrow\rangle, |\downarrow\rangle\}$, with projections of $\pm 1/2$ along the z-axis and zero energy. The corresponding excited states are denoted by $\{|\Uparrow\rangle, |\Downarrow\rangle\}$, with projection $\pm 3/2$, and energy ω_0. Transitions from $|\uparrow\rangle \to |\Uparrow\rangle$ (or $|\downarrow\rangle \to |\Downarrow\rangle$) are induced by right (or left) circularly polarized photons, which have ellipticity of $+1(-1)$, respectively. In the context of quantum dots, these transitions occur through the emission of single photons via the decay of the trion.

Here, we add to the Hamiltonian Eq. (4.2) an external magnetic field oriented perpendicularly to the growth direction along the x-direction. This is known as the Voigt configuration (refer to Fig. 5.1). The magnetic field is assumed to be weak enough to ensure that the Zeeman effect only causes a level splitting comparable to the spectral linewidth, hence the 4LS remains (quasi)degenerate. Consequently, when the system interacts with light, only the vertical transition $|\uparrow\rangle \to |\Uparrow\rangle$ ($|\downarrow\rangle \to |\Downarrow\rangle$) is promoted by right (left) polarized light, and diagonal transitions can be disregarded for our analysis [75, 63] (see App. B).

To account for the magnetic field interaction we add the following term to Eq. (4.2):

$$H_{\mathrm{B}} = H_{B,tr} + H_{B,el}. \tag{5.1}$$

Here, $H_{B,tr}$ and $H_{B,el}$ represent the magnetic field interactions for the trion and electron spins, respectively. The presence of an external magnetic field $\vec{B}$ causes the spin states to undergo precession around its axis. Specifically, for the trion state, we have:

$$H_{B,tr} = \frac{\Omega_e}{2}\hat{u} \cdot \vec{\sigma}^{tr}, \tag{5.2}$$

where Ω_e represents the Larmor frequency of the excited state, $\hat{u}$ is the unity vector that defines the direction of the magnetic field perceived by the trion, and $\vec{\sigma}^{tr}$ represents the vector of Pauli matrices acting on the space $\{|\Uparrow\rangle, |\Downarrow\rangle\}$. Similarly, for the electron spin state, we have:

$$H_{B,el} = \frac{\Omega_g}{2}\hat{n}_g \cdot \vec{\sigma}^{el}, \tag{5.3}$$

where Ω_g represents the Larmor frequency of the ground state, $\hat{n}_g$ is the unity vector that defines the direction of the magnetic field perceived by the electron, and $\vec{\sigma}^{el}$ represents the vector of Pauli matrices acting in the space $\{|\uparrow\rangle, |\downarrow\rangle\}$.

The electron possesses an s-type orbital wavefunction, meaning that there is a strong localization on the lattice site and dominant interaction with nuclei through Fermi-contact interaction. The spin states are sensitive to the random magnetic fields present in the solid-state matrix. Notably, the Overhauser field originates from the hyperfine interaction with the nuclei surrounding the quantum dot [159, 121]. Another component to take into account for the magnetic field is the one that emerges from the nuclear quadrupolar fields in strained quantum dots. This ensemble is referred to as *parasitic fields*, and their action on the spin is modeled by the unity vector $\hat{n}_g$. In the excited state, the physical system is a hole with a p-type orbital, which is not localized on the lattice site. Consequently, the Fermi-contact interaction is

suppressed, and the heavy hole becomes sensitive only to the dipole-dipole interaction and the external magnetic field. Since it points in the $x-$direction we have the unity vector $\hat{u} = \hat{x} = (1, 0, 0)$ [160]. These different physical wavefunctions give rise to a fundamental difference in the Larmor frequencies. The excited state exhibit precession characterized by the Larmor frequency:

$$\Omega_e \equiv \Omega = g_h \mu_B |\vec{B}_{\text{ext}}|. \tag{5.4}$$

Here, $|\vec{B}_{\text{ext}}|$ represents the magnitude of the external magnetic field, g_h is the g-factor of the hole and μ_B is the Bohr magneton. The frequency Ω can be experimentally controlled by manipulating the magnitude of the external magnetic field. The ratio between the ground state Larmor frequency Ω_g and the excited state Larmor frequency Ω is defined by:

$$r_{ge} \equiv \frac{\Omega_g}{\Omega}, \tag{5.5}$$

Using (5.13) and $\hat{u} = \hat{x}$ allows us to re-write Eq. (5.1) as:

$$H_B = \frac{\Omega}{2} \left(\sigma_x^{tr} + r_{ge} \hat{n}_g \cdot \vec{\sigma}^{el} \right). \tag{5.6}$$

Now that we have defined the system under consideration, let us review the Lindner-Rudolph protocol (LRP) operating under ideal conditions, as proposed in Ref. [68].

5.2.2 The ideal Lindner-Rudolph protocol

The system is initially prepared in $|\uparrow\rangle$ and is taken to the superposition state

$$|\psi_0\rangle = |-i\rangle = \frac{|\uparrow\rangle - i|\downarrow\rangle}{\sqrt{2}}. \tag{5.7}$$

The ideal protocol involves two main components:

1. $\pi-$**pulses:** These pulses induce a complete inversion of the population between the ground state and the excited state. When applied with precision timing and intensity, π-pulses effectively flip the quantum system's population from its initial state in the ground state to the corresponding excited state, and vice versa.

2. **Instantaneous rotations on the spin states:** These rotations create superpositions of the electronic spin states by performing $\pi/2$ rotations of the spin.

In a real experimental setup, the rotation component (2) is implemented using the in-plane magnetic field (Voigt configuration). The rotation corresponds to the Larmor precession of the spin around the x-axis, occurring over a finite period of Ω_g^{-1}, where Ω_g represents the Larmor frequency of rotation between the states $|\uparrow\rangle$ and $|\downarrow\rangle$. Hence, the rotation is described by

$$R_x(t) = \exp\left\{ -i \frac{\Omega_g}{2} t X \right\}, \tag{5.8}$$

where $X = |\uparrow\rangle\langle\downarrow| + |\downarrow\rangle\langle\uparrow|$ is the spin-flip Pauli operator. Ideally, a $\pi/2$ rotation creates the desired superposition, Eq. (5.7), within a period of

$$t_g = \frac{\pi}{2\Omega_g} = \frac{\pi}{2r_{ge}\Omega}. \tag{5.9}$$

Regarding the pulses, the field is horizontally polarized to simultaneously excite both transitions. We introduce the notation $|1_{\mathrm{j}}\rangle_n$, where $j = \mathrm{R,L}$ represents the photon polarization, and $n > 0$ representing the single photons emitted by the 4LS subsequent to the $(n-1)-$th pulse.

The ideal protocol proceeds as follows:

$$\begin{aligned}
&\frac{|\uparrow\rangle - i|\downarrow\rangle}{\sqrt{2}} \xrightarrow{\pi\text{–pulse}} \frac{|\uparrow\rangle|1_{\mathrm{R}}\rangle_1 - i|\downarrow\rangle|1_{\mathrm{L}}\rangle_1}{\sqrt{2}} \\
&\xrightarrow{R_x(\pi/2)} \frac{(|\uparrow\rangle - i|\downarrow\rangle)|1_{\mathrm{R}}\rangle_1 - i(|\uparrow\rangle + i|\downarrow\rangle)|1_{\mathrm{L}}\rangle_1}{\sqrt{2}\sqrt{2}} \\
&\xrightarrow{\pi\text{–pulse}} \frac{(|\uparrow\rangle|1_{\mathrm{R}}\rangle_2 - i|\downarrow\rangle|1_{\mathrm{L}}\rangle_2)|1_{\mathrm{R}}\rangle_1 - i(|\uparrow\rangle|1_{\mathrm{R}}\rangle_2 + i|\downarrow\rangle|1_{\mathrm{L}}\rangle_2)|1_{\mathrm{L}}\rangle_1}{\sqrt{2}\sqrt{2}} \\
&= \frac{1}{\sqrt{2}}\left(|\uparrow\rangle\left(\frac{|1_{\mathrm{R}}\rangle_1 - i|1_{\mathrm{L}}\rangle_1}{\sqrt{2}}\right)|1_{\mathrm{R}}\rangle_2 - i|\downarrow\rangle\left(\frac{|1_{\mathrm{R}}\rangle_1 + i|1_{\mathrm{L}}\rangle_1}{\sqrt{2}}\right)|1_{\mathrm{L}}\rangle_2\right)
\end{aligned} \tag{5.10}$$

By repeating the aforementioned process N times, a linear cluster state consisting of $N+1$ entities is generated, composed of N photons and the spin. This spin can be decoupled by performing a polarization measurement on the last emitted photon. For instance, if the photon is measured as $|1_{\mathrm{R}}\rangle_2$, then the spin state is $|\uparrow\rangle$, and we have the state:

$$\frac{|1_{\mathrm{R}}\rangle_1 - i|1_{\mathrm{L}}\rangle_1}{\sqrt{2}} \tag{5.11}$$

It is worth mentioning that after the first pulse, a Bell state is obtained. By repeatedly applying pulses without performing the rotation step (2), the GHZ-state can be built [161].

The crucial assumptions of this protocol are:

- The system is considered to be a degenerate 4LS. In realistic experimental conditions, this can be achieved by applying a magnetic field with a modulus that is sufficiently weak to ensure that the Zeeman effect only causes a level splitting comparable to the spectral linewidth, thereby maintaining the (quasi)degeneracy of the 4LS [75, 63]. This is considered in the model we proposed in Sec. 5.2.1, hence limiting its range of validity to weak magnetic fields.

- The magnetic field acting on the ground state $|\uparrow\rangle, |\downarrow\rangle$ is assumed to be perfectly aligned along the $x-$direction: $\hat{n}_g = \hat{x}$.

- It is implicitly assumed that the Larmor frequencies of the ground and excited states are the same: $r_{ge} = 1$.

- Lastly, we assume the feasibility of measuring the last emitted photon to decouple the spin state and rely on the fact that this measurement allows

us to accurately infer the spin state. Resonant π-pulses present a significant experimental challenge as the input and output fields have the same frequency. To overcome this limitation, a different excitation technique based on acoustic phonon-assisted excitation has been recently employed in Ref. [75]. By using a slightly blue-detuned laser, it has been demonstrated that the excited state $|\Uparrow\rangle$ or $|\Downarrow\rangle$ can be prepared with high fidelity, effectively acting as $\pi-$pulses. After reaching the excited state, the system relaxes, and under the condition that $\gamma^{-1} \ll \Omega^{-1}$, i.e., the system decays before it has time to precess in the excited state. Hence, another important ratio must be considered,

$$r_{\Omega\gamma} = \frac{\Omega}{\gamma} \tag{5.12}$$

If the preparation is $|\Uparrow\rangle$, a right-polarized photon (R-photon) is emitted, and its detection indicates that the spin is $|\uparrow\rangle$, initiating the timer to let the system precess to achieve the desired superposition state, Eq. (5.7).

In the following section, we solve the model proposed in Sec. 5.2.1 incorporating all these intrinsic realistic imperfections, and subsequently we reexamine the Lindner-Rudolph protocol (LRP) based on the obtained solution.

Our objective is to investigate the fidelity between the target superposition state and the real state of the system when $\pi-$pulses are applied, considering the relevant parameters and realistic imperfections (the step highlighted in red in Eq. (5.10)). Errors in this step accumulate during the process deteriorating the cluster state that is built.

Let us collect the important parameters:

1. The ratio between the Larmor frequencies of the ground state, Ω_g, and excited state, $\Omega_e \equiv \Omega$:

$$r_{ge} = \frac{\Omega_g}{\Omega}. \tag{5.13}$$

2. The direction of the magnetic field acting on the ground state, represented by the normalized vector

$$\hat{n}_g = (n_x, n_y, n_z), \ |n_g| = 1. \tag{5.14}$$

3. The ratio between the vacuum decay rate, denoted as γ, and the Larmor frequency in the excited state denoted as Ω:

$$r_{\Omega\gamma} = \frac{\Omega}{\gamma}. \tag{5.15}$$

The ideal protocol described in this section assumes that the following three conditions are fulfilled:

i. $r_{ge} = 1$,

ii. $\hat{n}_g = \hat{x} = (1, 0, 0)$, hence considering the modulus of the inner product: $\langle \hat{n}_g \cdot \hat{x} \rangle = 1$, and

iii. $r_{\Omega\gamma} = \frac{\Omega}{\gamma} \ll 1$.

These parameters form the foundation for an optimally functioning protocol. Any deviations from these ideal conditions are anticipated to lead to a deterioration of the protocol and compromise the quality of the generated cluster state.

We address two pragmatic questions:

- How do the deviations from the ideal conditions defined by (i)-(iii) impact the protocol? For that, we must study the impact of these parameters in evolving the system to the correct superposition state when the (effective) $\pi-$pulse is applied.
- How reliable is the measurement of the emitted photon to infer the state of the spin? This is quantified by the cBhat.

To answer these questions we solve the joint dynamics of the 4LS and light with the collisional model.

5.2.3 Collisional model

Under the assumption of a weak magnetic field, we may set a new notation decoupling the spin and energy degrees of freedom to solve the dynamics. We define the following mapping:

$$\begin{aligned} |\Uparrow\rangle &\to |e\rangle \otimes |\uparrow_z\rangle \\ |\Downarrow\rangle &\to |e\rangle \otimes |\downarrow_z\rangle \\ |\uparrow\rangle &\to |g\rangle \otimes |\uparrow_z\rangle \\ |\downarrow\rangle &\to |g\rangle \otimes |\downarrow_z\rangle. \end{aligned} \tag{5.16}$$

In this mapping, $|g\rangle$ and $|e\rangle$ represent the energy degrees of freedom (DOFs), while $|\downarrow_z\rangle$ and $|\uparrow_z\rangle$ represent the spin DOFs. It is important to note that the *mathematical spin* $|\uparrow_z\rangle$ has a sub-index z that distinct it from the *physical electron spin* denoted by $|\uparrow\rangle$.

We define the following lowering operators:

$$\begin{aligned} s &= |\downarrow_z\rangle\langle\uparrow_z|, \\ \sigma &= |g\rangle\langle e|. \end{aligned} \tag{5.17}$$

The states with spin $|\uparrow_z\rangle$ are connected through a right-polarized field, while the states with $|\downarrow_z\rangle$ are connected through a left-polarized field. Additionally, we define the Pauli operators for each subsystem in the usual manner: $s_z = |\uparrow_z\rangle\langle\uparrow_z| - |\downarrow_z\rangle\langle\downarrow_z|$ and $\sigma_z = |e\rangle\langle e| - |g\rangle\langle g|$, for instance.

The Hamiltonian describing the system is given by Eq. (4.2) with the addition of Eq. (5.1):

$$H = H_{\text{wg}} + (H_{\text{en}} + H_{\text{B}} + V_{\text{L}} + V_{\text{R}}), \tag{5.18}$$

where the bare Hamiltonians are defined as:

$$H_{\text{en}} = \omega_0 \sigma^\dagger \sigma \tag{5.19}$$

$$H_{\text{wg}} = \sum_{j=\text{R,L}} \sum_{k=0}^{\infty} \omega_{j,k} a_{j,k}^\dagger a_{j,k} \tag{5.20}$$

Here, $a_{j,k}$ represents the annihilation operator of a photon with polarization j and momentum k (with frequency $\omega_{j,k}$). They obey the usual bosonic algebra $[a_{j,k}, a_{i,q}^\dagger] = \delta_{ji}\delta_{kq}$, where δ_{ij} is the Dirac delta. Using Eq. (5.16), the magnetic field Hamiltonian in Eq. (5.1) can be cast as:

$$H_{\text{B}} = \frac{\Omega}{2} \left(r_{ge} |g\rangle\langle g| \otimes \hat{n}_g \cdot \vec{s} + |e\rangle\langle e| \otimes s_x \right), \tag{5.21}$$

$$V_{\text{L(R)}} = i g_0 \sum_{k=0}^{\infty} \left(a_{L(R),k}^\dagger \sigma - \sigma^\dagger a_{L(R),k} \right) \otimes |\downarrow_z (\uparrow_z)\rangle\langle\downarrow_z (\uparrow_z)|. \tag{5.22}$$

We now move to the interaction picture with respect to $H_0 = H_{\text{wg}}$, this choice is convenient because the spin operators do not gain a time dependency. The resultant interaction picture Hamiltonian is:

$$V_{\text{L(R)}} \to V_{\text{L(R)}}(t) = i\sqrt{\gamma} \left[\left(b_L^\dagger(t)\sigma - \sigma^\dagger b_L(t) \right) \right] \otimes |\downarrow_z (\uparrow_z)\rangle\langle\downarrow_z (\uparrow_z)|. \tag{5.23}$$

Here, the vacuum decay rate is given by:

$$\gamma = g_0^2 \delta. \tag{5.24}$$

We define the temporal bosonic operators for each polarization $p \in \{L, R\}$ as:

$$b_p(t) = \frac{1}{\sqrt{\delta}} \sum_k e^{-i\omega_{p,k} t} a_{p,k}, \tag{5.25}$$

where $\delta = L/v$ represents the density of modes in the waveguide, and it satisfies the bosonic algebra $[b_p(t), b_{p'}(t')] = \delta_{p,p'}\delta(t - t')$. Rearranging the terms, we obtain:

$$H_{\text{en}} + H_B = \sigma^\dagger \sigma \otimes \hat{C}_e(\vec{s}) - \sigma\sigma^\dagger \otimes \hat{C}_g(\vec{s}), \tag{5.26}$$

where

$$\hat{C}_e(\vec{s}) = \omega_0 + \frac{\Omega}{2} s_x, \tag{5.27}$$

$$\hat{C}_g(\vec{s}) = r_{ge} \frac{\Omega}{2} \hat{n}_g \cdot \vec{s}. \tag{5.28}$$

We introduce the (mathematical) spin rotation operators:

$$\mathscr{R}_g(t) = \exp\left\{-i\hat{C}_g(\vec{s})t\right\} \tag{5.29}$$
$$\mathscr{R}_e(t) = \exp\left\{-i\hat{C}_e(\vec{s})t\right\}.$$

The first operator is associated with rotations in the ground state, while the second operator corresponds to rotations in the excited state. These definitions will prove valuable for our subsequent analysis.

5.2.4 Realistic LRP

The goal of our study is to benchmark the fidelity of the building block of the LRP [68], specifically the mapping between the spin state and the photon state [162].

The crucial step, as we have seen in the Sec. 5.2.2 is the preparation of the system in the superposition state and the subsequent decoupling of the spin by measuring the polarization of the last emitted photon. We review the process from the very beginning where the preparation of the superposition state is concerned. Based on Ref. [75] it is known that a $|\Uparrow (\Downarrow)\rangle$ state can be prepared with high fidelity. Hence, the system is left to decay and once a R(L)-photon is detected it is known that the state at that time is $|\uparrow (\downarrow)\rangle$, this starts the clock for the spin precession. Let's analyze this situation:

1. At time $t = 0^-$, the 4LS and field are prepared in the state

$$|\Psi^{\uparrow_z}(0^-)\rangle = |e\rangle \otimes |\uparrow_z\rangle \otimes |\emptyset\rangle \otimes |\emptyset\rangle. \tag{5.30}$$

2. In a very short time interval $\delta t = \gamma^{-1}$ the system decays, emitting a single right (R) circularly polarized photon,

$$|\Psi^{\uparrow_z}(\delta t)\rangle = |g\rangle \otimes |\uparrow_z\rangle \otimes |1_{\mathrm{R}}\rangle_0 \otimes |\emptyset\rangle_0, \tag{5.31}$$

   where $\Omega\delta t \to 0^+$. Here, $|1_{\mathrm{R}}\rangle_0$ represents the heralding photon. It informs that the system is in the state $|g\rangle \otimes |\uparrow_z\rangle$, starting the clock.

3. Once in the ground state, the spin is allowed to precess freely under the action of the magnetic field for a time until t_{pulse}. Ideally, the interval is,

$$t_{\mathrm{pulse}} = t_g = \frac{\pi}{2r_{ge}\Omega}. \tag{5.32}$$

   During this time the state evolves to:

$$|\Psi^{\uparrow_z}(0^+)\rangle \xrightarrow{t_g} |\Psi^{\uparrow_z}(t_g)\rangle = |g\rangle \otimes |-i_y\rangle \otimes |1_{\mathrm{R}}\rangle_0 \otimes |\emptyset\rangle_0, \tag{5.33}$$

   where $|-i_y\rangle = (|\uparrow_z\rangle - i|\downarrow_z\rangle)/\sqrt{2}$.

4. At time t_{pulse}, the effective $\pi-$pulse is applied. The system is excited and rapidly decays to the ground state emitting an R and an L right-polarized

photons in an infinitesimally short decay time $\varepsilon \to 0^+$, then:

$$|\Psi^{\uparrow_z}(t_g+\varepsilon)\rangle = |g\rangle \otimes \left[\frac{|\uparrow_z\rangle|1_{\mathrm{R}}\rangle_1|\emptyset\rangle_1 - i|\downarrow_z\rangle|\emptyset\rangle_1|1_{\mathrm{L}}\rangle_1}{\sqrt{2}}\right] \otimes |1_{\mathrm{R}}\rangle_0 \otimes |\emptyset\rangle_0 \quad (5.34)$$

where the sub-index "1" in the photonic states refers to the first emission event. This defines the building block of the LRP, corresponding to the line highlighted in red of Eq. (5.10).

A crucial observation is that the time interval of the spin precession during step 3 is essential. In ideal conditions, described by the conditions (i)-(iii) the state at time t_g is $|-i\rangle$, which serves as our target state. But in the presence of parasitic magnetic fields this state is not perfectly achieved at this time.

Next, we solve the joint wave function of the SPI subjected to the magnetic field as described in the experiments of Refs. [75, 63]. The main advantage of this approach is that it enables us to derive an analytical expression for the fidelity of the system as a function of time and the parameters $r_{\Omega\gamma}, r_{ge}$ and $\hat{n}_g$.

5.3 Spontaneous emission solution

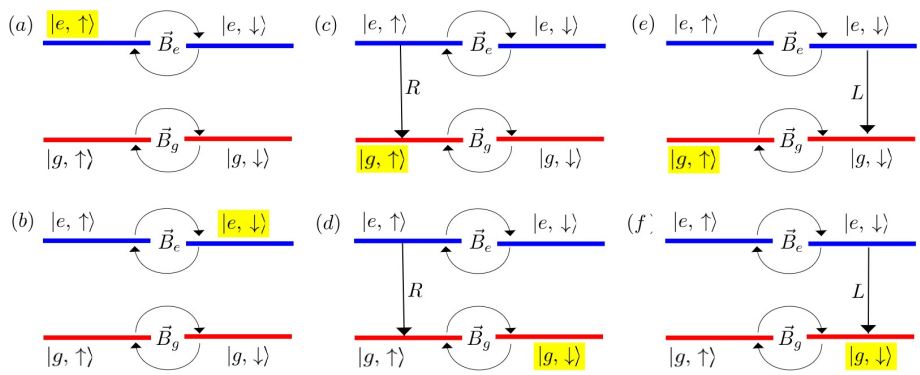

Figure 5.2: **Possible processes.** Assuming the spin is initially in the excited state $|e,\zeta\rangle$, the presence of the magnetic field allows for the following processes: (a) It precesses in the excited state without emitting any photon, resulting in the state $|e,\uparrow\rangle$. (b) It precesses in the excited state without emitting any photon, resulting in the state $|e,\downarrow\rangle$. (c) It processes in the excited state for a duration of u and reaches the intermediate spin state $|e,\uparrow\rangle$, emitting a R-polarized photon. Then, it continues to precess in the ground state for a duration of $t-u$ and ends in the state $|g,\uparrow\rangle$. (d) It precesses in the excited state for a duration of u and reaches the intermediate spin state $|e,\uparrow\rangle$. Then, it precesses in the ground state for a duration of $t-u$ and ends in the state $|g,\downarrow\rangle$. (e) It precesses in the excited state for a duration of u and reaches the intermediate spin state $|e,\downarrow\rangle$, emitting an L-polarized photon. Then, it continues to precess in the ground state for a duration of $t-u$ and ends in the state $|g,\uparrow\rangle$. (f) It precesses in the excited state for a duration of u and reaches the intermediate spin state $|e,\downarrow\rangle$, emitting a R-polarized photon. Then, it precesses in the ground state for a duration of $t-u$, flips the spin, and ends in the state $|g,\downarrow\rangle$.

We assume the system is initially in the state $|e\rangle \otimes |\zeta\rangle \equiv |e, \zeta\rangle$ with a specific spin $\zeta \in \{\uparrow_z, \downarrow_z\}$, and the field is initially in the vacuum state $|\emptyset, \emptyset\rangle$. In this situation, two processes can occur:

1. Spontaneous emission, leading to the creation of an R or L photon, i.e., right and left circularly polarized photon respectively, and

2. Coherent precession of the (mathematical) spin, $|\uparrow_z\ (\downarrow_z)\rangle$, in the excited and ground states induced by the magnetic field.

To analyze the dynamics of the system, we employ the collisional model, following the approach outlined in Chap. 2 by writing a wave function *Ansatz* and finding the necessary coefficients. The detailed calculations can be found in App. D.

By starting from the initial state $|\Psi^\zeta(0)\rangle = |e, \zeta, \emptyset, \emptyset\rangle$, we can determine the resulting wave function at any time t as

$$\begin{aligned}
|\Psi^\zeta(t)\rangle = &\left(\exp\left\{-\frac{\gamma}{2}t\right\} \langle\uparrow_z |\mathscr{R}_e(t)|\zeta\rangle\right) |e\rangle|\uparrow_z\rangle|\emptyset\rangle|\emptyset\rangle \text{ (Fig. 5.2a)} \\
&+ \left(\exp\left\{-\frac{\gamma}{2}t\right\} \langle\downarrow_z |\mathscr{R}_e(t)|\zeta\rangle\right) |e\rangle|\downarrow_z\rangle|\emptyset\rangle|\emptyset\rangle \text{ (Fig. 5.2b)} \\
&+ \left(\int_0^t du\ \langle\uparrow_z |\mathscr{R}_g(t-u)|\uparrow_z\rangle \sqrt{\gamma} b_{\mathrm{R}}^\dagger \exp\left\{-\frac{\gamma}{2}u\right\} \langle\uparrow_z |\mathscr{R}_e(u)|\zeta\rangle\right) |g\rangle|\uparrow_z\rangle|\emptyset\rangle|\emptyset\rangle \text{ (Fig. 5.2c)} \\
&+ \left(\int_0^t du\ \langle\uparrow_z |\mathscr{R}_g(t-u)|\downarrow_z\rangle \sqrt{\gamma} b_{\mathrm{L}}^\dagger \exp\left\{-\frac{\gamma}{2}u\right\} \langle\downarrow_z |\mathscr{R}_e(u)|\zeta\rangle\right) |g\rangle|\uparrow_z\rangle|\emptyset\rangle|\emptyset\rangle \text{ (Fig. 5.2d)} \\
&+ \left(\int_0^t du\ \langle\downarrow_z |\mathscr{R}_g(t-u)|\uparrow_z\rangle \sqrt{\gamma} b_{\mathrm{R}}^\dagger \exp\left\{-\frac{\gamma}{2}u\right\} \langle\uparrow_z |\mathscr{R}_e(u)|\zeta\rangle\right) |g\rangle|\downarrow_z\rangle|\emptyset\rangle|\emptyset\rangle \text{ (Fig. 5.2e)} \\
&+ \left(\int_0^t du\ \langle\downarrow_z |\mathscr{R}_g(t-u)|\downarrow_z\rangle \sqrt{\gamma} b_{\mathrm{L}}^\dagger \exp\left\{-\frac{\gamma}{2}u\right\} \langle\downarrow_z |\mathscr{R}_e(u)|\zeta\rangle\right) |g\rangle|\downarrow_z\rangle|\emptyset\rangle|\emptyset\rangle \text{ (Fig. 5.2f)}
\end{aligned} \tag{5.35}$$

The wave function presented above has a straightforward physical interpretation. The first and second lines are represented schematically in 5.2(a) and (b) respectively, describe the Larmor precession between the state $|\zeta\rangle$ and the spin state $|\uparrow_z\ (\downarrow_z)\rangle$ in the excited state. The third line showed in 5.2(c), represents the Larmor precession in the excited state for a duration u, starting from the initial state $|\zeta\rangle$ and transitioning to the intermediate spin state $|\uparrow_z\rangle$. This is followed by a jump to the ground state, resulting in the creation of an R-photon (depicted in orange). Finally, the wave function describes the Larmor precession in the ground state from the intermediate spin state $|\uparrow_z\rangle$ to the final spin state $|\uparrow_z\rangle$(in blue). Similar interpretations can be made for the remaining lines. Consequently, the wavefunction represents a coherent superposition of various processes, each of which is illustrated in Fig. 5.2.

To validate our model, we employ it to fit the data obtained from the experiment reported in Ref. [75]. In this experiment, the system is excited using acoustic phonons instead of resonant excitation. The use of a slightly blue-detuned pulse allows the selection of the polarization of optical transitions and facilitates the initialization and measurement of single spin states. The authors of Ref. [75] examine the coherence of the trion in a low transverse magnetic field and monitor the spin Larmor precession during the radiative emission process of the excited state. Our model is capable of

fitting this data, as demonstrated in Fig. 5.3. By utilizing Eq. (5.35), we compute the intensities for a spin initially in the $|\uparrow_z\rangle$ state, given by:

$$I_R^{\uparrow_z}(t) = \langle b_R^\dagger b_R(t)\rangle = \gamma \left|\exp\left\{-\frac{\gamma}{2}t\right\} \langle\uparrow_z |\mathscr{R}_e(t)|\uparrow_z\rangle\right|^2 = \gamma e^{-\gamma t}\cos^2\left(\frac{\Omega}{2}t\right), \tag{5.36}$$
$$I_L^{\uparrow_z}(t) = \langle b_L^\dagger b_L(t)\rangle = \gamma \left|\exp\left\{-\frac{\gamma}{2}t\right\} \langle\downarrow_z |\mathscr{R}_e(t)|\uparrow_z\rangle\right|^2 = \gamma e^{-\gamma t}\sin^2\left(\frac{\Omega}{2}t\right).$$

Here, the notation $I_{\text{Polarization}}^{\text{initial spin}}$ represents the intensities. The degree of circular polarization is given by:

$$DCP = \frac{I_R^{\uparrow_z} - I_L^{\uparrow_z}}{I_R^{\uparrow_z} + I_L^{\uparrow_z}} \tag{5.37}$$

Our model predicts:

$$DCP = \cos(\Omega t). \tag{5.38}$$

In Fig. 5.3, we compare these quantities with the experimental data presented in Figure 2 of Ref. [75]. The dashed black line represents the results of our closed model dynamics, neglecting any dephasing effects. We observe a remarkable agreement between the data points[1] and our analytical results, strongly corroborating the accuracy of our model. For details on the parameters, we refer to App. B.1. The importance of this figure is that it shows that the high hole spin Landé factor g_h allows a relatively weak magnetic field to be sufficient for the implementation of a large number of precession cycles during the time of spin coherence, which is longer than the trion lifetime $T_1^{(\text{trion})}$. Within these experimental conditions, it is possible to implement the LRP as reported in Ref. [63].

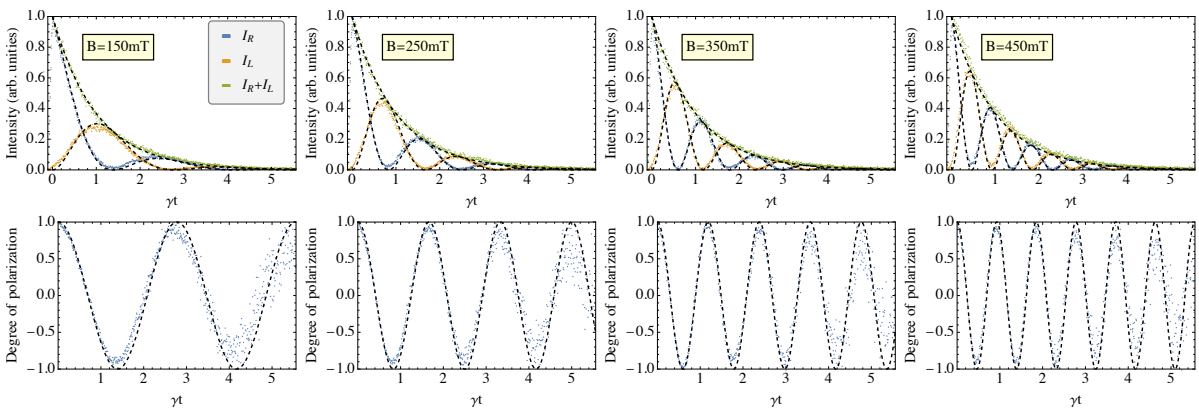

Figure 5.3: **Model validation.**This figure replicates Figure 2 from Ref. [75]. The dashed black line corresponds to the result of our closed model dynamics, neglecting any dephasing effects. In color we show the experimental data points, demonstrating a remarkable agreement with our analytical results. The parameters match those used in Ref. [75], with a vacuum decay rate of $\gamma = 1$, see App. B.1.

[1]The data belong to C2N-Paris and were kindly provided by the corresponding author of Ref. [75], who allowed the reproduction in this thesis.

5.4 Protocol benchmark: fidelity and cBhat

In this section, our main focus will be on studying spin dynamics using our analytical solution. To carry out this analysis, it is crucial to compute the reduced spin state, which is the primary objective of this section. When the system initially possesses spin ζ, $|\Psi^{\zeta}(0)\rangle = |\Phi(0)\rangle \otimes |\zeta\rangle$, where $|\Phi(0)\rangle$ is a general field and energy state[2]and is subjected to a magnetic field, the total wave function at time t can be represented as follows:

$$|\Psi^{\zeta}(t)\rangle = |\psi^{\zeta}_{\zeta}(t)\rangle|\zeta\rangle + |\eta^{\zeta}_{i}(t)\rangle|i\rangle, \quad \zeta(i) \in \{\uparrow_z (\downarrow_z), \downarrow_z (\uparrow_z)\}. \tag{5.39}$$

In the above expressions, $|\zeta\rangle$ and $|i\rangle$ denote the (mathematical) spin states, while $|\psi^{\zeta}_{\zeta}\rangle$ and $|\eta^{\zeta}_{i}\rangle$ correspond to the joint state of the field and energy. The superscript indicates the initial spin, while the subscript highlights the final spin state. Consequently, we can express the density matrix of the total state, $\rho^{\zeta}(t)$, as follows:

$$\begin{aligned}\rho^{\zeta}(t) = {} & |\psi^{\zeta}_{\zeta}\rangle\langle\psi^{\zeta}_{\zeta}|\otimes|\zeta\rangle\langle\zeta| + |\psi^{\zeta}_{\zeta}\rangle\langle\eta^{\zeta}_{i}|\otimes|\zeta\rangle\langle i| \\ & + |\eta^{\zeta}_{i}\rangle\langle\psi^{\zeta}_{\zeta}|\otimes|i\rangle\langle\zeta| + |\eta^{\zeta}_{i}\rangle\langle\eta^{\zeta}_{i}|\otimes|i\rangle\langle i|\end{aligned} \tag{5.40}$$

To obtain the reduced state, we perform a partial trace over the field and energy states (All) but the spin (sp), resulting in:

$$\begin{aligned}\rho^{\zeta}_{\mathrm{sp}}(t) &= \mathrm{tr}_{\mathrm{All/sp}}\{\rho^{\zeta}(t)\} \\ &= \langle\psi^{\zeta}_{\zeta}|\psi^{\zeta}_{\zeta}\rangle|\zeta\rangle\langle\zeta| + \langle\eta^{\zeta}_{i}|\psi^{\zeta}_{\zeta}\rangle|\zeta\rangle\langle i| \\ &+ \langle\psi^{\zeta}_{\zeta}|\eta^{\zeta}_{i}\rangle|i\rangle\langle\zeta| + \langle\eta^{\zeta}_{i}|\eta^{\zeta}_{i}\rangle|i\rangle\langle i|.\end{aligned} \tag{5.41}$$

where the cyclic property of the trace in the subspace of the field and energy states were used to obtain the reduced state. The elements of the matrix $\rho^{\zeta}_{\mathrm{sp}}(t)$ are given by the three overlaps:

$$\begin{aligned}\rho^{\zeta}_{\zeta\zeta} &= \langle\psi^{\zeta}_{\zeta}|\psi^{\zeta}_{\zeta}\rangle, \\ \rho^{\zeta}_{ii} &= \langle\eta^{\zeta}_{i}|\eta^{\zeta}_{i}\rangle, \\ \rho^{\zeta}_{i\zeta} &= \langle\eta^{\zeta}_{i}|\psi^{\zeta}_{\zeta}\rangle.\end{aligned} \tag{5.42}$$

[2]Although the results are going to be applied to the SE wavefunction, Eq. (5.35), they are general for any field.

Now, using the solution Eq. (5.35), we can compute the necessary overlaps for the case of $\zeta = \uparrow_z$ and $i = \downarrow_z$. We have:

$$
\begin{aligned}
|\psi^{\uparrow_z}_{\uparrow_z}\rangle &= \exp\{-\frac{\gamma}{2}t\}\langle\uparrow_z|\mathscr{R}_e(\vec{s},t)|\uparrow_z\rangle|e,\emptyset,\emptyset\rangle \\
&+ \sqrt{\gamma}\int_0^t du\langle\uparrow_z|\mathscr{R}_g(\vec{s},t-u)|\uparrow_z\rangle f^{(0),\uparrow}_{\uparrow,e}(u)b^\dagger_R(u)|g,\emptyset,\emptyset\rangle \\
&+ \sqrt{\gamma}\int_0^t du\langle\uparrow_z|\mathscr{R}_g(\vec{s},t-u)|\downarrow_z\rangle f^{(0),\uparrow}_{\downarrow,e}(u)b^\dagger_L(u)|g,\emptyset,\emptyset\rangle
\end{aligned}
\tag{5.43}
$$

$$
\begin{aligned}
|\eta^{\uparrow_z}_{\downarrow_z}\rangle &= \exp\{-\frac{\gamma}{2}t\}\langle\downarrow_z|\mathscr{R}_e(\vec{s},t)|\uparrow_z\rangle|e,\emptyset,\emptyset\rangle \\
&+ \sqrt{\gamma}\int_0^t du\langle\downarrow_z|\mathscr{R}_g(\vec{s},t-u)|\uparrow_z\rangle f^{(0),\uparrow}_{\uparrow,e}(u)b^\dagger_R(u)|g,\emptyset,\emptyset\rangle \\
&+ \sqrt{\gamma}\int_0^t du\langle\downarrow_z|\mathscr{R}_g(\vec{s},t-u)|\downarrow_z\rangle f^{(0),\uparrow}_{\downarrow,e}(u)b^\dagger_L(u)|g,\emptyset,\emptyset\rangle
\end{aligned}
\tag{5.44}
$$

where $f^{(0),i}_{j,e}(u)$ is the coefficient of zero photon emission connecting the spin states i to j in the excited state e (see App. D).We can easily compute the overlaps, resulting in:

$$
\begin{aligned}
\rho^{\uparrow_z}_{\uparrow_z\uparrow_z} &= \exp\{-\gamma t\}|\langle\uparrow_z|\mathscr{R}_e(\vec{s},t)|\uparrow_z\rangle|^2 \\
&+ \gamma\int_0^t du|\langle\uparrow_z|\mathscr{R}_g(\vec{s},t-u)|\uparrow_z\rangle|^2|f^{(0),\uparrow}_{\uparrow,e}(u)|^2 + \gamma\int_0^t du|\langle\uparrow_z|\mathscr{R}_g(\vec{s},t-u)|\downarrow_z\rangle|^2|f^{(0),\uparrow}_{\downarrow,e}(u)|^2 \\
\rho^{\uparrow_z}_{\downarrow_z\downarrow_z} &= \exp\{-\gamma t\}|\langle\downarrow|\mathscr{R}_e(\vec{s},t)|\uparrow\rangle|^2 \\
&+ \gamma\int_0^t du|\langle\downarrow_z|\mathscr{R}_g(\vec{s},t-u)|\uparrow_z\rangle|^2|f^{(0),\uparrow}_{\uparrow,e}(u)|^2 + \gamma\int_0^t du|\langle\downarrow_z|\mathscr{R}_g(\vec{s},t-u)|\downarrow_z\rangle|^2|f^{(0),\uparrow}_{\downarrow,e}(u)|^2 \\
\rho^{\uparrow_z}_{\downarrow_z\uparrow_z} &= \exp\{-\gamma t\}\langle\downarrow_z|\mathscr{R}_e(\vec{s},t)|\uparrow_z\rangle^*\langle\uparrow_z|\mathscr{R}_e(\vec{s},t)|\uparrow_z\rangle \\
&+ \gamma\int_0^\infty du\langle\downarrow_z|\mathscr{R}_g(\vec{s},t-u)|\uparrow_z\rangle^*\langle\uparrow_z|\mathscr{R}_g(\vec{s},t-u)|\uparrow_z\rangle|f^{(0),\uparrow}_{\uparrow,e}(u)|^2 \\
&+ \gamma\int_0^\infty du\langle\downarrow_z|\mathscr{R}_g(\vec{s},t-u)|\downarrow_z\rangle^*\langle\uparrow_z|\mathscr{R}_g(\vec{s},t-u)|\downarrow_z\rangle|f^{(0),\uparrow}_{\downarrow,e}(u)|^2.
\end{aligned}
\tag{5.45}
$$

Here, z^* represents the complex conjugation. This procedure provides the reduced state in the mathematical spin subspace, but not in the physical spin subspace that corresponds to the ground state. To find the physical spin state, we assume that spontaneous emission has occurred, $\exp\{-\gamma t\} \to 0$, and normalize the density matrix accordingly.

5.4.1 Fidelity

The fidelity between two quantum states, ρ_a and ρ_b, is defined as [23]

$$
\mathscr{F}(\rho_a,\rho_b) = \mathrm{tr}\{\sqrt{\sqrt{\rho_a}\rho_b\sqrt{\rho_a}}\}, \tag{5.46}
$$

and it measures how similar are ρ_a and ρ_b.

A general qubit state can be expressed using the Pauli basis as

$$\rho_{\text{gen}} = \frac{1}{2}\left(1 + r_x s_x + r_y s_y + r_z s_z\right), \tag{5.47}$$

where $r_i = \langle s_i \rangle$, represents the expectation value of the Pauli operator s_i (with $i = x, y, z$). We consider ρ_{gen} to be the state of the mathematical spin, which corresponds to the physical electron state after the system has fully relaxed to the ground state. For the physical spin, assuming it initially started in the state $|g\rangle \otimes |\uparrow_z\rangle$, the target state is given by

$$\rho^{\uparrow}_{\text{target}} = |-i\rangle\langle -i| = \frac{1}{2}\begin{bmatrix} 1 & i \\ -i & 1 \end{bmatrix} \tag{5.48}$$

The fidelity between ρ_{gen} and $\rho^{\uparrow}_{\text{target}}$ is

$$\begin{aligned} \mathscr{F}(\rho_{\text{gen}}, \rho^{\uparrow}_{\text{target}}) &= \frac{1 - r_y}{2} \\ &= \frac{1}{2} + \Im\left\{\rho^{\uparrow}_{\downarrow\uparrow}\right\}, \end{aligned} \tag{5.49}$$

where we used that $r_y = \text{tr}\{\sigma_y \rho^{\uparrow}_{\text{sp}}\} = -2\Im\left\{\rho^{\uparrow}_{\uparrow\downarrow}\right\}$. We can analytically compute the fidelity for a time $t \gg \gamma^{-1}$, where the spontaneous emission process has concluded and the mathematical spins ($\uparrow_z$ /$\downarrow_z$) accurately represent the physical spins ($\uparrow$ /$\downarrow$). The fidelity has a cumbersome analytical expression, it might be found in the Mathematica notebook available in the dedicated GitHub repository [76]. We can find a simple approximated expression by neglecting the terms of order $r^3_{\Omega\gamma}$ or higher, leading to the approximated expression:

$$\mathscr{F}_{\text{approx}} = \frac{1}{2} + \frac{n_x}{2} f_x\left(r_{ge}, r_{\Omega\gamma}; t\right) + \frac{n_y n_z}{2} f_{yz}\left(r_{ge}, r_{\Omega\gamma}; t\right), \tag{5.50}$$

where $f_x(\Omega, r_{ge}, r_{\Omega\gamma}; t)$ and $f_{yz}(\Omega, r_{ge}, r_{\Omega\gamma})$ are defined as follows:

$$f_x(r_{ge}, r_{\Omega\gamma}, \Omega; t) = k_1(r_{ge}, r_{\Omega\gamma})\cos(r_{ge}\Omega t) - k_2(r_{ge}, r_{\Omega\gamma})\sin(r_{ge}\Omega t), \tag{5.51}$$

and

$$f_{yz}(r_{ge}, r_{\Omega\gamma}, \Omega) = k_3(r_{ge}, r_{\Omega\gamma}) + k_4(r_{ge}, r_{\Omega\gamma})\cos(r_{ge}\Omega t) + k_5(r_{ge}, r_{\Omega\gamma})\sin(r_{ge}\Omega t) + \mathscr{O}(r_{\Omega\gamma})^3 \tag{5.52}$$

with the coefficients given by:

$$
\begin{aligned}
k_1(r_{ge}, r_{\Omega\gamma}) &= -\frac{r_{ge} r_{\Omega\gamma}\left[1 + (r_{ge}^2 - 1) r_{\Omega\gamma}^2\right]}{2(1 + r_{ge}^2) r_{\Omega\gamma}^2 + (r_{ge}^2 - 1) r_{\Omega\gamma}^2} \\
k_2(r_{ge}, r_{\Omega\gamma}) &= \frac{1 + (1 + r_{ge}^2) r_{\Omega\gamma}^2}{1 + 2(1 + r_{ge}^2) r_{\Omega\gamma}^2 + (r_{ge}^2 - 1) r_{\Omega\gamma}^2} \\
k_3(r_{ge}, r_{\Omega\gamma}) &= -\frac{1 + 2(r_{ge}^2 + 1) r_{\Omega\gamma}^2}{(1 + r_{\Omega\gamma}^2)\left[1 + (r_{ge}^2 - 1)^2 r_{\Omega\gamma}^2\right](r_{ge}^2 + 1) r_{\Omega\gamma}^2} \\
k_4(r_{ge}, r_{\Omega\gamma}) &= \frac{r_{ge} r_{\Omega\gamma}}{(1 + r_{\Omega\gamma}^2)\left[1 + (r_{ge} - 1)^2 r_{\Omega\gamma}^2\right]\left[1 + (r_{ge} + 1)^2 r_{\Omega\gamma}^2\right]} \\
k_5(r_{ge}, r_{\Omega\gamma}) &= \frac{1 + (1 + r_{ge}^2) r_{\Omega\gamma}^2}{\left[1 + 2(r_{ge}^2 + 1) r_{\Omega\gamma}^2 + (r_{ge}^2 - 1) r_{\Omega\gamma}^2\right]}
\end{aligned}
\tag{5.53}
$$

It is worth noting that the expression (5.50) has a term proportional to the $x-$component of $\hat{n}_g$ and a component proportional to the components y and z.

Armed with these analytical expressions, we can examine the behavior of fidelity for different parameters. Figure 5.4 illustrates our investigation of the case where both the electron and hole solely respond to the external magnetic field, $\hat{n}_g = \hat{x}$. We compute the fidelity for t_g. In Fig. 5.4(a), we present contour plot illustrating the relationship between r_{ge}, $r_{\Omega\gamma}$, and the fidelity for t_g. In Fig. 5.4(b), we consider the scenario where the Larmor frequencies are equal ($r_{ge} = 1$) for t_g, respectively.

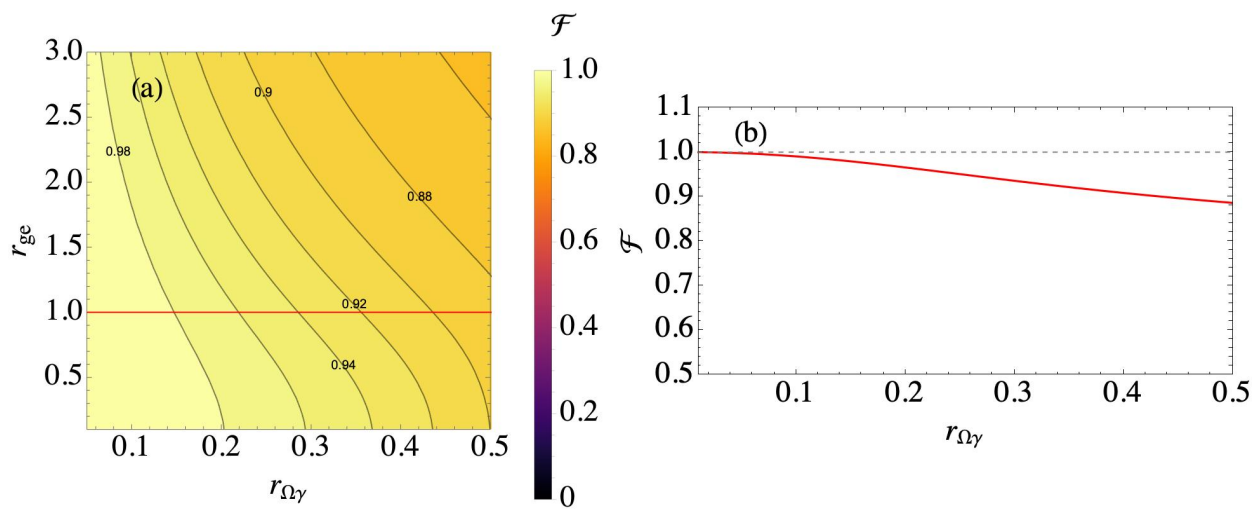

Figure 5.4: **Fidelity at the time of re-excitation with perfect magnetic field alignment.** The plots show the fidelity of the spin state for the time of re-excitation. (a) Contour plot: For t_g given by Eq. (5.32) varying r_{ge} and $r_{\Omega\gamma}$. (b) Ideal case: $t_g = \pi/2r_{ge}\Omega$, $r_{ge} = 1$, $\hat{n}_g = \hat{x}$. The horizontal gray line hallmarks the unity fidelity. The vacuum decay rate is $\gamma = 1$.

Next, we investigate the impact of the parasitic magnetic field on the interaction with the electronic spin. In Fig. 5.5 we examine the scenario where the electron

is subjected to a field with components $\hat{n}_g = (1, n, n)/|(1, n, n)|$, with the same component in the y and z directions. We compute the fidelities for t_g.

In Figs. 5.5(a), 5.5(b), and 5.5(c) we consider the ratios of the Larmor frequencies to be $(1, 1.5, 2.5)$, respectively, and present a contour plot of the fidelity for t_g. Here, we observe that the region where the fidelity exceeds 0.95 shrinks as r_{ge} increases, and the lower the inner product $\langle \hat{n}_g, \hat{x} \rangle$ the worse the fidelity, that's to say the shorter the x component of the magnetic field in the ground state, the worst will be the fidelity. This is expected, as it signifies that the parasitic fields are tilting the direction of precession and taking the system to an undesired state.

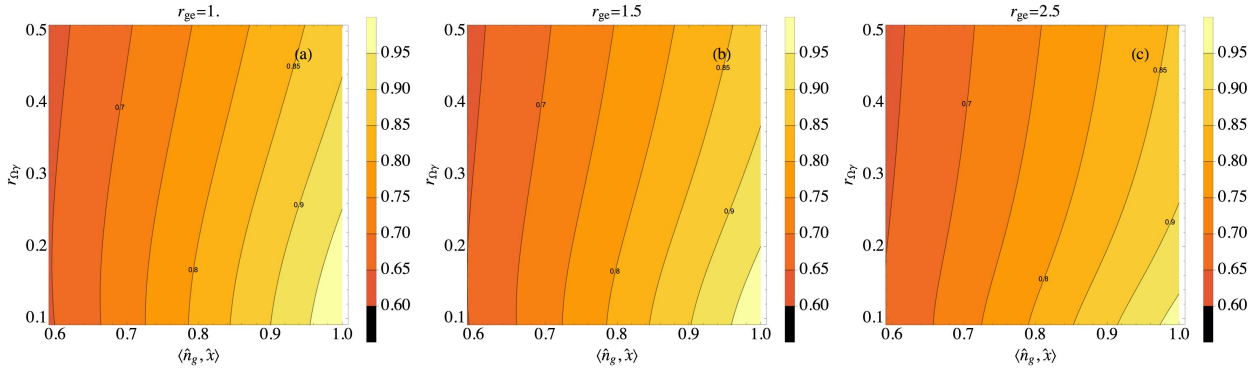

Figure 5.5: **Fidelity at the time of re-excitation influenced by parasitic fields.** The Larmor frequency ratio is denoted by r_{ge}, where Ω. The vacuum decay rate is set to $\gamma = 1$. The unity vector $\hat{n}_g = (1, n, n)/|(1, n, n)|$ represents the direction of the magnetic field. We present fidelity t_g, given by Eq. (5.32), for (a) $r_{ge} = 1$, (b) $r_{ge} = 1.5$, and (c) $r_{ge} = 2.5$

5.4.2 cBhat

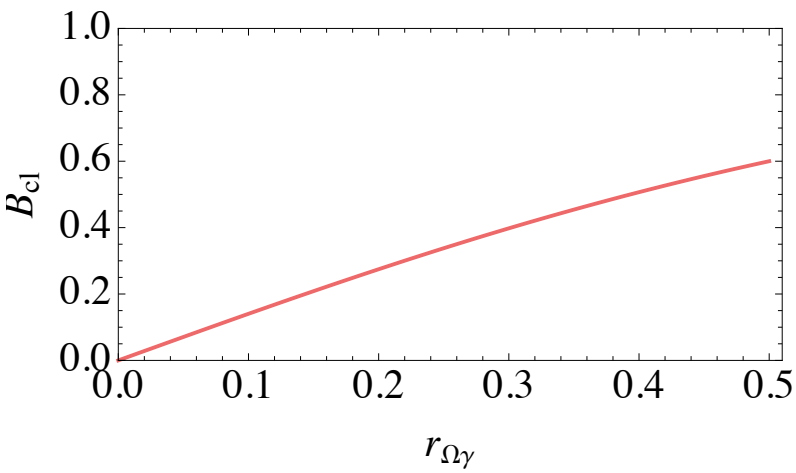

Figure 5.6: **cBhat for the Lindner-Rudolph protocol.**

To conclude our analysis, we evaluate the precision of the spin decoupling stage by measuring the last emitted photon using the cBhat method, as described in Eq.

(1.18). The intensity functions can be expressed as follows:

$$I_R^{\uparrow_z}(t) = I_L^{\downarrow_z}(t) = \gamma e^{-\gamma t} \cos^2\left(\frac{\Omega}{2}t\right). \tag{5.54}$$

The cBhat is computed based on the probabilities of a click event:

$$p_\uparrow(\text{click}) = \int_0^{t_{\text{click}}} dt\, I_R^{\uparrow_z}(t), \tag{5.55}$$

where t_{click} represents the interval between the excitation pulse and the final click in the detector. If $t \gg \gamma^{-1}$ the probability becomes:

$$p_\uparrow(\text{click}) = \frac{1}{2}\left[1 + \frac{1}{1 + r_{\Omega\gamma}^2}\right], \tag{5.56}$$

The cBhat can be expressed as:

$$\begin{aligned} B_{\text{cl}} &= 2\sqrt{p_\uparrow(\text{click})\,[1 - p_\uparrow(\text{click})]}, \\ &= r_{\Omega\gamma}\frac{\sqrt{2 + r_{\Omega\gamma}^2}}{1 + r_{\Omega\gamma}^2}. \end{aligned} \tag{5.57}$$

In the ideal limit $r_{\Omega\gamma} \ll 1$, we have

$$B_{\text{cl}} \approx \sqrt{2} r_{\Omega\gamma} \tag{5.58}$$

The accuracy of the measurement is primarily influenced by the ratio $r_{\Omega\gamma}$. The cBhat is directly proportional to this quantity, meaning that lower ratios result in more distinguishable probability distributions. The fundamental limitation arises from the fact that the decay process occurs with a finite time γ^{-1}. The ideal condition (iii) assumes an immediate decay upon excitation; however, if $r_{\Omega\gamma} \ll 1$ is not fulfilled, a fundamental error related to spin decoupling emerges.

5.5 Discussion and perspectives

In this chapter, we made a comprehensive analysis of the LRP within the realistic experimental conditions [75, 63]. We took into account the critical intrinsic imperfections that affect the protocol's performance, including the ratio of Larmor frequencies, r_{ge}, and the presence of parasitic magnetic fields that affect the electronic spin state, $\hat{n}_g$. Through the use of the collisional model, we solved the dynamics of the emitter and the field, with a particular focus on the spontaneous emission process.

To verify the validity of our model, we compared its predictions with experimental data presented in previous studies in Fig. 5.3. The agreement between our model's results and the experimental data serves as a robust validation, showing the accuracy and reliability of our proposed model. This validation step holds significant weight

as it demonstrates the model's capability to capture the essential aspects of the physical system under investigation.

Furthermore, by deriving analytical expressions for the spin state and thoroughly investigating the fidelity of the process, we gained insights into the behavior of spin precession during the protocol. This analysis plays an important role in enhancing the quality of generated linear cluster states. Armed with this knowledge, experimentalists can make informed decisions regarding the timing of pulse delivery, leading to improved outcomes in practical implementations.

There are promising prospects for conducting characterization experiments in the continuous wave (CW) regime, where the initial state of the field is coherent. This direction opens up possibilities to explore the cross-correlation function between circular polarizations, such as $g^{(2)}_{\mathrm{RL}}(\tau)$, which can provide valuable insights into charge dynamics and coherence times. Such experiments hold paramount importance and the framework presented in this chapter can be readily extended to address these scenarios, enriching our understanding and control over the system and the protocol.

Conclusions and perspectives

"It's gone. It's done

Yes, Mr. Frodo. It's over now."– Frodo Baggins and Samwise Gamgee, Lord of the rings - The return of the king

The primary contribution of this thesis is centered around employing a comprehensive Hamiltonian solution for physical systems relevant to quantum technological applications. Our focus primarily revolved around exploring pertinent and contemporary instances of non-classical resource generation, such as non-Gaussian fields and entanglement, along with applications in quantum technology, including photon-photon gates with error characterization and LRP analysis involving essential parameters. In essence, we extensively employed a technique that closes systems typically treated within the framework of open quantum systems. This approach provided us with complete information about the combined state of the quantum system under investigation. Our study has been conducted within the fundamental framework of quantum measurements, as presented in Chapter 1, and their applications in the context of quantum information processing. To develop our solutions, we have built upon the framework of WGQED, as explained in Chapter 2. This theoretical tool allows us to solve the closed dynamics of a quantum emitter coupled with a bosonic field at every moment in time, hence grating access the joint wavefunction.

Regarding our original contributions, in Chapter 3, we have explored the emergence of non-classical behavior in a strong resonant coherent field. Based on fundamental results, we have observed two independent signatures of quantum contextuality: the emergence of anomalous weak values and the negativity of the Wigner function. By analytically computing the weak values and conditional Wigner function using the Hamiltonian solution, we have identified the origins of these anomalies and negativities. These findings have been published in Ref. [53].

In Chapter 4, we have investigated the non-destructive measurement of the spin state in a degenerate four-level system (4LS). The 4LS has been made to interact with fields of different natures: a resonant coherent field with Poissonian (classical) statistics and a superposition of vacuum and a single photon with sub-Poissonian (quantum) statistics. Our results have shown that, when limited to a one-photon energy budget, we achieve quantum advantage in the pre-measurement process and in the collapse step, provided the experiment is designed to target the appropriate degree of freedom. These results are particularly relevant for key quantum information protocols, such as the generation of cluster states [63]. Further details on these findings can be found in Ref. [74]. Additionally, we have proposed a single-rail

photon-photon gate, which serves as a two-qubit photonic gate based on the presence (single photon) or absence (vacuum) of a photon as the logical basis. We have considered the ideal scenario where the only imperfection arises from the change in the temporal shape of the scattered field due to the finite duration of the pulse. To assess the gate's performance, we have characterized the error by computing the state-averaged fidelity and the error process matrix. This analysis provided insights into the types of errors and their nature, paving the way for the design of suitable error correction protocols.

Finally, in Chapter 5, we have addressed the realistic scenario where the LRP is implemented. We have extended the solutions obtained in Chapter 2 to include the action of an in-plane magnetic field that is present throughout the dynamics and used it to further characterize the protocol through relevant figures of merit.

Looking ahead, the closed system formalism offers promising perspectives, such as the investigation of protocols to generate spin-spin entanglement through spin photon entanglement generation [163, 164, 165]. We can also envision the proposition of new protocols for building non-classical states of light. On a fundamental level, this approach can be extended to investigate the thermodynamics of quantum systems using quantum optical systems, offering insights into the energetic properties of these platforms [39, 166].

Appendix A

General solution of time dependent Hamiltonians

This appendix is devoted to the basis of the approach we use to solve the dynamics of the systems of interest in this thesis, i.e. the collisional model. The problem is simple: we want to solve the dynamics of a quantum system described by an arbitrary time-dependent Hamiltonian $H(t)$,

$$\partial_t|\Psi(t)\rangle = -iH(t)|\Psi(t)\rangle. \tag{A.1}$$

We will use the information that in the case of a *time independent* Hamiltonian H the solution is given by [93],

$$|\Psi(t)\rangle = e^{-iHt}|\Psi(t_0)\rangle \tag{A.2}$$

where $|\Psi(t_0)\rangle$ is the initial state of the quantum system.

A.1 Coarse-graining of time

We assume that the Hamiltonian $H(t)$ is piecewise constant at intervals Δt, in which it has the value $H(n\Delta t)$ in the time window $t \in [n\Delta t, (n+1)\Delta t]$. Hence, from Eq. (A.2) we know that the solution in *one* interval is given by,

$$|\Psi((n+1)\Delta t)\rangle = e^{-i\Delta t H(n\Delta t)}|\Psi(n\Delta t)\rangle, \tag{A.3}$$
$$= U_n|\Psi(n\Delta t)\rangle \tag{A.4}$$

from this point on we introduce the short-hand notation $|\Psi_n\rangle = |\Psi(n\Delta t)\rangle$. Hence, for a time interval $t \in [t_0 = M\Delta t, t = N\Delta t]$, with $N > M$ integers, and $\Delta t = (t - t_0)/(N - M)$ we have the solution as a composition [167],

$$\boxed{|\Psi_N\rangle = e^{-i(N-1)\Delta t H_{N-1}} e^{-i(N-2)\Delta t H_{N-2}} \dots e^{-iM\Delta t H_M}|\Psi_M\rangle = \left(\prod_{k=M}^{N-1} U_k\right)|\Psi_M\rangle = \mathscr{U}(t_N, t_M)|\Psi_M\rangle} \tag{A.5}$$

where the total evolution operator from time t_M to t_N $\mathscr{U}(t_N, t_M)$ was defined as (from now on $H(n\Delta t) = H_n$),

$$\mathscr{U}(t_N, t_M) = e^{-i(N-1)\Delta t H_{N-1}} e^{-i(N-2)\Delta t H_{N-2}} \dots e^{-iM\Delta t H_M} \tag{A.6}$$

$$= U_{N-1} U_{N-2} \dots U_M = \prod_{k=M}^{N-1} U_k \tag{A.7}$$

where U_k are the evolution operators in the interval Δt in which the Hamiltonian is constant. In the continuous-time limit $\Delta t \to 0$ the solution becomes exact. Notice that for $\Delta t \ll 1$ we might expand the constant evolution operator in a Taylor series,

$$\boxed{U_n = e^{-in\Delta t H_n} \approx \mathbb{1} - in\Delta t H_n + \frac{(-in\Delta t H_n)^2}{2!} + \frac{(-in\Delta t H_n)}{3!} + \dots,} \tag{A.8}$$

the Eqs. (A.5) and (A.8) form the building block of the collisional model.

The time-dependent evolution operator has the following properties,

$$\mathscr{U}(t_M, t_M) = 1 \tag{A.9}$$

$$\mathscr{U}(t_N, t_j)\mathscr{U}(t_j, t_M) = U(t_N, t_M), \ \forall j \in [M, N] \tag{A.10}$$

$$\mathscr{U}(t, s)\mathscr{U}^\dagger(t, s) = 1 \ \forall t, s \tag{A.11}$$

$$\mathscr{U}^\dagger(t, s) = U(s, t) \tag{A.12}$$

which are the same properties as the time-independent case. Importantly, the semigroup property, Eq. (A.10), implies that the solution can be broken down into pieces. Thus, Eqs. (A.5) and (A.6) provide a general way of dealing with time-dependent dynamics. If the Hamiltonian turns out to commute at different times, i.e $[H_i, H_j] = \delta_{ij}$, the exponential can be simply recombined and the solution for the continuous time evolution operator $\mathscr{U}(t, t_0)$ becomes,

$$\mathscr{U}(t, t_0) = \lim_{\Delta t \to 0} \exp\left\{-i \sum_{k=M}^{N} \Delta t H(k\Delta t)\right\}$$

$$= \exp\left\{-i \int_{t_0}^{t} ds \ H(s)\right\}. \tag{A.13}$$

But this is not true in general. We consider now the non-commuting case, $[H_i, H_j] \neq \delta_{ij}$. To write the solution in a similar way as Eq. (A.13) we have to define the time-ordering operator $\mathscr{T}$ whose action is to always bring later times to the left. Let A, B represent arbitrary time-dependent operators, then

$$\mathscr{T} A(t_1)B(t_2) = \begin{cases} A(t_1)B(t_2) & \text{, if } t_1 > t_2 \\ B(t_2)A(t_1) & \text{, if } t_2 > t_1 \end{cases}$$

Thus, it is easy to see that when this operator acts upon commutators it makes them vanish, i.e. $\mathscr{T}([A(t_1), B(t_2)]) = 0$, and in the BCH formula, (2.15), only the first two

terms contribute. Hence, we are allowed to write,

$$\mathscr{T} \exp \{A(t_2) + B(t_1)\} = \exp \{A(t_2)\} \exp \{B(t_1)\} .$$

Finally, thanks to the protection of the time-ordering operator, we may write the generic solution of a time-dependent problem as,

$$\mathscr{U}(t, t_0) = \mathscr{T} \exp \left\{ -i \int_{t_0}^{t} ds \; H(s) \right\} .$$

Appendix B

Confining charges in quantum dots

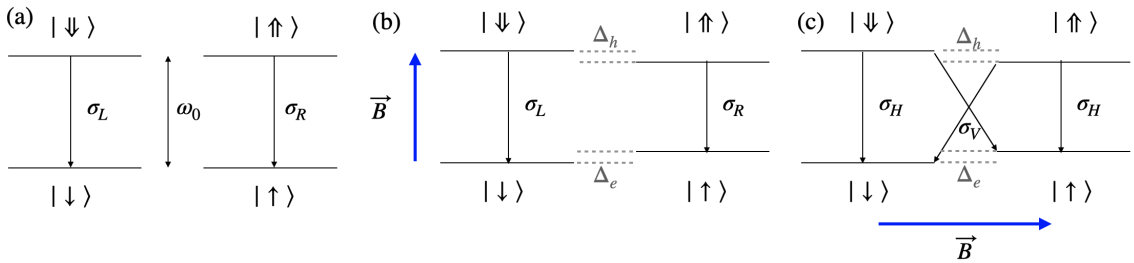

Figure B.1: **Magnetic field configurations.** Level diagram for (a) the absence of the magnetic field. (b) Faraday configuration. (c) Voigt configuration.

As outlined in the thesis introduction, quantum dots are tiny structures embedded within semiconductor matrices. They are formed by combining materials with distinct lattice parameters, usually InAs or GaAs [58]. These structures give rise to discrete bound states, leading to well-defined optical transitions owing to the confinement of charge movement in all three dimensions at the nanoscale. These materials possess a direct band gap and exhibit radiative decay characteristics. Particularly, at cryogenic temperatures (approximately 4 Kelvins), these materials display precise optical transitions between discrete energy levels, making them excellent candidates for generating single photons, serving as artificial atoms [42]. This characteristic allows us to model a quantum dot as a qubit [59].

Charge carriers can be trapped within these quantum dots, which can be either excess electrons in the conduction state or holes (electron vacancies) in the valence states. The simplest form of charged quantum dots involves a single electron (or hole) confined within the quantum dot. The electron possesses a spin of 1/2, with relevant spin states denoted as $\{|\uparrow\rangle, |\downarrow\rangle\}$, with spin projection $\pm 1/2$, respectively. States featuring a single charge can be optically excited by creating an electron-hole pair alongside the initially confined charge. When a quantum dot holds a single electron, due to the Pauli exclusion principle, the excited state comprises a singlet configuration (two electrons with opposite spins) coupled with a hole. The hole states exhibit a spin of 3/2, giving rise to four possible spin projections of $\pm 1/2$ and $\pm 3/2$. The former are termed light-holes, while the latter are referred to as heavy-holes. Although light and heavy holes are theoretically degenerate in energy, experimental

setups typically involve quantum dots with a height significantly smaller than their width. This vertical confinement accentuates the energy level differences between light and heavy holes, lifting their degeneracy. In practice, only the energy levels corresponding to heavy-holes are populated, represented as $\{|\Uparrow\rangle, |\Downarrow\rangle\}$. These heavy holes are termed trions. The transitions $|\downarrow\rangle \rightarrow |\Downarrow\rangle$ and $|\uparrow\rangle \rightarrow |\Uparrow\rangle$ are selectively driven by left (L) and right (R) circularly polarized light, corresponding to helicities of -1 and $+1$, respectively, in accordance with angular momentum conservation.

It is possible to modify the optical properties of QD subjecting it to an external magnetic field. The magnetic field can be oriented mainly in two manners:

1. Along the growth axis of the quantum dot: referred to as the Faraday configuration. In this case, the magnetic field introduces Zeeman splittings to both the spin and trion states, while the eigenstates remain associated with spin projections along the z-axis.

2. Perpendicular to the growth axis: known as the Voigt configuration. This orientation breaks rotational symmetry, resulting in a transformation of the eigenstates. The newly defined eigenstates align with the in-plane axis. Zeeman splittings are $\Delta_{e(h)} = \hbar g_{e(h)} \mu_B |\vec{B}|$, where $\hbar$ is the Planck constant, $g_{e(h)}$ is the transverse electron (hole) Landé factor, μ_B is the Bohr magneton and $|\vec{B}|$ is the magnitude of the magnetic field.

B.1 Experimental details

In this section we provide the experimental parameters used to plot Fig. 5.3.

The experiment realized in Ref. [75] has the following parameters: The QD that emits a photon with wavelength $\lambda_0 = 927$nm. The authors use a blue-detuned laser such that $\Delta\lambda = \lambda_{\text{laser}} - \lambda_0 = 1$nm. The duration of the excitation pulse is of 20ps, it adiabatically dresses and undresses the QD ground and excited states. The fast relaxation of a longitudinal acoustic phonon is the mechanism that allows to efficiently populate the excited state with high probability $p_{\text{excited}} > 0.85$. The advantage of the LA assisted excitation scheme lies in the possibility of filtering the emitted photon spectrally and not the polarization. The field is put in the $x-$direction only (Voigt configuration) with magnitudes $|B_x|= 150, 250, 350$, and 450mT. The hole Landé factor is of $g_h = 0.38 \pm 0.01$. The trion radiative decay time is of $T_1^{(\text{trion})} = 450 \pm 20$ps and the hole spin coherence time is $T_2^{\star} \geq 15 \pm 5$ns. These values provide a lower bound for the electron spin coherence time $T_2^{(\text{spin})}$, that is limited by the lifetime of the excited state.

The high hole spin Landé factor g_h allows a relatively weak magnetic field to be sufficient for the implementation of a large number of precession cycles during the time of spin coherence, which is longer than the trion lifetime $T_1^{(\text{trion})}$, this is the content of Fig. 5.3. In the Fig. 5.3 the vacuum decay rate γ was set to unity by normalizing all the experimental values by the trion lifetime $\gamma_{\text{exp}} = 1/T_1^{(\text{trion})}$. Within these experimental conditions it is possible to implement the LRP for cluster state generation as reported in Ref. [63].

Appendix C

Detailed calculation of the final real photonic states

In this appendix, we provide detailed calculations based on the map (4.59) that leads to the final photonic states in Eq. (4.66). We follow the protocol described in Sec. 4.5.1:

1. **First pulse:** After the spin is in the $|+\rangle$ state, the first step involves sending the initial light pulse, $|\Phi_{\text{in}}^{[1]}\rangle$. This can be expressed as follows:

$$\left(\frac{|\emptyset\rangle_1 + |\mathrm{R}\rangle_1}{\sqrt{2}}\right)\left(\frac{|\downarrow\rangle + |\uparrow\rangle}{\sqrt{2}}\right) = \frac{1}{2}\left(|\emptyset\rangle_1 + |\mathrm{R}\rangle_1\right)|\downarrow\rangle + \left(|\emptyset\rangle_1 + |\mathrm{R}\rangle_1\right)|\uparrow\rangle \tag{C.1}$$
$$\xrightarrow{\text{Map. (4.59)}} \frac{1}{2}\left[\left(|\emptyset\rangle_1 + |\mathrm{R}\rangle_1\right)|\downarrow\rangle + \left(|\emptyset\rangle_1 - |\tilde{\mathrm{R}}\rangle_1\right)|\uparrow\rangle\right]$$

2. **Spin rotation:** Following the first pulse, a second rotation, denoted as $U^{[1]}$, is applied to the spin:

$$\frac{1}{2}\left[\left(|\emptyset\rangle_1 + |\mathrm{R}\rangle_1\right)|\downarrow\rangle + \left(|\emptyset\rangle_1 - |\tilde{\mathrm{R}}\rangle_1\right)|\uparrow\rangle\right] \tag{C.2}$$
$$\rightarrow \frac{1}{2\sqrt{2}}\left(|\emptyset\rangle_1 + |\mathrm{R}\rangle_1\right)\left(|\downarrow\rangle - |\uparrow\rangle\right) + \left(|\emptyset\rangle_1 - |\tilde{\mathrm{R}}\rangle_1\right)\left(|\downarrow\rangle + |\uparrow\rangle\right)$$
$$= \frac{1}{\sqrt{2}}\left(\left(|\emptyset\rangle + \left(\frac{|\mathrm{R}\rangle_1 - |\tilde{\mathrm{R}}\rangle_1}{2}\right)\right)|\downarrow\rangle - \left(\frac{|\mathrm{R}\rangle_1 + |\tilde{\mathrm{R}}\rangle_1}{2}\right)|\uparrow\rangle\right)$$

3. **Second pulse:** Subsequently, the second pulse, denoted as $|\Phi_{\text{in}}^{[2]}\rangle$, is sent:

$$\left(\frac{|\emptyset\rangle_2 + |\mathrm{R}\rangle_2}{\sqrt{2}}\right)\frac{1}{\sqrt{2}}\left(\left(|\emptyset\rangle + (\frac{|\mathrm{R}\rangle_1 - |\tilde{\mathrm{R}}\rangle_1}{2})\right)|\downarrow\rangle - (\frac{|\mathrm{R}\rangle_1 + |\tilde{\mathrm{R}}\rangle_1}{2})|\uparrow\rangle\right) \tag{C.3}$$

$$= \frac{1}{2}\left(|\emptyset\rangle_2 + |\mathrm{R}\rangle_2\right)\left(\left(|\emptyset\rangle + (\frac{|\mathrm{R}\rangle_1 - |\tilde{\mathrm{R}}\rangle_1}{2})\right)|\downarrow\rangle - (\frac{|\mathrm{R}\rangle_1 + |\tilde{\mathrm{R}}\rangle_1}{2})|\uparrow\rangle\right)$$

$$\xrightarrow{\text{Map. (4.59)}} \frac{1}{2}\left(|\emptyset\rangle_2\left(|\emptyset\rangle + (\frac{|\mathrm{R}\rangle_1 - |\tilde{\mathrm{R}}\rangle_1}{2})\right)|\downarrow\rangle + |\mathrm{R}\rangle_2\left(|\emptyset\rangle + (\frac{|\mathrm{R}\rangle_1 - |\tilde{\mathrm{R}}\rangle_1}{2})\right)|\downarrow\rangle\right)$$

$$\frac{1}{2}\left(-|\emptyset\rangle_2(\frac{|\mathrm{R}\rangle_1 + |\tilde{\mathrm{R}}\rangle_1}{2})|\uparrow\rangle + |\tilde{\mathrm{R}}\rangle_2(\frac{|\mathrm{R}\rangle_1 + |\tilde{\mathrm{R}}\rangle_1}{2})|\uparrow\rangle\right)$$

4. **Erase spin state information:** Rotating the spin and rearranging the we obtain,

$$\frac{1}{2\sqrt{2}}|\downarrow\rangle\left(|\emptyset\rangle_2\left(|\emptyset\rangle_1 + (\frac{|\mathrm{R}\rangle_1 - |\tilde{\mathrm{R}}\rangle_1}{2})\right) + |\mathrm{R}\rangle_2\left(|\emptyset\rangle + (\frac{|\mathrm{R}\rangle_1 - |\tilde{\mathrm{R}}\rangle_1}{2})\right)\right. \tag{C.4}$$

$$\left. -|\emptyset\rangle_2(\frac{|\mathrm{R}\rangle_1 + |\tilde{\mathrm{R}}\rangle_1}{2}) + |\tilde{\mathrm{R}}\rangle_2(\frac{|\mathrm{R}\rangle_1 + |\tilde{\mathrm{R}}\rangle_1}{2})\right)$$

$$+\frac{1}{2\sqrt{2}}|\uparrow\rangle\left(-|\emptyset\rangle_2\left(|\emptyset\rangle_1 + (\frac{|\mathrm{R}\rangle_1 - |\tilde{\mathrm{R}}\rangle_1}{2})\right) - |\mathrm{R}\rangle_2\left(|\emptyset\rangle + (\frac{|\mathrm{R}\rangle_1 - |\tilde{\mathrm{R}}\rangle_1}{2})\right)\right.$$

$$\left. -|\emptyset\rangle_2(\frac{|\mathrm{R}\rangle_1 + |\tilde{\mathrm{R}}\rangle_1}{2}) + |\tilde{\mathrm{R}}\rangle_2(\frac{|\mathrm{R}\rangle_1 + |\tilde{\mathrm{R}}\rangle_1}{2})\right)$$

$$= \frac{1}{\sqrt{2}}\left[|\downarrow\rangle|\psi_{\downarrow}^{\text{real}}\rangle - |\uparrow\rangle|\psi_{\uparrow}^{\text{real}}\rangle\right]$$

where $|\psi_j^{\text{real}}\rangle$ are given by Eq. (4.66).

Appendix D

4LS subjected to a magnetic field: spontaneous emission solution

By utilizing the LA-phonon assisted excitation scheme, it becomes feasible to prepare the spin in the excited state with a high probability [75]. In this context, we aim to address the experimental setup investigated in Ref. [75], which was further employed for implementing the Lindner-Rudolph protocol [63]. The experimental procedure is as follows: a slightly off-resonant coherent pulse, characterized by $\omega_p = \omega_0 + \delta\omega$, where ω_p represents the pump frequency, prepares the system in the excited state with the spin $|\uparrow\rangle$ or $|\downarrow\rangle$, after which it is allowed to relax through spontaneous emission.

Considering the experimental situation outlined in the previous paragraph, we assume that there are no excitations in the R and L polarizations and the system are initially in the excited state for one of the spins. The vacuum state of the temporal mode j with polarization 'pol' is denoted as $|\emptyset\rangle_{\text{pol},j}$, and the single photon state is denoted as $|1\rangle_{\text{pol},j} \equiv b^\dagger_{\text{pol}}(t_j)|\emptyset\rangle_{\text{pol},j}$ (where the subscript will be dropped when obvious). Thus, the initial state can be expressed as

$$|\Psi^\zeta(0)\rangle = |e\rangle \otimes |\zeta\rangle \otimes |\emptyset\rangle \otimes |\emptyset\rangle. \tag{D.1}$$

In other words, we assume that the QD is in the excited state due to the absorption of a previous photon, the spin can be either up or down, and the R and L modes are in vacuum. Depending on the spin state, the system will spontaneously emit either one R or L photon. Therefore, we can restrict the search for solutions to the subspace consisting of a vacuum and a single photon, as the Hamiltonian we are considering conserves the number of excitations in the system. This implies that we truncate our Fock basis for each temporal mode to the space spanned by $\{|\emptyset\rangle_{R(L),j}, |1\rangle_{R(L),j}\}$.

The state at time $t_N = N\Delta t$ can be written with the wavefunction *ansatz*

$$
\begin{aligned}
|\Psi^{\zeta}(t_N)\rangle = & f^{(0),\zeta}_{\uparrow,e}(t_N)|e\rangle|\uparrow\rangle|\emptyset\rangle|\emptyset\rangle + f^{(0),\zeta}_{\downarrow,e}(t_N)|e\rangle|\downarrow\rangle|\emptyset\rangle|\emptyset\rangle \\
& + \sum_{j=0}^{N-1}\left[f^{(1,R),\zeta}_{\uparrow,g}(t_N,t_j)|g\rangle|\uparrow\rangle|1_{R,j}\rangle|\emptyset\rangle + f^{(1,R),\zeta}_{\downarrow,g}(t_N,t_j)|g\rangle|\downarrow\rangle|1_{R,j}\rangle|\emptyset\rangle\right] \\
& + \sum_{j=0}^{N-1}\left[f^{(1,L),\zeta}_{\uparrow,g}(t_N,t_j)|g\rangle|\uparrow\rangle|\emptyset\rangle|1_{L,j}\rangle + f^{(1,L),\zeta}_{\downarrow,g}(t_N,t_j)|g\rangle|\downarrow\rangle|\emptyset\rangle|1_{L,j}\rangle\right].
\end{aligned}
\tag{D.2}
$$

Here, $|\Psi^{\zeta}(t_N)\rangle$ indicates that at time $t_0 = 0$, the state was $|\Psi^{\zeta}(0)\rangle$, and the notation of the coefficients provide the following information:

$$
f^{(\text{number of photons,polarization}),\text{initial spin state}}_{\text{final spin state,energetic state}}. \tag{D.3}
$$

This wavefunction encompasses all the possible processes that can take place. Thus, the objective of the following sections is to determine the coefficients of Eq. (D.2). That is the goal of the next sections. To achieve this, we will gather the necessary components. As discussed in Sec. A.1, the evolved state can be expressed as follows (we assume, without loss of generality $\zeta = \uparrow_z$):

$$
\begin{aligned}
|\Psi^{\uparrow}(t_N)\rangle = & \left(\prod_{k=0}^{N-1} U_k\right)|\Psi^{\uparrow}(0)\rangle \\
= & f^{(0),\uparrow}_{\uparrow,e}(t_N)|e\rangle|\uparrow\rangle|\emptyset\rangle|\emptyset\rangle + f^{(0),\uparrow}_{\downarrow,e}(t_N)|e\rangle|\downarrow\rangle|\emptyset\rangle|\emptyset\rangle \\
& + \sum_{j=0}^{N-1}\left[f^{(1,R),\uparrow}_{\uparrow,g}(t_N,t_j)|g\rangle|\uparrow\rangle|1_{R,j}\rangle|\emptyset\rangle + f^{(1,R),\uparrow}_{\downarrow,g}(t_N,t_j)|g\rangle|\downarrow\rangle|1_{R,j}\rangle|\emptyset\rangle\right] \\
& + \sum_{j=0}^{N-1}\left[f^{(1,L),\uparrow}_{\uparrow,g}(t_N,t_j)|g\rangle|\uparrow\rangle|\emptyset\rangle|1_{L,j}\rangle + f^{(1,R),\uparrow}_{\downarrow,g}(t_N,t_j)|g\rangle|\downarrow\rangle|\emptyset\rangle|1_{L,j}\rangle\right]
\end{aligned}
\tag{D.4}
$$

We consider a small time interval, $\Delta t \ll 1$, which allows us to truncate U_k and other terms to first order in Δt. Any term that appears with $\Delta t^n, n > 1$, is neglected in the evolution. Thus, we can express the evolution as follows:

$$
\begin{aligned}
U_1 = & \mathbb{1} - i\Delta t\left(\hat{C}_{eg}(\vec{s})\sigma^{\dagger}\sigma - \hat{C}_{g}(\vec{s})\sigma_z\right) \\
& + \sqrt{\Delta t\gamma}\left[\left(b^{\dagger}_L(t)\sigma - \sigma^{\dagger}b_L(t)\right)\otimes ss^{\dagger} + \left(b^{\dagger}_R(t)\sigma - \sigma^{\dagger}b_R(t)\right)\otimes s^{\dagger}s\right] \\
& + \Delta t\frac{\gamma}{2}\left[\left(b^{\dagger}_L(t)\sigma - \sigma^{\dagger}b_L(t)\right)^2\otimes ss^{\dagger} + \left(b^{\dagger}_R(t)\sigma - \sigma^{\dagger}b_R(t)\right)^2\otimes s^{\dagger}s\right]
\end{aligned}
\tag{D.5}
$$

It will be useful to define the rotation operators as follows:

$$\mathscr{R}_g(\vec{s}) = \exp\left\{-i\Delta t\hat{C}_g(\vec{s})\right\}, \tag{D.6}$$

$$\begin{aligned}\mathscr{R}_e(\vec{s}) &= \exp\left\{-i\Delta t\left(\hat{C}_{eg}(\vec{s}) - \hat{C}_g(\vec{s})\right)\right\} \\ &= \exp\left\{-i\Delta t\omega_0\right\}\exp\left\{-i\Delta t\frac{\Omega_e}{2}s_x\right\}\end{aligned} \tag{D.7}$$

These operators can be expressed as:

$$\mathscr{R}_g(\vec{s}) = \cos\left(\Delta t\frac{\Omega_g}{2}\right) - i\vec{n}\vec{s}\sin\left(\Delta t\frac{\Omega_g}{2}\right), \tag{D.8}$$

$$\mathscr{R}_e(\vec{s}) = \exp\left\{-i\Delta t\omega_0\right\}\left[\cos\left(\Delta t\frac{\Omega_e}{2}\right) - is_x\sin\left(\Delta t\frac{\Omega_e}{2}\right)\right]. \tag{D.9}$$

Note that the first rotation operator, $\mathscr{R}_g(\vec{s})$, depends only on Ω_g, while the second rotation operator, $\mathscr{R}_e(\vec{s})$, depends only on Ω_e. Therefore, the first operator is responsible for the physical precession in the ground state, while the second operator promotes rotations in the excited state. With these essential tools in place, we are now equipped to determine the coefficients needed for further analysis.

D.1 Finding the $f^{(0),\uparrow}_{\uparrow(\downarrow),e}(t_N)$

Before proceeding with the calculation, let's consider the expected physical behavior. As the system is in the excited state, we anticipate the emergence of spontaneous emission, which will be accompanied by an exponential factor proportional to the decay rate γ. Additionally, we must consider the influence of the magnetic field on the spin. In the excited state, the field is oriented in the x-direction, implying a rotation term proportional to the excited state Larmor frequency Ω_e, causing precession around the x-axis.

To determine $f^{(0),\uparrow}_{\uparrow(\downarrow),e}(t_N)$, we need to project the final state $|\Psi^{\uparrow}(t_N)\rangle$onto the subspace spanned by $\{|e,\uparrow(\downarrow),\emptyset,\emptyset\rangle\}$. Thus, we can write:

$$\begin{aligned}f^{(0),\uparrow}_{\uparrow(\downarrow),e}(t_N) &= \langle e,\uparrow(\downarrow),\emptyset,\emptyset|\Psi^{\uparrow}(t_N)\rangle \\ &= \langle\uparrow(\downarrow)|\left(\prod_{k=0}^{N-1}\langle\emptyset,\emptyset|U_k|\emptyset,\emptyset\rangle\right)|\uparrow\rangle\end{aligned} \tag{D.10}$$

To find the matrix element $\mathfrak{U}^{\emptyset\emptyset}_{\emptyset\emptyset}$, which is defined as:

$$\begin{aligned}\mathfrak{U}^{\emptyset\emptyset}_{\emptyset\emptyset} \equiv \langle\emptyset,\emptyset|U_1|\emptyset,\emptyset\rangle &= \langle\emptyset,\emptyset|\left[\mathbb{1} - i\Delta t\left(\hat{C}_{eg}(\vec{s})\sigma^\dagger\sigma - \hat{C}_g(\vec{s})\sigma_z\right)\right]|\emptyset,\emptyset\rangle \\ &+ \sqrt{\Delta t\gamma}\langle\emptyset,\emptyset|\left[\left(b_L^\dagger(t)\sigma - \sigma^\dagger b_L(t)\right)\otimes ss^\dagger + \left(b_R^\dagger(t)\sigma - \sigma^\dagger b_R(t)\right)\otimes s^\dagger s\right]|\emptyset,\emptyset\rangle \\ &+ \Delta t\frac{\gamma}{2}\langle\emptyset,\emptyset|\left[\left(b_L^\dagger(t)\sigma - \sigma^\dagger b_L(t)\right)^2\otimes ss^\dagger + \left(b_R^\dagger(t)\sigma - \sigma^\dagger b_R(t)\right)^2\otimes s^\dagger s\right]|\emptyset,\emptyset\rangle\end{aligned} \tag{D.11}$$

In this context, the Kramer's operator is denoted by the symbol $\mathfrak{U}$ (gothic U), represented as

$$\mathfrak{U}^{\text{intial field state R,intial field state L}}_{\text{final field state R, final field state L}}.$$

Doing the algebra, we obtain that $\mathfrak{U}^{\emptyset\emptyset}_{\emptyset\emptyset}$ can be cast as:

$$\boxed{\mathfrak{U}^{\emptyset\emptyset}_{\emptyset\emptyset} = \langle\emptyset,\emptyset|U_1|\emptyset,\emptyset\rangle = \exp\left\{-i\Delta t\left[\left(\hat{C}_{eg}(\vec{s})\sigma^\dagger\sigma - \hat{C}_g(\vec{s})\sigma_z\right) - i\frac{\gamma}{2}\sigma^\dagger\sigma\right]\right\}} \tag{D.12}$$

Assuming that the quantum dot (QD) is initially in the excited state $|e\rangle$ and that $\sigma_z|e\rangle = |e\rangle$ and $\sigma^\dagger\sigma|e\rangle = |e\rangle$, we can find the action of this operator on $|e\rangle$:

$$\begin{aligned}\mathfrak{U}^{\emptyset\emptyset}_{\emptyset\emptyset}|e\rangle &= \exp\left\{-i\Delta t\left[\left(\hat{C}_{eg}(\vec{s}) - \hat{C}_g(\vec{s})\right) - i\frac{\gamma}{2}\right]\right\}|e\rangle \\ &= \exp\left\{-\frac{\gamma}{2}\Delta t\right\}\mathscr{R}_e(\vec{s})|e\rangle\end{aligned} \tag{D.13}$$

We also consider the action of this operator on the ground state $|g\rangle$ using $\sigma_z|g\rangle = -|g\rangle$ and $\sigma^\dagger\sigma|g\rangle = 0$,

$$\begin{aligned}\mathfrak{U}^{\emptyset\emptyset}_{\emptyset\emptyset}|g\rangle &= \exp\left\{-i\Delta t\left[\left(\hat{C}_{eg}(\vec{s})\sigma^\dagger\sigma - \hat{C}_g(\vec{s})\sigma_z\right) - i\frac{\gamma}{2}\sigma^\dagger\sigma\right]\right\}|g\rangle \\ &= \exp\left\{-i\Delta t\hat{C}_g(\vec{s})\right\}|g\rangle = \mathscr{R}_g(\vec{s})|g\rangle\end{aligned} \tag{D.14}$$

It is worth highlighting the following identities:

$$\prod_{k=m}^{N-1}(\mathfrak{U}^{\emptyset\emptyset}_{\emptyset\emptyset})_k|g\rangle = \exp\left\{-i(t_N - t_m)\hat{C}_g(\vec{s})\right\}|g\rangle = \mathscr{R}_g^{N-m}(\vec{s})|g\rangle \tag{D.15}$$

and,

$$\prod_{k=m}^{N-1}(\mathfrak{U}^{\emptyset\emptyset}_{\emptyset\emptyset})_k|e\rangle = \exp\left\{-\frac{\gamma}{2}(t_N - t_m)\right\}\mathscr{R}_e^{N-m}(\vec{s})|e\rangle \tag{D.16}$$

The coefficient $f^{(0),\uparrow}_{\uparrow(\downarrow),e}(t_N)$ is given by[1]:

$$\begin{aligned}f^{(0),\uparrow}_{\uparrow(\downarrow),e}(t_N) &= \langle\uparrow(\downarrow)|\left(\prod_{k=m}^{N-1}\langle\emptyset,\emptyset|U_k|\emptyset,\emptyset\rangle\right)|\uparrow\rangle \\ &= \exp\left\{-\frac{\gamma}{2}(N-m)\Delta t\right\}\langle\uparrow(\downarrow)|\mathscr{R}_e^{(N-m)}(\vec{s})|\uparrow\rangle\end{aligned} \tag{D.17}$$

Finally,

$$\boxed{f^{(0),\uparrow}_{\uparrow(\downarrow),e}(t_N) = \exp\left\{-\frac{\gamma}{2}t_N\right\}\langle\uparrow(\downarrow)|\mathscr{R}_e^N(\vec{s})|\uparrow\rangle} \tag{D.18}$$

The calculation is completely analogous if the initial spin is down, resulting in

[1] For the sake of generality we take the productory from $k \in [m, N-1]$, in our particular case $m = 0$.

the boxed expression:

$$\boxed{f^{(0),\downarrow}_{\uparrow(\downarrow),e}(t_N) = \exp\left\{-\frac{\gamma}{2}t_N\right\}\langle\uparrow(\downarrow)|\mathscr{R}^N_e(\vec{s})|\downarrow\rangle} \tag{D.19}$$

D.2 Finding the $f^{(1,R),\uparrow}_{\uparrow(\downarrow),e}(t_N, t_j)$

In this section we are going to find all the coefficients $f^{(1,\text{pol}),\uparrow}_{\uparrow(\downarrow),g}(t_N, t_j)$, pol $\in \{R, L\}$. We are computing concretly the coefficient $f^{(1,R),\uparrow}_{\uparrow(\downarrow),e}(t_N, t_j)$, for L-polarization the steps are completly analogous.The procedure is similar, we project the final state $|\Psi^{\uparrow}(t_N)\rangle$ onto the subspace spanned by$\{|g, \uparrow(\downarrow), 1_{R,j}, \emptyset_L\rangle\}$.

Due to the semigroup property of the unitary operator, the total evolution operator can be split into three terms as follows:

$$\mathscr{U}(t_N, 0) = \left(\prod_{k=j+1}^{N-1} U_k\right) U_j \left(\prod_{l=0}^{j-1} U_l\right) \tag{D.20}$$

Therefore, we can express the inner product $\langle g, \uparrow(\downarrow), 1_{R,j}, \emptyset|\Psi^{\uparrow}(t_N)\rangle$ as:

$$\begin{aligned}
\langle g, \uparrow(\downarrow), 1_{R,j}, \emptyset|\Psi^{\uparrow}(t_N)\rangle &= \langle g, \uparrow(\downarrow), 1_{R,j}, \emptyset|[,]\,|\Psi^{\uparrow}(0)\rangle \\
&= \langle g, \uparrow(\downarrow), 1_{R,j}, \emptyset|\left[\left(\prod_{k=j+1}^{N-1} U_k\right) U_j \left(\prod_{l=0}^{j-1} U_l\right)\right]|e, \uparrow, \emptyset, \emptyset\rangle \\
&= \langle g, \uparrow(\downarrow)|\left[\left(\prod_{k=j+1}^{N-1}\bigotimes_{k=j+1}^{N-1}\langle\emptyset_{R,k}, \emptyset_{L,k}|U_k|\emptyset_{R,k}, \emptyset_{L,k}\rangle\right)\right. \\
&\qquad \left.\langle 1_{R,j}, \emptyset_{L,j}|U_j|\emptyset_{R,j}, \emptyset_{L,j}\rangle\left(\prod_{l=0}^{j-1}\bigotimes_{l=j+1}^{j-1}\langle\emptyset_{R,l}, \emptyset_{L,l}|U_l|\emptyset_{R,l}, \emptyset_{L,l}\rangle\right)\right]|e, \uparrow\rangle
\end{aligned} \tag{D.21}$$

The last expression may not appear aesthetically pleasing, but the separation of indexes will be useful in the subsequent lines. Reading from right to left, we observe that the coefficient $f^{(0)}$ that we previously computed will appear in the purple terms since we know how to handle the unitary between vacuum states. Now, let's focus on the new ingredient highlighted in red, which connects the vacuum subspace to the subspace containing one R-photon. This implies that the photon was created at some point in time.

Computing the operator $\mathfrak{U}^{\emptyset\emptyset}_{1\emptyset}$, we obtain:

$$\boxed{\mathfrak{U}^{\emptyset\emptyset}_{1\emptyset} = \sqrt{\Delta t\gamma}\sigma \otimes s^{\dagger}s} \tag{D.22}$$

Inserting this result in Eq. (D.21), we find:

$$\begin{aligned}\langle g, \uparrow (\downarrow), 1_{R,j}, \emptyset | \Psi^{\uparrow}(t_N)\rangle &= \sqrt{\Delta t \gamma} \langle \uparrow (\downarrow) | \mathscr{R}_g^{N-j}(\vec{s}) | \uparrow \rangle f_{\uparrow,e}^{(0),\uparrow}(t_j) \\ &= \sqrt{\Delta t \gamma} r_g^{\uparrow(\downarrow),\uparrow} f_{\uparrow,e}^{(0),\uparrow}(t_j).\end{aligned} \tag{D.23}$$

Here, $r_g^{\uparrow(\downarrow),\uparrow}(t_N, t_j) = \langle \uparrow (\downarrow) | \mathscr{R}_g^{N-j}(\vec{s}) | \uparrow \rangle$. Finally, we have:

$$\boxed{f_{\uparrow(\downarrow),g}^{(1,R),\uparrow}(t_N, t_j) = \langle g, \uparrow (\downarrow), 1_{R,j}, \emptyset | \Psi^{\uparrow}(t_N)\rangle = \sqrt{\Delta t \gamma} r_g^{\uparrow(\downarrow),\uparrow} f_{\uparrow,e}^{(0),\uparrow}(t_j)} \tag{D.24}$$

This elegant result has a clear physical interpretation: on the right-hand side, we have the coefficient $f_{\uparrow,e}^{(0),\uparrow}(t_j)$. The system rotates and can emit a photon. If the intermediate spin state is $|\uparrow\rangle$, it can only emit an R-photon, and the system ends up in the state $|g, \uparrow\rangle$. Once in the ground state with an initial spin of $\uparrow$, it starts precessing under the influence of the magnetic field and ends up in one of the possible spin states. The calculation is completely analogous for L-polarization. [2], , leading to:

$$\boxed{f_{\uparrow(\downarrow),g}^{(1,L),\uparrow}(t_N, t_j) = \langle g, \uparrow (\downarrow), 1_{L,j}, \emptyset | \Psi^{\uparrow}(t_N)\rangle = \sqrt{\Delta t \gamma} r_g^{\uparrow(\downarrow),\downarrow} f_{\downarrow,e}^{(0),\uparrow}(t_j)} \tag{D.25}$$

It is important to note that the intermediate spin state here is $\downarrow$. With these insights, we have obtained all the coefficients and, consequently, the wave function.

The wave-function coefficients:

We have,

$$f_{\uparrow(\downarrow),e}^{(0),\uparrow}(t_N) = \exp\left\{-\frac{\gamma}{2} t_N\right\} \langle e, \uparrow (\downarrow) | \mathscr{R}_e^N(\vec{s}) | e, \uparrow \rangle \tag{D.26}$$

$$f_{\uparrow(\downarrow),g}^{(1,R),\uparrow}(t_N, t_j) = \langle g, \uparrow (\downarrow), 1_{R,j}, \emptyset | \Psi^{\uparrow}(t_N)\rangle = \sqrt{\Delta t \gamma} \langle g, \uparrow (\downarrow) | \mathscr{R}_g^{N-j}(\vec{s}) | g, \uparrow \rangle f_{\uparrow,e}^{(0),\uparrow}(t_j) \tag{D.27}$$

$$f_{\uparrow(\downarrow),g}^{(1,L),\uparrow}(t_N, t_j) = \langle g, \uparrow (\downarrow), 1_{R,j}, \emptyset | \Psi^{\uparrow}(t_N)\rangle = \sqrt{\Delta t \gamma} \langle g, \uparrow (\downarrow) | \mathscr{R}_g^{N-j}(\vec{s}) | g, \uparrow \rangle f_{\downarrow,e}^{(0),\uparrow}(t_j) \tag{D.28}$$

where,

$$\mathscr{R}_g^k(\vec{s}) \equiv \mathscr{R}_g(\vec{s}, t_k) = \mathbb{1} \cos\left(t_k \frac{\Omega_g}{2}\right) - i\vec{n}\vec{s} \sin\left(t_k \frac{\Omega_g}{2}\right), \tag{D.29}$$

$$\mathscr{R}_e^k(\vec{s}) \equiv \mathscr{R}_e(\vec{s}, t_k) = \exp\{-i t_k \omega_0\} \left[\mathbb{1} \cos\left(t_k \frac{\Omega_e}{2}\right) - i\sigma_x \sin\left(t_k \frac{\Omega_e}{2}\right)\right]. \tag{D.30}$$

[2] In this case, we find that $\langle \emptyset | b_L(t_N) \langle \emptyset_{R,N} | U_N | \emptyset_{R,N} \rangle | \emptyset_{L,N} \rangle = \sqrt{\Delta t \gamma} \sigma \otimes s s^{\dagger}$

D.3 Continuous time wave-function

To obtain the continuous time limit, we make the following substitutions:

$$
\begin{aligned}
t_N &\to t \\
t_j &\to u, \text{ (just a dummy integration variable)} \\
\frac{b_N}{\sqrt{\Delta t}} &\to b(u) \\
\sum_{j=0}^{N-1} \Delta t &\to \int_0^t du
\end{aligned}
$$

By following the procedure, we obtain the wave function in continuous time:

$$
\begin{aligned}
|\Psi^{\uparrow(\downarrow)}(t)\rangle = \exp\left\{-\frac{\gamma}{2}t\right\} &\left[\langle e,\uparrow|\mathscr{R}_e(\vec{s},t)|e,\uparrow(\downarrow)\rangle|e\rangle|\uparrow\rangle|\emptyset\rangle|\emptyset\rangle + \langle e,\downarrow|\mathscr{R}_e(\vec{s},t)|e,\uparrow(\downarrow)\rangle|e\rangle|\downarrow\rangle|\emptyset\rangle|\emptyset\rangle\right] \\
&+ \sqrt{\gamma}\int_0^t du \left[\langle g,\uparrow|\mathscr{R}_g(\vec{s},t-u)|g,\uparrow\rangle f^{(0),\uparrow(\downarrow)}_{\uparrow,e}(u) b^\dagger_R(u)\right]|g\rangle|\uparrow\rangle|\emptyset\rangle|\emptyset\rangle \\
&+ \sqrt{\gamma}\int_0^t du \left[\langle g,\uparrow|\mathscr{R}_g(\vec{s},t-u)|g,\downarrow\rangle f^{(0),\uparrow(\downarrow)}_{\downarrow,e}(u) b^\dagger_L(u)\right]|g\rangle|\uparrow\rangle|\emptyset\rangle|\emptyset\rangle \\
&+ \sqrt{\gamma}\int_0^t du \left[\langle g,\downarrow|\mathscr{R}_g(\vec{s},t-u)|g,\uparrow\rangle f^{(0),\uparrow(\downarrow)}_{\uparrow,e}(u) b^\dagger_R(u)\right]|g\rangle|\downarrow\rangle|\emptyset\rangle|\emptyset\rangle \\
&+ \sqrt{\gamma}\int_0^t du \left[\langle g,\downarrow|\mathscr{R}_g(\vec{s},t-u)|g,\downarrow\rangle f^{(0),\uparrow(\downarrow)}_{\downarrow,e}(u) b^\dagger_L(u)\right]|g\rangle|\downarrow\rangle|\emptyset\rangle|\emptyset\rangle
\end{aligned}
\tag{D.31}
$$

Bibliography

[1] M. Planck, "On an Improvement of Wien's Equation for the Spectrum," in *The Old Quantum Theory*, pp. 79–81, Elsevier, 1967.

[2] M. Planck, "On the Law of Distribution of Energy in the Normal Spectrum,"

[3] G. N. Lewis, "The Conservation of Photons," *Nature*, vol. 118, pp. 874–875, Dec. 1926. ADS Bibcode: 1926Natur.118..874L.

[4] A. Einstein, *The Collected Papers of Albert Einstein, Volume 2 (English): The Swiss Years: Writings, 1900-1909. (English translation supplement)*. Princeton University Press, Dec. 1989. Google-Books-ID: LbfTzQEACAAJ.

[5] S. T. Thornton and A. Rex, *Modern Physics for Scientists and Engineers*. Cengage Learning, Jan. 2012. Google-Books-ID: pWAKAAAAQBAJ.

[6] N. B. Archive, "Niels Bohr Collected Works," Nov. 2015. Publisher: University of Copenhagen.

[7] E. Schrödinger, *Collected Papers on Wave Mechanics*. American Mathematical Soc., 2003. Google-Books-ID: 8ZROAgAAQBAJ.

[8] W. Heisenberg, "Über quantentheoretische Umdeutung kinematischer und mechanischer Beziehungen.," *Zeitschrift für Physik*, vol. 33, pp. 879–893, Dec. 1925.

[9] I. J. R. Aitchison, D. A. MacManus, and T. M. Snyder, "Understanding Heisenberg's 'Magical' Paper of July 1925: a New Look at the Calculational Details," *American Journal of Physics*, vol. 72, pp. 1370–1379, Nov. 2004. arXiv:quant-ph/0404009.

[10] T. S. Kuhn, *The structure of scientific revolutions*. University of Chicago press, 2012.

[11] S. Haroche and J.-M. Raimond, *Exploring the Quantum: Atoms, Cavities, and Photons*. Oxford Graduate Texts, Oxford: Oxford University Press, 2006.

[12] A. Einstein, B. Podolsky, and N. Rosen, "Can Quantum-Mechanical Description of Physical Reality Be Considered Complete?," *Physical Review*, vol. 47, pp. 777–780, May 1935. Publisher: American Physical Society.

[13] A. Peres, "Quantum Theory: Concepts and Methods,"

[14] N. Bohr, "Can Quantum-Mechanical Description of Physical Reality be Considered Complete?," *Physical Review*, vol. 48, pp. 696–702, Oct. 1935. Publisher: American Physical Society.

[15] J. S. Bell, "On the Problem of Hidden Variables in Quantum Mechanics," *Reviews of Modern Physics*, vol. 38, pp. 447–452, July 1966. Publisher: American Physical Society.

[16] J. F. Clauser, M. A. Horne, A. Shimony, and R. A. Holt, "Proposed Experiment to Test Local Hidden-Variable Theories," *Physical Review Letters*, vol. 23, pp. 880–884, Oct. 1969.

[17] A. Aspect, "Bell's Theorem : The Naive View of an Experimentalist," Feb. 2004. arXiv:quant-ph/0402001.

[18] A. Aspect, P. Grangier, and G. Roger, "Experimental Tests of Realistic Local Theories via Bell's Theorem," *Physical Review Letters*, vol. 47, pp. 460–463, Aug. 1981.

[19] A. Aspect, J. Dalibard, and G. Roger, "Experimental Test of Bell's Inequalities Using Time- Varying Analyzers," *Physical Review Letters*, vol. 49, pp. 1804–1807, Dec. 1982.

[20] S. Haroche and D. Kleppner, "Cavity Quantum Electrodynamics," *Physics Today*, vol. 42, pp. 24–30, Jan. 1989.

[21] M. Brune, F. Schmidt-Kaler, A. Maali, J. Dreyer, E. Hagley, J. M. Raimond, and S. Haroche, "Quantum Rabi Oscillation: A Direct Test of Field Quantization in a Cavity," *Physical Review Letters*, vol. 76, pp. 1800–1803, Mar. 1996.

[22] J. M. Raimond, M. Brune, S. Haroche, and L. K. Brossel, "Colloquium: Manipulating quantum entanglement with atoms and photons in a cavity," *Rev. Mod. Phys.*, vol. 73, no. 3, 2001.

[23] M. A. Nielsen and I. L. Chuang, "Quantum Computation and Quantum Information: 10th Anniversary Edition," Dec. 2010. ISBN: 9780511976667 Publisher: Cambridge University Press.

[24] O. Freire Junior, "Alain Aspect's experiments on Bell's theorem: a turning point in the history of the research on the foundations of quantum mechanics," *The European Physical Journal D*, vol. 76, p. 248, Dec. 2022.

[25] J. P. Dowling and G. J. Milburn, "Quantum technology: the second quantum revolution," *Philosophical Transactions of the Royal Society of London. Series A: Mathematical, Physical and Engineering Sciences*, vol. 361, pp. 1655–1674, Aug. 2003.

[26] C. E. Shannon, "A Mathematical Theory of Communication," p. 55.

[27] O. Ezratty, "Understanding Quantum Technologies 2022,"

[28] C. H. Bennett and G. Brassard, "Quantum cryptography: Public key distribution and coin tossing," *Theoretical Computer Science*, vol. 560, pp. 7–11, Dec. 2014. arXiv:2003.06557 [quant-ph].

[29] C. H. Bennett, G. Brassard, C. Crépeau, R. Jozsa, A. Peres, and W. K. Wootters, "Teleporting an unknown quantum state via dual classical and Einstein-Podolsky-Rosen channels," *Physical Review Letters*, vol. 70, pp. 1895–1899, Mar. 1993. Publisher: American Physical Society.

[30] C. H. Bennett and S. J. Wiesner, "Communication via one- and two-particle operators on Einstein-Podolsky-Rosen states," *Physical Review Letters*, vol. 69, pp. 2881–2884, Nov. 1992. Publisher: American Physical Society.

[31] H. J. Kimble, "The quantum internet," *Nature*, vol. 453, pp. 1023–1030, June 2008.

[32] A. S. Sheremet, M. I. Petrov, I. V. Iorsh, A. V. Poshakinskiy, and A. N. Poddubny, "Waveguide quantum electrodynamics: Collective radiance and photon-photon correlations," *Reviews of Modern Physics*, vol. 95, p. 015002, Mar. 2023. Publisher: American Physical Society.

[33] V. Giesz, N. Somaschi, G. Hornecker, T. Grange, B. Reznychenko, L. De Santis, J. Demory, C. Gomez, I. Sagnes, A. Lemaître, O. Krebs, N. D. Lanzillotti-Kimura, L. Lanco, A. Auffeves, and P. Senellart, "Coherent manipulation of a solid-state artificial atom with few photons," *Nature Communications*, vol. 7, p. 11986, June 2016. Number: 1 Publisher: Nature Publishing Group.

[34] E. Distante, S. Daiss, S. Langenfeld, L. Hartung, P. Thomas, O. Morin, G. Rempe, and S. Welte, "Detecting an Itinerant Optical Photon Twice without Destroying It," *Physical Review Letters*, vol. 126, p. 253603, June 2021. Publisher: American Physical Society.

[35] X. Gu, A. F. Kockum, A. Miranowicz, Y.-x. Liu, and F. Nori, "Microwave photonics with superconducting quantum circuits," *Physics Reports*, vol. 718-719, pp. 1–102, Nov. 2017.

[36] H.-P. Breuer, F. Petruccione, and S. o. P. a. A. P. F. Petruccione, *The Theory of Open Quantum Systems*. Oxford University Press, 2002. Google-Books-ID: 0Yx5VzaMYm8C.

[37] H. Carmichael, *An Open Systems Approach to Quantum Optics: Lectures Presented at the Université Libre de Bruxelles October 28 to November 4, 1991*, vol. 18 of *Lecture Notes in Physics Monographs*. Berlin, Heidelberg: Springer, 1993.

[38] M. Maffei, P. A. Camati, and A. Auffèves, "Closed-System Solution of the 1D Atom from Collision Model," *arXiv:2112.09672 [quant-ph]*, Dec. 2021. arXiv: 2112.09672.

[39] M. Maffei, P. A. Camati, and A. Auffèves, "Probing nonclassical light fields with energetic witnesses in waveguide quantum electrodynamics," *Physical Review Research*, vol. 3, p. L032073, Sept. 2021.

[40] F. Ciccarello, S. Lorenzo, V. Giovannetti, and G. M. Palma, "Quantum collision models: open system dynamics from repeated interactions," *Physics Reports*, vol. 954, pp. 1–70, Apr. 2022. arXiv:2106.11974 [quant-ph].

[41] A. Blais, A. L. Grimsmo, S. Girvin, and A. Wallraff, "Circuit quantum electrodynamics," *Reviews of Modern Physics*, vol. 93, p. 025005, May 2021. Publisher: American Physical Society.

[42] L. Lanco and P. Senellart, "A highly efficient single photon-single quantum dot interface," Feb. 2015. arXiv:1502.01062 [cond-mat, physics:quant-ph].

[43] P. Lodahl, S. Mahmoodian, and S. Stobbe, "Interfacing single photons and single quantum dots with photonic nanostructures," *Reviews of Modern Physics*, vol. 87, pp. 347–400, May 2015.

[44] Q. A. Turchette, C. J. Hood, W. Lange, H. Mabuchi, and H. J. Kimble, "Measurement of Conditional Phase Shifts for Quantum Logic," *Physical Review Letters*, vol. 75, pp. 4710–4713, Dec. 1995.

[45] I. Buluta, S. Ashhab, and F. Nori, "Natural and artificial atoms for quantum computation," *Reports on Progress in Physics*, vol. 74, p. 104401, Oct. 2011.

[46] A. Blais, R.-S. Huang, A. Wallraff, S. M. Girvin, and R. J. Schoelkopf, "Cavity quantum electrodynamics for superconducting electrical circuits: An architecture for quantum computation," *Physical Review A*, vol. 69, p. 062320, June 2004.

[47] T. Picot, A. Lupaşcu, S. Saito, C. J. P. M. Harmans, and J. E. Mooij, "Role of relaxation in the quantum measurement of a superconducting qubit using a nonlinear oscillator," *Physical Review B*, vol. 78, p. 132508, Oct. 2008.

[48] P. Campagne-Ibarcq, L. Bretheau, E. Flurin, A. Auffèves, F. Mallet, and B. Huard, "Observing interferences between past and future quantum states in resonance fluorescence," *Physical Review Letters*, vol. 112, p. 180402, May 2014. arXiv:1311.5605 [quant-ph].

[49] A. Lupaşcu, S. Saito, T. Picot, P. C. de Groot, C. J. P. M. Harmans, and J. E. Mooij, "Quantum non-demolition measurement of a superconducting two-level system," *Nature Physics*, vol. 3, pp. 119–123, Feb. 2007. Number: 2 Publisher: Nature Publishing Group.

[50] M. Ansmann, H. Wang, R. C. Bialczak, M. Hofheinz, E. Lucero, M. Neeley, A. D. O'Connell, D. Sank, M. Weides, J. Wenner, A. N. Cleland, and J. M. Martinis, "Violation of Bell's inequality in Josephson phase qubits," *Nature*, vol. 461, pp. 504–506, Sept. 2009. Number: 7263 Publisher: Nature Publishing Group.

[51] A. Palacios-Laloy, F. Mallet, F. Nguyen, P. Bertet, D. Vion, D. Esteve, and A. N. Korotkov, "Experimental violation of a Bell's inequality in time with weak measurement," *Nature Physics*, vol. 6, pp. 442–447, June 2010. Number: 6 Publisher: Nature Publishing Group.

[52] J. Stevens, D. Szombati, M. Maffei, C. Elouard, R. Assouly, N. Cottet, R. Dassonneville, Q. Ficheux, S. Zeppetzauer, A. Bienfait, A. N. Jordan, A. Auffèves, and B. Huard, "Energetics of a Single Qubit Gate," *Physical Review Letters*, vol. 129, p. 110601, Sept. 2022. arXiv:2109.09648 [quant-ph].

[53] M. Maffei, C. Elouard, B. O. Goes, B. Huard, A. N. Jordan, and A. Auffèves, "Anomalous energy exchanges and Wigner-function negativities in a single-qubit gate," *Physical Review A*, vol. 107, p. 023710, Feb. 2023.

[54] M. F. Pusey, "Anomalous Weak Values Are Proofs of Contextuality," *Physical Review Letters*, vol. 113, p. 200401, Nov. 2014. arXiv: 1409.1535.

[55] R. I. Booth, U. Chabaud, and P.-E. Emeriau, "Contextuality and Wigner Negativity Are Equivalent for Continuous-Variable Quantum Measurements," *Physical Review Letters*, vol. 129, p. 230401, Nov. 2022.

[56] A. Serafini, *Quantum Continuous Variables: A Primer of Theoretical Methods*. CRC Press, Taylor & Francis Group, 2017. Google-Books-ID: zHtgvgAACAAJ.

[57] M. Walschaers, "Non-Gaussian Quantum States and Where to Find Them," *PRX Quantum*, vol. 2, p. 030204, Sept. 2021.

[58] J. P. Zwolak and J. M. Taylor, "Colloquium: Advances in automation of quantum dot devices control," *arXiv:2112.09362 [cond-mat, physics:quant-ph]*, Dec. 2021. arXiv: 2112.09362.

[59] A. M. Fox, *Quantum Optics: An Introduction*. OUP Oxford, Apr. 2006. Google-Books-ID: 2YESDAAAQBAJ.

[60] E. M. Purcell, H. C. Torrey, and R. V. Pound, "Resonance Absorption by Nuclear Magnetic Moments in a Solid," *Physical Review*, vol. 69, pp. 37–38, Jan. 1946. Publisher: American Physical Society.

[61] P. Senellart, "Semiconductor single-photon sources: progresses and applications," *Photoniques*, no. 107, pp. 40–43, 2021. Publisher: EDP Sciences.

[62] V. Giesz, N. Somaschi, L. D. Santis, S. L. Portalupi, C. Arnold, O. Gazzano, A. Nowak, A. Lemaitre, I. Sagnes, L. Lanco, and P. Senellart, "Quantum dot based quantum optics," in *Advanced Photonics 2015 (2015), paper IS4A.3*, p. IS4A.3, Optica Publishing Group, June 2015.

[63] N. Coste, D. A. Fioretto, N. Belabas, S. C. Wein, P. Hilaire, R. Frantzeskakis, M. Gundin, B. Goes, N. Somaschi, M. Morassi, A. Lemaître, I. Sagnes, A. Harouri, S. E. Economou, A. Auffeves, O. Krebs, L. Lanco, and P. Senellart, "High-rate entanglement between a semiconductor spin and indistinguishable photons," *Nature Photonics*, Apr. 2023.

[64] N. Somaschi, V. Giesz, L. De Santis, J. C. Loredo, M. P. Almeida, G. Hornecker, S. L. Portalupi, T. Grange, C. Antón, J. Demory, C. Gómez, I. Sagnes, N. D. Lanzillotti-Kimura, A. Lemaítre, A. Auffeves, A. G. White, L. Lanco, and P. Senellart, "Near-optimal single-photon sources in the solid state," *Nature Photonics*, vol. 10, pp. 340–345, May 2016.

[65] D. P. DiVincenzo, "The Physical Implementation of Quantum Computation," *Fortschritte der Physik*, vol. 48, pp. 771–783, Sept. 2000.

[66] L. Zaporski, N. Shofer, J. H. Bodey, S. Manna, G. Gillard, D. M. Jackson, M. H. Appel, C. Schimpf, S. C. da Silva, J. Jarman, G. Delamare, G. Park, U. Haeusler, E. A. Chekhovich, A. Rastelli, D. A. Gangloff, M. Atatüre, and C. L. Gall, "Ideal refocusing of an optically active spin qubit under strong hyperfine interactions," June 2022. arXiv:2206.01223 [cond-mat, physics:quant-ph].

[67] D. Loss and D. P. DiVincenzo, "Quantum computation with quantum dots," *Physical Review A*, vol. 57, pp. 120–126, Jan. 1998.

[68] N. H. Lindner and T. Rudolph, "Proposal for Pulsed On-Demand Sources of Photonic Cluster State Strings," *Physical Review Letters*, vol. 103, p. 113602, Sept. 2009.

[69] R. Jozsa, "An introduction to measurement based quantum computation," *arXiv:quant-ph/0508124*, Sept. 2005. arXiv: quant-ph/0508124.

[70] P. Hilaire, C. Millet, J. C. Loredo, C. Antón, A. Harouri, A. Lemaître, I. Sagnes, N. Somaschi, O. Krebs, P. Senellart, and L. Lanco, "Deterministic assembly of a charged-quantum-dot–micropillar cavity device," *Physical Review B*, vol. 102, p. 195402, Nov. 2020. Publisher: American Physical Society.

[71] C. Arnold, J. Demory, V. Loo, A. Lemaître, I. Sagnes, M. Glazov, O. Krebs, P. Voisin, P. Senellart, and L. Lanco, "Macroscopic rotation of photon polarization induced by a single spin," *Nature Communications*, vol. 6, p. 6236, May 2015.

[72] E. Mehdi, M. Gundin-Martinez, C. Millet, N. Somaschi, A. Lemaître, I. Sagnes, L. L. Gratiet, D. Fioretto, N. Belabas, O. Krebs, P. Senellart, and L. Lanco, "Controlling photon polarisation with a single quantum dot spin," Dec. 2022. arXiv:2212.03767 [cond-mat, physics:physics, physics:quant-ph].

[73] M. Maffei, P. A. Camati, and A. Auffèves, "Closed-System Solution of the 1D Atom from Collision Model," *Entropy*, vol. 24, p. 151, Jan. 2022.

[74] M. Maffei, B. O. Goes, S. C. Wein, A. N. Jordan, L. Lanco, and A. Auffèves, "Energy-efficient quantum non-demolition measurement with a spin-photon interface," *Quantum*, vol. 7, p. 1099, Aug. 2023.

[75] N. Coste, M. Gundin, D. Fioretto, S. E. Thomas, C. Millet, E. Medhi, M. Gundin, N. Somaschi, M. Morassi, M. Pont, A. Lemaitre, N. Belabas,

O. Krebs, L. Lanco, and P. Senellart, "Probing the dynamics and coherence of a semiconductor hole spin via acoustic phonon-assisted excitation," July 2022. arXiv:2207.05981 [cond-mat, physics:quant-ph].

[76] B. O. Goes, "PhD Thesis SPI Codes Repository." https://github.com/BrunoOGoes/PhDThesisSPI, 2023.

[77] J. Johansson, P. Nation, and F. Nori, "QuTiP: An open-source Python framework for the dynamics of open quantum systems," *Computer Physics Communications*, vol. 183, pp. 1760–1772, Aug. 2012.

[78] J. Johansson, P. Nation, and F. Nori, "QuTiP 2: A Python framework for the dynamics of open quantum systems," *Computer Physics Communications*, vol. 184, pp. 1234–1240, Apr. 2013.

[79] G. T. Landi, "Melt! A Mathematica library for quantum simulations.," 2023.

[80] J. v. Neumann, *Mathematical Foundations of Quantum Mechanics: New Edition*. Princeton University Press, Feb. 2018. Google-Books-ID: B3OYDwAAQBAJ.

[81] C. Gardiner and P. Zoller, *Quantum Noise: A Handbook of Markovian and Non-Markovian Quantum Stochastic Methods with Applications to Quantum Optics*. Springer Science & Business Media, Aug. 2004. Google-Books-ID: a_xsT8oGhdgC.

[82] W. H. Zurek, "Decoherence, einselection, and the quantum origins of the classical," *Reviews of Modern Physics*, vol. 75, pp. 715–775, May 2003.

[83] V. B. Braginsky, F. Y. Khalili, and K. S. Thorne, *Quantum Measurement*. Cambridge: Cambridge University Press, 1992.

[84] G. T. Landi, M. J. Kewming, M. T. Mitchison, and P. P. Potts, "Current fluctuations in open quantum systems: Bridging the gap between quantum continuous measurements and full counting statistics," Mar. 2023. arXiv:2303.04270 [cond-mat, physics:quant-ph].

[85] B. O. Goes and G. T. Landi, "Entropy production dynamics in quench protocols of a driven-dissipative critical system," *Physical Review A*, vol. 102, p. 052202, Nov. 2020.

[86] C. A. Fuchs and C. M. Caves, "Mathematical techniques for quantum communication theory," *Open Systems & Information Dynamics*, vol. 3, pp. 345–356, Oct. 1995.

[87] C. Fuchs and J. van de Graaf, "Cryptographic distinguishability measures for quantum-mechanical states," *IEEE Transactions on Information Theory*, vol. 45, pp. 1216–1227, May 1999.

[88] K. A. Fischer, R. Trivedi, V. Ramasesh, I. Siddiqi, and J. Vučković, "Scattering into one-dimensional waveguides from a coherently-driven quantum-optical system," *Quantum*, vol. 2, p. 69, May 2018. arXiv: 1710.02875.

[89] A. H. Kiilerich and K. Mølmer, "Input-Output Theory with Quantum Pulses," *Physical Review Letters*, vol. 123, p. 123604, Sept. 2019.

[90] J. A. Gross, C. M. Caves, G. J. Milburn, and J. Combes, "Qubit models of weak continuous measurements: markovian conditional and open-system dynamics," *Quantum Science and Technology*, vol. 3, p. 024005, Feb. 2018. Publisher: IOP Publishing.

[91] R. Loudon, *The Quantum Theory of Light*. OUP Oxford, Sept. 2000. Google-Books-ID: AEkfajgqldoC.

[92] C. W. Gardiner and M. J. Collett, "Input and output in damped quantum systems: Quantum stochastic differential equations and the master equation," *Physical Review A*, vol. 31, pp. 3761–3774, June 1985.

[93] J. J. Sakurai and J. Napolitano, "Modern Quantum Mechanics," Sept. 2017. ISBN: 9781108499996 Publisher: Cambridge University Press.

[94] F. Ciccarello, "Collision models in quantum optics," *Quantum Measurements and Quantum Metrology*, vol. 4, Dec. 2017.

[95] D. Manzano, "A short introduction to the Lindblad Master Equation," *AIP Advances*, vol. 10, p. 025106, Feb. 2020. arXiv: 1906.04478.

[96] S. Das, L. Zhai, M. Čepulskovskis, A. Javadi, S. Mahmoodian, P. Lodahl, and A. S. Sørensen, "A wave-function ansatz method for calculating field correlations and its application to the study of spectral filtering and quantum dynamics of multi-emitter systems," Dec. 2019. arXiv:1912.08303 [physics, physics:quant-ph].

[97] V. Weisskopf and E. Wigner, "Berechnung der natürlichen Linienbreite auf Grund der Diracschen Lichttheorie," *Zeitschrift für Physik*, vol. 63, pp. 54–73, Jan. 1930.

[98] M. Le Bellac, *Quantum Physics*. Cambridge: Cambridge University Press, 2006.

[99] J. Larson and T. K. Mavrogordatos, *The Jaynes-Cummings model and its descendants*. Dec. 2021. arXiv:2202.00330 [cond-mat, physics:physics, physics:quant-ph].

[100] W.-L. L. a. G. Zhang and R.-B. Wu, "On the Control of Flying Qubits," Oct. 2021. arXiv:2111.00143 [quant-ph].

[101] A. Dąbrowska, D. Chruściński, S. Chakraborty, and G. Sarbicki, "Eternally non-Markovian dynamics of a qubit interacting with a single-photon wavepacket," *New Journal of Physics*, vol. 23, p. 123019, Dec. 2021.

[102] J. T. Shen and S. Fan, "Coherent photon transport from spontaneous emission in one-dimensional waveguides," *Optics Letters*, vol. 30, pp. 2001–2003, Aug. 2005. Publisher: Optica Publishing Group.

[103] C. Budroni, A. Cabello, O. Gühne, M. Kleinmann, and J.- Larsson, "Kochen-Specker Contextuality," *Reviews of Modern Physics*, vol. 94, p. 045007, Dec. 2022. arXiv:2102.13036 [math-ph, physics:physics, physics:quant-ph].

[104] R. Raussendorf, "Contextuality in measurement-based quantum computation," *Physical Review A*, vol. 88, p. 022322, Aug. 2013.

[105] M. Howard, J. Wallman, V. Veitch, and J. Emerson, "Contextuality supplies the 'magic' for quantum computation," *Nature*, vol. 510, pp. 351–355, June 2014. Number: 7505 Publisher: Nature Publishing Group.

[106] J. Bermejo-Vega, N. Delfosse, D. E. Browne, C. Okay, and R. Raussendorf, "Contextuality as a Resource for Models of Quantum Computation with Qubits," *Physical Review Letters*, vol. 119, p. 120505, Sept. 2017.

[107] J. S. Bell, "On the Einstein Podolsky Rosen paradox," *Physics Physique Fizika*, vol. 1, pp. 195–200, Nov. 1964. Publisher: American Physical Society.

[108] R. W. Spekkens, "Negativity and Contextuality are Equivalent Notions of Nonclassicality," *Physical Review Letters*, vol. 101, p. 020401, July 2008.

[109] E. Wigner, "On the Quantum Correction For Thermodynamic Equilibrium," *Physical Review*, vol. 40, pp. 749–759, June 1932.

[110] A. Kenfack and K. Yczkowski, "Negativity of the Wigner function as an indicator of non-classicality," *Journal of Optics B: Quantum and Semiclassical Optics*, vol. 6, pp. 396–404, Oct. 2004.

[111] Y. Aharonov, D. Z. Albert, and L. Vaidman, "How the result of a measurement of a component of the spin of a spin- *1/2* particle can turn out to be 100," *Physical Review Letters*, vol. 60, pp. 1351–1354, Apr. 1988.

[112] Y. Aharonov, A. Botero, S. Popescu, B. Reznik, and J. Tollaksen, "Revisiting Hardy's paradox: counterfactual statements, real measurements, entanglement and weak values," *Physics Letters A*, vol. 301, pp. 130–138, Aug. 2002.

[113] J. Dressel, M. Malik, F. M. Miatto, A. N. Jordan, and R. W. Boyd, "*Colloquium* : Understanding quantum weak values: Basics and applications," *Reviews of Modern Physics*, vol. 86, pp. 307–316, Mar. 2014.

[114] H. M. Wiseman, "Weak values, quantum trajectories, and the cavity-QED experiment on wave-particle correlation," *Physical Review A*, vol. 65, p. 032111, Feb. 2002.

[115] H. M. Wiseman and G. J. Milburn, *Quantum Measurement and Control*. Cambridge: Cambridge University Press, 2009.

[116] P. Bertet, S. Osnaghi, A. Rauschenbeutel, G. Nogues, A. Auffeves, M. Brune, J. M. Raimond, and S. Haroche, "A complementarity experiment with an interferometer at the quantum–classical boundary," *Nature*, vol. 411, pp. 166–170, May 2001. Number: 6834 Publisher: Nature Publishing Group.

[117] S. Gammelmark, B. Julsgaard, and K. Mølmer, "Past Quantum States of a Monitored System," *Physical Review Letters*, vol. 111, p. 160401, Oct. 2013.

[118] S. Gammelmark, B. Julsgaard, and K. Mølmer, "Past quantum states," *Physical Review Letters*, vol. 111, p. 160401, Oct. 2013. arXiv:1305.0681 [quant-ph].

[119] F. A. M. de Oliveira, M. S. Kim, P. L. Knight, and V. Buek, "Properties of displaced number states," *Physical Review A*, vol. 41, pp. 2645–2652, Mar. 1990.

[120] K. E. Cahill and R. J. Glauber, "Ordered Expansions in Boson Amplitude Operators," *Physical Review*, vol. 177, pp. 1857–1881, Jan. 1969.

[121] M. Atatüre, D. Englund, N. Vamivakas, S.-Y. Lee, and J. Wrachtrup, "Material platforms for spin-based photonic quantum technologies," *Nature Reviews Materials*, vol. 3, pp. 38–51, May 2018. Number: 5 Publisher: Nature Publishing Group.

[122] R. Raussendorf and H. J. Briegel, "A One-Way Quantum Computer," *Physical Review Letters*, vol. 86, pp. 5188–5191, May 2001. Publisher: American Physical Society.

[123] D. E. Browne and T. Rudolph, "Resource-Efficient Linear Optical Quantum Computation," *Physical Review Letters*, vol. 95, p. 010501, June 2005. Publisher: American Physical Society.

[124] M. Gimeno-Segovia, P. Shadbolt, D. E. Browne, and T. Rudolph, "From Three-Photon Greenberger-Horne-Zeilinger States to Ballistic Universal Quantum Computation," *Physical Review Letters*, vol. 115, p. 020502, July 2015. Publisher: American Physical Society.

[125] H.-J. Briegel, W. Dür, J. I. Cirac, and P. Zoller, "Quantum Repeaters: The Role of Imperfect Local Operations in Quantum Communication," *Physical Review Letters*, vol. 81, pp. 5932–5935, Dec. 1998.

[126] K. Azuma, K. Tamaki, and H.-K. Lo, "All-photonic quantum repeaters," *Nature Communications*, vol. 6, p. 6787, Apr. 2015. Number: 1 Publisher: Nature Publishing Group.

[127] D. Buterakos, E. Barnes, and S. E. Economou, "Deterministic Generation of All-Photonic Quantum Repeaters from Solid-State Emitters," *Physical Review X*, vol. 7, p. 041023, Oct. 2017. Publisher: American Physical Society.

[128] S. Wehner, D. Elkouss, and R. Hanson, "Quantum internet: A vision for the road ahead," *Science*, vol. 362, p. eaam9288, Oct. 2018. Publisher: American Association for the Advancement of Science.

[129] J. Borregaard, H. Pichler, T. Schröder, M. D. Lukin, P. Lodahl, and A. S. Sørensen, "One-Way Quantum Repeater Based on Near-Deterministic Photon-Emitter Interfaces," *Physical Review X*, vol. 10, p. 021071, June 2020. Publisher: American Physical Society.

[130] M. Pompili, S. L. N. Hermans, S. Baier, H. K. C. Beukers, P. C. Humphreys, R. N. Schouten, R. F. L. Vermeulen, M. J. Tiggelman, L. dos Santos Martins, B. Dirkse, S. Wehner, and R. Hanson, "Realization of a multinode quantum network of remote solid-state qubits," *Science*, vol. 372, pp. 259–264, Apr. 2021. Publisher: American Association for the Advancement of Science.

[131] C. Y. Hu, "Spin-based single-photon transistor, dynamic random access memory, diodes, and routers in semiconductors," *Physical Review B*, vol. 94, p. 245307, Dec. 2016. Publisher: American Physical Society.

[132] C. Y. Hu, A. Young, J. L. O'Brien, W. J. Munro, and J. G. Rarity, "Giant optical Faraday rotation induced by a single-electron spin in a quantum dot: Applications to entangling remote spins via a single photon," *Physical Review B*, vol. 78, p. 085307, Aug. 2008. Publisher: American Physical Society.

[133] C. Bonato, F. Haupt, S. S. R. Oemrawsingh, J. Gudat, D. Ding, M. P. van Exter, and D. Bouwmeester, "CNOT and Bell-state analysis in the weak-coupling cavity QED regime," *Physical Review Letters*, vol. 104, p. 160503, Apr. 2010. Publisher: American Physical Society.

[134] K. Kojima, H. F. Hofmann, S. Takeuchi, and K. Sasaki, "Efficiencies for the single-mode operation of a quantum optical nonlinear shift gate," *Physical Review A*, vol. 70, p. 013810, July 2004. Publisher: American Physical Society.

[135] I. Schwartz, D. Cogan, E. R. Schmidgall, Y. Don, L. Gantz, O. Kenneth, N. H. Lindner, and D. Gershoni, "Deterministic Generation of a Cluster State of Entangled Photons," *Science*, vol. 354, pp. 434–437, Oct. 2016. arXiv: 1606.07492.

[136] P. Grangier, J. A. Levenson, and J.-P. Poizat, "Quantum non-demolition measurements in optics," *Nature*, vol. 396, pp. 537–542, Dec. 1998. Number: 6711 Publisher: Nature Publishing Group.

[137] M. J. Kewming, S. Shrapnel, and G. J. Milburn, "Designing a physical quantum agent," *Physical Review A*, vol. 103, p. 032411, Mar. 2021.

[138] L. H. Pedersen, N. M. Møller, and K. Mølmer, "Fidelity of quantum operations," *Physics Letters A*, vol. 367, pp. 47–51, July 2007.

[139] J. Ghosh, A. Galiautdinov, Z. Zhou, A. N. Korotkov, J. M. Martinis, and M. R. Geller, "High-fidelity controlled- Z gate for resonator-based superconducting quantum computers," *Physical Review A*, vol. 87, p. 022309, Feb. 2013.

[140] A. N. Korotkov, "Error matrices in quantum process tomography," Nov. 2013. arXiv:1309.6405 [quant-ph].

[141] B. W. Roberts, "Kramers degeneracy without eigenvectors," *Physical Review A*, vol. 86, p. 034103, Sept. 2012.

[142] A. Auffèves-Garnier, C. Simon, J.-M. Gérard, and J.-P. Poizat, "Giant optical nonlinearity induced by a single two-level system interacting with a cavity in the Purcell regime," *Physical Review A*, vol. 75, p. 053823, May 2007.

[143] C. A. Fuchs and C. M. Caves, "Ensemble-Dependent Bounds for Accessible Information in Quantum Mechanics," *Physical Review Letters*, vol. 73, pp. 3047–3050, Dec. 1994.

[144] S. L. McCall and E. L. Hahn, "Self-Induced Transparency by Pulsed Coherent Light," *Physical Review Letters*, vol. 18, pp. 908–911, May 1967.

[145] S. L. McCall and E. L. Hahn, "Self-Induced Transparency," *Physical Review*, vol. 183, pp. 457–485, July 1969.

[146] V. A. Alekseev and B. Y. Zel'dovich, "Derivation of the area theorem in self-induced transparency," *Soviet Journal of Quantum Electronics*, vol. 5, pp. 589–590, May 1975.

[147] J. Eberly, "Area Theorem rederived," *Optics Express*, vol. 2, p. 173, Mar. 1998.

[148] J. C. Delagnes and M. A. Bouchene, "Beyond the pulse-area theorem: Role of the absorption and the dispersion in the propagation of weak ultrashort resonant pulses," *Optics Communications*, vol. 281, pp. 5824–5829, Dec. 2008.

[149] E. Knill, R. Laflamme, and G. J. Milburn, "A scheme for efficient quantum computation with linear optics," *nature*, vol. 409, no. 6816, pp. 46–52, 2001.

[150] L.-M. Duan and H. J. Kimble, "Scalable Photonic Quantum Computation through Cavity-Assisted Interactions," *Physical Review Letters*, vol. 92, p. 127902, Mar. 2004.

[151] P. Kok, W. J. Munro, K. Nemoto, T. C. Ralph, J. P. Dowling, and G. J. Milburn, "Review article: Linear optical quantum computing," *Reviews of Modern Physics*, vol. 79, pp. 135–174, Jan. 2007. arXiv:quant-ph/0512071.

[152] D. Gottesman, "An Introduction to Quantum Error Correction and Fault-Tolerant Quantum Computation," Apr. 2009. arXiv:0904.2557 [quant-ph].

[153] D. E. Chang, V. Vuletić, and M. D. Lukin, "Quantum nonlinear optics — photon by photon," *Nature Photonics*, vol. 8, pp. 685–694, Sept. 2014.

[154] K. Reuer, J.-C. Besse, L. Wernli, P. Magnard, P. Kurpiers, G. J. Norris, A. Wallraff, and C. Eichler, "Realization of a Universal Quantum Gate Set for Itinerant Microwave Photons," June 2021. arXiv:2106.03481 [quant-ph].

[155] M. R. Geller and Z. Zhou, "Efficient error models for fault-tolerant architectures and the Pauli twirling approximation," *Physical Review A*, vol. 88, p. 012314, July 2013.

[156] I. L. Chuang and M. A. Nielsen, "Prescription for experimental determination of the dynamics of a quantum black box," *Journal of Modern Optics*, vol. 44, pp. 2455–2467, Nov. 1997.

[157] J. F. Poyatos, J. I. Cirac, and P. Zoller, "Complete Characterization of a Quantum Process: the Two-Bit Quantum Gate," *Physical Review Letters*, vol. 78, pp. 390–393, Jan. 1997. arXiv:quant-ph/9611013.

[158] R. Raussendorf, D. E. Browne, and H. J. Briegel, "Measurement-based quantum computation on cluster states," *Physical Review A*, vol. 68, p. 022312, Aug. 2003. Publisher: American Physical Society.

[159] W. A. Coish and D. Loss, "Hyperfine interaction in a quantum dot: Non-Markovian electron spin dynamics," *Physical Review B*, vol. 70, p. 195340, Nov. 2004. Publisher: American Physical Society.

[160] J. H. Prechtel, A. V. Kuhlmann, J. Houel, A. Ludwig, S. R. Valentin, A. D. Wieck, and R. J. Warburton, "Decoupling a hole spin qubit from the nuclear spins," *Nature Materials*, vol. 15, pp. 981–986, Sept. 2016. Number: 9 Publisher: Nature Publishing Group.

[161] C. Schön, K. Hammerer, M. M. Wolf, J. I. Cirac, and E. Solano, "Sequential generation of matrix-product states in cavity QED," *Physical Review A*, vol. 75, p. 032311, Mar. 2007.

[162] E. M. González-Ruiz, F. T. Østfeldt, R. Uppu, P. Lodahl, and A. S. Sørensen, "Entanglement properties of a quantum-dot biexciton cascade in a chiral nanophotonic waveguide," Jan. 2023. arXiv:2301.04444 [quant-ph].

[163] C. Cabrillo, J. I. Cirac, P. García-Fernández, and P. Zoller, "Creation of entangled states of distant atoms by interference," *Physical Review A*, vol. 59, pp. 1025–1033, Feb. 1999. Publisher: American Physical Society.

[164] L.-M. Duan, M. D. Lukin, J. I. Cirac, and P. Zoller, "Long-distance quantum communication with atomic ensembles and linear optics," *Nature*, vol. 414, pp. 413–418, Nov. 2001. Number: 6862 Publisher: Nature Publishing Group.

[165] D. L. Moehring, P. Maunz, S. Olmschenk, K. C. Younge, D. N. Matsukevich, L.-M. Duan, and C. Monroe, "Entanglement of single-atom quantum bits at a distance," *Nature*, vol. 449, pp. 68–71, Sept. 2007. Number: 7158 Publisher: Nature Publishing Group.

[166] I. M. d. B. Wenniger, S. E. Thomas, M. Maffei, S. C. Wein, M. Pont, N. Belabas, S. Prasad, A. Harouri, A. Lemaître, I. Sagnes, N. Somaschi, A. Auffèves, and P. Senellart, "Experimental analysis of energy transfers between a quantum emitter and light fields," June 2023. arXiv:2202.01109 [quant-ph].

[167] M. Suzuki, "Generalized Trotter's formula and systematic approximants of exponential operators and inner derivations with applications to many-body problems," *Communications in Mathematical Physics*, vol. 51, pp. 183–190, June 1976.